Cancer-Host Interactions Influencing Disease Progression and Therapy

Cancer-host interactions influencing disease progression and therapy

A dissertation presented

by

Camilla Engblom

to

The Division of Medical Sciences

in partial fulfillment of the requirements

for the degree of

Doctor of Philosophy

in the subject of

Immunology

Harvard University
Cambridge, Massachusetts

April 2017

Dissertation Advisor: Dr. Mikael Pittet Camilla Engblom

Cancer-host interactions influencing disease progression and therapy

Abstract

Solid tumors are infiltrated by non-malignant cells that actively shape cancer growth. These include immune cells, which are comprised of various lymphoid and myeloid cell subsets displaying diverse tumor-regulatory functions. In the past decade, targeting the immune system has been validated as an effective strategy to treat cancer, as therapeutically manipulating certain immune cells, such as T lymphocytes, can durably control cancer progression in some patients. Despite these remarkable advances in cancer therapy, our mechanistic understanding of tumor-immune interactions remains incomplete. For example, cancer-exerted effects on host responses beyond the local tumor microenvironment are less studied, but could be highly relevant since tumor-infiltrating immune cells are dynamically replenished by bone marrow-derived cells. Additionally, which, and how, immune cell subsets control tumor progression, and to what extent these processes are perturbed by (and can be harnessed for) anticancer therapies, require clarification. Addressing these types of questions could not only expand our fundamental knowledge of tumor progression, but also have far-reaching consequences by offering new therapeutic avenues.

With these ultimate goals in mind, we have begun to interrogate various aspects of tumor-immune interactions using pre-clinical tumor models. We focused on lung cancer, as it remains the number one cause of cancer-related deaths worldwide and many patients lack effective treatments. First, we investigated long-range interactions between lung tumors and the bone. Our findings newly link bone marrow stromal cells to distant tumor outgrowth via the production

of cancer-promoting myeloid cells. Second, we asked whether selecting chemotherapeutic drugs to exploit their immune stimulatory capacities could generate a T cell rich tumor stroma amenable to immunotherapy targeting. Here, we identified a drug combination that controls cancer growth, stimulates tumor T cell infiltration, and sensitizes tumors to checkpoint blockade therapy. Third, we comprehensively mapped tumor-infiltrating immune cell transcriptomes on a single cell level to reveal previously unappreciated cancer- and immunotherapy-induced myeloid cell substates in the lung.

Combined, we provide new insight into local and systemic tumor-host interactions and drug effects on tumor microenvironments, which could be harnessed for clinical translation.

Table of Contents

Acknowledgements

Completing this PhD has been an exhilarating and challenging journey. I feel very fortunate to have shared this time with such incredible people.

I am deeply grateful for the outstanding support that I have received from my thesis advisor and mentor, Mikael Pittet. Your scientific creativity and curiosity, efficiency, humility, critical feedback, artistic skills(!), and thoughtful leadership is something that I aspire to. I truly appreciate what you have given me.

Christina Pfirschke, my lab partner in crime, we are a great team! I admire your commitment, smarts, organizational skills, and I appreciate your positive attitude when my spirits are low. The studies presented in this thesis are a product of our collective hands, minds, and hearts.

Thank you to all the Pittet lab members, past and present (Ferdinando, Chris, Marie, Hsin-Wei, Virna, Andita, Jaclyn, Martin, honorary member Sean, and all of our fantastic rotation students) not only for your scientific input, but also for your kindness, humor, and excitement. I have learned a lot from all of you and I am proud to be your colleague.

Thank you to all of my wonderful collaborators! Without you, these projects would not have been possible, or half as fun. Specials thanks to Miriam Bredella and Stijn Bos who performed the tour de force that was the human bone density analysis. Thanks to Rapo, Virginia and Allon for the exciting '*inDrops*' collaboration! It is a pleasure working with and learning from you. Janaina da Silva Martins, thank you for the beautiful bone histology and for your kindness. Gabriel Courties, thank you for always having the answer (and the antibodies) I need, and for the many things you have taught me in the lab (and for imaging during the fireworks)! Ninib and Nicolas, thank you for your unwavering support that was critical in starting up the bone project, friendship, feedback, 70uM filters, and of course, the never-ending Swedish coffee supply.

Thank you to my thesis exam chair, Diane Mathis, for providing critical and helpful feedback throughout my thesis. Thank you Henry Kronenberg for your thoughtful questions regarding our 'bone story'. Shiv Pillai, Sandra McAllister, Stefanie Spranger, Shawn Demehri,

and Glenn Dranoff: thank you for the invaluable feedback and for serving as a member of my PQE, DAC, or thesis committee.

I am indebted to the Harvard Immunology PhD Program who gave me the opportunity to try my ‘immunology’ wings. A special thank you to our current and former program leadership Shiv Pillai, Mike Carroll, Wendy Garrett, and Shannon Turley for the support and guidance. Susan Perkins and Megan Eruzione deserve an eloge for the efficient and kind administrative support. Thanks also to Tatevik Holmgren at DMS, for the help during the last stretch. A shoutout to all the immunology students- I cherish your scientific input and community deeply!

My funding source Boehringer Ingelheim Funds deserves recognition, not just for the financial support which was much appreciated, but also the exceptional workshops and the scientific exchange that was offered.

To all the current and former CSB members - thank you for the scientific discussions, lunch room celebratory cakes/donuts, and communal problem solving when machines stop working or obscure reagents were needed. You made coming to work fun and exciting and I value the community that we have. Thank you! Thank you to our CSB Director Ralph Weissleder for creating an excellent scientific environment. Thank you to Tina, Diane, Serena, Sharon, and Misha for always having our backs.

Thanks also to the Graduate student division at MGH (Thilo, Anna, Donna) who provided great support and the opportunity to engage with the MGH graduate community.

To the scientists and mentors that supported me before and during my PhD, thank you! Devavani, you were the one who showed me the beauty of the immune system and you are responsible for so many aspects of my becoming a researcher. Thank you for always believing in me and for ‘cheering me on wildly from the sidelines’. Thank you also to O-chem professor extraordinaire and supporter Brisbois- I still hear your words ‘Don’t make it harder than it has to be’! Gunnar Nilsson and Carolina Lunderius Andersson (and all of L2:04!!)- thank you for welcoming me to the world of mast cells at Karolinska which set the stage for my PhD.

Friends, I cannot name you all here, but know that you have a special place in my heart

and I could not have done this without you. You kept me happy, fed, running and sane. I love you all! A few special shout-outs are in order: Yi-Jang- you are responsible for so many happy moments during my PhD. A friend like you is hard to find! 34 Williams st (Lisa, Josie, Jonas, Duygu, honorary member Yael), my dear roomies- it was NEVER BORING thanks to you! My PhD would not have been the same without you. My Swedish Boston family (Patricia, Eduardo, Tiiu, Isabel and now Emilia), you were there from the start, both in the lab as scientific role models and at home for so many beautiful memories. My Macalester family (Sarah, the Dream Team, Estela, Leo, Lellie, Skadi, Scotch Tape, the Swedes), you are always in my heart and mind wherever I am in the world. My Swedish family, Stephi (no. 1 fan!), Lotta, and Camilla, we go way back and I am so thankful for our friendship.

Thank you to my extended family who has cheered me on from afar!

My family, you mean the world to me and you make all the days better. Mamma and Pappa, Vendi, and Eyvind thank you for your love, kindness and unwavering support.

Ernesto, I am so lucky to have such an incredible partner in you. You have been there with me at every high, every low and all the in-betweens. I could not have done it without you.

With gratitude,

Camilla

To Mamma and Pappa,

for showing me that the world is full of beautiful music.

“För kvällen gör så vackra visor själv”

- Alf Hambe

Glossary of terms

Carbo	Carboplatin
CSF-1/R	Colony stimulating factor-1/Receptor
CXCL/R	C-X-C Motif Chemokine Ligand/Receptor
Cyc	Cyclophosphamide
DC	Dendritic cell
DTR	Diphtheria toxin receptor
EGFR	Epidermal growth factor receptor
FMT	Fluorescence-mediated tomography
G-CSF	Granulocyte colony-stimulating factor
GN	Granulocyte
HMGB1	High-mobility group box 1 protein
HSC	Hematopoietic stem cell
HSPC	Hematopoeitic stem-and progenitor cell
ICB	Immune checkpoint blockade
IL	Interleukin
KP	Kras/p53 mutant
KRAS	Kirsten rat sarcoma viral oncogene homolog
LLC	Lewis Lung Carcinoma
MM	Macrophage/Monocyte
NSCLC	Non Small Cell Lung Cancer
OCN	Osteocalcin
OVA	Ovalbumin
Oxa	Oxaliplatin
p53	Tumor suppressor 53
PD-1	Programmed cell death 1
PD-L1	Programmed cell death 1 ligand 1
Ptax	Paclitaxel
TLR4	Toll-like receptor 4
YFP	Yellow fluorescent protein
μCT	Micro-computed tomography

List of Figures

Chapter 2

Chapter 3

Chapter 4

Appendix A2

Appendix A3

List of Tables

Appendix A2

Chapter 1: Thesis outline and background

1.1 Overview

The research described in this thesis aims to address issues related to fundamental tumor-host interactions involving the immune system. Principally we aspire to contribute to the field of cancer immunology research on three fronts by

i) asking fundamental mechanistic questions regarding the less-often studied tumor-host responses that occur outside the local tumor microenvironment (Chapter 2);

ii) testing whether carefully selecting drugs based on their capacity to kill tumor cells in an immune-stimulatory manner could amplify antitumor responses in the tumor microenvironment and whether this could sensitize otherwise treatment-resistant tumors to immune checkpoint blockade (Chapter 3);

iii) mapping the tumor-infiltrating immune composition on a single cell level, using an unbiased approach, with the goal to uncover previously unappreciated cell substates and to study their response to a clinically relevant myeloid targeting agent (Chapter 4).

In summary, our objectives are not only to improve the understanding of the underlying mechanisms that drive and/or inhibit tumor progression, but also to open up new vantage points for anticancer therapy.

In the next section, I first outline the broader significance of and challenges to cancer research today, specifically highlighting the recent developments in immunotherapy, which has revolutionized cancer therapy. In Section 1.3, I present a short background on tumor immunology and emphasize key areas of research that could benefit from further study, with the goal to set the stage for the subsequent data-driven chapters (Chapter 2-5). This is followed in Section 1.4 by a brief overview of the approach we have taken to study cancer immunology in the lab. The thesis outline and our main findings discussed in the following chapters are summarized in Section 1.5 (Scope of thesis).

1.2 Significance

Cancer remains a critical public health problem, with nearly fifteen million new cases and over eight million reported cancer-related deaths in the world every year[1]. It has become increasingly clear that cancer represents a collection of heterogeneous diseases that are unlikely to be cured by one 'magic bullet' drug. This diversity of tumor pathology represents a serious challenge for researchers and clinicians; nonetheless, in the past few decades, the fight against cancer has been reinvigorated by several important developments:

i) dramatic advances in next-generation sequencing technologies has enabled a broad-scale interrogation of the cancer genome and transcriptome,

ii) the access to genomic and transcriptomic information has driven cancer care towards 'personalized medicine', in which treatment regimes are selected based on an individual patients' mutational load and tumor stromal components,

iii) the increased appreciation of the tumor microenvironment as a regulator of cancer growth has led to basic discoveries which has provided novel therapeutic targets,

iv) the ability to control cancer progression by manipulating the immune system has dramatically expanded the horizon of cancer therapy.

Thus, although there are many challenges ahead, these types of efforts, and combinations thereof, will likely make more than mere incremental improvements for cancer patients across the globe in the coming few decades.

For the studies presented in this thesis, we aimed to address a set of outstanding basic questions relating to host regulation of cancer progression, involving the immune system. Our work has primarily focused on lung cancer, which remains the number one cause of cancer-related deaths world-wide[1]. Specifically, we have mainly investigated non-small cell lung cancer (NSCLC), which represents the majority of lung cancer cases[2]. The standard of care for NSCLC patients is a combination of surgery, chemotherapy, radiotherapy, and/or targeted therapy (depending on the mutational status of the tumor)[2]. Targeted therapies, such as inhibitors of Epidermal Growth Factor Receptor (EGFR), can dramatically decrease tumor load in some

patients, but drug resistance frequently develops in patients, making the effect short-lasting[3]. Immune checkpoint blockade (ICB) therapies targeting programmed cell death 1/ligand 1 (PD-1/PD-L1) were recently FDA-approved to treat NSCLC and have resulted in unprecedented durable responses in a subset of patients, but many unfortunately fail to respond[4]. In addition, NSCLC patients are typically diagnosed at more advanced stages of disease, since the cancer is often asymptomatic at early stages, making effective treatment even more challenging[2]. Therefore, for a large portion of NSCLC patients, anticancer therapies still offer limited increases in survival[2]. Given the recent successes, and limitations, of immunotherapy-based treatment of NSCLC patients, it is therefore a critical time for basic scientists to investigate relevant fundamental questions involving tumor-immune interactions with the goal to both broaden the scope of pre-existing anticancer therapies and help define novel therapeutic targets.

1.3 Background

Part of this section is reproduced with permission from the following publication
Engblom, C, Pfirschke, C, Pittet, MJ. The role of myeloid cells in cancer therapies. Nat. Rev. Cancer 16, 447–462 (2016).

1.3.1 Overview

In this section, I will present an overview of immune cell regulation of cancer growth both locally (1.3.2) in the tumor stroma and systemically (1.3.3) in the host. In addition, I discuss immune cell involvement in anticancer therapies (1.3.4). This section aims to provide context for the subsequent chapters (2-6), which will further expand on these multifaceted interactions between tumors and the host.

1.3.2 Tumor-infiltrating immune cells shape cancer growth

Solid tumors develop and progress as intricate cellular eco-systems composed of neoplastic and seemingly normal host cell populations. Notably, tumor microenvironments are

home to various immune cell types that, depending on the cell and cancer type, differentially (both positively and negatively) affect tumor cell-associated functions[5–10]. Among these immune cells, tumor-infiltrating T lymphocytes are now regarded as a critical component of the tumor stroma because therapeutically activating these cells using immunotherapy can durably control various cancer types and their infiltration into tumors can be indicative of improved disease outcome[11]. While these advances are revolutionizing cancer therapy by validating immune cell targeting as a relevant approach to fight human cancer, only a fraction of patients benefit from current immunotherapies[4] and our knowledge of the diverse and complex tumor microenvironments across cancer types remains limited.

Beyond T cells, myeloid cells have emerged as key regulators of cancer growth based on their abundance in the patient stroma, association with disease outcome, and their abilities to both promote or inhibit tumor growth in pre-clinical models[5–8]. Myeloid cells come in many different shapes, including macrophages, neutrophils, eosinophils, mast cells, monocytes, and dendritic cells. Understanding myeloid cell functions in cancer is an area of intense investigation within tumor immunology and has been reviewed in detail by our lab[8] (Appendix 1) and others[5–8,12,13]. For the most part, the presence of myeloid cells, macrophages and neutrophils in particular, at the tumor site tend to correlate with adverse prognosis in patients[7,14,15]. However, other, typically less abundant cells such as dendritic cells (DC), can have important antitumor functions and instead associate with improved disease outcome in some cancers[5,8,16]. The reality is even more complex as different cellular subsets (such as macrophage ‘activation states’) can have divergent functions within the same tumor microenvironment and between tumor types. Additionally, whether a cell has tumor promoting or suppressive functions may change dramatically during tumor progression and/or therapy. Therefore, despite a wealth of research regarding tumor-infiltrating immune cells in the most recent years, we still lack understanding of the complete immune cell repertoire and its heterogeneity at different tumor sites, which cells are immunosuppressive or antitumoral and, besides T cells, which are the most appropriate cellular and molecular targets for next-generation immunotherapies.

1.3.3 Cancer as a systemic disease

In addition to the local regulation of tumor growth, it has been appreciated, though much less studied, that tumors can affect, and be affected by, systemic host responses. For instance, most tumor-infiltrating immune cells are continuously replenished by circulating precursors[17,18]. This requires the constant production and release of hematopoietic cells by the bone marrow, or in some cases other tissues such as the spleen. Increased levels of circulating myeloid progenitor and more mature precursor populations have been observed in patients with solid tumors, which in some studies was associated with disease outcome[19–21], indicating relevance of systemically amplified hematopoietic responses in human cancers. Lymph nodes are also important sites for tumor antigen presentation and activation of T cells, which in turn are critical processes for tumor control and antitumor immunity. In addition, the metastatic cascade, which includes tumor cell migration to and seeding of distant sites to the primary tumor can be regulated locally by events in the tumor microenvironment but also distally through several mechanisms, including killing of circulating tumor cells[30], regulating intravasation and seeding of tumor cells at the metastatic site[31,32], or inhibiting or suppressing antitumor immune responses against metastatic tumor cells[33–36]. Broadly speaking, extra-tumoral tissues thus have many important tumor-regulatory functions as hematopoietic production sites (bone marrow and others), traffic routes between distant tissues and tumors (blood), transit of antigen (lymph), activation or suppression of antitumoral responses (lymph nodes, spleen).

These key processes can be remotely modulated by distant tumors. Factors produced and released by tumors act on tissues to amplify and skew hematopoietic cell production, e.g. G-CSF[22], GM-CSF[23], angiotensin II[24], PF4[25], and osteopontin[26], to name a few. Additionally, tumor-derived vesicles interact with hematopoietic components in lymph nodes[27] or other extra-tumoral tissues[28,29], which may in turn feed back into systemic antitumoral or protumoral responses. These types of signals, and others, are further used by cancers to orchestrate immune cell recruitment to the tumor site from the blood. Taken together, it is clear that tumors

are in constant bi-directional conversations with both local and systemic host components. To fully dissect tumor-associated immune responses in cancer, it is therefore important to consider critical events that occur outside the immediate tumor microenvironment.

1.3.4 Anticancer therapies perturb tumor-immune interactions

Host responses to tumors are profoundly affected by anticancer therapies, both directly and indirectly. The relevance of immune cells to current cancer treatments remains largely unexplored, particularly in the clinical setting, although virtually all therapeutic modalities, including surgery, chemotherapy, radiotherapy, immunotherapy and targeted therapy, likely involve these cells. Notably, myeloid cells are required to clear killed tumor cells and orchestrate the healing response that follows treatment-induced cancer regression. Furthermore, emerging evidence indicates that immune cells and cancer treatments are linked at other, sometimes unexpected, levels and that these connections can both improve and worsen treatment outcome. As an example, in addition to killing cancer cells directly, some chemotherapeutics may control tumor growth by reducing myeloid cells or limiting bone marrow-derived myeloid progenitors[37–39]. In other settings, myeloid cells can be beneficial for cytotoxic therapy, e.g. certain types of chemotherapeutic-induced cell death stimulate antitumor immune responses that require antigen-presenting cells[40]. Interestingly, even when immune cells appear to be specifically targeted, drug effects on hosts can involve additional seemingly off-target immune cells. For instance, the efficacy of anti-CTLA4 treatment, initially developed to unleash cytotoxic T cell activity by removing inhibitory signals, may depend on the depletion of suppressive regulatory T cells by Fc Receptor expressing monocytes[41–43]. In fact, Fc receptor expression by myeloid cells may be broadly important for the successful treatment with a range of antibody-based anticancer drugs[44]. Combined, it is likely that we have only begun to appreciate the role of non-cancerous cells in mediating the ability or failure to respond to a particular anticancer therapy.

1.3.5 Summary

To conclude, it is clear that immune cells have emerged as important regulators of cancer growth, but many mechanisms of tumor-associated immune cell-mediated responses require clarification. These include, but are not limited to, the functions of various tumor-infiltrating immune cells, cancer-exerted systemic interactions with the host involving extra-tumoral tissues such as the bone marrow, dynamic mechanisms of immune cell replenishment at the tumor site, and drug-induced effects on tumor-associated immune responses. Answering these questions is important because there is an urgent need to improve our understanding of the complex interactions that drive tumor progression and the ways in which we can best exploit these to improve anticancer therapies. With these goals in mind, we have begun to interrogate several of these questions listed above. These will be outlined in Section 1.5 ('Scope of Thesis').

1.4 Approach to studying cancer immunology

Cancer can be studied on multiple fronts, ranging from conducting clinical trials, implanting tumors in mice, studying patient cancer cells in vitro, or analyzing gene expression databases. To model NSCLC in the lab, we needed an experimental system in which we could mechanistically interrogate cellular and molecular host responses influencing tumor progression and anticancer therapies. We opted for using immunocompetent mice since it enables us to observe and manipulate immunologically compatible tumor-host interactions involving the local tumor microenvironment as well as tissues located away from the tumor stroma. To induce tumors, we have used a genetic mouse model of lung adenocarcinoma in which tumor cells transform from somatic cells after adenoviral-based delivery of the Cre enzyme resulting in cancer-causing mutations, namely activation of the genes encoding Kirsten rat sarcoma viral oncogene homolog (*KRAS*) and tumor suppressor p53 (*TP53)*[45,46]. This model allows tumors to initiate in their normal tissue microenvironment and it faithfully recapitulates various aspects of human disease, such as immune infiltration and disease progression through several tumor

stages[45,46]. Additionally, *KRAS* and p53 mutations are frequently found in NSCLC patients (~25% and 50%, respectively). When appropriate, we also used an orthotopic KP lung tumor model[46]. This model is useful and relevant because of its compatibility with various genetically engineered mouse models on a B6 background, reproducibility, and shorter time-course, while maintaining the relevant lung tumor tissue tumor microenvironment. We believe that the latter is particularly important when studying the tumor stroma, since immune cell composition and function is highly tissue specific even at steady state, as exemplified by their heterogeneous homeostatic functions across the body[47,48]. Furthermore, using immunocompetent mouse models to study cancer is critical to assess the complexity of drug responses which may require an intact immune response. In such studies, *in vivo* imaging can be a powerful tool to quantify and visualize drug uptake in tumor or host cells, as well as other aspects of pharmacokinetics.

Clinical translation from murine tumor models to patients is a challenge that needs to be addressed. Dissecting phenotypes in patients is undoubtedly critical to understanding cancer progression and treatment response in human disease. Therefore, we have, whenever feasible, worked to anchor our findings in patient pathology. However, there are major ethical, technical, and practical considerations that precludes asking and testing certain fundamental biological questions in patients. Here cancer mouse models are invaluable tools in driving discovery. It is also worth remembering that some of the most critical recent developments in anticancer therapies, such as the development of ICB, were based on pre-clinical work in the mouse. Thus, studying cancer using immunocompetent mouse models remains a relevant approach to mechanistically address cellular and molecular components that drive tumor progression.

1.5 Thesis Outline

Below, I summarize our findings and outline the content of each chapter.

In Chapter 2, I will present our work investigating systemic cancer-host interactions involving bi-directional crosstalk between lung tumors and the bone marrow. In this chapter, we

show in both mice and cancer patients that lung adenocarcinomas increased bone stromal activity in the absence of local metastasis. Animal studies further revealed that the cancer-induced bone phenotype involved bone-resident osteoblastic cells. These cells promote cancer by remotely supplying a distinct subset of tumor-infiltrating neutrophils, which were defined by a unique combination of cell surface markers and exhibited discrete cancer-promoting properties. Furthermore, conditionally reducing bone marrow osteoblastic cells is sufficient to interrupt both the neutrophil response and lung tumor outgrowth. Taken together, these findings uncovered a role for osteoblasts as remote enhancers of lung cancer and identify a novel neutrophil subtype as myeloid cell effectors of the osteoblast-driven protumoral response.

In Chapter 3, I will discuss our findings related to harnessing tumor drug responses to convert immunologically ‘cold’ tumor microenvironment to those more amenable to checkpoint blockade therapy. Here, we show that mouse lung tumors that lack T cell infiltration and resist current treatment options can be successfully sensitized to host antitumor T cell immunity when using appropriately selected immunogenic chemotherapeutic drugs. The antitumor response was triggered by direct drug actions on tumor cells, relied on innate immune sensing through pattern recognition receptors, and ultimately depended on T cell antitumor immunity. Furthermore, instigating tumor infiltration by T cells sensitized tumors to checkpoint blockade inhibition and controls cancer durably. These findings indicate that the proportion of cancers responding to checkpoint therapy can be feasibly and substantially expanded by combining checkpoint blockade treatment with immunogenic drugs.

In Chapter 4, I will present our study aimed at mapping all immune cell states in murine lung tumors. To do this, we used cutting-edge single cell RNA-seq to define the immune cell composition in healthy and lung tumor tissues. Through this approach, we identified distinct myeloid cell subtypes that were unique to tumor tissue. We further interrogated single cell molecular phenotypes of tumor-infiltrating immune cells following targeting of the colony-stimulating factor-1/R pathway, which is key to myeloid differentiation and a promising therapeutic target. Taken together, our analysis revealed previously unappreciated tumor- and

drug- associated immunoregulatory cell states. These findings should help clarify myeloid cell complexity within tumors and in response to myeloid-based immunotherapy.

In Chapter 5, I will highlight additional projects to which I contributed to during my thesis. These different studies ask questions within the realm of tumor immunology but cover a wide range of research areas from macrophage imaging technologies within tumors, tumor-derived vesicle and lymph node macrophage interactions in the context of skin tumors, tissue distribution of nanoparticle-encapsulated drugs, and the role of microbiota in chemotherapy-induced anticancer immune responses.

In Chapter 6, the final part of my thesis, I will highlight critical next steps to extend our work.

Chapter 2: Systemic cancer-host interactions

2.1 Overview

Osteoblasts remotely supply lung tumors with cancer-enhancing SiglecF^{high} neutrophils

Camilla Engblom*, Christina Pfirschke*, Rapolas Zilionis, Janaina da Silva Martins, Stijn A. Bos, Gabriel Courties, Steffen Rickelt, Nicolas Severe, Ninib Baryawno, Julien Faget, Virginia Savova, David Zemmour, Jaclyn Kline, Marie Siwicki, Christopher Garris, Ferdinando Pucci, Yi-Jang Lin, Andita Newton, Omar Yaghi, Yoshiko Iwamoto, Benoit Tricot, Gregory R. Wojtkiewicz, Matthias Nahrendorf, Virna Cortez-Retamozo, Etienne Meylan, Richard O. Hynes, Marie Demay, Allon Klein, Miriam A. Bredella, David T. Scadden, Ralph Weissleder, Mikael J. Pittet

*These authors contributed equally to this work.

This work is unpublished.

Summary

Bone marrow-derived myeloid cells can accumulate in high numbers within solid tumors and mediate functions that foster cancer outgrowth. Immune-neoplastic interactions in the local tumor microenvironment have been intensively investigated, but the contribution of the host systemic environment to tumor growth remains poorly understood. Here, we show in both mice and cancer patients that lung adenocarcinomas increase bone stromal activity even in the absence of local metastasis. Animal studies further reveal that the cancer-induced bone phenotype involves bone-resident osteocalcin-expressing (Ocn$^+$) osteoblastic cells. These cells promote cancer by remotely supplying a distinct subset of tumor-infiltrating SiglecF^{high} neutrophils, which exhibit discrete cancer-promoting properties. Furthermore, conditionally reducing Ocn$^+$ cells is sufficient to interrupt both the neutrophil response and lung tumor outgrowth. These observations uncover a role for osteoblasts as remote enhancers of lung

cancer and identify SiglecF^{high} neutrophils as myeloid cell effectors of the osteoblast-driven pro-tumoral response.

Attributions

For this study, I, together with C.P., performed the majority of the experiments, analyzed the data, and wrote the manuscript.

2.2 Introduction

Extensive research of the tumor stroma has revealed that hematopoietic cells, including myeloid cells, can promote cancer[8,17,49,50]. The majority of tumor-infiltrating myeloid cells are not made at the tumor site, but are continuously replenished by circulating bone marrow-derived precursors[8,17,18]. Tumors can also regulate myeloid cells before they enter the tumor stroma by skewing hematopoiesis towards the myeloid lineage[22,23,51] or increasing myeloid cell populations or their precursors in the periphery[22,23,51]. There is human relevance for these long-range interactions between tumors and distant hematopoietic production sites, as amplified circulating levels of hematopoietic myeloid progenitor populations can be detected in patients across cancer types[19]. Similarly, elevated levels of circulating neutrophils often correlate with poorer clinical outcome[20,21]. To more fully understand the biological processes underlying tumor development and growth, it is therefore important to consider host changes that occur away from the tumor stroma.

The bone marrow is a tissue of particular interest as the main hematopoietic cell production site for all circulating blood lineages in the adult[52,53]. In addition to its hematopoietic cell constituents, the bone marrow contains resident cell populations that not only participate in bone maintenance but also regulate hematopoiesis and immune cell fate[54–56]. The idea that hematopoiesis, and stem cell activity in particular, was controlled by stromal elements in the

bone marrow microenvironment was first proposed almost half a century ago (reviewed in[52,54]). This early, seminal work, set the stage for today's on-going investigations into the various cell types that make up the 'bone marrow stroma'. Thus far, the bone marrow stromal microenvironment has been broadly defined as cells of mesenchymal origin (which can give rise to bone-forming osteoblasts, chondrocytes and adipocytes), endothelial cells and nerves[54–56], although this field is continuously evolving and gaining in cellular resolution.

Cells of the osteoblastic lineage are a main component of the bone marrow stroma. Osteoblasts are bone-forming cells responsible for producing and maintaining the mineralized protein matrix that makes up our bones[57]. They also regulate the development and activity of osteoclasts, the osteoblast's cellular antagonist, whose main function is to break down bone, referred to as bone resorption. In the adult, osteoblastic cells are thought to derive from skeletal progenitor cells that are present in the marrow space, and whose commitment to becoming osteoblasts depends on several transcription factors, most notably Runt-related transcription factor 2 (Runx2)[57–60] and Osterix (Osx)[57,61]. As osteoprogenitors develop into mature and active osteoblasts, they upregulate osteocalcin (Ocn) along with a slew of genes related to bone formation, such as collagen, type 1, alpha 1 and alkaline phosphatase[62,63]. Some osteoblasts further develop into osteocytes, which are bone-embedded cells critical for bone maintenance, and whose differentiation depends on Dentin Matrix Acidic Phosphoprotein 1 (*Dmp1*) expression in mice[64,65]. Osteocytes can also control osteoblast development, as evidenced by their production of sclerostin, a molecular inhibitor of the WNT pathway, whose targeting amplifies osteoblast activity and bone formation.

Osteoblastic cells were the first bone marrow stromal cells identified to regulate hematopoiesis at steady state[52,54]. Seminal studies demonstrated that genetic manipulation of osteoblasts and their progenitors in mice dramatically altered hematopoietic stem cells (HSCs) and the B cell lineage in the bone marrow[66–69]. More recent experiments have reported that osteoblastic cells likely do not interact directly with HSCs, but mainly with more mature precursor populations, primarily of the lymphoid lineage[70–74]. The stromal population(s) that

dominantly regulate myeloid progenitor populations remain less studied. However, the osteoblastic lineage may be relevant here as well, since osteocyte deletion of G-protein subunit α (Gsα) resulted in myeloid cell expansion, mediated in part by osteocyte-derived G-CSF[75]. Different genetic mouse models have also revealed that various molecular mediators regulate hematopoeisis[52,54]. These include C-X-C Motif Chemokine Ligand (CXCL12)[73,74], angiopoietin[76], osteopontin[77], prostaglandins[78], stem cell factor[79], Notch signaling[52,66], and presumably many more that remain undefined. Thus, it is evident that osteoblasts are significant players in a complex system, involving multi-cellular and molecular interactions, that is critical to steady state hematopoietic cell production and egress from the bone marrow.

It has also become clear that osteoblastic cells are important and active participants in both local and systemic inflammation and disease, which typically perturb bone marrow hematopoiesis. For instance, the osteoblast lineage has been implied as an instigator of local bone marrow hematopoietic malignancies[80,81]. A seminal study showed that genetic mutations in the osteoblast lineage, i.e. *Dicer* deletion in osteoprogenitor cells, instigated myelodysplasia and subsequent acute myelogenous leukemia[80]. Osteoblast specific β-catenin activation also resulted in acute myeloid leukemia-like disease in mice, which was mediated by osteoblast expression of the Notch ligand Jagged-1; intriguingly, β-catenin activation in osteoblast was also observed in 41 out of 107 patients diagnosed with acute myeloid leukemia or myelodysplastic syndrome (but not in healthy controls)[81]. Additionally, osteoblasts may contribute to bone metastasis by regulating tumor seeding and growth through ligand-receptor interactions, and conversely, bone metastatic tumor cells can profoundly disrupt homeostatic bone forming and resorptive processes, generating both osteoblastic and osteolytic tumors[82]. In addition to their involvement in local bone marrow pathologies, osteoblastic lineage cells can also contribute to systemic inflammatory processes, although this remains less studied. For example, one study showed that granulocyte colony-stimulating factor (G-CSF)-induced hematopoietic stem and progenitor cell (HSPC) exit from the bone marrow was impaired in diabetic patients, and mechanistic studies in mice demonstrated that G-CSF-induced HSPC egress was mediated in

part by osteoblasts in addition to Nestin^{+} mesenchymal cells[83]. Another group showed that osteoblasts were ablated during sepsis and that loss of osteoblastic-expression of interleukin (IL-7) critically impaired lymphocyte production[84].

Taken together, osteoblastic cells, in addition to their roles in bone formation, contribute to steady state maintenance of hematopoiesis and to both local and systemic disease conditions that involve hematopoietic cells. However, it is not clear whether an already established malignancy, such as a solid tumor, with known effects on hematopoietic cells, induces changes in osteoblasts, and whether this has an impact on distant tumor growth and related immune responses. To address this knowledge gap, here we asked whether bones may not only be affected by a common solid cancer—lung adenocarcinoma—but also shape tumor-associated hematopoietic responses and remotely control cancer outgrowth.

2.3 Results

2.3.1 Bone activity is increased in lung tumor-bearing mice

To test whether lung tumors disrupt bone homeostatic activity, we initially used a fluorescent bisphosphonate derivative (OsteoSense-750EX)[85] that binds hydroxyapatite minerals in areas of active bone formation and is detectable *in vivo* by fluorescence-mediated tomography (FMT)[86]. We considered a mouse model of lung adenocarcinoma in which tumors are induced by intratracheal delivery of Adenovirus (Ad)-Cre, which activates oncogenic *Kras* and deletes the tumor suppressor *Trp53* (thereafter referred to as KP; Figure S2.1A-C), and whose growth recapitulates key aspects of the human disease[45]. For some experiments, we also used the KP1.9 tumor cell line, which derives from KP lung tumors and behaves similarly to its autochthonous counterpart[46], and the Lewis Lung Carcinoma (LLC) cell line, a commonly used murine lung tumor model. *In vivo* FMT analysis of the femoral-tibial joint (Figure S2.2A)

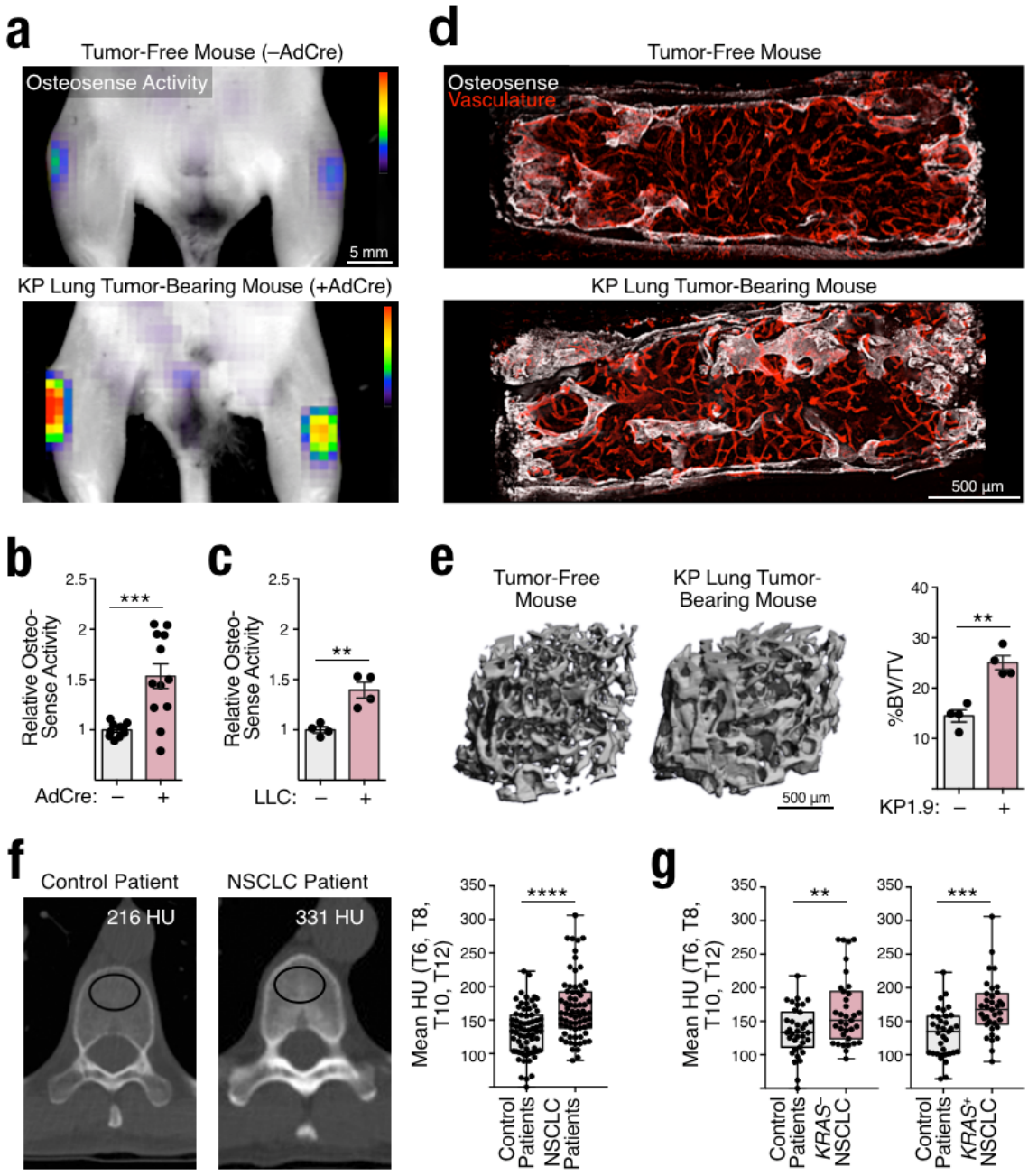

Figure 2.1 Lung tumors modulate bones.

(a) *Representative image of in vivo* FMT-based detection of OsteoSense signal in the femoral-tibial joint of KP lung tumor-bearing mice and their respective age- and sex-matched littermate tumor-free controls.

(b) Quantification of (a) (n = 10-12).

(c) Detection of OsteoSense signal as in (a) but in LLC lung tumor-bearing mice and their controls (n = 4).

(d) *Ex vivo* confocal microscopy of representative OsteoSense (white) and vasculature signal (red; labeled with anti-Sca-1, anti-CD31 and anti-CD144 mAbs) in the sternum of tumor-free (top) and KP1.9 lung tumor-bearing (bottom) mice.

Figure 2.1 (Continued)

(e) 3D reconstruction of μCT scans (left) and quantification of trabecular bone volume fraction (BV/TV) (right) in the distal femoral metaphysis of KP1.9 lung tumor-bearing and control mice (n = 4).
(f) CT-based trabecular bone density in NSCLC and control patients. *Left:* representative axial non-contrast CT image of the 10th thoracic vertebra (T10) in a 53-year-old healthy woman who underwent non-contrast chest CT for cough and was found to have no abnormalities (control patient) and a 53-year-old woman with *KRAS*$^{+}$ NSCLC showing higher bone density. Images are presented using the same window and level. The mean trabecular bone density of the region of interest depicted by a black oval was calculated in Hounsfield Units (HU) for all investigated individuals. *Right:* quantitative data from control (n = 70) and NSCLC (n = 70) patients.
(g) As in (f), but showing mean trabecular bone density of NSCLC patients separated based on tumor *KRAS* mutational status. *Left: KRAS*$^{-}$ (negative) and matched controls. *Right: KRAS*$^{+}$ (positive) and matched controls.
**p*<0.05, ***p*<0.01, ****p*<0.001, *****p*<0.0001. AdCre: adenovirus-Cre; FMT: fluorescence molecular tomography; KP: Kras and p53 mutant lung tumors; LLC: Lewis Lung Carcinoma; μCT: micro-computed tomography; NSCLC: non-small cell lung cancer.

showed significantly elevated OsteoSense activity in both KP (Figure2.1A-B) and LLC (Figure 2.1C and Figure S2.2B) lung tumor-bearing mice, when compared to tumor-free controls.

Ex vivo analysis of explanted bones from KP tumor-bearing mice further revealed that this activity extended across all compartments analyzed, including the elbow joint, sternum, ribs, vertebrae and pelvic bone (Figure S2.2C-E). Control experiments confirmed that OsteoSense signal originated from bone but not from other tissues including lung, spleen, liver and kidney (data not shown). Bone metastases have not been reported for mice bearing KP tumors[45], which we confirmed by histology, PCR-based methods, and micro-computed tomography (μCT) (Figure S2.3A-E and data not shown). These studies indicate that lung tumors can disrupt bone stromal activity in absence of local metastasis.

By using confocal microscopy, we also found increased OsteoSense signal in the sternum (Figure 2.1D and Figure S2.4A) and distal femur (Figure S2.4B) of KP1.9 tumor-bearing mice. We further identified that the signal's location was separate from vasculature and enriched in areas of active bone remodeling, including the edges of sternebrae, which are associated with areas of increased bone in the sternum (Figure 2.1D and Figure S2.4A), and the metaphysis of the femur, which is an area of active trabecular bone formation adjacent to the growth plate (Figure S2.4B). OsteoSense signal was also found in the epiphysis and diaphysis of the femur (Figure S2.4B).

These data suggested that KP tumors' impact on bone may influence bone microarchitecture. Accordingly, high-resolution μCT showed increased trabecular bone volume (Figure 2.1E and Figure S2.5A-C) and higher mineral density of distal femoral metaphysis (Figure S2.5D) in mice bearing KP tumors. The same mice also showed more (Figure S2.5E) and thicker (Figure S2.5F) trabeculae and decreased space between those trabeculae (Figure S2.5G). Cortical bone morphology in the femoral mid-diaphysis showed similar tumor-induced phenotypes (Figure S2.5H). Figure S2.5I includes a complete tabulation of the μCT results.

2.3.2 Bone density is increased in non-small cell lung cancer patients

To define our findings' relevance for human disease, we examined 70 non-small cell lung cancer (NSCLC) patients who had undergone non-contrast chest CT measurements prior to cancer therapy and did not have osseous metastases. These patients were matched by age, sex and body mass index to control individuals who did not have active malignancy, chronic illness or medication use known to affect bone metabolism (Table S2.1). This analysis revealed significantly higher trabecular bone density in the thoracic vertebrae of NSCLC patients compared to controls (Figure 2.1F and Table S2.1). The equivalent analysis done in *KRAS*$^{-}$ versus *KRAS*$^{+}$ NSCLC patients separately revealed comparable results, suggesting that the increased bone is not dependent on the *KRAS* mutational status (Figure 2.2G). Taken together, lung tumor-induced changes in bone can be observed in both mice and humans.

2.3.3 Lung tumors activate osteoblasts

The bone phenotypes may be explained by altered osteoblast and/or osteoclast activity[57]. Histological analysis of these cell lineages in the distal femur identified more osteoblasts in KP tumor- bearing mice than in tumor-free controls (Figure 2.2A and B). Osteoblasts in tumor-bearing mice also exhibited features of increased activity, including cuboidal shape and association with newly formed osteoid (Figure 2.2A). Accordingly, the

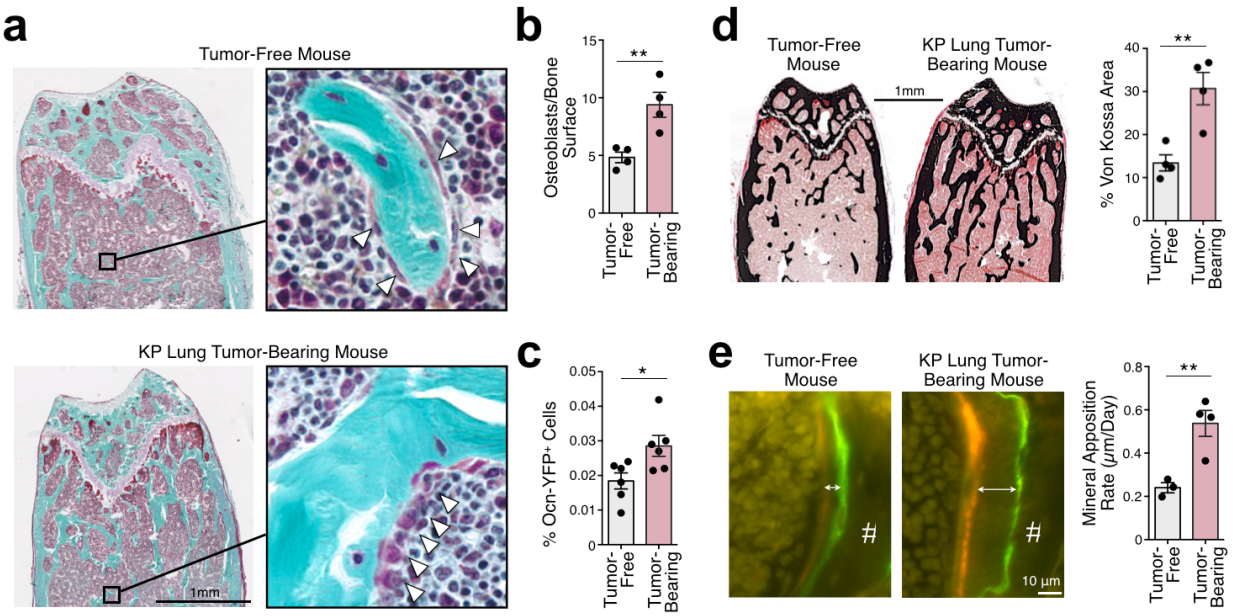

Figure 2.2 Lung tumors change osteoblast activity.

(a) Representative trichrome staining of distal femur sections from tumor-free (top) and KP lung tumor-bearing (bottom) mice (n = 4). Osteoblasts are indicated with white arrowheads.

(b) Number of osteoblasts per bone surface in distal femur trabecular bone from the same mice as in (a) (n = 4).

(c) Flow cytometry-based quantification of the percentage of bone marrow Ocn-YFP$^+$ cells isolated from tumor-free or KP lung tumor-bearing *Ocn*$^{Cre;Yfp}$ mice (n = 6).

(d) Representative Von Kossa staining (left) and quantification of mineralized bone (% Von Kossa area, right) in femurs from the same mice as in (a).

(e) Left: Bone formation in trabecular bone of femurs from tumor-free or KP lung tumor-bearing mice (left). Double arrows depict distance between sequential injections of calcein (green) and demeclocycline (red). # denotes trabecular bone. Right: quantification of mineral apposition rate (n = 3-4 mice). See fig. S2.7 for additional measurements.

*p<0.05, **p<0.01. KP: Kras and p53 mutant lung tumors; Ocn: osteocalcin; YFP: yellow fluorescent protein.

osteoid surface, characterizing newly formed bone, expanded in tumor-bearing mice (Figure S2.6A). By contrast, osteoclast numbers (Figure S2.6B) and eroded bone surfaces (Figure S2.6C) were not different in tumor-bearing mice, although there was a trend for lower osteoclast- related indices compared to tumor-free controls.

To trace osteoblastic lineage cells by genetic means, we generated mice that expressed Cre-driven yellow fluorescence protein (YFP) under the control of the osteoblastic cell reporter osteocalcin (Ocn). Ocn is mainly expressed by mature osteoblasts and constitutes the major non-collagenous protein in the bone[62,87]. We found that Ocn-YFP$^+$ cells expanded in KP tumor-bearing mice when compared to tumor-free controls (Figure 2.2C). Femurs of tumor-bearing

mice showed increased mineralized bone and bone formation, as assessed by Von Kossa staining (Figure 2.2D) and dynamic histomorphometry (Figure 2.2E; Figure S2.7). We concluded that KP tumors increase osteoblastic activity *in vivo*.

2.3.4 Ocn$^+$ cells control distant tumor progression

Because increased osteoblastic activity can affect hematopoiesis[66,70], and some hematopoietic cells control cancer growth[8,17,49], we sought to determine whether the osteoblastic activity in KP tumor- bearing mice indeed regulates cancer growth. To this end, we examined tumor progression in Ocn$^{Cre;Dtr}$ mice, in which Ocn$^+$ cells can be reduced following diphtheria toxin (DT) injection. We also used OcnCre;$^{Dtr/Yfp}$ mice to track Ocn$^+$ cells based on YFP expression. DT treatment did not affect body weight (Figure S2.8A and B) but significantly reduced Ocn$^+$ cell numbers, as detected by flow cytometry, immunohistochemistry, in situ microscopy and bone histomorphometry (Figure S2.8C-F). Importantly, DT treatment in Ocn$^{Cre;Dtr}$ mice was sufficient to interrupt the progression of established KP lung tumors (Figure 2.3A and B). Control experiments further indicated that tumor reduction required Ocn$^+$ cell targeting because DT treatment did not suppress KP tumor progression in mice lacking the Ocn or DT receptor (DTR) transgenes (Figure 2.3A). Also, tumor control was not merely triggered by nonspecific DT-induced cell death in bone because DT targeting of CD169$^+$ bone marrow cells did not suppress KP lung tumor progression in Cd169^{Dtr} mice (Figure S2.9). These findings indicated that osteoblastic activity affects lung tumor progression.

2.3.5 Ocn$^+$ cells control tumor-infiltrating granulocytes

We hypothesized that osteoblasts may affect cancer by supplying discrete hematopoietic components of the tumor microenvironment. We thus compared KP lung tumor immune infiltrates in mice with either unmanipulated or reduced Ocn$^+$ cell numbers. We found similar pools of monocytes, macrophages, B cells and T cells in both cohorts; however, mice with fewer

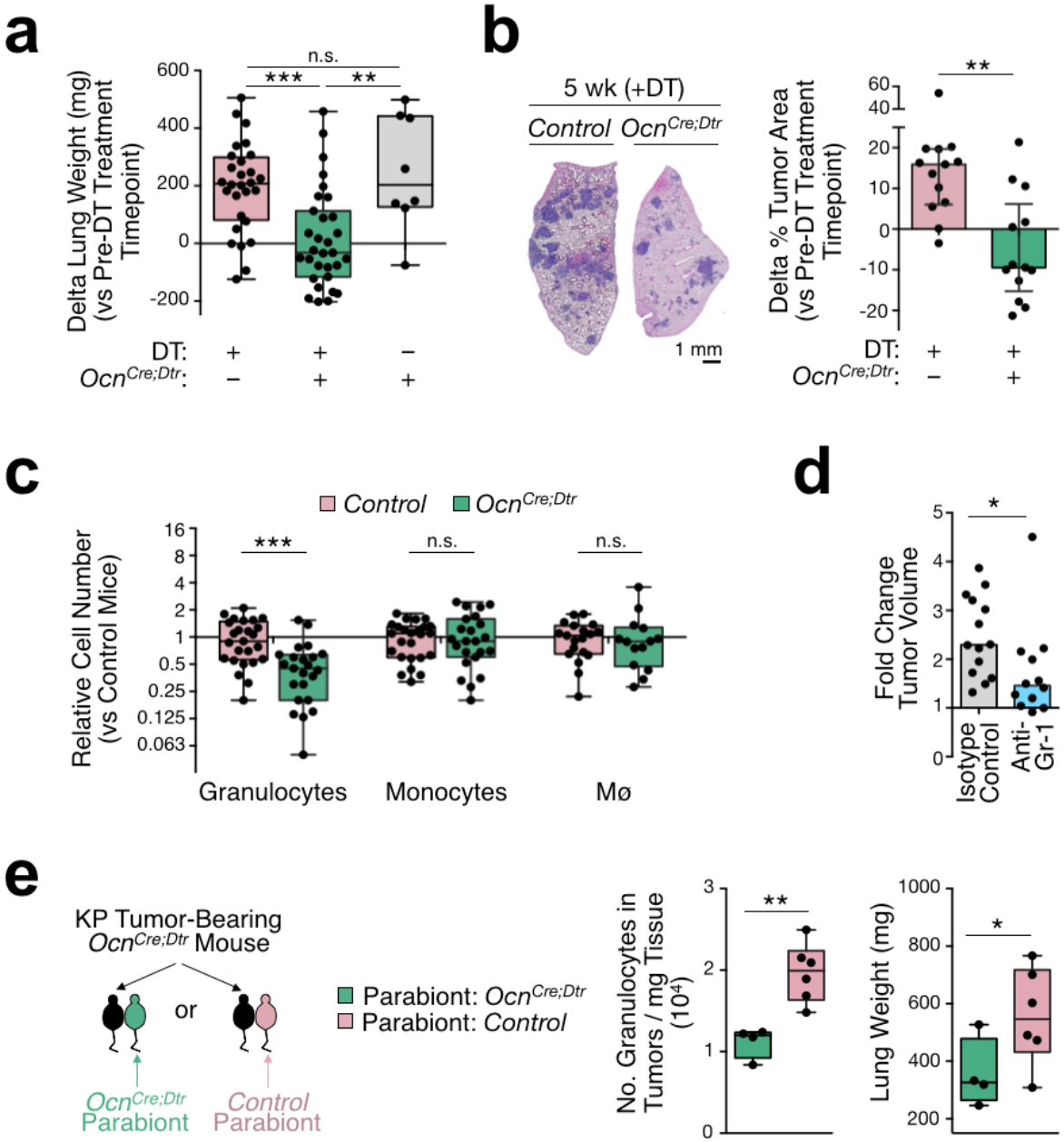

Figure 2.3 Ocn⁺ cells foster a tumor-promoting neutrophil response.

(a) Delta lung weight pre-post DT treatment in control mice (lacking Cre or DTR transgene; pink) and *Ocn*$^{Cre;Dtr}$ mice (green). *Ocn*$^{Cre;Dtr}$ mice that did not receive DT were used as additional controls (grey). Data are pooled from four separate experiments (n = 8-29 mice).

(b) Representative H&E stained lung tissue sections (left) for quantification (right) of percent change in tumor area following DT treatment in tumor-bearing control (pink) and *Ocn*$^{Cre;Dtr}$ mice (green). Data are pooled from three independent experiments (n = 13 mice).

(c) *Ex vivo* flow cytometry-based evaluation of granulocytes, monocytes and macrophages in lungs of tumor-bearing mice as in (b). Data are normalized to control (Ocn-sufficient) mice and pooled from three independent experiments (n = 14-29 mice).

(d) Fold change of KP lung tumor nodule volume measurement by μCT pre and post anti-Gr-1 or isotype mAb treatment (n= 2-3 tumor nodules per mouse, 4-5 mice total).

Figure 2.3 (Continued)

(e) Outline of parabiosis experiments (left) and quantification of lung tumor-infiltrating granulocytes by flow cytometry (middle) and lung weight (right) in tumor-bearing $Ocn^{Cre;Dtr}$ mice (mice in black) parabiosed to either $Ocn^{Cre;Dtr}$ (green) or control (pink) mice (n = 4-6 mice).
*p<0.05, **p<0.01, ***p<0.001, n.s. not significant. DT: diphtheria toxin; Mø: macrophages; Ocn: osteocalcin.

Ocn^+ cells showed a ~2-3-fold reduction in $CD11b^+$ $Ly\text{-}6G^+$ granulocytes (Figure 2.3C and Figure S2.10). These mice also had more $CD49b^+$ $NK1.1^+$ NK cells (Figure S2.10), which were likely not required for KP tumor control because NK cell depletion did not restore cancer growth in these mice (Figure S2.11A-D). Importantly, DT did not target granulocytes directly because wild-type mice treated with DT maintained their granulocyte counts (Figure S2.12A and B). Also, $CD11b^+$ myeloid cells from $Ocn^{Cre;Dtr}$ mice were not killed by DT in vitro, confirming no functionally relevant DT receptor expression by these cells (Figure S2.12C and D), whereas positive control experiments showed DT's ability to kill DTR^+ cells in vitro (Figure S2.12E and F).

We next considered whether controlled KP tumor progression in Ocn^+ cell-reduced mice involves the altered granulocyte response. With this scenario, removing granulocytes should delay cancer outgrowth even in presence of Ocn^+ cells. Accordingly, targeting granulocytes with depleting antibodies (Figure S2.13A and B) significantly suppressed KP lung tumor outgrowth in Ocn^+ cell-sufficient mice, as defined by longitudinal and noninvasive μCT monitoring of lung tumor nodules (Figure 2.3D). To further define whether Ocn^+ cells support tumor-infiltrating granulocytes via circulating precursor cells, we assessed tumor microenvironments upon circulatory chimerism between mice by parabiosis. We found that joining osteoblast-reduced mice to osteoblast-sufficient mice increased tumor-infiltrating $CD11b^+$ $Ly\text{-}6G^+$ granulocyte numbers by 2.6 ± 0.3 fold (mean ± SEM) in the former (Figure 2.3E). This increase was comparable to the one seen in control (osteoblast-sufficient, nonparabiosed) mice (2.2 ± 0.4 fold; p = n.s.). Also, tumors in osteoblast-reduced mice grew faster when joined to osteoblast-sufficient parabionts (Figure 2.3E) and similarly to tumors in control (osteoblast-sufficient, nonparabiosed) mice (lung weights: 557.1 ± 68.34 mg and 551.4 ± 30.24, respectively, p = n.s.). Thus, both tumor granulocyte counts and tumor progression were fully restored in osteoblast-

reduced mice when parabiosed to Ocn$^+$ cell sufficient mice. Combined, these data not only indicated that Ocn$^+$ cells contribute tumor-infiltrating granulocytes, but also suggested that these cells display tumor-promoting functions.

2.3.6 Tumor-specific neutrophil-like cells are defined by Ly6G and SiglecF expression

Considering that granulocytes are heterogenous[17], we wondered whether those supplied by Ocn$^+$ cells have distinct attributes, which can accelerate tumor progression. To address this question, we initially delved deeper into lung granulocyte phenotypes and found that CD11b$^+$ Ly-6G$^+$ cells can be divided into two subsets according to expression levels of the lectin SiglecF (Figure 2.4A). The SiglecF^{low} subset appeared at high numbers in healthy lungs and expanded only slightly in lungs from tumor- bearing mice; by contrast, the SiglecF^{high} subset was rare in the healthy lung but expanded ~70-fold in tumor-bearing lungs (Figure 2.4A and B). The SiglecF^{high}/SiglecF^{low} cell subset ratio positively correlated with KP lung tumor burden (Figure S2.14A and B), further indicating that the SiglecF^{high} subset continued to accumulate in growing tumors.

Both the cell surface phenotype and forward/side scatter profiles of the SiglecF^{high} cells closely resembled those of neutrophils and were distinct from those of other myeloid cell types including SiglecF$^+$ eosinophils and SiglecF$^+$ alveolar macrophages (Figure S2.15). Immunohistochemical SiglecF and Ly-6G staining further revealed the presence of Ly-6G$^+$ and SiglecF^{high} neutrophil-like cells within tumor nodules (Figure 2.4C and Figure S2.16A and B), suggesting that the SiglecF^{high} neutrophils localize proximal to tumor cells. SiglecF$^+$ cells outside the tumor stroma instead resembled alveolar macrophages based on their morphology and Ly-6G$^-$ phenotype (Figure S2.16C-E).

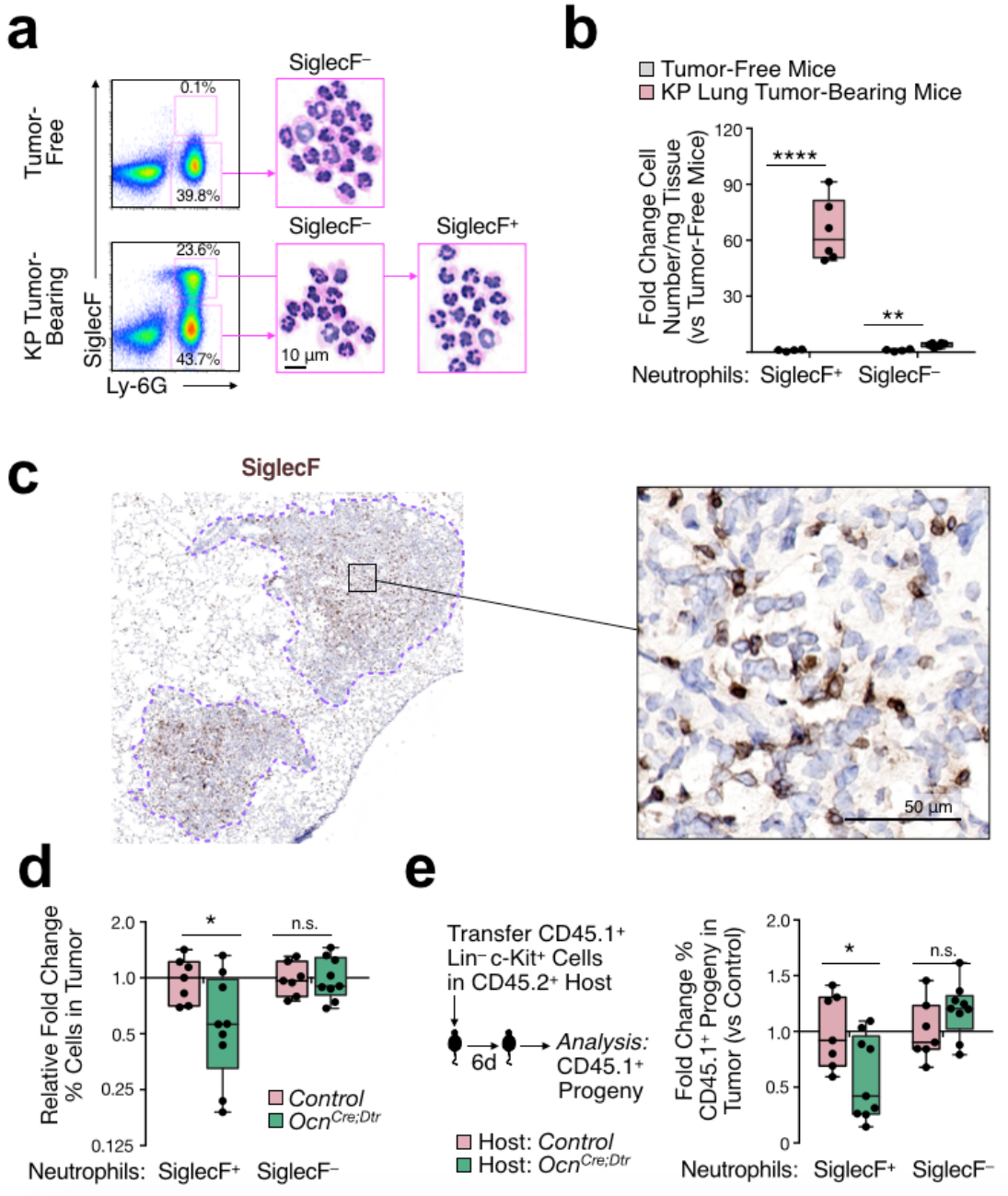

Figure 2.4 Ocn⁺ cells foster contribute tumor-infiltrating SiglecF^{high} neutrophils.

(a) Flow cytometry-based detection (left) of Ly-6G⁺ SiglecF$^{+/-}$ granulocytes from healthy lung tissue (top) and KP1.9 lung tumors (bottom). Plots are shown for gated live CD45⁺ CD11b⁺ cells. Representative cytospin images (right) from FACS-sorted populations stained with H&E.

(b) Fold change Ly-6G⁺ SiglecF⁺ and Ly-6G⁺ SiglecF⁻ cell numbers in lung tumor tissue compared to tumor-free tissue as defined by flow cytometry (n = 6).

(c) Representative SiglecF mAb staining on cryo-preserved KP lung tumor tissue. Tumor areas are highlighted by dotted purple lines.

(d) Flow cytometry-based quantification of Ly-6G⁺ SiglecF⁺ and Ly-6G⁺ SiglecF⁻ cells in tumor-bearing lungs of control (pink) or *Ocn$^{Cre;Dtr}$* mice (green) (n = 7-9).

Figure 2.4 (Continued)

(e) Ability of CD45.1$^+$ Lin$^-$ cKit$^+$ hematopoietic precursors to produce tumor-infiltrating SiglecF$^+$ and SiglecF$^-$ neutrophils upon transfer into KP tumor-bearing CD45.2$^+$ recipient mice which had either unmanipulated (control recipients; pink) or reduced Ocn$^+$ cell numbers (*Ocn$^{Cre;Dtr}$* recipients; green). All mice received DT. Results are shown as fold change relative to control mice. **p*<0.05, ***p*<0.01, *****p*<0.0001, n.s. not significant.

2.3.7 Osteoblasts control tumor-infiltrating SiglecF^{high} neutrophils

To study whether osteoblasts preferentially contribute SiglecF^{high} lung neutrophils, we quantified both SiglecF^{high} and SiglecF^{low} subsets in tumor-bearing mice with reduced or unchanged Ocn$^+$ cell numbers. We found that Ocn$^+$ cell deficiency significantly reduced the percentage of SiglecF^{high}, but not SiglecF^{low}, neutrophil subset (Figure 2.4D). To further investigate whether SiglecF^{high} neutrophil accumulation in tumors requires Ocn$^+$ cells, we mapped the fate of donor CD45.1$^+$ c-Kit$^+$ hematopoietic cells upon adoptive transfer into CD45.2$^+$ tumor-bearing recipient mice that had either reduced or unchanged Ocn$^+$ cell numbers. We found that the c-Kit$^+$ cells' ability to produce SiglecF^{high} lung neutrophils was reduced in Ocn deficient (Figure 2.4E). By contrast, the c-Kit$^+$ cells were equally able to produce tumor-infiltrating SiglecFlow neutrophils (Figure 2.4E), as well as macrophages (Figure S2.17A) and B cells (albeit at frequencies >25-times lower than myeloid cells; Figure S2.17B), in Ocn$^+$ cell-reduced and sufficient mice. We typically failed to detect c-Kit$^+$-derived T cells in the tumor stroma. These findings indicated that KP tumor accumulation of SiglecF^{high} neutrophils, in contrast to other immune cells, depends on Ocn$^+$ cells.

2.3.8 SiglecF^{high} neutrophils exhibit distinct tumor-promoting phenotypes

We next asked whether SiglecF^{high} neutrophils have cancer-promoting properties. To this end, we interrogated single-cell transcriptomic data of neutrophils from healthy lungs or KP tumors. By defining a single-cell SiglecF expression score (Table S2.2; detailed in Section 2.6)

we defined two neutrophil populations: SiglecF^{low} and SiglecF^{high} cells. We confirmed that neutrophils in healthy lungs were SiglecF^{low}, whereas tumor tissue contained both SiglecF^{low} and SiglecF^{high} subsets (Figure S2.18A). We thus compared gene expression of three neutrophil populations: SiglecF^{high} cells in tumor-bearing lung (T-SiglecF^{high}; n = 1,502 cells), SiglecF^{low} cells in tumor-bearing lung (T-SiglecF^{low}; n = 273), and SiglecF^{low} cells in healthy lung (H-SiglecFlow; n = 4,245). Differential gene expression analysis revealed that T-SiglecF^{high} cells substantially diverged from both T-SiglecF^{low} and H-SiglecF^{low} cells (1,769 and 1,798 differentially expressed genes, respectively; Figure 2.5A, table S2.3 and Figure S2.18B). Instead, T-SiglecF^{low} and H-SiglecF^{low} cells were more similar (123 differentially expressed genes; Figure S2.18C). Accordingly, the majority of differentially expressed genes between T-SiglecF^{high} cells and either H-SiglecF^{low} or T-SiglecF^{low} cells were the same (n = 1,289).

T-SiglecF^{high} cells upregulated the expression of genes associated with tumor-promoting processes (Figure 2.5B and Figure S2.18D), including angiogenesis (Vegfa, Hif1a, Sema4d), myeloid cell differentiation and recruitment (Csf1, Ccl3, Il1a), extracellular matrix remodeling (Adamdec1, Adam17, various cathepsins), suppression of T cell responses (Cd274/PDL1, Fcgr2b, Havcr2) and tumor cell proliferation and growth (Tnf, Tgfb1, Il1a). T-SiglecF^{high} cells also showed decreased expression of genes involved with cytotoxicity (Cd244, Itgal, Fas) (Figure 2.5A-B). Other genes overexpressed in T- SiglecF^{high} cells included Xbp1 and Ffar2 (Figure 2.5A); Xbp1 impairs myeloid antitumor functions[88] and positively regulates Ffar2 expression[89]. Gene set enrichment analysis further indicated upregulation of genes involved in oxidative phosphorylation, fatty acid metabolism and glycolysis, indicating that T- SiglecF^{high} cells undergo a metabolic switch (Figure S2.19A). Genes involved in Myc signaling and E2F gene targets were also amplified, suggesting that T-SiglecF^{high} cells are more proliferative and resistant to apoptosis (Figure S2.19A). Simultaneously, gene pathways associated with antitumor functions, such as interferon-gamma signaling, were downregulated in T-SiglecF^{high} cells (Figure S2.19B). Taken together, these findings suggest that SiglecF^{high} neutrophils undergo metabolic changes in the tumor microenvironment and are poised to support tumor-promoting functions[8,17,49,50]

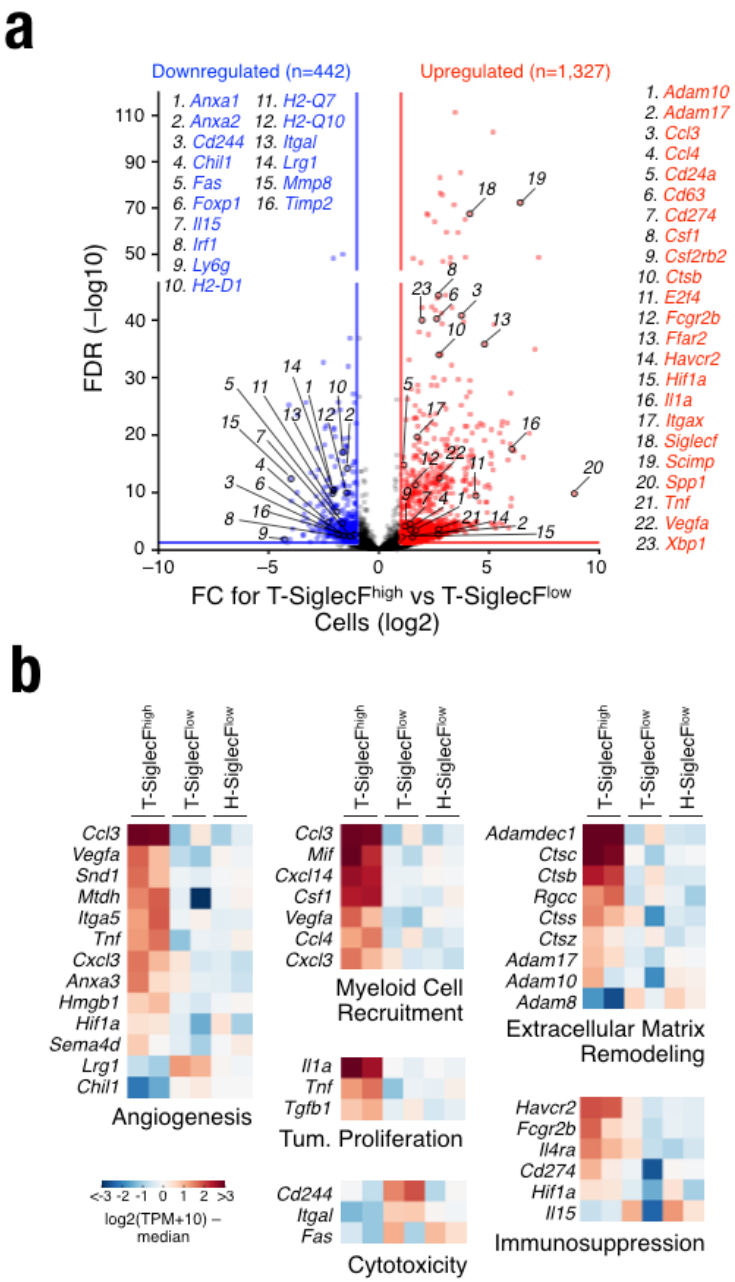

Figure 2.5 Tumor-infiltrating SiglecF^{high} neutrophils show discrete tumor-promoting phenotypes.

(a) Volcano plot showing significantly differential gene expression between T-SiglecF^{high} and T-SiglecF^{low} cells. Genes with false discovery rate (FDR) <5% and an absolute fold change (FC) >2 were highlighted in blue and red denoting down- and up-regulated genes, respectively, in T-SiglecF^{high} cells versus T-SiglecF^{low} cells.

(b) Average expression levels of genes involved in angiogenesis, myeloid cell recruitment, tumor proliferation, cytotoxicity, extracellular matrix remodeling and immunosuppression in T-SiglecF^{high}, T-SiglecF^{low} and H-SiglecF^{low} cells. T- Tumor

including tumor angiogenesis, tumor cell proliferation, extracellular matrix remodeling and immunosuppressive myeloid cell recruitment.

2.3.9 SiglecF^{high} gene signature in patients is associated with worse disease outcome

We next determined whether a mouse SiglecF^{high} neutrophil signature (detailed in methods, Table S2.4-5) might have translational value through differential survival associations in lung adenocarcinoma patients. To do this, we harnessed patient tumor transcriptome and survival data[25,90,91]. A Cox proportional hazards model revealed a statistically significant ($p = 1.4*10^{-6}$) association of the SiglecF^{high} neutrophil signature with worse human patient survival. In contrast, a SiglecF^{low} neutrophil signature did not associate with disease outcome in lung cancer patients ($p = 0.26$). The survival of top 25% vs. bottom 25% of SiglecF^{high} and SiglecF^{low} neutrophil signature expressers is shown in Kaplan-Meier plots in Figure 2.6. These findings suggest that the SiglecF^{high} signature has a predictive value in lung adenocarcinoma patients.

2.4 Discussion and Future Directions

This study identifies Ocn^{+} osteoblastic cells as remote enhancers of lung cancer, and SiglecF^{high} neutrophils as myeloid cell effectors of the osteoblast-driven protumoral response (Figure 2.7). Previous work has attributed several functions to osteoblastic-lineage cells, including control of bone formation[57,68,92] and regulation of hematopoiesis at steady-state[66,69], with reported impacts on both B cell[70,71,73,74] and T cell[72,73] production. Also, genetic perturbations of osteoblast-lineage cells have been shown to deregulate myelopoiesis and induce myeloid hematopoietic malignancies[75,80,81]. Here we found that Ocn^{+} osteoblastic cell activity is enhanced in the presence of distant solid tumors; this activity did not detectably alter tumor-infiltrating B or T cell responses, but was responsible for promoting the expansion of a

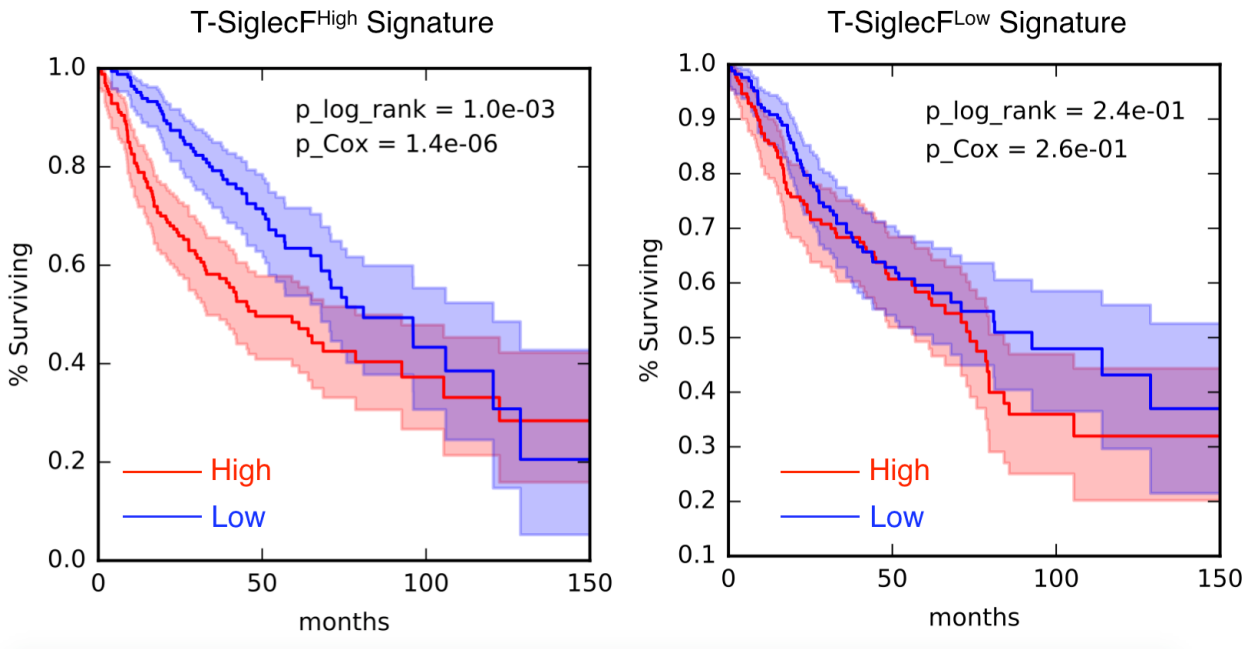

Figure 2.6 A SiglecF^{high} neutrophil gene signature associate with adverse survival in lung cancer patients.

(a) Survival (Kaplan-Meier) plots of lung adenocarcinoma patients. Patients were stratified based on high (SiglecF^{high}, top 25%) versus low (SiglecF^{low}, bottom 25%) expression of the humanized SiglecF neutrophil gene signature. *p* valued calculated using Cox regression method. See 2.6 Experimental Procedures for details. T- Tumor

distinct tumor-infiltrating subset of myeloid cells, SiglecF^{high} neutrophils, that contributed to the malignancy. These findings align with other data showing that granulocytes, most notably neutrophils, promote cancer in some animal models[22,36,93–97]. Human studies also indicate that high blood neutrophil-to-lymphocyte ratios are associated with adverse overall survival in many solid tumors, including lung adenocarcinoma[98], and that lung adenocarcinoma infiltration by neutrophils is strongly linked to poorer clinical outcome[14]. The SiglecF^{high} neutrophil subset identified here was tumor-promoting and exhibited phenotypes resembling those of granulocytic myeloid-derived suppressor cells[50]. In addition, single cell transcriptome analyses indicated that SiglecF^{high} neutrophils' functions likely are not limited to immunosuppression but extend to other tumor-promoting activities, including angiogenesis and extracellular matrix remodeling. Because both Ocn^{+} osteoblasts and SiglecF^{high} neutrophils contribute to shaping the tumor microenvironment and altering tumor progression, they may be relevant clinical biomarkers and vantage points for anticancer therapy.

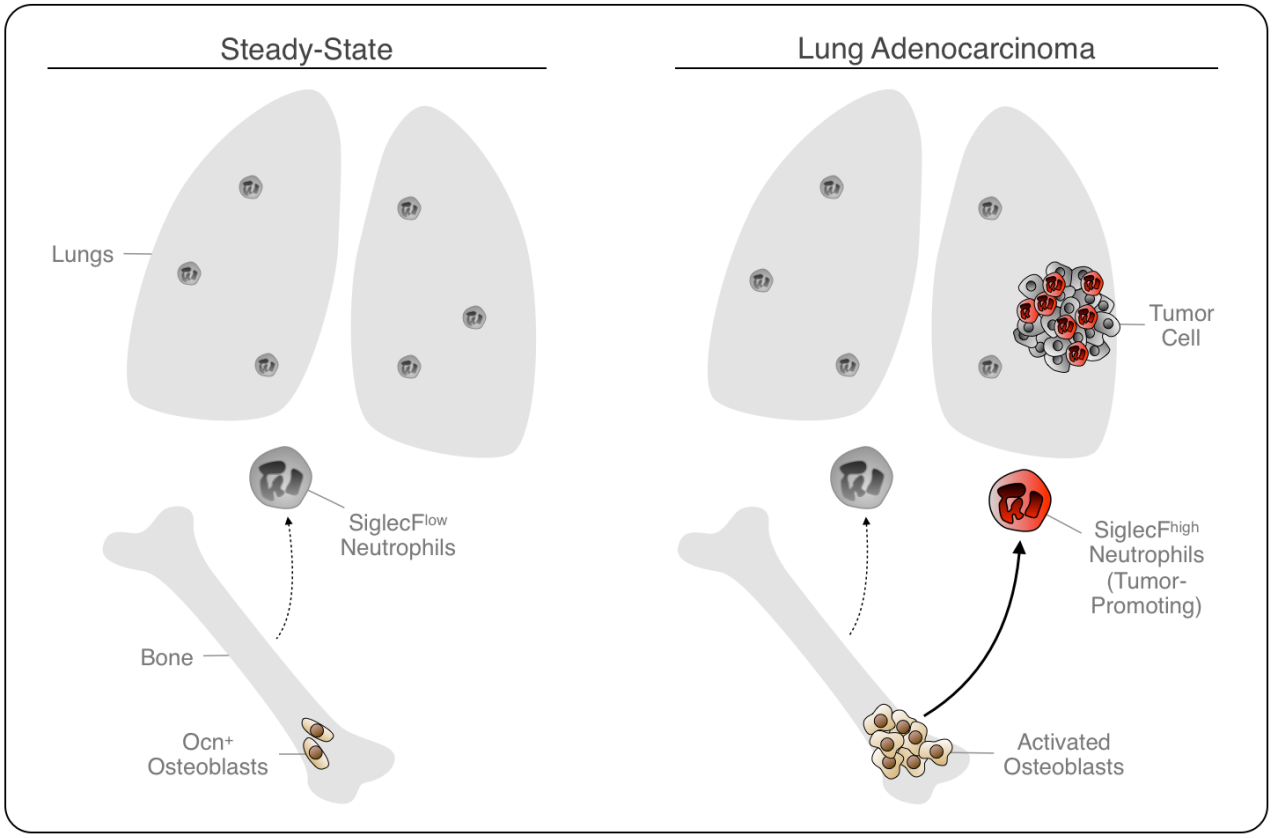

Figure 2.7 Cartoon depicting Ocn$^+$ osteoblast-mediated control of tumor-infiltrating SiglecF^{high} neutrophils.

To summarize, we report herein of a bi-directional relationship between lung tumors and the bone marrow; linking osteoblastic activity with a tumor-infiltrating neutrophil population. These long-range interactions can be broken down into several key processes: i) lung tumors' effect on osteoblast activity, ii) osteoblastic regulation of neutrophil production, iii) neutrophil precursor differentiation into SiglecF^{high} cells, and iv) SiglecF^{high} cell function at the tumor site (and putative similarities with MDSCs). These processes, and their (v) relevance to human disease will be discussed below.

2.4.1 Mechanisms of tumor-induced bone activity

We found that lung tumors increased bone density both in patients and in mice. There is precedent in the literature for tumor-bone marrow crosstalk via the blood, either through soluble mediators[22–26] or tumor-derived vesicles[99]. Preliminary experiments show that serum from tumor-bearing KP mice can increase osteoblastic differentiation *in vitro*, compared to serum from littermate tumor free mice, suggesting that there may be tumor-associated circulating factors or vesicles that could promote osteoblast activity. While we have not formally ruled out the potential contribution of vesicles as stimulators of osteoblastic activity in our system, *in vivo* tracking of tumor-derived vesicles in our lab for other studies found little vesicle uptake by bone marrow cells (as opposed to lymph node resident cells), suggesting that vesicles may be of minor relevance in this setting[27]. It is likely that the tumor-bone interaction is complex, and may involve multiple factors and other components in the bone marrow, including the nervous system, hematopoietic cells, or the vasculature. Nonetheless, our initial findings suggest that there are circulating components that appear sufficient to expand osteoblastic colony formation, at least *in vitro*.

Various tumor-associated soluble mediators have been investigated for their ability to act remotely on the bone marrow. For example, osteopontin, PF4, G-CSF, GM-CSF, and angiotensin II are elevated in the blood of tumor-bearing mice, and these factors act on cells in bone marrow and/or spleen to amplify hematopoietic cells that ultimately infiltrate the tumor[22–26]. Some lung cancer patients produce high levels of parathyroid hormone like protein (PTHrP), which has known bone-related effects; however, PTHrP in lung cancer is typically related to humoral hypercalcemia of malignancy, a paraneoplastic syndrome mainly found in squamous cell carcinoma lung cancer (as opposed to NSCLC), which manifests as osteolytic bone phenotypes, contrary to what we observe in our model[100]. In a genetic mammary tumor model, G-CSF is amplified systemically in tumor-bearing mice and promotes neutrophil and myeloid precursor expansion[22]. In our setting, we did not detect amplified G-CSF, GM-CSF, or osteopontin levels in the blood of KP tumor-bearing mice (data not shown), and G-CSF has also

been shown to reduce osteoblasts in tumor free mice (contrary to our findings), most notably when given exogenously at high doses to mobilize HSPCs[101]. Additionally, in previous studies, our lab showed that angiotensin II acts directly on hematopoietic precursors and promoted monocyte-derived macrophage, rather than neutrophil, influx into tumors, suggesting that angiotensin II is a less likely mediator of increased osteoblastic activity[24]. Therefore, it is plausible that other mediators are involved. We are currently investigating a set of tumor-associated factors that were increased in the serum from KP tumor-bearing mice, compared to healthy mice, measured by protein array. Identifying tumor-associated factors that amplify bone activity could reveal important insight into tumor-bone crosstalk and novel bone regulatory molecules, which could also be of therapeutic relevance to bone pathologies such as osteoporosis.

2.4.2 Osteoblastic interactions with SiglecF^{high} neutrophils in cancer

Our findings demonstrate that the depletion of bone marrow resident Ocn-expressing cells results in a reduction of tumor infiltrating neutrophils in the lung. This was not due to cell-intrinsic deficiencies in neutrophils since fate-mapping experiments using WT hematopoietic precursors transferred into Ocn depleted or control mice recapitulated these findings and in vitro delivery of DT to Ocn$^{Cre;Dtr}$ bone marrow cells did not deplete neutrophils. Further experiments should aim to clarify how Ocn^{+} cells affect amplification of tumor-associated neutrophils. We hypothesize that Ocn^{+} cells could be involved with the production, maturation, retention, or release of tumor-infiltrating SiglecF^{high} neutrophils (or their precursors, see Section 2.4.3).

It is possible that Ocn cells directly control SiglecF^{high} neutrophils or their precursors in the bone marrow. Fate-mapping experiments demonstrated that the development of tumor-infiltrating SiglecF^{high} neutrophils from transferred hematopoietic progenitor populations was significantly reduced in Ocn depleted mice (Figure 2.4D). Extending our analysis to the bone marrow, we found that Ocn reduction dramatically reduces the total number of hematopoietic cells in the bone marrow, in accordance with other osteoblast depletion models[69,71,102]. This

includes decreased numbers of both lymphoid and myeloid populations, with the largest numeric cellular losses in the $CD11b^{+}Ly6G^{+}$ and B cell compartments. Surprisingly, in Ocn depleted mice, only granulocyte numbers, and not B cells, decreased at the tumor site, with $SiglecF^{high}$ neutrophils being disproportionately affected (Figure 2.3C and S2.10). Granulocyte depletion and profiling experiments further indicated tumor-promoting properties of these neutrophils (Figure 2.3D and 2.5). In contrast, experiments for other studies in the lab showed that B cell depletion or deficiency by itself did not significantly alter KP tumor growth (not shown). These results suggested that Ocn-mediated control of tumor growth was mainly mediated by granulocytes, and $SiglecF^{high}$ neutrophils in particular.

Osteoblastic cells may also mediate neutrophil maturation or release from the bone marrow. Neutrophils may leave the bone marrow at a more immature state during inflammatory conditions, such as cancer[17]. Neutrophil egress from the bone marrow is tightly regulated by CXCR2 interactions with its chemokine ligands, which include CXCL1 and CXCL2, and by the CXCR4-CXCL12 axis[17]. It is possible that osteoblastic cells are involved in this process, as osteoblastic cells have been shown to express CXCL1/2[103] and CXCL12, although osteoblasts are not likely the main producer of the latter[73,73]. G-CSF, which is critical to neutrophil maturation, can be produced by osteoblastic lineage cells, including human osteoblasts[104] and murine osteocytes[75], and could be relevant in this context; however, it may be more complex since exogenous G-CSF may also negatively affect osteoblasts, as mentioned previously. Osteoblast gene expression or protein profiling from tumor-bearing versus tumor free mice should help to clarify these questions.

2.4.3 $SiglecF^{high}$ neutrophil precursors

Based on the dramatic changes in gene expression in $SiglecF^{high}$ compared to $SiglecF^{low}$ neutrophils at the tumor site, it is possible that these cell populations are derived from different circulating precursors. We know that adoptively transferred cKit expressing lineage negative

hematopoietic precursors can develop into both SiglecF^{high} and low tumor-infiltrating neutrophils in osteoblast sufficient WT tumor-bearing mice (Figure 2.3E), so presumably, if they arise from different cell populations, they must diverge at a later timepoint in granulopoiesis. As mentioned, under inflammatory conditions, less mature neutrophils may prematurely egress from the bone marrow[17]. A few studies have identified tumor-infiltrating neutrophil populations that share some characteristics of more immature neutrophils[17], such as increased *KIT* expression[36].

In our work, SiglecF^{high} versus SiglecF^{low} neutrophils could in theory represent cells at different maturational stages of the same developmental trajectory. In support of this idea, SiglecF^{high} cells express high levels of *Xbp1*, a transcription factor typically associated with ER-related stress, but with recently discovered roles in hematopoiesis[105]. In this study, X*bp1* expression was high in GMPs, which can develop into various myeloid cells including neutrophils, but exclusively retained in bone marrow eosinophil precursors that are downstream of GMPs[106]. It is plausible that these *Xbp1*-expressing eosinophil precursors could diverge towards neutrophil differentiation in the context of cancer or that more mature GMP-derived cells aberrantly retain *Xbp1* expression in tumor-bearing mice. As such, there could be a bone marrow *Xbp1*-expressing precursor population that could re-locate to the lung upon inflammatory cues and have the potential to differentiate into both neutrophils or eosinophils depending on the type of signals it receives; in line with this, a recent study identified a Ly6G expressing SiglecF eosinophil population in lungs of allergen-challenged but not healthy mice[107].

Preliminary gene expression analysis of blood and bone marrow neutrophil populations indicate that the upregulation of at least some SiglecF^{high}-associated genes can be observed prior to arrival at the tumor site. This would indicate that the differentiation towards SiglecF^{high}-like cells occurs beyond the tumor stroma and would support the idea that they arise from a more immature or distinct neutrophil precursor in the bone marrow, but does not exclude the possibility that SiglecF^{low} cells have the potential to differentiate into SiglecF^{high} cells at the tumor site. Of note, we do not observe SiglecF expression on circulating neutrophils, which

indicates that this particular marker is selectively amplified at the tumor site (data not shown). Further experiments, using fate mapping approaches and profiling of neutrophils and their precursors in the blood and bone marrow, are needed to test these hypotheses. It will also be important to define the mechanisms driving SiglecF^{high} neutrophil recruitment to the tumor site from circulation. Addressing these unknowns will also help to clarify the specific interactions between SiglecF^{high} neutrophils or precursor populations and osteoblasts in the bone marrow (Section 2.4.2).

2.4.4 SiglecF^{high} neutrophil functions at the tumor site

The majority of pre-clinical studies indicate that neutrophils have tumor-promoting properties. In support of these findings, elevated levels of neutrophils at the tumor site[14] or neutrophil to lymphocyte ratios in the blood[98] associate with poorer disease prognosis in several different cancer types. Mechanistic studies in mice have indicated that neutrophils may support tumor growth by various mechanisms, including stimulating tumor proliferation[108], inhibiting cancer cell senescence[109], promoting angiogenesis[93,94], or suppressing antitumor T cell activities[22,36]. For example, a recent study from Karin de Visser's lab showed that neutrophils promoted metastatic tumor growth by inhibiting cytotoxic T cell proliferation[36]. A smaller number of studies show that neutrophils can have antitumoral properties, plausibly at earlier stages of tumor progression although this requires investigation[110–112].

In our study, single-cell RNAseq profiling of tumor-infiltrating granulocytes revealed that SiglecFhigh, compared to SiglecF^{low}, neutrophils expressed high levels of many genes associated with tumor-promoting activities, including *csf1* (differentiation and recruitment of tumor-promoting macrophages), *nt5e* (CD73; immunosuppression), and *vegf* (angiogenesis). This analysis led us to hypothesize that SiglecF^{high} neutrophils likely accelerate tumor progression, which will need to be further interrogated in follow-up experiments. In vivo, the putative tumor-promoting activities of SiglecF^{high} cells (versus SiglecF^{low} neutrophils) could be

tested by gain- or -loss of function experiments. The latter remains technically challenging since as of today, there is no *single* cell surface marker that allows the detection and depletion of these cells. SiglecF itself is shared between SiglecF^{high} tumor-infiltrating neutrophils, eosinophils, alveolar macrophages and potentially a subset of CD11b^{+} macrophages in the tumor. Therefore, while SiglecF expression in combination with other markers is useful to define this particular subset of tumor-infiltrating neutrophils, it is not appropriate as a target for cell depletion studies, at least in mouse models. Conversely, gain-of-function experiments could be performed in which we sort SiglecF^{high} or SiglecF^{low} neutrophils from the lung tumor microenvironment and co-inject these cells with tumor cells to test their respective abilities to stimulate tumor growth in vivo.

SiglecF^{high} neutrophils may exhibit other tumor-promoting functions, which can be tested via ex vivo and in vitro assays. For example, reactive oxygen species (ROS)[22,113,114] and cathepsins[115,116], which have been shown to have tumor promoting properties, can be measured by fluorescent imaging probes *ex vivo*. These readouts require minimal manipulation of neutrophils, which is preferable since neutrophils are easily activated during isolation procedures. Based on their high expression of *csf1*, we also hypothesized that SiglecF^{high} neutrophils, compared to SiglecF^{low} cells, promote the infiltration, polarization, and/or differentiation of tumor-promoting monocyte-derived macrophages. KP tumor growth is supported, at least in part, by tumor-infiltrating macrophages[24,51], and it is possible that SiglecF^{high} neutrophils orchestrate macrophage-mediated tumor-promoting activities. This idea could be tested using in vitro systems by isolating different neutrophil populations from tumor-bearing lung tissue and co-culturing them with macrophages or their precursors. Finally, it is also possible that SiglecF expression by neutrophils is critical to their putative tumor-promoting activities. Other siglecs, such as SiglecE, can have tumor promoting properties when expressed in the myeloid lineage[117]'; SiglecF-associated functions in neutrophils (as opposed to eosinophils) are virtually unexplored. Whether KP tumors express SiglecF ligands is also not clear, but deciphering this could have implications for human tumors, since high levels of Siglec

ligands in tumors have been associated with worsened disease outcome and immunosuppression in some cancer types[117–119]. Taken together, our findings suggest that SiglecF^{high} neutrophils have unique tumor-promoting functions compared to SiglecF^{low} neutrophils, but further experiments are needed to clarify their precise roles in the tumor microenvironment.

2.4.5 SiglecF^{high} neutrophil and myeloid-derived suppressor cells

It is plausible that the SiglecF^{high} neutrophil population overlaps, at least in part, with the previously described myeloid derived suppressor cell (MDSC) population or tumor-infiltrating 'immature' myeloid cells. However, while there are some reports that distinguish MDSCs from neutrophils and monocytes based on developmental stage, cell density, or transcriptional activity, there is still no cell surface marker combination that allows the unique identification of MDSCs in mice[13,17]. In fact, the majority of murine MDSC studies use CD11b in combination with Gr-1, Ly6G and/or Ly6C to define MDSCs; these are the exact cell surface proteins used to identify neutrophils and monocytes. In addition, MDSCs are typically defined based on their ability to suppress T cell activity, often measured in vitro. We believe that this definition is incomplete for two main reasons. First, there are other immune cells that are potent T cell suppressors, such as macrophages, that are not included under this umbrella term. Second, 'MDSCs' are likely dynamically changing cells that can take on different functions based on their tissue microenvironment and context. Thus, the classification of cells as MDSCs is misleading as it obscures our abilities to distinguish these cells from other myeloid cells in the tumor microenvironment with certainty. In accordance with a recent review, we therefore consider Ly6G^{+} 'MDSCs' as neutrophils with immunosuppressive properties[17]. To help clarify the distinctions between different bone marrow-derived granulocytic cells, it could be relevant to test whether SiglecF labels neutrophil sub-populations in other tumor models. It may be a valuable marker to separate tumor-associated neutrophils with tumor-promoting functions from other

neutrophils, especially those present at steady state, and it would be informative to determine whether it is a useful marker to distinguish the cells identified as 'MDSCs' from other 'healthy' neutrophils.

2.4.6 Human relevance of SiglecF^{high} neutrophils

It is critical to determine whether SiglecF^{high} neutrophils would be useful prognostic and therapeutic targets in lung adenocarcinoma patients. Our initial results show that patients whose tumors expressed high, compared to those with low, levels of the SiglecF^{high} neutrophil gene signature at time of diagnosis had shorter survival (Figure 2.6). In contrast, high levels of a SiglecF^{low} neutrophil gene signature was not significantly correlated with disease outcome. These findings support the hypothesis that SiglecF^{high}-like cells exist in human tumors and have tumor-promoting activities. Specifically identifying these neutrophils in human tumor samples could potentially serve as a prognostic marker that is superior to bulk neutrophil analysis.

SiglecF^{high} neutrophils could also be putative therapeutic targets. There is no direct human ortholog of SiglecF, but Siglec8 may serve related functions in humans[118]. However, as with SiglecF in mice, Siglec8 expression has mainly been reported for eosinophils and other granulocytes, such as mast cells, and basophils[118]. Therefore, other alternative receptors or targetable proteins associated with SiglecF^{high} neutrophils cells could potentially be superior for clinical applications. It will be important to further phenotypically and functionally characterize neutrophils in human tumors with the goal to determine whether SiglecF^{high}-like cells are suitable therapeutic targets or can serve as prognostic indicators.

2.4.7 Conclusion

In summary, our findings introduce bone marrow osteoblasts as a novel player in regulating tumor-associated myeloid cell responses. Specifically, we find that lung tumors

expand bone activity in lung adenocarcinoma patients and in lung tumor-bearing mice. Preliminary data suggests that circulating tumor-associated factors may at least in part be responsible for the tumor-induced bone phenotype, but additional experiments are on-going to address this question further. In addition, we find that osteoblastic cells participate in a feedforward loop that results in the production of tumor-promoting neutrophil responses in the tumor microenvironment. Furthermore, our work provides a novel method to detect a unique tumor-specific neutrophil population *in vivo* with relevance to human disease. Taken together, our results support the continued exploration of systemic cancer-host interactions, in particular including the bone marrow stroma and myeloid cells, in both basic and translational research.

2.5 Acknowledgements

We thank the Harvard stem cell institute for help with FACS sorting; Daniel Brooks, Matthew Scott and Dr. Mary Bouxsein from the Center for Skeletal Research Core (NIH P30 AR066261) for micro-CT bone analysis services; members of the Hope Babette Tang Histology Facility at the Koch Institute Swanson Biotechnology Center for technical support; Dr. Marc Wein for helpful discussions and technical assistance; and Drs. Diane Mathis, Christophe Benoist, Shiv Pillai, Sandra McAllister and Glenn Dranoff for their input. This work was supported in part by the Samana Cay MGH Research Scholar Fund and NIH grants R01-AI084880 and P50-CA86355 (to M.J.P.); NIH grant U54-CA126515 (to R.W.); NIH grant U54-CA163109 and the Howard Hughes Medical Institute (to R.O.H.); Boehringer Ingelheim Funds PhD fellowships (to C.E. and D.P.Z.), Deutsche Forschungsgemeinschaft (DFG) PF809/1-1 and MGH ECOR Tosteson and Fund for Medical Discovery Fellowship (to C.P.); and a Metastasis/ Cancer Research Postdoc fellowship from the MIT Ludwig Center for Molecular Oncology Research (to S.R.).

2.6 Experimental procedures

Mice

Kras$^{LSL\text{-}G12D/WT}$*;p53*$^{Flox/Flox}$ (referred to as KP) mice were used as a conditional mouse model of non-small cell lung cancer (NSCLC)[45] and bred in our laboratory in the C57BL/6 background or in the laboratory of Dr. Meylan. To track and deplete osteoblastic lineage cells by genetic means, we generated mice that expressed Cre-driven yellow fluorescence protein (YFP) under the control of the osteoblastic cell reporter osteocalcin (Ocn)[92,120,121]. In detail, *Ocn*^{Cre} transgenic mice were bred to *Rosa*^{Dtr} (*C57BL/6-Gt(ROSA)26Sor*$^{tm1(HBEGF)Awai}$*/J)* and *Rosa*^{Yfp} mice (B6.129X1-*Gt(ROSA)26Sor*$^{tm1(EYFP)Cos}$/J) (Jackson Laboratory) to generate *Ocn*$^{Cre;Dtr}$, *Ocn*$^{Cre;Dtr/Yfp}$ or Ocn$^{Cre;Yfp}$ mice, respectively. *Cd11c*^{Dtr} mice (B6.FVB-Tg(Itgax-DTR/EGFP)57Lan/J) were obtained from Jackson Laboratory. *Cd169*^{Dtr} transgenic mice (*Siglec1*$^{tm1(HBEGF)Mtka}$) were kindly provided by the Riken Institute (Japan). Wild type and CD45.1 C57BL/6 mice were purchased from Jackson Laboratory. All animal experiments were performed according to approved IACUC guidelines, except experiments in KP mice for anti-Gr-1 antibody (Ab) depletion that were approved by the Veterinary Authority of the Canton de Vaud, Switzerland (license number VD2391) and the Réseau des animaleries lémaniques (RESAL) competent ethic committee.

Following primers were used for genotyping Ocn$^{Cre;Dtr/Yfp}$ mice:
iDTR = WSS-F: 5‘-GGCTACTGCTGACTCTCAACATT-3’; DTR-R: TCATGGTGGCGAATTCGAT
Cre = OcnCre-F: CAA ATA GCC CTG GCA GAT TC; OcnCre-R: TGA TAC AAG GGA CAT CTT CC
GFP (Jackson Laboratory) = oIMR0872: TTC ATC TGC ACC ACC G; oIMR1416: TTG AAG AAG ATG GTG CG

Tumor models

Adenovirus-Cre (AdCre) was delivered intratracheally (i.t.) to KP mice as previously described[45,46]. Mice were analyzed for bone or tumor phenotypes 12-14 weeks post-tumor

initiation. Tumor burden was scored by measuring post-mortem lung weight and by histological analyses of lung tissue using hematoxylin and eosin (H&E) stainings. For some experiments micro-computed tomography (μCT) was used to monitor tumor burden in the lung. The lung adenocarcinoma cell line KP1.9 was used to induce lung tumors in male wild-type C57BL/6, $Ocn^{Cre;Dtr}$ or $Ocn^{Cre;Yfp}$ mice via intravenous (i.v.) tail vein injection ($0.25x10^6$ cells in 100μl PBS). Male mice with KP1.9 tumors were typically euthanized between 28-41 days post-tumor cell injection. Cells of the lewis lung cancer line (LLC, $1.5x10^6$ cells in 150μl PBS) were injected i.v. into wild-type C57BL/6 mice and the mice were euthanized 32 days post-tumor cell injection. Diphtheria toxin (DT) was used to deplete Ocn^+ cells in $Ocn^{Cre;Dtr}$ and $Ocn^{Cre;Dtr/Yfp}$ mice; for the detailed depletion protocol see section: *In vivo* osteoblast depletion.

Cell lines

The KP1.9 cell line, derived from lung tumor nodules of a C57BL/6 KP mouse, was kindly provided by Dr. Zippelius (University Hospital Basel, Switzerland). The LLC cell line was obtained from ATCC. All cell lines were maintained in Iscove's DMEM media supplemented with 10% fetal bovine serum (FBS) and 1% penicillin/streptomycin.

Patient bone density measurements

The study was conducted using IRB approval (2016P000394/MGH) and complied with HIPAA guidelines with exemption status for individual informed consent. A retrospective search was performed to identify patients with non-small cell lung cancer (NSCLC) who were KRAS positive and KRAS negative, and who had undergone non-contrast chest CT prior to therapy at MGH between 2011 and 2017. Patients with osseous metastases, paraneoplastic syndrome or therapy prior to or at time of chest CT were excluded. Control subjects (referred to as control patients) who had undergone non-contrast chest CT using the same imaging protocols as the patient group were identified and 1:1 matched for sex, age and BMI, and smoking (pack-years). Potential controls with active malignancy, significant chronic illness or medication use known to

affect bone metabolism were excluded. Trabecular bone density was determined from non-contrast chest CT (16- or 64-MDCT scanner Biograph 16 or 64, Siemens Healthcare; or Discovery CT750HD, GE Healthcare) using an axial slice thickness of 2.5 or 5 mm, 120 kVp and 11-40 mAs. Scans were then reviewed offline on an IMPAX workstation (AGFA Diagnostic Software, version 4, Afga). Circular regions of interest (exemplarily shown in Figure 2.1F) within trabecular bone of the T6, T8, T10 and T12 vertebral bodies were placed manually, avoiding cortical bone and posterior veins. The mean trabecular bone density of each vertebral body in Hounsfield Units (HU) was determined and an average thoracic trabecular bone density of the four vertebral bodies was calculated.

Fluorescence molecular tomography (FMT)

OsteoSense-750EX[85] was injected retro-orbitally (4nmol/100µl, Perkin Elmer) according to manufacturer's instructions. The mice (for *in vivo* study) or cleaned bones (for *ex vivo* investigation) were imaged with FMT no earlier than 4 h and no later than 24 h post OsteoSense injection using an FMT imaging system (VisEn Medical). For *in vivo* imaging, hair from hind legs and lower abdomen were removed by shaving and chemical depilation. Mice were anaesthetized using isoflurane during the entire scanning procedure. The positioning of the mice relative to the detector were kept consistent throughout the experiments and groups. Detected OsteoSense signal in the femoral-tibial joint (region of interest, ROI) was analyzed using TrueQuant software and normalized against age and sex-matched control values.

Micro-computed tomography (µCT) for lung tumor measurements

Lung tumor volumes were received through repeated µCT measurements and pre- versus post-treatment measurements calculated. Mice were anaesthetized using isoflurane during the entire scanning procedure. Lungs were imaged with a CT (Quantum FX, PerkinElmer) at a 50-m voxel size, with retrospective respiratory gating. Individual tumor volumes were measured and calculated using the Analyze software (PerkinElmer).

Micro-computed tomography (μCT) for bone microarchitecture

Femurs from KP1.9 tumor-bearing versus age-and sex matched tumor-free controls were dissected out, cleaned, fixed in 10% formalin for 24 h, washed in PBS and transferred to 70% ethanol (EtOH) prior to μCT analysis. Trabecular bone microarchitecture and cortical bone morphology in the distal femoral metaphysis and mid-diaphysis, respectively, were quantified using a high-resolution desktop micro-tomographic imaging system (μCT40, Scanco Medical AG). The scans were performed using the following settings: 10μm^3 isotropic voxel size, 70 kVp peak x-ray tube intensity, 114 mA x-ray tube current, 200 ms integration time, and were subjected to Gaussian filtration and segmentation. Image acquisition and analysis protocols were performed according to μCT guidelines for the assessment of bone microstructure in rodents[122]. Trabecular bone was analyzed in a region (1500 μm; 150 transverse slices) extending proximally from 200 μm above the peak of the distal growth plate. A threshold of 339 mgHA/cm^3 was used to segment trabecular bone from soft-tissue and then, trabecular bone volume fraction (BV/TV, %), trabecular thickness (Tb.Th, mm), trabecular number (Tb.N, mm-1), trabecular separation (Tb.Sp, mm), and trabecular bone mineral density (Tb.BMD, mgHA/cm^3) were measured using the Scanco Evaluation program trabecular morphology script. Cortical bone was evaluated in a 500μm long (50 transverse slices) region at the femoral mid-diaphysis and was segmented using a threshold of 700 mgHA/cm^3 and then analyzed using the Scanco mid-shaft evaluation script to measure total cross-sectional area (Tt.Ar, mm^2), cortical bone area (Ct.Ar, mm^2), medullary area (Ma.Ar, mm^2), bone area fraction (Ct.Ar/Tt.Ar, %), cortical tissue mineral density (Ct.TMD, mgHA/cm^3), cortical thickness (Ct.Th, mm), cortical porosity (%), as well as the maximum, minimum and polar moments of inertia (I_{max}, I_{min}, and J, mm^4).

Histology and immunohistochemistry (IHC)

For histological analysis of tumor burden in mice, lung tissues and femurs were harvested, formaldehyde-fixed and paraffin-embedded following standard procedures and

consecutive sections were prepared. Lung tissue sections were stained with H&E to define tumor tissue areas in the lung as described earlier[46].

IHC on mouse tissue sections was performed as previously described[46]. Briefly, mouse lung and bone sections were prepared using a Leica RM2255 rotary microtome (Leica Biosystems), dried at 60°C for 1 h, dewaxed and rehydrated before treated with heat-induced epitope-retrieval (HIER) prior immunostaining. Therefore, the sections were incubated in 10mM Tris (pH9.0) or 10mM sodium-citrate (pH6.0) buffered solution containing 0.05% Tween and, depending on the Ab used, if needed heated at 120°C for 2 min using a pressure cooker. To obtain consistent and reliable staining the LabVision Autostainer 360 (Thermo Fisher Scientific) was used. The sections were pretreated using BLOXALL endogenous enzyme blocking solution (Vector Laboratories) for 10 min to destroy all endogenous peroxidase activity. After blocking with normal goat serum, the sections were incubated with rat anti-mouse Ly-6G (clone 1A8, Biolegend) or anti-mouse osteocalcin (clone M-15, Santa Cruz) monoclonal Abs (mAbs) for 1 h followed by several washes and secondary ImmPRESS polymer detection system (Vector Laboratories) according to the manufacturer's protocol. DAB Quanto (Thermo Fisher Scientific) was applied as substrate and hematoxylin used as counterstain.

Prior to preparation of bone tissue sections, femurs were harvested and cleaned, fixed for 24 h in 10% formalin, washed in PBS and transferred to 70% EtOH. The samples were then decalcified in 14% EDTA for up to two weeks and stored in 70% EtOH until paraffin embedding.

For anti-SiglecF stainings (rat anti-mouse Siglec-F mAb, clone E50-2440, BD Pharmingen), IHC on murine lung tissue of tumor-bearing KP mice was performed on frozen tissue sections. Spleen tissue sections were prepared for reference positive control stainings. Frozen tissue sections were generated as described before[46], air-dried and fixed in acetone (−20°C) for 10 min. The sections were rehydrated and treated as described above, but without HIER.

For histological evaluation of tumor metastases (femur), 10 regions of interest (n = 8) on paraffin embedded decalcified H&E stained femur sections were defined at 20x and blindly

scored for the presence or absence of tumor cell clusters. Positive control evaluations were done on histological sections from KP tumor-bearing lungs.

For cytospins, SiglecF^{high} neutrophils (CD45$^+$CD11b$^+$Ly-6G$^+$SiglecF$^+$), SiglecF^{low} (CD45$^+$CD11b$^+$Ly-6G$^+$SiglecF$^-$) neutrophils and lung alveolar macrophages (CD45$^+$CD11b$^-$ F4/80$^+$SiglecF$^+$CD11c$^+$) were FACS sorted from lung tissue of KP tumor-bearing or tumor-free mice based on marker expression using the following anti-mouse mAbs: CD45 (clone 30-F11, Biolegend), Ly-6G (clone 1A8, Biolegend), CD11b (clone M1/70, BD), SiglecF (clone E50-2440, BD), Ly-6C (clone HK1.4, Biolegend), CD11c (clone N418, eBioscience). Cytospins were performed using a Shandon Cytospin 4 centrifuge (Thermo Fisher Scientific). In detail, 5x10^4 cells were centrifuged (500 rpm, 3 min) onto Tissue Path Superfrost Plus Gold microscope slides (Thermo Fisher Scientific) and dried overnight at RT. Cytospins were then fixed in 4% formaldehyde-buffered solution and H&E stained following standard procedures.

For all histological sections, image documentation was performed using the NanoZoomer 2.0-RS slide scanner system (Hamamatsu).

Bone histomorphometry

Bone histomorphometric analysis was performed on femurs from KP1.9 tumor-bearing or age and sex-matched tumor-free controls as previously described[123]. In brief, calcein (20mg/kg; Sigma) and demeclocycline (50mg/kg, Sigma) were injected at 9 days and 2 days prior to animal euthanasia, respectively. Dissected, cleaned, formalin-fixed (10%, 24 h) femurs were washed in PBS and transferred to 70% EtOH. Fixed non-decalcified femurs were dehydrated (graded ethanol) and subsequently infiltrated and embedded in methylmethacrylate. Longitudinal sections (5μM) were cut using a microtome (RM2255, Leica) and stained with Goldner Tricrome for measurements of cellular parameters and by the method of Von Kossa[124] to evaluate bone mineralization. Dynamic bone parameters were evaluated on unstained sections by measuring the distance between double labels using the Osteomeasure analyzing system (Osteometrics Inc.). Measurements were made in the area 200μm below the growth

plate. Quantification of bone parameters was done in a blinded manner. The structural, dynamic and cellular parameters were evaluated using standardized guidelines[125].

Confocal microscopy

Confocal microscopy was performed based on a previously published protocol[126]. The mice were injected with OsteoSense retro-orbitally to label bone (< 24 h before mice were sacrificed) and with fluorescently conjugated mAbs (anti-CD31 (clone MEC13.3, Biolegend), anti-CD144 (clone BV13, Biolegend), anti-Sca1 (clone D7, eBioscience)) 30 min prior to euthanasia via cardiac perfusion with PBS and subsequent 4% methanol-free paraformaldehyde (Alfa Aesar). After fixation, the femurs or sternums were quickly dissected out, cleaned of tissue and cut for imaging. In brief, sternum marrow was exposed by cutting longitudinally along the bone and subsequently scanned at 10x (3-4 partially overlapping field of views). Femurs were OCT embedded, frozen at -80^{o}C ($\geq$1 h), and marrow tissue was exposed using a cryostat. Z-stack images from femur and sternum were immediately acquired at 2-5μM steps (Olympus IV100 confocal microscope) and analyzed in FIJI (ImageJ). Non-injected controls or non-fluorescent mice were used as staining controls.

In vivo Gr-1^{+} cell depletion

Twelve-to-fourteen weeks old KP mice were infected i.t. with 1500 Cre-active lentiviral units using a protocol described earlier[45]. KP mice bearing well-established tumors (identified by μCT) were treated 20 weeks post tumor initiation with anti-Gr-1 mAb (10 mg/kg, clone RB6-8C5, BioXcell) intraperitoneally (i.p.) three times per week for 2 weeks. Neutrophil depletion was validated by tail-vein blood sampling at day 7 followed by flow cytometry analyses of SSC^{hi} Ly-6G^{+} circulating cells. Control mice were injected with IgG control mAb (10 mg/kg, clone 2A3, Jackson Immunoresearch). At the end of the experiment tumor-bearing lungs were collected and single cell suspension were obtained using the GentleMACS tissue octo dissociator (Miltenyi) and an enzymatic digestion mix composed of DMEM, 0.02 mg/ml DNAse I (Sigma)

and 1 mg/ml collagenase (Sigma) applied for 35 min at 37°C. Cells were washed with medium then resuspended in PBS supplemented by 2% FBS and 0.5mM EDTA. To obtain single cell suspensions, cells were passed through 70µm cell strainer. Cell number was determined and $1x10^7$ cells were used for flow cytometry staining. Cells were first stained with live and dead blue dye (Life Technologies) in PBS containing Fc-Block reagent (Miltenyi) for 20 min at 4°C. After washing, mAb staining (anti-Ly-6G-FITC, clone RB6-8C5; anti-CD11b-BV711, clone M1/70; anti-Ly-6C-AlexaFluor700, clone HK1.4; anti-CD11c-BV450, clone N418 and anti-CD45-PerCP, clone 30-F11; all from Biolegend) was performed on ice or a 4°C in PBS supplemented with 2% FBS and 0.5mM EDTA for 15 min. All acquisitions were performed using the LSRII SORP (BD), a 5-laser and 18-detector analyzer at the EPFL Flow Cytometry Core Facility. Data analyses were performed using FlowJo X (FlowJo LLC).

In vivo osteoblast depletion

$Ocn^{Cre;Dtr}$, $Ocn^{Cre;Dtr/Yfp}$ and control mice lacking either transgene were treated i.p. with DT (100µl; 20µg/kg, Sigma-Aldrich) every other day for 9 days with a total of five injections per mouse. Body weight was monitored to control for DT-induced toxicity. Osteoblast depletion was verified using histological evaluation of femurs, IHC for osteocalcin and *ex vivo* whole mount immunofluorescence of $Ocn^{Cre;Dtr/Yfp}$ mice. Performing *in vitro* DT titration studies and *in vivo* cellular stainings using flow cytometry, we ensured that the used DT concentration did not effect the viability of hematopoietic cells in this murine model.

In vivo NK cell depletion

NK cells were depleted in tumor-bearing $Ocn^{Cre;Dtr}$ or control mice performing i.p. injections of anti-NK1.1 Ab (clone PK136, BioXcell, 200µg/mouse, i.p.) every fourth day. The detailed treatment schema is outlined in Figure S2.11A. NK cell mAb depletion in osteoblast reduced tumor-bearing mice was evaluated using flow cytometry and was efficient in

substantially decreasing lung NK cells (detected by CD49b and NKp46 double staining since the NK1.1 epitope may be masked by the depleting mAb).

In vitro assay to test potential DT-mediated direct effects on hematopoietic cells

Splenocytes from WT or $Ocn^{Cre;Dtr}$ mice were harvested by gently meshing a spleen through a 40μm filter. The cells were washed, plated in medium (RPMI, 10% FBS, 1% P/S) and treated with 0, 1, 10, 100, 1000 ng/ml of DT. Cells were harvested after 20 h of incubation at 37°C and stained with mAbs for flow cytometry, see section on flow cytometry for staining procedure.

Parabiosis

In some experiments, parabiosis was used to study the contribution of circulating cells to osteoblast-controlled tumor-infiltrating immune cells. The experimental procedure was performed as previously described[27]. In brief, one week post-tumor injection, lung tumor-bearing $Ocn^{Cre;Dtr}$ mice were parabiosed to $Ocn^{Cre;Dtr}$ or control mice (lacking either transgene). Both types of parabionts were treated with DT following the procedure described in section: *In vivo* osteoblast depletion.

Granulocyte single cell RNAseq

Single cell RNA sequencing (scRNA-Seq) data were obtained from $CD45^+$ cells collected from either tumor-free or KP tumor-bearing lungs from two independent experimental replicates using droplet microfluidic barcoding technology (inDrops) as previously described[127]. Due to the limited sensitivity of scRNA-Seq at the single cell level, which leads to gene 'drop-out' events, SiglecF expression alone could not be reliably used to distinguish $SiglecF^{high}$ and $SiglecF^{low}$ cells. Therefore, we defined a SiglecF expression score, among granulocytes (n = 6,020 cells), for each single cell *k* as $S_k=(X_k-Y_k)$, where $X_k = \sum_{i=1}^{50} r_{k,i}$ and $r_{k,i}$ is the percentile gene expression (dense ranking) of cell *k* for gene *i*, for the 50 most correlated genes to SiglecF

(Spearman correlation), and $Y_k = \sum_{i=N\text{-}49}^{N} r_{k,i}$ is the corresponding sum of percentiles of the 50 most anticorrelated genes to SiglecF (Table S2.2). As anticipated from FACS data, the distribution of granulocytes by Siglecf expression score was bimodal in tumor tissue, with SiglecF^{low} cells overlapping with healthy granulocytes. By visual inspection of Figure S2.18A, we set a threshold of -7 to separate between SiglecF^{high} and SiglecF^{low} granulocytes in tumor tissue.

For differential gene expression (DGE) analysis of healthy, tumor SiglecF^{low}, and tumor SiglecF^{high} granulocyte populations, we used a parameter-free permutation-based test to calculate p-values, with the difference in means as the test statistic. We accounted for multiple hypothesis testing with a false discovery rate of 5% using the Benjamini-Hochberg procedure[128]. To be considered for differential gene expression analysis, genes had to be expressed at least by 5% of cells in at least one of the two groups of cells compared. Significantly differentially expressed genes with an absolute fold-change of 2 were selected for further analysis. Genes judged as significant by the permutation test but with a p-value less than the specified accuracy of the permutation test were assigned an approximate p value using a t-test assuming unequal variances for representation on volcano plots.

For gene set enrichment analysis[129,130], we performed the same pre-filtering as for DGE analysis: only genes expressed by at least 5% of cells in at least one the two groups in a comparison were considered. Then we used the GSEA PreRanked tool[129,130] on genes ranked by log2 (fold-change) and considered gene sets that were enriched based on an FDR of 25%.

Bioinformatical analyses of lung adenocarcinoma patients

In silico analyses were performed similarly as previously described[25], with a modification in patient stratification. Tumor transcriptome and survival data from lung adenocarcinoma patients were obtained from six databases (DFCI, MI, HLM, Ladanyi, Gerald, MSKCC)[25,90,91]. For each patient *k*, a SiglecF^{high} gene signature was computed as $S_k = \frac{\sum_{i=1}^{100} r_{k,i}}{100}$ where $r_{k,i}$ is the percentile gene expression (dense ranking) of patient *k* for gene *i*, for the top 100 genes

ordered by decreasing fold-change in SiglecF^{high} cells compared to SiglecF^{low} cells in tumors defined by scRNAseq analysis of murine lung tumors (Table S2.2). Only murine genes with human orthologs that were differentially expressed (statistical significance determined as described above) at >100TPM in SiglecF^{high} cells were considered. The SiglecF^{low} gene signature was defined in an analogous way. Cox proportional hazards model with sample origin by database as a categorical variable was used to determine whether the SiglecF^{high} signature predicted human patient survival. For Kaplan-Meier plots, survival data of top 25% and bottom 25% SiglecF^{high} signature expressers was used. Survival analysis was performed using the Lifelines package in Python[131].

In vivo cell fate mapping

To track the progeny of hematopoietic precursors in tumor-bearing control or Ocn depleted mice, we performed cell fate mapping experiments. We used bead enrichment (Miltenyi) followed by FACS-based sorting of live lineage negative congenic CD45.1 cKIT$^+$ (CD117) cells (here lineage = B220, CD19, Ter119, CD11c, CD11b, NK1.1, CD49b, CD127, Ly-6G, CD90.2). The purity of the sorted CD45.1$^+$ cKIT$^+$ cells was above 95%. 2.5 x 10^5 cells were injected i.v. into tumor-bearing control or Ocn depleted mice (both CD45.2 genotypes) at 29 days post tumor-injection. 7 days post-cKit$^+$ cell transfer, lung tumor tissue was harvested and CD45.1$^+$ immune cell infiltrates were quantified using flow cytometry. Non-injected biological controls, Fluorescence Minus One (FMO)-staining controls and unstained cells were used to analyze the CD45.1$^+$ cell progeny in the tissue.

p53 recombined PCR for tumor cell detection

Detection of p53 recombined locus (only present in KP tumor cells after exposure to Cre recombinase) was used to survey bone and marrow tissues for KP tumor cell metastases. In brief, DNA was extracted from bone marrow or calvarial bone (after digestion) using DNeasy blood and tissue kit (Qiagen) according to manufacturer's instructions. KP1.9 tumor cells were

used as positive control. Different DNA concentrations from KP1.9 tumor cells were used to determine PCR detection limit to <10 cells (with the estimate of ~6pg DNA/cell). DNA was isolated from Gel PCR products from a primary PCR run. A second PCR amplification run on these DNA samples was performed to detect low levels of DNA in the isolated tissues. The following primers were used: A: 5' CAC AAA AAC AGG TTA AAC CCA G 3'; B: 5' AGC ACA TAG GAG GCA GAG AC 3'; C: 5' GAA GAC AGA AAA GGG GAG GG 3'. Following bands were amplified: p53 recombined 1lox: 612bp, WT band: 288bp and a background band: 400bp.

Flow cytometry

Single cell suspensions were obtained from lung tumors, bone marrow, spleen and bone tissue. The respective tissues and isolated single cell fractions were kept on ice for all steps if not stated otherwise. Tumor tissue was received by dissecting out tumor-bearing lungs. Small tissue pieces were generated using scissors and digested (RPMI containing 0.2 mg/ml collagenase type I, Worthington Biochemical Corporation) for 1 h at 37°C while shaking. Femurs and for some experiments tibias were harvested, cleaned and the bone marrow flushed out using cold staining buffer (PBS containing 0.5% BSA and 2mM EDTA). Digested lung tissue and harvested bone marrow were gently meshed through 40µM cell strainers using a plunger. Spleens were harvested and also meshed through 40µM cell strainer as described before.

Red blood cells were removed using 1 ml ACK lysis buffer (Lonza) per cell pellet for 1 min (for lung cells) or 2 min (for spleen cells) and the reaction was stopped with RPMI media. The resulting single-cell suspensions were washed and resuspended in staining buffer. In order to investigate bone cells by flow cytometry, in general, long bones were harvested, cleaned and crushed gently and the released cells were collected (fraction 1) and lysed with ACK lysis buffer. In parallel, the bone fragments (fraction 2) were cut into small pieces with scissors, filtered through 70µM cell strainer, digested (PBS containing 20% FBS and 0.25% collagenase type I) for 1 h at 37^{o}C, washed and finally pooled with the cells derived from fraction 1. Single cell suspensions were incubated with FcBlock (clone 93, Biolegend) for 15 min at 4^{o}C, followed by

staining with fluorescent conjugated Abs for 45 min at 4°C. The cells were washed with staining buffer and analysed on a LSRII flow cytometer (BD). 7-aminoactinomycin (7AAD, Sigma) positivity was used to exclude dead cells.

Following cell populations were identified based on cell marker expression: Ocn^+ cells ($Lin^-CD45^-CD31^-Ter119^-YFP^+$), granulocytes ($CD45^+CD11b^+Ly\text{-}6G^+$), $SiglecF^{high}$ granulocytes ($CD45^+CD11b^+Ly\text{-}6G^+SiglecF^+$), $SiglecF^{low}$ granulocytes ($CD45^+CD11b^+Ly\text{-}6G^+SiglecF^-$), monocytes ($CD45^+CD11b^+Ly\text{-}6G^-Ly\text{-}6C^{high}$), $CD11b^-$ lung macrophages ($CD45^+CD11b^-F4/80^+SiglecF^+CD11c^+$), T cells ($CD45^+CD3^+CD4^+$ or $CD8^+$), B cells ($CD45^+B220^+CD19^+$), NK cells ($CD45^+CD49b^+NK1.1^+$ or $CD45^+CD49b^+NKp46^+$).

The lineage (Lin) Ab mix contained the following Abs unless otherwise noted: B220, CD19, Ter119, CD11c, CD11b, NK1.1, CD49b, CD127, Ly-6G, CD90.2.

Following Abs were purchased from BD if not specified otherwise: B220 (553089, clone RA3-6B2); CD19 (553786, clone 1D3); Ter119 (553673, clone TER-119); CD11c (12-0114-83, clone N418, eBioscience); CD11b (557397, clone M1/70); NK1.1 (553165, 550627, clone PK136); CD49b (553858, clone DX5); CD127 (12-1271-82, clone A7R34, eBioscience); Ly-6G (551461, 560599, clone 1A8); CD90.2 (553006, clone 53-2.1); SiglecF (564514, clone E50-2440); CD4 (557956, clone RM4-5) or Biolegend: CD117 (105812, clone 2B8); F4/80 (123115, clone BM8); CD45.1 (110738, clone A20); CD45.2 (109831, clone 104); CD3e (100306, clone 145-2C11); CD8 (100725, clone 53.-6.7); CD19 (115530, clone 6D5); CD11c (117333, clone N418); Nkp46 (137619, clone 29A1.4); CD45 (103126, clone 30-F11).

Statistical methods

Unpaired t-test was used to compare two groups. Multiple t-test was performed to compare several cell populations between two groups and multiple testing was accounted for in the calculation of significant differences between groups using the Holm-Sidak method. One-way ANOVA with subsequent post-hoc analysis was done to compare three or more groups. GraphPad Prism was used to test for statistical significance except for when noted. Matlab and

Python were used for scRNAseq analysis, corresponding statistical testing is described above in section: *Granulocyte single cell RNAseq.* *p<0.05, **p<0.01, ***p<0.001, ****p<0.0001, n.s. not significant.

Chapter 3: Transforming the tumor stroma by immunogenic drugs

3.1 Overview

Immunogenic chemotherapeutics sensitize tumors to checkpoint blockade therapy

Christina Pfirschke*,**Camilla Engblom***, Steffen Rickelt, Virna Cortez-Retamozo, Christopher Garris, Ferdinando Pucci, Takahiro Yamazaki, Vichnou Poirier Colame, Andita Newton, Younes Redouane, Yi-Jang Lin, Gregory Wojtkiewicz, Yoshiko Iwamoto, Mari Mino-Kenudson, Tiffany G. Huynh, Richard O. Hynes, Gordon J. Freeman, Guido Kroemer, Laurence Zitvogel, Ralph Weissleder, Mikael J. Pittet

Immunity (2016) 44, 343–354

*These authors contributed equally to this work

Summary

Checkpoint blockade immunotherapies can be extraordinarily effective, but may benefit only the minority of patients whose tumors are pre-infiltrated by T cells. Here, using lung adenocarcinoma mouse models, including genetic models that are driven by mutant *Kras* and deleted *Trp53* genes, we showed that autochthonous tumors that lacked T cell infiltration and resisted current treatment options could be successfully sensitized to host antitumor T cell immunity when using appropriately selected immunogenic drugs (oxaliplatin combined with cyclophosphamide). The antitumor response was triggered by direct drug actions on tumor cells, relied on innate immune sensing through toll-like receptor 4 signaling, and ultimately depended on $CD8^+$ T cell antitumor immunity. Furthermore, instigating tumor infiltration by T cells sensitized tumors to checkpoint blockade inhibition and controlled cancer durably. These findings indicate that the proportion of cancers responding to checkpoint therapy can be feasibly and substantially expanded by combining checkpoint blockade treatment with immunogenic drugs.

Attributions

For this project, I, together with C.P. designed the study, performed experiments, analyzed data and wrote the manuscript.

3.2 Introduction

The ability of the immune system to control tumor cells was proposed more than a century ago, demonstrated during the last decade, and recently harnessed for therapy[11,132]. A foundational principle of tumor immunology is that cancer cells can be eliminated by host cytotoxic $CD8^+$ T cells[6,133–135]. Accordingly, $CD8^+$ T cell infiltration of various solid tumor types has positive prognostic value[136], although these cells can be subject to various suppressive mechanisms including inhibition by regulatory T (Treg) cells and induced expression of programmed death-1 (PD-1) and other inhibitory checkpoint receptors, all limiting the antitumor functions of lymphocytes[11,132].

Therapies targeting T cell inhibitory checkpoint signaling pathways are redefining cancer therapy because clinical trials have shown unprecedented rates of durable responses in patients with common cancer types, including lung adenocarcinoma[132]. Lung adenocarcinoma was long considered to be nonimmunogenic and is the leading cause of cancer incidence and mortality worldwide, with more than one million deaths per year[137]. Yet, only a minority of cancer patients respond to checkpoint blockade inhibition and evidence suggests that those patients may preferentially have tumors that have favorable mutational landscapes, express the PD-1 ligand (PD-L1) and/or contain pre-existing tumor-infiltrating $CD8^+$ T cells that are inhibited locally, e.g., by PD-1 engagement[35,132,134,138–141]. In order to define the proportion of patients who could ultimately benefit from immunotherapies, it appears important to clarify whether strategies can be employed for converting tumor microenvironments lacking T cell infiltration to ones displaying antitumor T cell immunity and then to determine whether this process sensitizes tumors to checkpoint blockade therapy.

One approach to achieving this goal may involve the induction of immunogenic conditions in the tumor microenvironment. For example, some chemotherapeutics and other treatments have been shown to shape clinical outcome by influencing tumor-host interactions to stimulate T cell immunosurveillance[142–144]. The drugs prescribed today against lung adenocarcinomas only marginally increase survival. Despite their low success rate, these drugs deserve re-consideration for several reasons, especially when combined with immunotherapy: *i)* they were originally selected for their capacity to prevent human tumor cell growth *in vitro* and in xenotransplanted immunodeficient mouse models without considering the relevance of immune reactions to treatment outcomes; *ii)* they are generally given indiscriminately even though their impact may vary across individuals and tumor microenvironments and *iii)* improved understanding of drug effects *in vivo* may help to identify synergistic treatment options.

To address these knowledge gaps we explored conditional genetic lung adenocarcinoma models (with *Kras* and *Trp53* mutations), in addition to orthotopic lung tumor models. In the genetic models, cancer cells are derived from somatic cells that are transformed in their normal tissue microenvironment and progress to high-grade tumors that lack T cell infiltration and resisted prescribed chemo- and immunotherapeutic treatments. These models can also be used to study autochthonous tumors that express model neoantigens, which are important drivers of antitumor T cell immunity[135,145] and targets of checkpoint blockade therapy[134]. The genetic tumor models we used for this study also avoided the inherent limitations of tumor grafts, including sensitivity to numerous chemotherapeutic agents[146].

Here, we investigated whether distinct immunogenic chemotherapeutics could trigger $CD8^+$ T cell influx into tumors and sensitization to immune checkpoint therapy using orthotropic tumor models that resist current standard anticancer treatments and in which tumors are poorly infiltrated by T cells. To this end, we defined a combination of clinically approved chemotherapeutic drugs (oxaliplatin-cyclophosphamide; Oxa-Cyc) that elicited immunogenic phenotypes on lung tumor cells *in vitro* and *in vivo*. We showed that challenging tumor-bearing mice with Oxa-Cyc resulted in tumor T cell infiltration and controlled tumor progression. Oxa-

Cyc limits disease via direct drug actions on tumor cells and host components such as $CD8^+$ T cells and intact TLR4 signaling. Furthermore, we demonstrated that immunogenic chemotherapy successfully sensitizes mice to immune checkpoint blockade and that this treatment combination durably controls cancer outgrowth in several cancer models. These findings highlight that appropriately selecting immunogenic drugs can transform 'T cell poor tumors' into 'T cell rich tumors' and present a possible approach to expand the proportion of patients that respond to checkpoint blockade therapy.

3.3 Results

3.3.1 KP lung adenocarcinomas resist current treatment options

Kirsten rat sarcoma viral oncogene homolog *(KRAS)* and tumor suppressor p53 (*TP53)* genes are mutated in ~25% and 50%, respectively, in non-small cell lung cancer (NSCLC) patients. Initially, we examined *Kras*$^{LSL\text{-}G12D/+}$;*Trp53*$^{flox/flox}$ (hereafter KP) mice that express endogenous mutant *Kras* and deleted *Trp53* alleles in lung epithelial cells upon administration of adenovirus expressing Cre recombinase[24]. These mice develop lung adenocarcinomas with both pathophysiological and molecular features of the human disease. Evaluation of the lungs of KP tumor-bearing mice revealed the presence of $CD3^+$ T cells only within the normal tissue parenchyma and at frequencies that were comparable to those in tumor-free mice; by contrast, all the KP lung adenoma and adenocarcinoma nodules lacked $CD3^+$ T cell infiltration (Figure 3.1A and S1A-C**)**. As anticipated for tumors lacking pre-infiltrated T cells, anti-PD-1 monoclonal antibody (mAb) treatment failed to delay KP tumor progression (data not shown) and did not increase KP mouse survival as defined by the Kaplan-Meier estimator (Figure 3.1B). Similar results were obtained for KP mice on the 129 and C57BL/6 backgrounds (data not shown).

We extended our examination to wild-type mice bearing orthotopic syngeneic KP1.9 lung adenocarcinoma cells harboring *Kras* and *Trp53* mutations. Anti-PD-1 treatment also failed to control tumor progression in this model (Figure 3.1C). Using a third mouse model, we examined

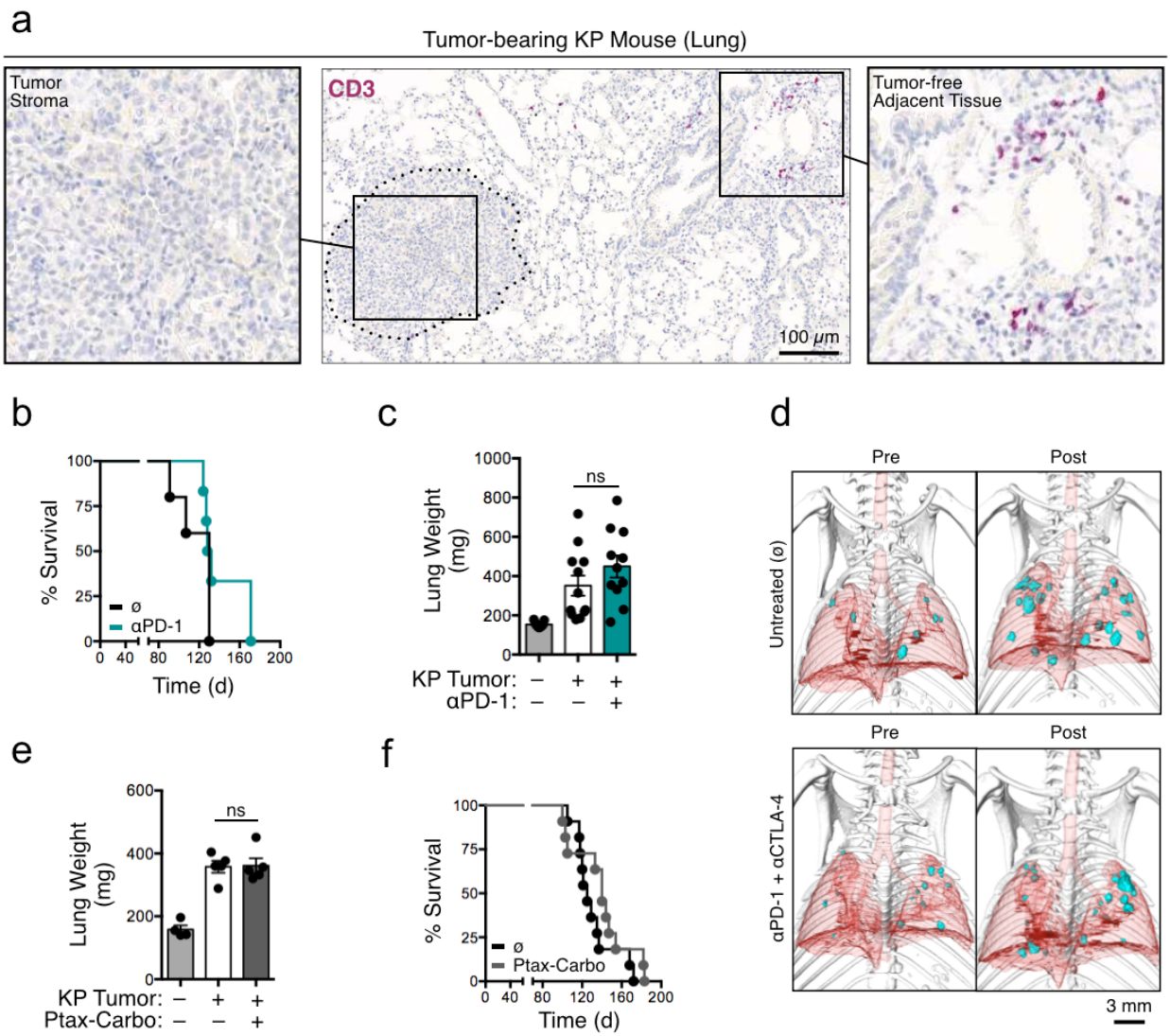

Figure 3.1 *Kras-Trp53*-mutated lung adenocarcinomas are inadequately infiltrated by T cells and resist current treatment options.

(a) Immunohistochemistry of $CD3^+$ cells in KP lung tumor tissue on day 66 after tumor initiation.
(b) Survival of KP mice treated or not with anti-PD-1 (αPD-1) mAbs (n=5-6 mice per group). Tumors were induced on day 0 by intratracheal intubation and inhalation (i.t.) of an adenovirus expressing Cre recombinase (AdCre). Mice were treated every third or fourth day with anti-PD-1 Abs intraperitoneally (i.p.) starting from day 60 to 86.
(c) Lung weight as proxy for tumor burden analyzed on day 44 of mice bearing orthotopic KP1.9 tumors and treated or not every third or fourth day with anti-PD-1 mAbs starting on day 25 till 42 after tumor cell injection (n=9-12 mice per group).
(d) Micro-computed tomography lung images of KP-OVA mice both pre- (day 122) and post-treatment (day 146) with no antibody (ø) or with anti-PD-1 and anti-CTLA-4 (αPD-1 + αCTLA-4) mAbs. Tumors were induced with a lentiviral vector containing OVA peptide sequences (LucOS) i.t. and Ab treatment performed every second or third day starting from day 133 to 145.
(e) Lung weight (n=4-5 mice per group) and **(f)** survival (n=11 mice per group) of KP mice treated or not with paclitaxel and carboplatin (Ptax-Carbo). Mice were treated once a week for three weeks starting on day 63 post i.t. tumor initiation and lungs analyzed three days after the last drug injection. For survival studies, Ptax-Carbo was injected i.p. once a week. ns, not significant. See also Figure S3.1.

whether introducing neoantigens sensitizes KP tumors to immune checkpoint therapy. We gave KP mice a Cre-based lentiviral vector containing ovalbumin (OVA) peptide sequences to produce KP-OVA mice bearing tumors expressing model OVA neoantigens[147]. These mice were treated with both anti-PD-1 and anti-cytotoxic T-lymphocyte-associated protein 4 (CTLA-4) mAbs because combined checkpoint blockade can increase response rates in cancer patients[11,148,149]. Treatment was initiated on day 133 when lung adenocarcinomas were detectable by micro-computed tomography (Figure 3.1D) and poorly infiltrated by $CD8^+$ T cells[147]. KP-OVA tumors remained refractory to anti-PD-1 and anti-CTLA-4 mAb combination therapy that was applied for two weeks (Figure 3.1D).

We also assessed the effects of mainstay lung cancer chemotherapeutics in KP mice. Besides cisplatin treatment, which only marginally controls KP tumor progression[150], we evaluated paclitaxel (Ptax) and carboplatin (Carbo), which are often administered in combination because of their synergistic effects on microtubule and DNA damage, respectively. We observed that Ptax-Carbo treatment failed both to curb KP tumor progression (Figure 3.1E and S3.1D) and to extend KP mouse survival (Figure 3.1F). We also assessed tumor infiltration by $CD8^+$ T cells in 76 tumor biopsy sections from NSCLC patients who were also genotyped for *KRAS*, *TP53* and epidermal growth factor receptor (*EGFR)* mutations. We did not detect differences in $CD8^+$ T cell infiltration based on the *KRAS* or *EGFR* status of tumors; however, *TP53*-mutated tumors as well as *TP53-KRAS*-double mutated lung tumors showed significantly reduced $CD8^+$ T cell infiltration compared to their nonmutated counterparts (Figures S3.1E and S3.1F). Taken together, these results indicate that the KP mouse model is relevant to explore tumors that shared important features with their human counterparts and, most importantly, resisted current immuno- and chemotherapeutic interventions.

3.3.2 Selected chemotherapeutics induce KP tumor cell immune phenotypes

Considering that KP tumor nodules lack T cells, we hypothesized that therapeutically reversing this phenotype might help control cancer progression. To this end, we initially tested

diverse chemotherapeutic drug combinations for their ability to induce immunogenic phenotypes in various KP tumor cell lines (KP L1-3, L1-5 and L2-9) *in vitro*. These proof of principle studies used high mobility group box 1 (HMGB1) release as a surrogate marker for drug-induced tumor cell immunogenicity[142] and evaluated Food and Drug Administration (FDA)-Approved chemotherapeutics to favor clinical translatability. We found that the NSCLC chemotherapeutics docetaxel (Dtax) and Carbo, alone or in combination, failed to induce HMGB1 release by all KP tumor cell lines tested (Figure 3.2A). Likewise, the anthracycline mitoxantrone (Mtx), which can have immunogenic effects[40], did not trigger HMGB1 release by KP tumor cells, even when combined with mafosfamide (Maf) (Figure 3.2B), which is the active metabolite of cyclophosphamide (Cyc)[151]. However, the oxaliplatin-mafosfamide (Oxa-Maf) combination stimulated HMGB1 release by all KP tumor cell lines (Figures 3.2A and 3.2B). This combination also triggered calreticulin (CRT) exposure by living KP tumor cells (Figure 3.2C), which is an additional marker of cell immunogenicity[142]. Building on these observations, we tested the combined Oxa-Cyc treatment in tumor-bearing KP mice using well tolerated drug concentrations (Figures S3.2A and S3.2B). Unlike Ptax-Carbo, Oxa-Cyc treatment significantly increased nuclear HMGB1 staining within KP tumor nodules (Figures 3.2D and S3.2C), a result that mirrors our *in vitro* findings. Consequently, these data demonstrate that selected chemotherapeutics can cause tumor cell immunogenic signatures in KP lung adenocarcinoma cells *in vitro* and *in vivo*.

3.3.3 Chemotherapeutics selected for their ability to induce immunogenicity in tumors delay KP cancer progression

KP mice sacrificed after 3 weeks of Oxa-Cyc treatment showed significantly lower tumor burden compared to Ptax-Carbo-treated or untreated mice (Figures 3.3A and S3.3A-C). We confirmed the ability of Oxa-Cyc treatment to control cancer growth in mice bearing KP1.9 tumors (Figures S3.3D-F). As the above experiments used terminal procedures to assess tumors at different time points and in different mice, we also used *in vivo* micro-computed

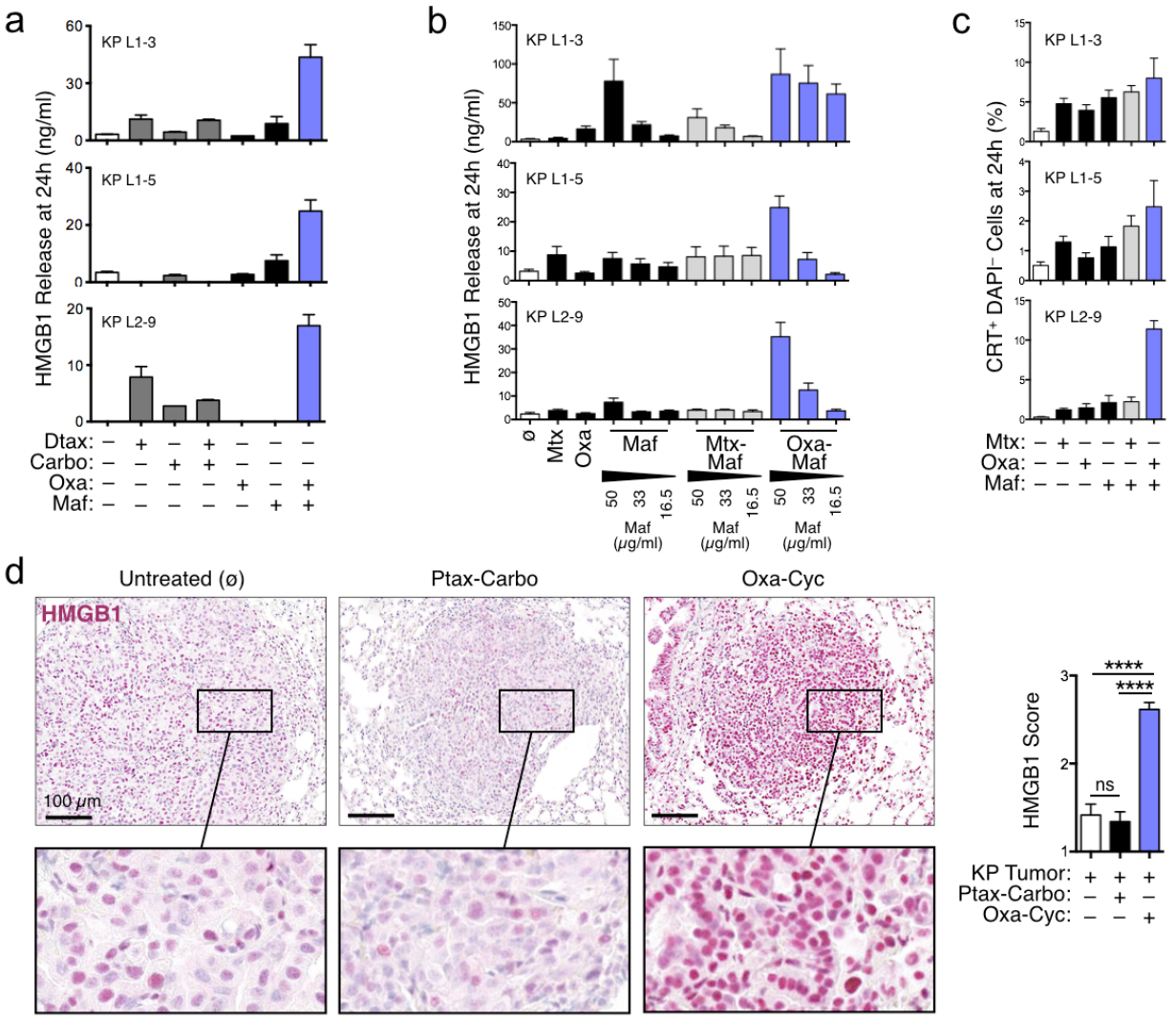

Figure 3.2 Selected drugs induce KP tumor cell immune phenotypes.

- **(a)** *In vitro* HMGB1 release by three KP tumor cell lines, generated from lung tissue of tumor-bearing KP mice, in response to various chemotherapeutic drug combinations as determined by ELISA (n=2-4 replicates).
- **(b)** HMGB1 release by tumor cell lines treated with Mitoxantrone (4 μM), Oxaliplatin (300 μM) and/or Mafosfamide at different concentrations (16.5, 33 or 50 μg/ml) (n=4 replicates).
- **(c)** Calreticulin exposure by tumor cell lines treated with defined drug combinations measured by flow cytometry (n=6 replicates).
- **(d)** HMGB1 immunohistochemistry (left) and scoring (right) in lung tumor nodules (n=39-48) of KP mice untreated (ø) or treated with Ptax-Carbo or Oxa-Cyc (See also Figure S3.2C for comparable images). Scale bars: 100 μm. ****P<0.0001; ns, not significant; CRT, Calreticulin; Carbo, Carboplatin; Cyc, Cyclophosphamide; Dtax, Docetaxel; Maf, Mafosfamide; Mtx, Mitoxantrone; Oxa, Oxaliplatin; Ptax, Paclitaxel. See also Figure S3.2.

tomography to monitor lung tumor volumes over time noninvasively to gain quantitative information on lung tumor progression in individual KP mice. This approach confirmed overall control of KP tumor growth during Oxa-Cyc treatment duration (Figure 3.3B). By contrast, Ptax-

Carbo treatment only showed a limited ability to suppress cancer progression. In Oxa-Cyc-treated mice we found that some tumor nodules progressed whereas others regressed (Figure 3.3B) and that tumor cell apoptosis, defined by cleaved caspase 3 staining, increased in some but not all tumor nodules (Figure S3.3G). These data demonstrate the possibility of significantly altering KP tumor growth with rationally selected and clinically approved chemotherapeutics.

3.3.4 Drug-induced tumor control involves a systemic host response

Having identified Oxa-Cyc as a model of successful treatment against KP tumors, we explored how it controlled cancer progression at a mechanistic level *in vivo*. First, we asked whether restricting Oxa-Cyc exposure to KP tumor cells is sufficient to alter cancer progression. To address this question, C57BL/6 mice received multiple injections of KP1.9 cells previously killed *in vitro* with either Oxa-Maf or Ptax-Carbo (days -8, -4, -2, 5, 12); the mice were also challenged with viable KP1.9 cells on day 0. We found that the tumors grew more slowly in mice vaccinated with cells killed with Oxa-Maf compared to mice vaccinated with tumor cells killed with Ptax-Carbo (Figure 3.4A). This difference highlights that tumor control is not just a consequence of immunization with dead cells. Of interest, the vaccinations had identical effects on tumors injected either ipsi- or contralaterally, thereby further indicating systemic rather than local vaccination-induced effects. Importantly, prophylactic vaccination (i.e. Oxa-Maf-killed tumor cells injected on days -8, -4, -2 only) was sufficient to reduce both ipsi- and contralateral tumor growth (Figure 3.4B). Consequently, these results indicate that Oxa-Maf-sensitized tumor cells induced systemic changes that subsequently reduce cancer progression.

3.3.5 Drug-induced tumor control involves adaptive immunity

Our next step evaluated whether Oxa-Cyc sensitization *in vivo* promoted an antitumor immune response. By collecting single cell suspensions from KP mouse lungs we found increased $CD8^+$ T cell:Treg cell ratios in Oxa-Cyc-treated mice as compared to untreated or

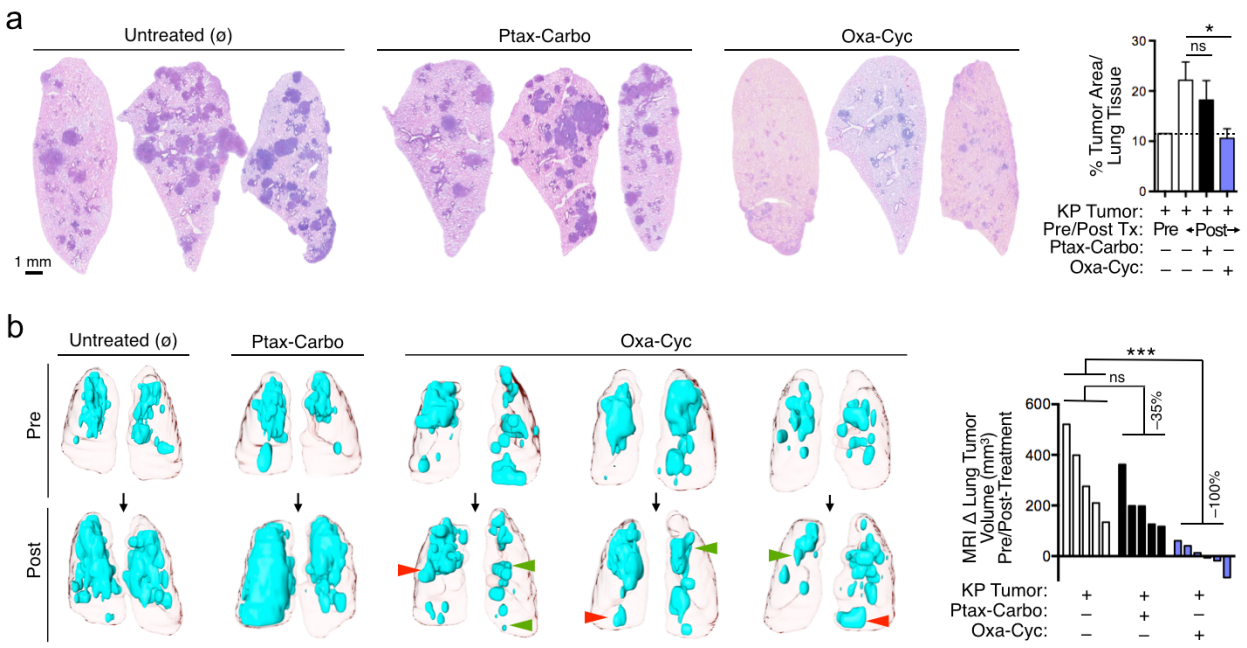

Figure 3.3 Drugs selected for their immunogenicity delay KP cancer progression.

(a) Lung tumor burden identification (left) and quantification (right) by hematoxylin and eosin (H&E) staining. Mice were treated with Ptax-Carbo or Oxa-Cyc after establishment of lung adenocarcinomas for a duration of 3 weeks.

(b) Lung tumor detection by noninvasive magnetic resonance imaging both pre- and post-treatment as in **(a)** (left) and quantification of tumor progression, defined as delta tumor volume in mm^3, in individual mice over time (right, n=5-6 mice per group). Red and green arrowheads show progressing and regressing tumor areas, respectively. **P*<0.05; ****P*<0.001; ns, not significant; Tx, treatment; Carbo, Carboplatin; Cyc, Cyclophosphamide; Oxa, Oxaliplatin; Ptax, Paclitaxel. See also Figure S3.3.

Ptax-Carbo-treated mice (Figure 3.4C). The increased $CD8^+$ T cell:Treg cell ratio favors $CD8^+$ T cell-mediated cancer immune surveillance and is associated with beneficial outcome[152,153]. In further assessing the distribution of T cells in KP mouse lungs by immunohistochemistry, we found that Oxa-Cyc treatment instigated $CD3^+$ T cell infiltration within tumor nodules (Figures 3.4D and S3.4A), with some $CD3^+$ cells proliferating locally as revealed by Ki67 staining (Figure S3.4B). The tumor-infiltrating $CD3^+$ T cells, which were absent in untreated or Ptax-Carbo-treated mice, were mostly $CD8^+$ and rarely $CD4^+$ (Figures 3.4E and S3.4C), thereby indicating Oxa-Cyc's ability to instigate $CD8^+$ T cell infiltration into, and proliferation within, KP tumors.

Since Cyc can suppress Tregs[154,155], Oxa-Cyc might promote antitumor responses by acting on Tregs directly. However, our data suggest that the $CD8^+$ T cell response induced by

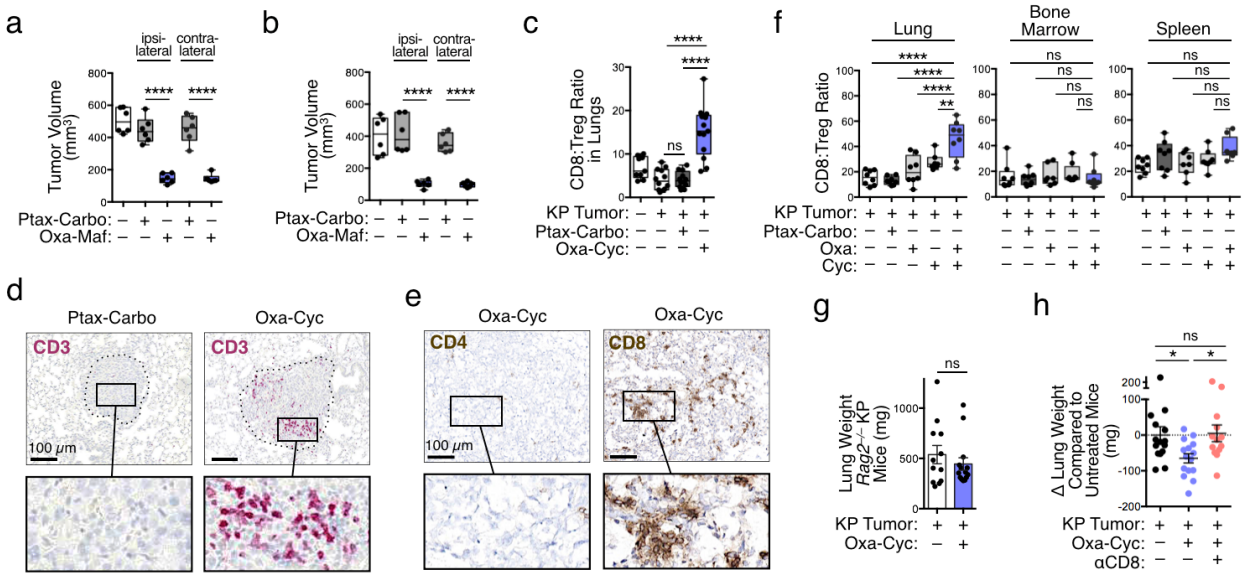

Figure 3.4 Drug-induced tumor control involves adaptive immunity.

(a and **b)** Impact of vaccinations with Ptax-Carbo- or Oxa-Maf-killed tumor cells on growth of KP1.9 tumors injected on day 0 ipsi- or contralaterally to the vaccination sites. Mice were injected with *in vitro* killed tumor cells on day -8, -4, -2, 5 and 12 (a) or only received prophylactic vaccination on day -8, -4 and -2 (b). The tumor burden was analyzed on day 19 (a) or day 14 (b), respectively (n=6 mice per group).

(c) $CD8^+$ T cell:Treg cell ratio in lungs of KP mice assessed by flow cytometry at 3 week post-treatment with Ptax-Carbo or Oxa-Cyc (n=9-13 mice per group).

(d) CD3 immunohistochemistry of representative lung tumor sections from KP mice treated as in (c) (see also Figure S3.4A for comparable images). Scale bars: 100 μm.

(e) CD4 and CD8 immunohistochemistry of lung tumor tissue from Oxa-Cyc-treated KP mice (see also Figure S3.4C for comparable images). Scale bars: 100 μm.

(f) $CD8^+$ T cell:Treg cell ratios assessed by flow cytometry in lung, bone marrow and spleen of KP1.9 lung tumor-bearing mice left untreated or that received Ptax-Carbo, Oxa, Cyc or Oxa-Cyc (n=7-8 mice per group).

(g) Lung weight of *Rag2*$^{-/-}$ KP mice treated or not with Oxa-Cyc as indicated in Figure S4D (n=12-14 mice per group).

(h) Lung weight of Oxa-Cyc-treated KP mice that received CD8 depleting mAbs (αCD8, n=13-15 mice per group). **P*<0.05; ***P*<0.01; *****P*<0.0001; ns, not significant. See also Figure S3.4.

Oxa-Cyc against KP tumors preferentially follows the induction of drug-mediated tumor cell immunogenicity because Oxa-Cyc treatment increased $CD8^+$ T cell:Treg cell ratios selectively in lung tumor tissue (i.e. not systemically, Figure 3.4F) and Tregs (as fractions of $CD3^+$ cells) were already absent from tumor nodules of untreated mice (Figure S3.4A). Also, lung $CD8^+$ T cell:Treg cell ratios increased more in mice that received both Oxa and Cyc (Figure 3.4F), a result that was in accordance with our *in vitro* observations that inducing tumor cell immunogenic phenotypes required the drug combination (Figures 3.2A-C).

To test whether therapeutically controlling KP tumor progression needs adaptive immunity, we generated *Rag2*$^{-/-}$ KP mice in the C57BL/6 background (Figures S3.4D-F). The inability of Oxa-Cyc to suppress tumor progression in these mice (Figures 3.4G and S3.4G) favors the hypothesis that KP tumor control requires CD8$^+$ T cells. Because *Rag2*$^{-/-}$ KP mice lack both T and B cells (Figures S3.4E and S3.4F), we also investigated the influence of selective CD8$^+$ T cell ablation in immunocompetent (*Rag2*$^{+/+}$) KP mice using CD8 depleting mAbs (Figure S3.4H). Oxa-Cyc failed to suppress tumor progression in CD8$^+$ T cell-depleted mice (Figure 3.4H), which indicated that Oxa-Cyc not only instigated tumor infiltration by CD8$^+$ T cells but also needed these cells to control cancer growth. Tumor control in KP mice was very efficient, especially considering that this mouse model resists all conventional treatments and develops tumors that are generally viewed as non-immunogenic.

3.3.6 Drug-induced tumor control involves innate immunity

To delve deeper into drug action mechanisms we next examined whether Oxa-Cyc-induced antitumor immunity required variables other than tumor-cell targeting and CD8$^+$ T cells. We investigated innate immune cells because they are found in the KP tumor stroma[51] and may be modulated by drugs to induce tumor control[5,156]. To uncover possible drug-induced changes on innate immune cell subsets, we collected lung tissue biopsies of KP tumor-bearing mice treated or not with Oxa-Cyc for comparative *ex vivo* analysis by multi-parameter flow cytometry. Furthermore, we isolated both tumor stroma biopsies and tumor-free adjacent lung tissue to assess whether drug-induced changes selectively control the immediate tumor microenvironment. By operationally dividing CD45$^+$ Lin$^-$ myeloid cells into CD11b$^-$ and CD11b$^+$ cell subsets, we observed a substantial decrease in the frequency of CD11b$^-$ cells in both the tumor stroma and adjacent tissue following Oxa-Cyc therapy (Figure 3.5A). This decrease was also observed in Ptax-Carbo-treated mice (data not shown), suggesting that this cell loss is insufficient to explain tumor control selectively in Oxa-Cyc-treated mice. In marked contrast,

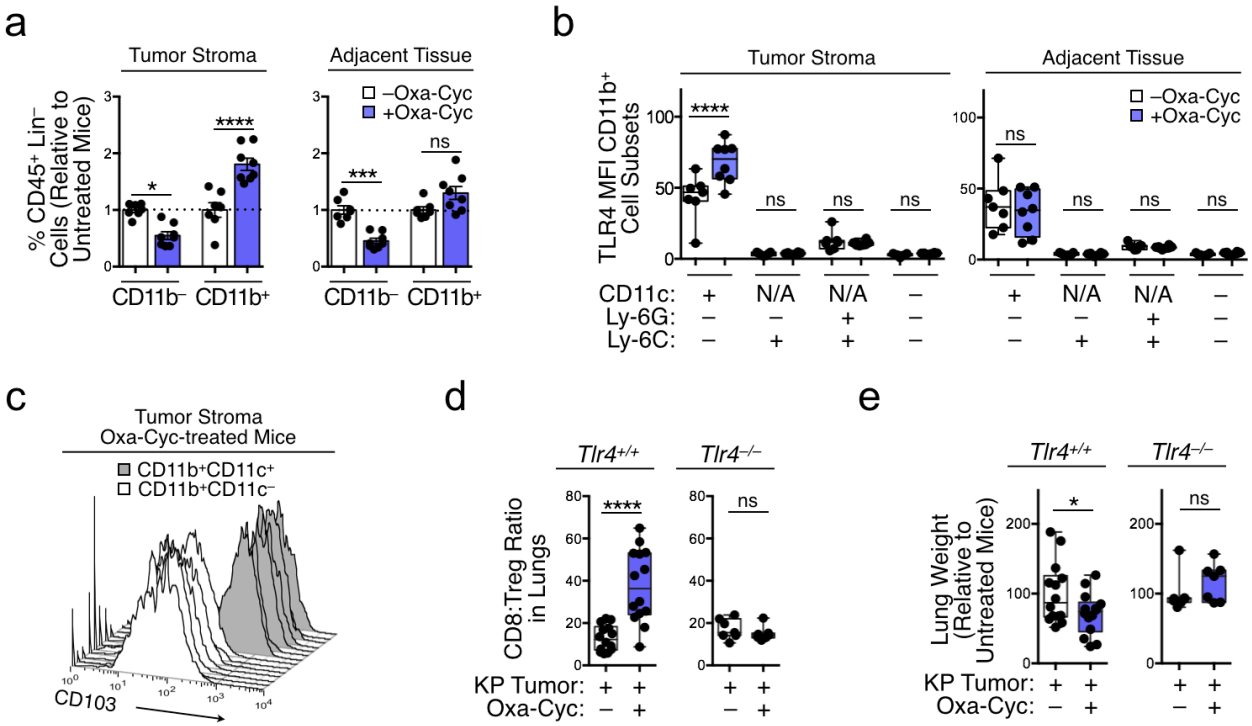

Figure 3.5 Drug-induced tumor control involves innate immunity and TLR4 signaling.

(a) $CD8^+$ T cell:$CD11b^-$ and $CD11b^+$ cells in lung tissue biopsies of KP mice that received Oxa-Cyc or were left untreated (n=7-8 mice per group). Lung tissue biopsies of tumor and tumor-free adjacent tissues were investigated in parallel.
(b) TLR4 mean fluorescence intensity (MFI) of $CD11b^+$ cell subsets in tumor and tumor-free lung tissues of Oxa-Cyc treated or untreated KP mice (n=7-8 mice per group).
(c) CD103 phenotype of $CD11b^+CD11c^-$ and $CD11b^+CD11c^+$ cells in tumor stroma of Oxa-Cyc-treated mice (n=7 mice per group).
(d and **e**) Lung $CD8^+$ T cell:Treg cell ratio (D) and lung weight (E) of KP1.9 tumor-bearing *Tlr4*$^{+/+}$ and *Tlr4*$^{-/-}$ mice treated or not with Oxa-Cyc (n=7-14 mice per group). Lineage (Lin) defined as (B220/CD49b/CD90.2/Ter119)$^+$. **P*<0.05; ****P*<0.001; *****P*<0.0001; ns, not significant; N/A, not applicable.

Oxa-Cyc treatment significantly and selectively increased the frequency of the $CD11b^+$ cell subset within the tumor stroma (Figure 3.5A). These findings indicate that the Oxa-Cyc treatment modulates innate immune system components within the tumor microenvironment.

We further analyzed $CD11b^+$ cells, and subsets thereof, and considered toll-like receptor 4 (TLR4) because it can be involved in innate immune activation and transition toward adaptive immunity in the context of drug-induced immunogenic cell death[40,157,157]. We found that Oxa-Cyc treatment upregulated TLR4 selectively in the dendritic cell (DC)/macrophage-like subset, defined as $CD11b^+$ $CD11c^+$ Ly-$6G^-$ Ly-$6C^-$. TLR4 upregulation occurred only within the tumor

stroma but not in tumor-free adjacent tissue (Figure 3.5B). By comparison, the mean fluorescent intensity (MFI) of cell surface TLR4 expression was low or undetectable in $CD11b^+$ $CD11c^-$ cells, $Ly\text{-}6G^+/Ly\text{-}6C^+$ granulocytes and $Ly\text{-}6C^+$ monocyte-like cells, both in absence or presence of Oxa-Cyc treatment (Figure 3.5B). We also found that $CD11b^+$ $CD11c^+$ cells, in contrast to their $CD11b^+$ $CD11c^-$ counterpart, uniformly unregulated the integrin CD103 (Figure 3.5C). $CD103^+$ DC-like cells are important in regulating antitumor immunity because they have enhanced abilities to activate $CD8^+$ T cells compared to $CD103^-$ DCs and tumor-associated macrophages[16,158,159].

To define whether $TLR4^+$ cells are required for generating drug-induced KP tumor control, we examined the impact of Oxa-Cyc treatment on tumor-associated T cell responses in *Tlr4*$^{-/-}$ mice. In contrast to their wild-type counterparts, *Tlr4*$^{-/-}$ mice failed to increase lung $CD8^+$ T cell:Treg cell ratios following Oxa-Cyc treatment (Figure 3.5D). Furthermore, we found that TLR4 deficiency reduced Oxa-Cyc-mediated control of KP tumor progression (Figure 3.5E). These data provide evidence that triggering successful antitumor T cell immunity against KP tumors with Oxa-Cyc depends on TLR4, in line with previous findings that this receptor can promote DC-mediated $CD8^+$ T cell activation[157].

3.3.7 Immunogenic chemotherapeutics sensitize lung adenocarcinomas to immune checkpoint therapy

With the ability to convert non-T cell infiltrated KP tumors into ones that display antitumor T cell immunity, we asked whether this process can be harnessed for sensitizing KP tumors to checkpoint blockade therapy. We used the KP-OVA mouse model because it is refractory to the anti-PD-1 and anti-CTLA-4 mAb combination therapy (Figure 3.1D) and allowed us to track $CD8^+$ T cells specific for the model antigen $OVA_{257\text{-}264}$. We found that Oxa-Cyc treatment in these mice favored or maintained four phenotypes that are potentially associated with response to PD-1 checkpoint inhibition, namely: *i)* increased $CD8^+$ T cell:Treg cell ratio in the lung tumor

tissue (Figure 3.6A); *ii)* presence of tumor-infiltrating $CD8^+$ T cells including those specific for OVA (Figure 3.6B); *iii)* PD-1 expression by these cells (Figure 3.6C) and *iv)* PD-L1 expression by tumor-associated host and/or tumor cells (Figure 3.6D).

We conducted a blinded preclinical study in which KP-OVA mice received Oxa-Cyc, anti-PD-1 + anti-CTLA-4 mAbs or both, with controls left untreated (Figure S3.5A). Treatments began on day 130 after tumor initiation and tumors were monitored noninvasively by high resolution micro-computed tomography in all mice at three time points (day 122, day 146, and day 193) to quantify changes in tumor burden *in vivo*. All mice were evaluated *ex vivo* at day 234.

Noninvasive tumor assessment at days 122, 146 and 193 (T_0, T_1 and T_2) revealed that Oxa-Cyc controlled KP tumors during the first 3 weeks of treatment ($T_0 \rightarrow T_1$) when compared to untreated mice ($p<0.05$) but was unable to control tumors at later time points ($T_0 \rightarrow T_2$, $p>0.05$) (Figure 3.6E). Checkpoint inhibition failed to delay KP tumor progression ($T_0 \rightarrow T_1$, $p>0.05$; $T_0 \rightarrow T_2$, $p>0.05$). By contrast, Oxa-Cyc combined with anti-PD-1 + anti-CTLA-4 mAb treatment controlled tumor progression at both time points ($T_0 \rightarrow T_1$, $p<0.01$; $T_0 \rightarrow T_2$, $p<0.05$) (Figures 3.6E and 3.6F).

Post mortem evaluation at day 234 (T_3) validated the advantage of the combination treatment to suppress KP tumors durably (i.e. over 16 weeks; $p<0.001$; Figures 3.6E and 3.6G). The combination treatment was significantly better than either Oxa-Cyc or anti-PD-1 + anti-CTLA-4 alone (Figures 3.6E and 3.6G).

Multiphoton microscopy of explanted lung tissue confirmed successful tumor control in the same mice. This approach further revealed the $CD8^+$ T cells' selective ability to accumulate and remain within tumor nodules of Oxa-Cyc-treated KP-OVA mice, whether or not they received the immune checkpoint blockers (Figure 3.6H, S3.6B and S3.6C). These data support the idea that tumor infiltration by $CD8^+$ T cells is insufficient to durably control cancer progression but can generate effective responses to checkpoint blockade treatment.

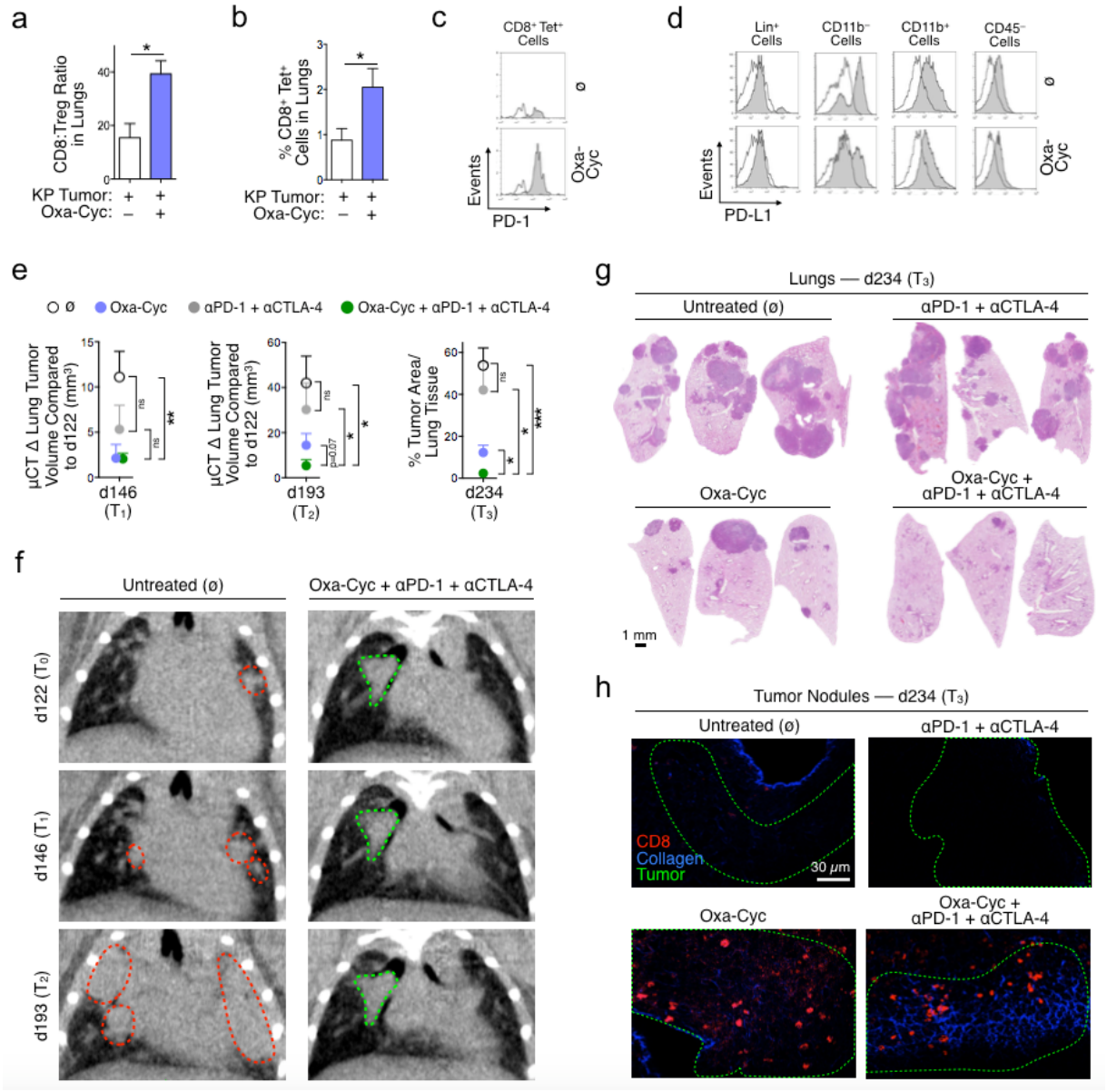

Figure 3.6 Drug-induced tumor infiltration by CD8⁺ T cells sensitizes lung adenocarcinomas to immune checkpoint therapy.

(a) Lung CD8⁺ T cell:Treg cell ratio, **(b)** percent of OVA-specific CD8⁺ T cells in lungs, **(c)** PD-1 expression by these cells and **(d)** PD-L1 surface expression by different tumor stroma cell populations (white histograms are fluorescence minus one (FMO) controls) in KP-OVA mice treated or not with Oxa-Cyc (n=2-5 mice per group).

(e) Figure S3.5A indicates the experimental scheme of micro-computed tomography imaging time points (d122, d146, d193) and *ex vivo* analysis (d234) of KP-OVA mice treated with Oxa-Cyc and anti-PD-1 + anti-CTLA-4 mAbs either alone or in combination (n=5 mice per group). Tumors were induced with a lentiviral vector containing OVA peptide sequences (LucOS). Change in tumor volume (defined by micro-computed tomography at d146 = T_1 and d193 = T_2) and tumor area in lung tissues (defined by H&E staining at d234 = T_3) in these mice.

(f) Coronal micro-computed tomography at d122, d146 and d193 of an untreated mouse (left) or mouse that received the combination therapy (right). Dotted lines identify tumor nodules that progress (red) or not (green).

Figure 3.6 (Continued)

(g) Lung tumor burden identification by H&E staining at d234 in the same mice.
(h) $CD8^+$ cell (red) infiltration in KP-OVA tumors (tumor contour defined with green dashed-lines, see also Figure S3.5B for comparable images) identified by multiphoton microscopy *ex vivo* at d234 in the same mice. Collagen is shown in blue. **P*<0.05; ***P*<0.01; ****P*<0.001; ns, not significant. See also Figure S3.5.

Additionally, when using the KP1.9 tumor-bearing mouse model, we found that Oxa-Cyc treatment significantly increased overall mouse survival when combined with anti-PD-1 + anti-CTLA-4 mAbs, whereas anti-PD-1 or anti-CTLA-4 alone did not confer protection (Figure S3.5D). Comparisons of various combination treatments suggested that anti-PD-1 mAb treatment was mostly responsible for improving Oxa-Cyc treatment efficacy in the KP1.9 tumor-bearing mice at least 20 days after initiation of treatment (Figure S3.5E). These data suggest that a drug combination of Oxa-Cyc combined with anti-PD-1 mAb might be optimal for treatment success.

3.3.8 Immunogenic chemotherapeutics can sensitize other tumors to immune checkpoint therapy

Finally, we tested whether other immunogenic chemotherapeutics can sensitize tumors to immune checkpoint therapy. We explored MCA205 fibrosarcoma-bearing mice because they failed to respond to anti-PD-1 + anti-CTLA-4 mAbs (Figure 3.7A). We found that cisplatin treatment, which does not induce immunogenic cell death, failed to improve immune checkpoint blockade treatment (Figure 3.7A). By contrast, doxorubicin, which induces MCA205 immunogenic cell death[142], significantly delayed tumor progression when combined with anti-PD-1 + anti-CTLA-4 mAb therapy (Figure 3.7A).

We also investigated CT26 colon carcinoma-bearing mice, which do not respond to anti-CTLA-4 mAb therapy (Figure 3.7B). Oxa treatment induces immunogenic CT26 tumor cell death[157,160] and increases $CD8^+$ T cell infiltration at the tumor site[161]. We found that Oxa treatment provided minimal control of CT26 tumor progression, similarly to cisplatin, which was used as a control agent (Figure 3.7B). Checkpoint blockade therapy with anti-CTLA-4 mAb,

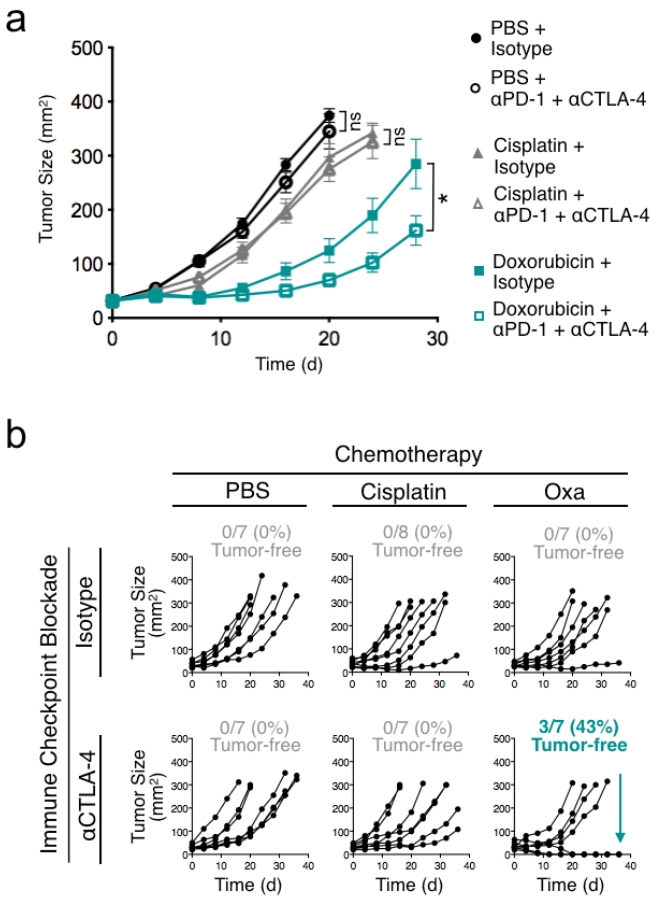

Figure 3.7 Immunogenic chemotherapeutics improve immune checkpoint blockade treatment against MCA205 fibrosarcoma and CT26 colon carcinoma.

(a) Tumor size measurement of MCA205 fibrosarcoma-bearing C57BL/6 mice (n=7-8 per group) treated with PBS or chemotherapy intratumoral (Cisplatin or Doxorubicin) together with anti-PD-1 + anti-CTLA-4 (αPD-1 + αCTLA-4) mAbs or isotype control mAbs that were injected on day 8, 12 and 16 following chemotherapy. Tumor cells were injected on day -8 before chemotherapeutic drug treatment.

(b) Tumor size measurement of CT26 colon carcinoma-bearing BALB/c mice (n=7-8 per group) treated with PBS or chemotherapy intratumoral (Cisplatin or Oxaliplatin (Oxa)) together with anti-CTLA-4 or isotype control mAbs that were injected on day 8, 12 and 16 post chemotherapeutic drugs. Tumor cells were injected on day -11 before chemotherapy Each line represents an individual mouse. *P<0.05; ns, not significant.

either as monotherapy or combined with cisplatin, was also largely ineffective. However, the Oxa + anti-CTLA-4 combination was able to reject CT26 tumors in ~40% of mice analyzed (Figure 3.7B). These results demonstrate that our findings in the KP mouse model can be extended to other tumor types; they also indicate that tailoring chemotherapy treatments to a given tumor type may be a generalizable approach to sensitize tumors to immune checkpoint therapy.

3.4 Discussion and Future Directions

We used genetically-engineered mouse models that closely recapitulate human disease to examine whether autochthonous tumors lacking pre-infiltrated T cells can also be sensitized therapeutically to induce T cell-mediated control of tumor progression. We investigated lung adenocarcinomas carrying common *KRAS* and/or *TP53* mutations because we found these tumors to be inadequately infiltrated by $CD8^+$ T cells in both humans and mice. In addition, we found that *Kras*/*Trp53* mutant tumors in mice resist current chemo- and immunotherapies even when tumors expressed neoantigens, which are targets of successful checkpoint blockade therapy. We report that appropriately selected and clinically approved therapeutics can produce $CD8^+$ T cell infiltration in otherwise non-T cell inflamed tumors and that this process inhibits cancer progression. Furthermore, the T cell response induced by immunogenic chemotherapeutics can be harnessed to sensitize lung adenocarcinomas to immune checkpoint therapy. The antitumor response triggered by the immunogenic chemotherapeutics depended on: 1) direct drug actions on tumor cells; 2) host $CD8^+$ T cell activation; and 3) intact TLR4 signaling.

First, Oxa-Cyc-induced effects on tumor cells alone can trigger a systemic antitumor response. Indeed, injecting tumor-bearing mice with KP1.9 tumor cells previously killed by Oxa-Maf (but not by Ptax-Carbo) efficiently inhibited tumor progression. Combined with our *in vitro* results, which showed Oxa-Cyc's ability to directly induce KP tumor cells with immunogenic phenotypes, our findings indicate that Oxa-Cyc-mediated effects on tumor cells instigated a cascade of events that ultimately led to tumor control. Whether some immunotherapeutics may overcome the limitations of poorly immunogenic chemotherapeutics requires further study. Nonetheless, considering the importance of initial tumor cell drug targeting, it may be possible to further improve clinical outcomes by increasing chemotherapeutic load at the tumor site. This may be achieved by encapsulating drugs within nanoparticles[162] or targeting the vasculature[163].

Second, the Oxa-Cyc-induced antitumor response depends on host $CD8^+$ T cells: the drugs failed to control tumor progression in mice lacking these cells (*Rag2*$^{-/-}$ KP mice as well as wild-type KP mice depleted with anti-CD8 mAbs). Another study using a genetic mammary cancer model showed that chemotherapeutics can have comparable effects against genetically engineered tumors growing in either *Rag*-competent or *Rag*-deficient mice[164]. These findings suggest that chemotherapy can limit tumor progression without $CD8^+$ T cells. Yet, the chemotherapeutics used in the mammary tumor models only delayed tumor growth, whereas accumulating evidence shows that potent tumor infiltration by $CD8^+$ T cells may be key to durably controlling cancer[6,138,159]. Our study indicates that drug-induced $CD8^+$ T cell tumor infiltration can contribute to tumor control in genetic mouse models and be harnessed for checkpoint blockade therapy. These findings accord with the observation in a mouse model of castrate-resistant prostate cancer that Oxa can induce $CD8^+$ T cell-dependent tumor eradication[144].

Third, the drug-induced antitumor T cell response needs intact TLR4 signaling. We observed that TLR4 deficiency prevented Oxa-Cyc from increasing $CD8^+$ T cell:Treg cell ratios within the tumor bed and controlling tumor progression. Accordingly, we found that Oxa-Cyc makes dying tumor cells release HMGB1, which activates TLR4 directly[157]. Also, systemic Oxa-Cyc treatment caused an influx of $TLR4^+$ DC-like cells specifically in the tumor stroma. These tumor-infiltrating cells expressed CD103 and thus resembled DCs previously identified as critical stimulators of antitumor $CD8^+$ T cell immunity[16,158,159]. Our results are in accordance with previous findings that TLR4 can promote DC tumor antigen cross-presentation and $CD8^+$ T cell activation following immunogenic tumor cell death[157] and that tumor-infiltrating DCs can be key regulators of antitumor immunity[16]. Although the detailed mechanisms shaping successful immune responses against KP tumors require further investigation, the aforementioned findings already provide evidence that shaping these immune responses will require a combination of variables including tumor cell targeting and both the adaptive and innate arms of the immune system. We hypothesize that Oxa-Cyc-induced enrichment of $TLR4^+$ antigen-presenting cells in

KP tumors precedes and facilitates the local influx of $CD8^+$ T cells. Since TLR4 genotype[207] and tumor-associated myeloid cell content[5] can vary across individuals and/or tissues, evaluating these innate immune variables may help select treatment options.

Checkpoint blockade therapies have yielded unprecedented clinical benefits against lung and other cancers but on their own may preferentially benefit patients whose tumors are pre-infiltrated by $CD8^+$ T cells[6,138]. We found that therapy-induced T cell infiltration enabled successful treatment with immune checkpoint inhibition, further indicating that appropriately selected drugs that transform ‘cold' tumor tissues into immunologically ‘hot' T cell-rich environments can be used to sensitize tumors to immune checkpoint therapy and improve clinical outcome.

Our results provide a proof-of-principle that chemotherapeutics selected for their ability to induce immunogenicity in tumors (e.g. Oxa-Cyc against KP tumors, Doxorubicin against MCA205, and Oxa against CT26) provide additive or synergistic benefits when combined with immune checkpoint blockers. It will be important to explore whether and when other drugs or drug combinations can achieve similar results. For example, it is possible that Oxa alone or Ptax-Carbo also sensitize KP tumors to immune checkpoint blockade or synergize with immunotherapy against other cancers. Also, preclinical studies using an ovarian cancer graft model indicate that PD-1 blockade can improve Ptax therapy[165] and ongoing clinical trials are testing the potential of Ptax-Carbo to enhance the efficacy of immune checkpoint blocking agents against various cancer types, including NSCLC (Liu et al. J Clin Oncol. 2015;33 (suppl; abstr 8030); Papadimitrakopoulou et al. J Clin Oncol. 2015;33 (suppl; abstr 8031)).

To achieve tumor sensitization and improved outcomes, we envision two scenarios: 1) re-evaluating the chemotherapeutics used in combination with checkpoint blockade agents to specifically include drugs with the potential to induce immunogenic cell death (e.g., Oxa and Cyc as investigated for the KP lung tumor model), and 2) using precision medicine to select drugs with the ability to promote tumor cells’ immunogenicity in a given patient. The first approach could provide immediate clinical benefit by expanding the proportion of cancer

patients who respond to current immune checkpoint treatments. The second approach involves screening drugs for individual patients and is thus more technically challenging, but because it takes into account that different tumor genetic drivers, tissues of origin and tumor microenvironments can profoundly modify a given drug's efficacy, the drug selection approach may benefit even more patients. The drug-induced readouts could be expanded to study various forms of cell death, including pyroptosis or necroptosis, which could also promote antitumor immunity. Regardless of the approach, drugs that are already FDA-approved could be used to accelerate clinical translation.

3.5 Acknowledgements

The authors thank the members of the Hope Babette Tang Histology Facility at the Koch Institute Swanson Biotechnology Center for technical support. This work was supported in part by the Samana Cay MGH Research Scholar Fund (to M.J.P.), NIH grants P50-CA86355 and R01-AI084880 (to M.J.P.), U54-CA126515 (to R.W.), 5U54CA163125 (to G.J.F.) and 5U54-CA163109 and the Howard Hughes Medical Institute (to R.O.H.). C.P. was supported by the Deutsche Forschungsgemeinschaft (DFG) PF809/1-1, C.E. by the Boehringer Ingelheim Fonds and S.R. by the DFG RI2408/1-1.

3.6 Experimental procedures

Mice

Kras$^{LSL\text{-}G12D/+}$;*Trp53*$^{flox/flox}$ (KP) mice were used as a conditional mouse model of NSCLC[24]. Details about all murine strains and tumor models are provided in the Supplemental Experimental Procedures. All animal experiments were approved by the Massachusetts General Hospital Subcommittee on Research Animal Care, except experiments in BALB/c and MCA205-bearing C57BL/6 mice that were approved by the Ethical Committee of the Gustave Roussy Cancer Campus (Villejuif, France).

Cell Lines

The lung adenocarcinoma cell line KP1.9 was derived from lung tumors of C57BL/6 KP mice and was kindly provided by Dr. A. Zippelius, University Hospital Basel, Switzerland. The lung adenocarcinoma cell lines KP L1-3, KP L1-5 and KP L2-9 were derived from 129 KP mouse lung tumors and all established in our laboratory. Additional information on further cell lines and cell culture conditions are detailed in Appendix 3.2.

Human Tumor Samples

Sections from paraffin-embedded biopsies of lung resections (n=76) from NSCLC patients with known *KRAS* and *EGFR* gene mutation status were obtained from the Department of Pathology at Massachusetts General Hospital. TP53 and CD8 immunohistochemistry were performed and evaluated blindly based on defined scoring systems as described in Appendix 3.2.

Micro-Computed Tomography (μCT) and Magnet Resonance Imaging (MRI)

Tumor burden was evaluated by μCT or MRI in anonymized mice. Details of the imaging protocols are provided in Appendix 3.2.

Mouse Histology, Immunohistochemistry (IHC) and Immunofluorescence Microscopy

Histological analysis of tumor burden in mice was done on formaldehyde-fixed and paraffin-embedded lung tissues using hematoxylin and eosin (H&E) staining. IHC was done on either paraffin-embedded (HMGB1, cleaved caspase-3, Ki67, CD3, CD4) or frozen (CD8) tissue sections. Detailed information regarding antibody clones and staining procedures are in Appendix 3.2.

Multiphoton Microscopy

Small lung pieces from tumor-bearing KP mice and tumor-free tissue were fixed, stained and imaged using an Ultima multiphoton microscope (Prairie Technologies). Images were pre-processed in R statistical computing environment using RStudio and stitched/analyzed with Fiji software. More information on staining procedures and image processing are described in Appendix 3.2.

HMGB1 and Calreticulin In Vitro Assays

The KP L1-3, KP L1-5 and KP L2-9 tumor lines were seeded in tissue culture plates before treatment with chemotherapeutic drugs for 24 h (Dtax, 30 μM; Carbo, 500 μM; Oxa, 300 μM; Maf, 16.5, 33, 50 μg/ml; Mtx, 4 μM). For the calreticulin assay, the cells were harvested from cell culture plates, fixed and incubated with rabbit anti-calreticulin Ab followed by anti-rabbit AlexaFluor 488 conjugated Ab and investigated by flow cytometry (CyAn ADP analyzer, Beckman Coulter). Detailed assay conditions are provided in Appendix 3.2.

In Vivo Drug Treatments

KP tumor-bearing mice were either left untreated or received chemotherapy intraperitoneally (i.p.) once a week for three weeks (Oxa, 2.5 mg/kg; Cyc, 50 mg/kg; Ptax, 10 mg/kg; Carbo, 10 mg/kg). BALB/c mice bearing CT26 flank tumors and MCA205 flank tumor-

bearing C57BL/6 mice received one intratumoral chemotherapeutic drug injection (Oxa, 1.25 mg/kg; Cisplatin, 0.25 mg/kg; Doxorubicin, 2.9 mg/kg). mAbs specific for PD-1 (clone 29F.1A12, provided by Dr. G. J. Freeman) and CTLA-4 (clone 9D9, BioXcell) were injected i.p.. Details about *in vivo* experiments including drug treatment conditions and cell depletion strategies are provided in Appendix 3.2.

Recovery of Cells from Murine Tissues and Flow Cytometry

Single cell suspensions were prepared from murine lung, spleen and bone marrow and investigated by flow cytometry (LSRII, BD Biosciences). Where indicated, equally sized pieces of tumor stroma and corresponding tumor-free adjacent tissue were isolated separately from lungs of Oxa-Cyc-treated or untreated tumor-bearing KP mice. Details about cell recovery strategies and flow cytometry staining procedures including Ab clones and identified cell populations are in Appendix 3.2.

Statistics

Results were expressed as mean±SEM. Statistical tests included one-way ANOVA followed by Tukey's or Dunnett's multiple comparison test. When applicable, unpaired one-tailed and two-tailed Student's t tests using Welch's correction for unequal variances were used. Comparison of survival curves was performed with the Log-rank Mantel-Cox test. *P* values of 0.05 or less were considered to denote significance (**P*<0.05; ***P*<0.01; ****P*<0.001; *****P*<0.0001; ns, not significant).

Chapter 4: Mapping tumor-infiltrating immune cell states by single cell RNA-seq

4.1 Overview

Single cell RNA-seq profiling reveals novel myeloid cell substates in lung tumors and healthy tissue that respond to myeloid-based immunotherapy

This work is a collaboration between Allon Klein's laboratory at Harvard Medical School and Mikael Pittet's laboratory at Massachusetts General Hospital. The manuscript, currently in preparation, will include four co-first authors (Virginia Savova, Rapolas Žilionis, **Camilla Engblom**, and Christina Pfirschke).

Summary

Myeloid cells frequently infiltrate human tumors and have been reported with diverse (sometimes seemingly opposite) effects on tumor growth. At present, we have a limited understanding of the complexity of cancer-associated myeloid cell subtypes and we cannot fully discriminate between tumor-promoting and tumor-suppressing cells. Here we used cutting-edge, unbiased single cell profiling to map the immune cell composition in healthy and tumor tissues to dissect out molecular phenotypes and gain fundamental new knowledge on tumor-infiltrating myeloid cell states and diversity. This is important to improve our understanding of myeloid activation states and functions in tumors, with the ultimate goal to discover new therapeutic targets. We further interrogated single cell molecular phenotypes of tumor-infiltrating immune cells following inhibition of the colony-stimulating factor-1/R pathway, which is key to myeloid differentiation and a promising clinical target. Taken together, our analysis revealed previously unappreciated tumor- and drug- associated immunoregulatory cell states. These findings should help clarify myeloid cell complexity in response to drug treatments, which could have important implications for on-going clinical trials with these agents.

Attributions

For this work, I, together with CP, designed and performed all mouse experiments, analyzed and interpreted data. VS and RZ performed single cell RNAseq and sequencing data analysis.

4.2 Introduction

Myeloid cells remain less studied than T lymphocytes but have emerged as potential cellular targets for cancer therapy. Not only are they a major component of tumor immune infiltrates in both patients and preclinical models, but the presence of certain myeloid cells can be correlated with clinical outcome in various human cancers[7,8,14]. However, our ability to distinguish cellular identity and functional properties of tumor-infiltrating myeloid cells remains limited. The main challenge is the vast diversity within the myeloid lineage, which is typically divided into the main myeloid cell types (i.e. macrophages, dendritic cells, neutrophils, monocytes, mast cells, eosinophils, basophils), and then further separated into subsets based on functional activation 'states' (e.g. M1/M2, etc.), cellular ontogeny (e.g. Zbtb46, Batf3, or other lineage restricted transcription factors), or molecular phenotypes (e.g. M1/M2, $CD103^+$ DCs, etc.). As a result of our increased understanding of this complexity, the question of how to define myeloid cells, even at steady state, remains a topic of hot discussion[13,17,166,167]. The current consensus is that to properly characterize myeloid cell function, we need to go beyond labeling cells based on a set of surface markers, and instead take into account a cell's ontogeny, plasticity, and local tissue microenvironment.

As referenced above, the diverse spectrum of myeloid cell types and activation states is also reflected in their various abilities to promote and/or inhibit cancer progression. The heterogeneity of myeloid cell responses in tumors has been extensively investigated in the cancer immunology field during the past several decades, with macrophages, neutrophils, monocytes, and dendritic cells having been the most intensely studied. In some contexts, certain myeloid cells exhibit functions that promote cancer growth and could be targeted in

therapy (e.g., production of factors such as cytokines that support tumor cell survival and proliferation[50,168], matrix degrading enzymes that favor tumor cell invasion and metastasis[115,169,170], pro-angiogenic factors that enable nutrient and oxygen delivery to tumors[168,171,172], immuno-regulatory cytokines and cell surface proteins that blunt antitumor immune activity[168,173,174]. In contrast, under different conditions, myeloid cells can also display critical antitumor functions which involve killing of tumor cells[111], activation of cytotoxic immune responses[16,34,175], or modulating the tumor microenvironment (vasculature, extracellular matrix, or lymph) in a way that limits tumor progression[143]. A critical goal, and challenge, for myeloid-based immunotherapy is therefore to fine-tune the balance between inhibiting protumoral functions, while preserving and boosting antitumoral functions.

Experimentally, myeloid cells are most commonly defined by antibody-based approaches, such as flow cytometry and histology. These tools have been pivotal in cataloguing immune cell activity in both patient and pre-clinical studies. However, they are inherently biased due to the need to pre-select markers for population analysis, whose cellular distribution may change in the context of disease. In particular, the use of broadly expressed markers, such as CD11c, CD11b, Ly6G/C, F4/80 and MHCII, to define myeloid cell subtypes in mice, often differ across tissues and are shared by several myeloid (and sometimes also lymphocyte) populations. This makes it challenging to define and compare the cellular ‘identity’ between cancer types and studies. A limited set of markers also rarely capture all of the myeloid cell subsets in a tissue and may further group cells together that have diverse and even opposite functions. There is therefore a critical need to use a more unbiased approach to resolve immune cell complexity within the tumor microenvironment.

Recent technological advances can be applied to, at least in part, address these issues. Developments in next-generation sequencing technologies, and single cell RNA-seq technologies especially, have dramatically improved our abilities to gather broad-scale data on transcriptional activity in an unbiased manner[176]. These types of analyses have permitted a deeper transcriptional analysis of various cells and tissues; instead of assessing a handful of

genes at a time, it is now possible to evaluate the expression of most, if not all, genes. Going further, single cell RNA-seq technology enables the unbiased clustering of cells based on their entire transcriptome, avoiding the bias of pre-selecting markers.

In this study, we used a cutting edge droplet microfluidics single cell RNA-seq technology, called *inDrops*[127,177], developed by the Klein laboratory, to interrogate tumor-infiltrating immune cell composition in mouse lung adenocarcinoma. *InDrops* has made particular strides compared to other microfluidics-based single cell approaches in the ability to capture and barcode large number of cells from diverse tissues in an efficient and cost-effective manner. The development of this technology has been driven by technical advances in droplet microfluidics, DNA barcode synthesis, sequencing approaches (driving down costs), and bioinformatics tools. Additionally, *inDrops* has very low technical variability or batch effects, outperforming many other single cell transcriptomics methods[127].

Using *inDrops*, we have started to comprehensively profile the transcriptome of tumor-infiltrating immune cells, specifically focusing on myeloid cell diversity, compared to healthy states in a more unbiased manner. Furthermore, we have begun to map immune cell populations in response to a myeloid cell targeting immunotherapy. We believe that these are critical areas of investigation that are needed to clarify outstanding issues regarding myeloid cell heterogeneity at the tumor site and their potential as therapeutic targets. This project is on-going and the results presented herein are a summary of our initial unpublished findings.

4.3 Results

4.3.1 Single cell RNA-seq profiling allows comprehensive mapping of tumor-associated cellular states

To transcriptionally map the immune cell states in matched healthy and lung tumor tissue, we first sorted $CD45^+$ hematopoietic cells from KP tumor-bearing and age- and sex-

matched control tumor free mice (2 mice per condition) (Figure 4.1A). We then barcoded and sequenced a total of ~17,000 cells. Generated sequence data was processed as previously described[127,177] and illustrated in Figure 4.1B. A total of 15,811 single cell transcriptomes remained after excluding cells based on viability (determined by mitochondrial load), doublet score (reflective of the transcriptome of two or more cells), and library complexity. We then generated an unbiased cell-type visualization of $CD45^+$ cells using SPRING analysis[178], which projects the distribution of cells in gene expression space into two-dimensions while preserving the topological relationships within high dimensional single cell data (Figure 4.1B). To define cellular lineage to each single cell, a novel classifier (Bayesian Cell Classifier) was further developed and used based on whole-transcriptome comparison with prior annotated transcriptional states. Here, we mapped our data to the IMMGEN database, a publicly available resource that contains transcriptome data from a range of immune populations across tissues[179] (Figure 4.1C). In accordance with historical lung flow cytometry data from the lab[25,46,51] (and unpublished observations) and others[180], we detected all expected major cellular lineages within the lung, including B cells, T cells, granulocytes (GN), monocytes/macrophages (MM), NK cells (ILCs), and dendritic cells (DC) (Figure 4.2A). Figure 4.2B shows a heat-map of cell type-specific genes identified from scRNAseq data. A gene was called specific to a given cell type if: i) its expression is at least 50% higher in the marked cell type compared to all other cell types; ii) it is statistically significantly differentially expressed in the marked cell type compared to all other cells in the dataset (permutation test, FDR<5%). A subset of genes are highlighted for each main cluster based on reported strong lineage specificity or function, thereby further validating the cluster assignment. For example, the macrophage/monocyte cluster (MM) expresses high levels of CSF1R and CD68, which are typically broadly used to classify the MM lineage[7] by flow cytometry and histology, and Chil3, Krt19, and Krt79, which are known to be highly expressed by alveolar macrophages[181]. In addition, the B cell cluster specifically expresses Pax5 and CD19, which are both B cell lineage restricted genes[182]. There was minimal separation between replicate samples from healthy control lung tissue (not shown); in contrast, there were dramatic

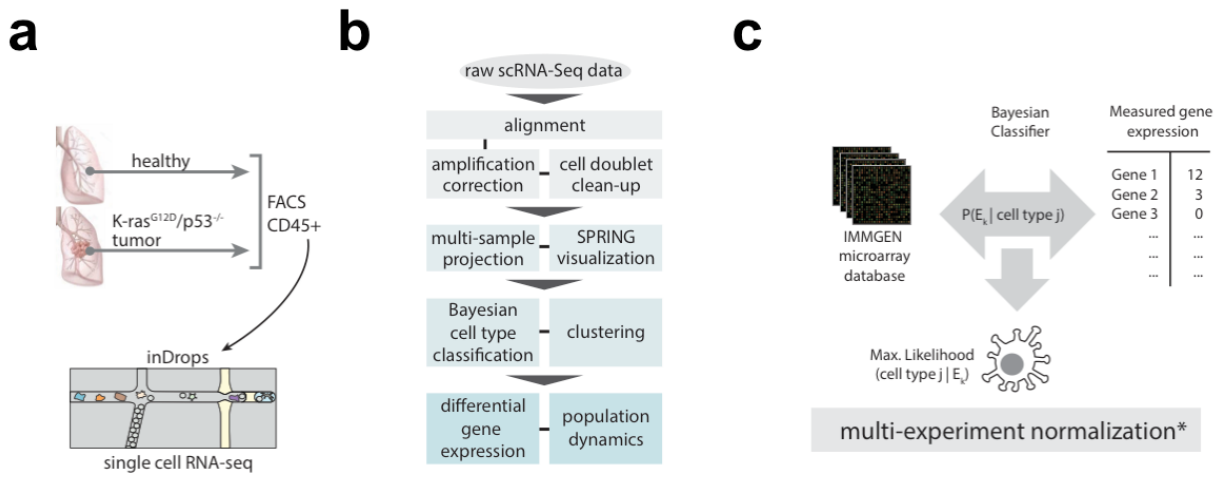

Figure 4.1 *InDrops* scRNA-Seq workflow.

(a) Schematic of droplet microfluidic platform (inDrops) to capture cells into droplets for barcoding by reverse transcription.
(b) Overview of scRNAseq bioinformatics analysis pipeline.
(c) Schematic of Bayesian cell type classification using the Immgen expression database.

shifts in immune cell cluster between healthy (blue) and tumor-bearing tissues (red) (Figure 4.2C).

4.3.2 The tumor stroma contains distinct myeloid cell substates

The most dramatic changes between tumor-bearing and healthy lung occurred within the myeloid population (Figure 4.2C), with parts of the MM, DC, and GN populations only appearing in either healthy or tumor tissue. As myeloid population structure clearly went beyond the classification into major cell types, we analyzed each of them separately, and identified 4, 7, and 5 cell states within DC, MM, and GN respectively. Several new myeloid substates were specifically enriched in tumor-bearing tissue (Figure 4.2D), e.g. GN2-3, DC1-4 and MM3-6 (Figure 4.2D). As a validation, subcluster MM7 separated clearly from the others and presented with high expression of multiple genes typically associated with alveolar macrophages (Krt79, Krt19, etc). Importantly, sub-clustering MM and GN cell states revealed several novel cell states previously unappreciated by flow cytometry analysis, such as MM3-6 and GN4. We then asked

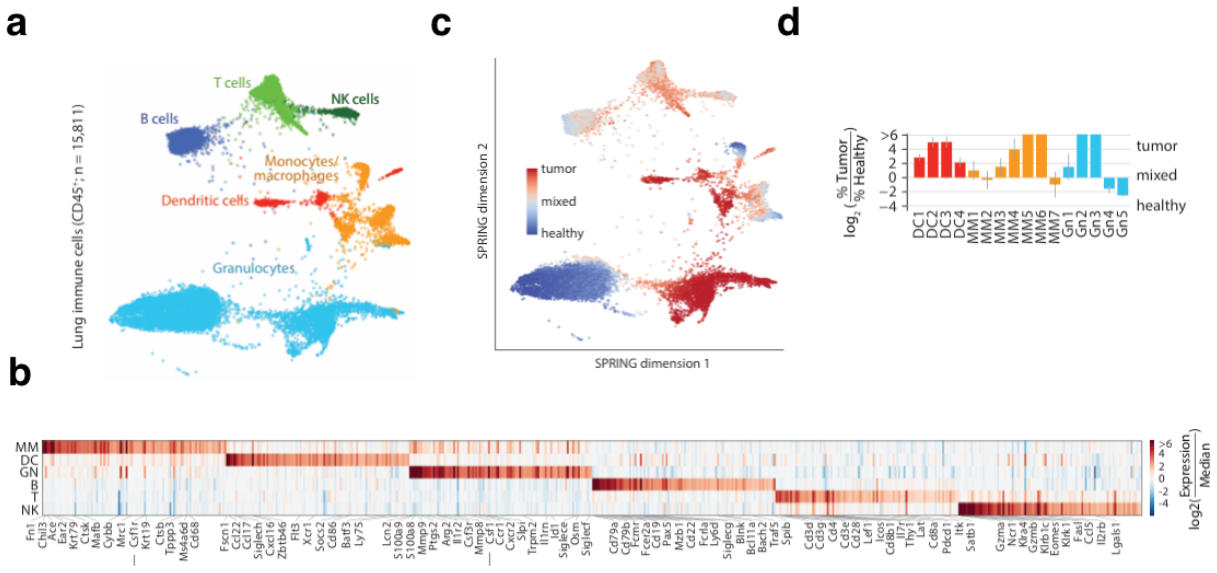

Figure 4.2 *InDrops* scRNA-Seq profiling reveals novel tumor-associated cellular states.

(a) SPRING visualization of scRNAseq data of 15,811 CD45⁺ cells FACS sorted from tumor and healthy lung tissue (pooled). Main immune cell clusters shown in different colors.
(b) Showing differentially expressed genes in cells clustered as in (a) compared to all other cell clusters.
(c) as in (a) but each cell is color coded based on sample identity (red= tumor sample; blue= healthy).
(d) Fold change in the proportion of cells within a given subcluster out of CD45⁺ in tumor versus healthy lung tissue.

whether the expression of key MM-associated markers (e.g. Mrc1, Arg1, CSF1R, etc.) typically used to split up MM subsets fell into particular subclusters. However, we found that the expression of these genes was heterogeneous, and not unique to one subcluster but instead shared among two or more subset (data not shown). Further interrogating the transcriptional activity of each subset should help generate hypotheses of distinct cell types' putative functions in the tumor microenvironment. In addition, relating this transcriptional information back to human disease should be highly relevant, in particular to determine whether specific cell subsets associate with disease outcome. Taken together, we have started to generate an unbiased map of the tumor immune infiltrate in a murine lung tumor using single cell RNAseq technology that has generated novel insights into myeloid population structure, molecular phenotypes and their change upon tumorigenesis.

4.3.3 Myeloid-targeting immunotherapy controls distinct macrophage subclusters

In light of the dramatic changes in MM clusters between tumor and healthy tissue, we then asked whether and how these immune cell clusters were changed upon myeloid cell-based immunotherapy on a single cell level. Specifically, we investigated the response to the CSF1R inhibitor because i) of its critical role in MM development and recruitment to the tumor microenvironment, ii) its high relevance to current anticancer therapies as several CSF1/R targeting agents are in clinical trials, iii) its potential to activate $CD8^+$ T cells in some contexts, and iv) the broad CSF1R expression among the MM cluster in KP tumors (data not shown).

We found that CSF1Ri (BLZ945[183]) substantially reduced KP tumor progression as evident by lung weight (Figure 4.3A-B), and histological examinations of tumor area (Figure 4.3C). These findings were intriguing, not only because KP tumors are notoriously difficult to treat[46], but also because CSF1/R targeting by itself only robustly controls cancer outgrowth in some pre-clinical studies[183,184]. In other experimental tumor models, CSF1/R targeting provided benefit in combination with other anticancer therapies, such as radiotherapy[185], chemotherapy[158], targeted therapy[186], androgen deprivation therapy[187], and immunotherapy[188]. In previous work, BLZ945 successfully limited tumor progression in a glioblastoma model[183], with treatment resistance eventually developing in approximately half of the mice[189], but has not been well characterized in primary lung tumor models. We found that a two-week treatment with daily intraperitoneal drug injections was sufficient to robustly limit KP tumor growth in the lung. Based on these findings, we hypothesized that there CSF1Ri treatment may suppress tumor-promoting populations within the lung, or conversely, amplify antitumoral myeloid cells.

Our initial scRNA-Seq studies (~40,000 cells) indicate that CSF1Ri does not simply ablate all macrophage populations in KP tumors (Figure 4.3D), but modulates macrophage subsets. These findings are in accordance with previous work from the Joyce lab, which defined immunosuppressive phenotypes in tumor-infiltrating MM to decrease in response to CSF1Ri[183]. Specifically, CSF1Ri treatment resulted in the reduction of mainly two tumor-associated

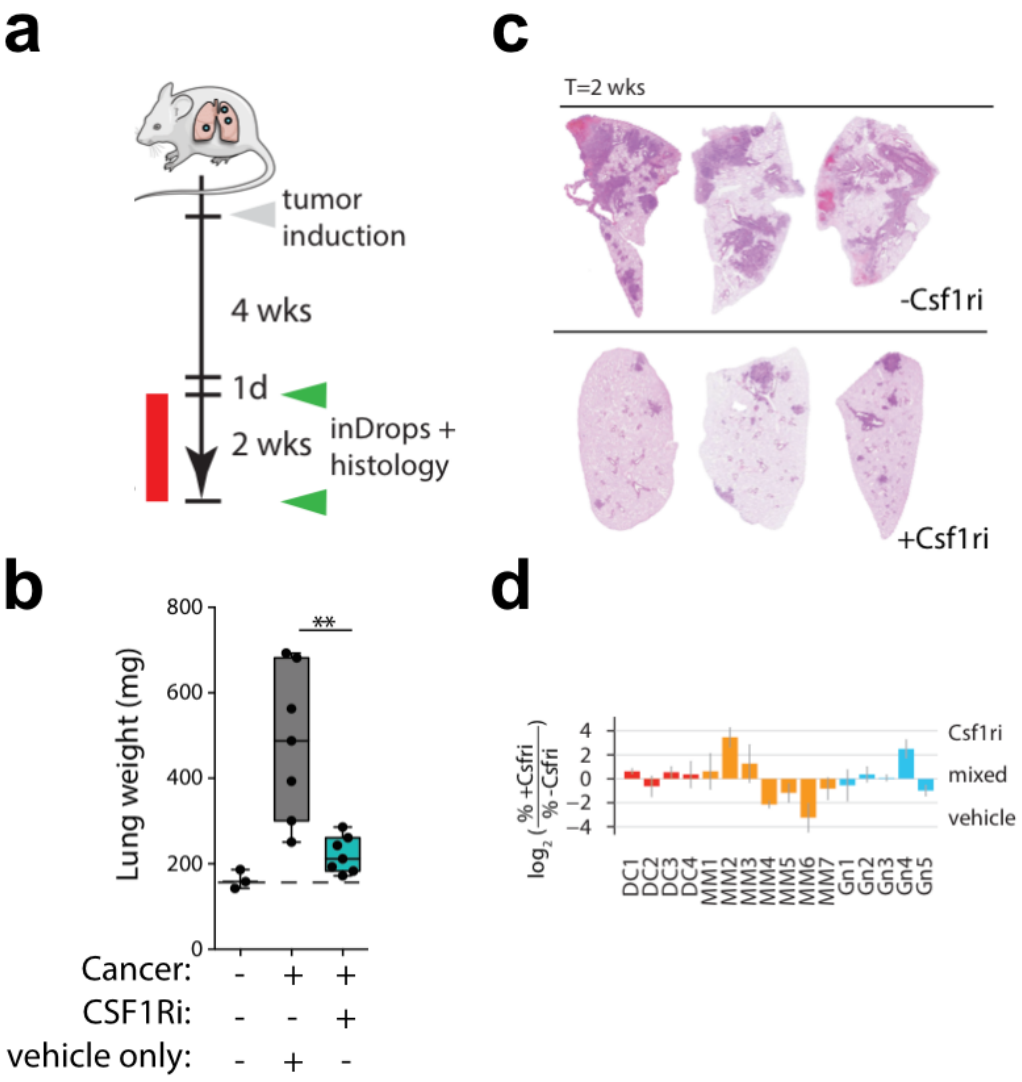

Figure 4.3 Myeloid-targeting immunotherapy controls distinct macrophage subclusters.

(a) BLZ945 treatment scheme in KP lung tumor bearing mice.
(b) Lung weight (as proxy for tumor burden) in healthy and tumor bearing vehicle treated or BLZ945 treated for two weeks.
(c) H&E of samples in (b).
(d) Fold change in the proportion of cells within a given subcluster out of $CD45^{+}$.in CSF1Ri treated mice compared to vehicle control.

macrophage sub-clusters (MM4, 6). Interestingly, MM4 and 6 both expressed high levels of Arginase 1 (Arg1), which has been shown to be strongly associated with T cell suppressive activity[190–193]. Simultaneously, other sub-clusters such as MM2 were enriched compared to vehicle treated control. There was also a remarkable increase in a granulocyte subset (GN4). CSFRi treatment did not noticeably alter the frequency of DC subsets. These findings suggest

that the response to CSF1Ri results in profound changes in the make-up of myeloid cells, and MM in particular, in the tumor stroma. Further investigations will need to clarify whether these changes are functionally relevant for CSF1Ri-induced treatment response.

4.3.4 CSF1Ri- induced tumor control requires CD8⁺ T cells

We hypothesized that KP lung tumor control by CSF1Ri may involve T cells, which display critical antitumor properties in patients and in mice[6]. In absence of treatment, KP tumors are generally poorly infiltrated by T cells[46]. Remarkably, the scRNA dataset revealed a five-fold expansion of CD3 expressing cells, e.g. T cells, in response to CSF1Ri (Figure 4.4A). We could also confirm increased tumor infiltration by CD3 positive T cells by using immunohistochemistry (Figure 4.4B), where the majority of tumor area was infiltrated by T cells in BLZ945-treated (67%) vs untreated (18%) mice (not shown). Furthermore, CSF1Ri treatment did not just amplify the proportion of tumor nodules that were infiltrated with CD3 T cells, but also enriched the T cell density within tumor tissue (Figure 4.4C). These findings resembled our previous results showing T cell infiltration into KP tumors induced by immunogenic chemotherapeutic treatment[46] (Chapter 3). The accumulating T cells were likely CD8⁺ T cells, as shown by additional CD8 immunohistochemical staining (Figure 4.4D). Making use of the single cell expression data, we performed GSEA pathway analysis of differentially expressed genes in CD8⁺ T cells in response to CSF1Ri revealed enrichment in genes associated with ‘positive regulation of T cell mediated immunity’, ‘positive regulation of T cell activation’, and ‘antigen processing and presentation’ (Figure 4.4E). These results suggested that not only were CD8⁺ T cells infiltrating tumor tissue, but they were also more active than CD8⁺ T cells from vehicle treated mice. We then asked whether CD8⁺ T cells were functionally relevant to CSF1Ri-induced tumor control; we found that CD8 depleting antibodies reversed CSF1Ri-induced tumor control (Figure 4.4F). These findings indicate that CSF1Ri is sufficient to i) modulate MM subset composition, ii) increase T cell numbers and activity within tumor tissue, iii) control KP tumor growth in a CD8⁺ T

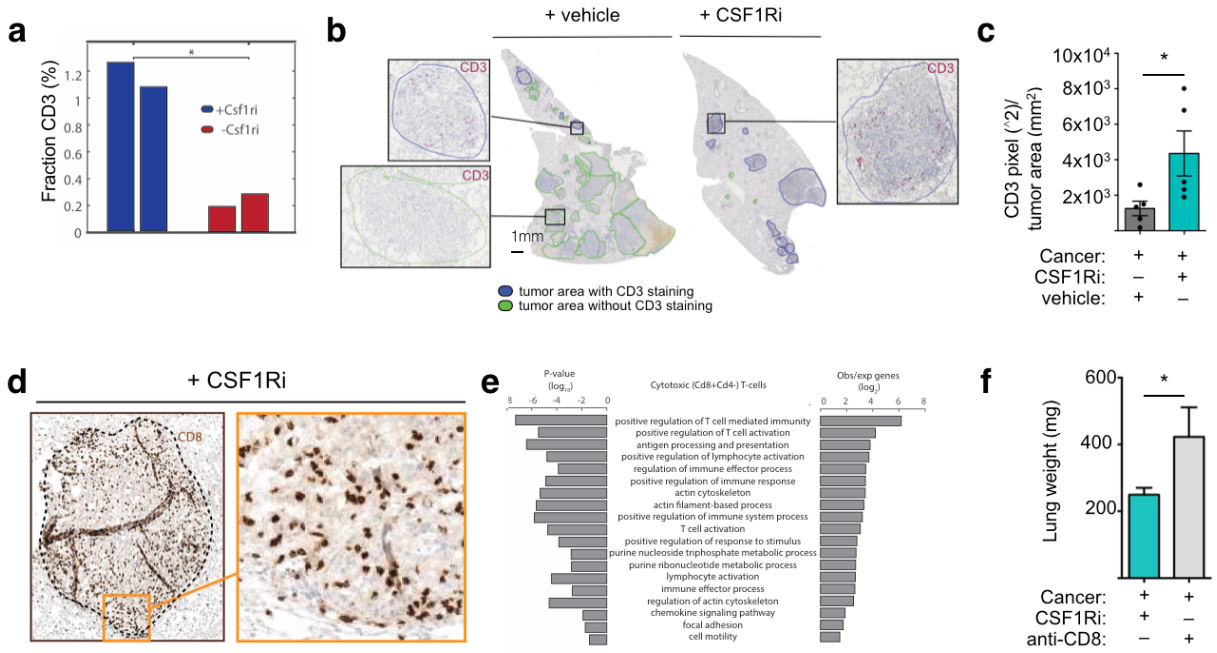

Figure 4.4 CSF1Ri-induced tumor control requires CD8⁺ T cells.

- **(a)** Fraction of CD3 expressing cells of CD45⁺ in tumor-bearing lungs treated with vehicle or CSF1Ri. Each bar is a biological replicate.
- **(b)** Representative CD3 immunohistochemical staining of paraffin embedded tissue sections in mice treated as in a). Blue or green outline denotes tumor region with or without CD3 staining, respectively.
- **(c)** Quantification of CD3 pixel area over total tumor area (n = 5), as shown in (b). Representative immunohistochemical CD8 staining of lung tumor nodule from a CSF1Ri-treated mouse.
- **(e)** GSEA Pathway enrichment analysis of CD8⁺ T cell gene expression from mice treated or not with CSF1Ri.
- **(f)** Lung weight for KP1.9 tumor-bearing mice treated with CSF1Ri with (n=5) or without (n=11) concomitant CD8 depleting antibodies. $p^* < 0.05$

cell dependent manner.

To summarize, in this study we present a comprehensive map of immune cell infiltrates in the healthy and tumor-bearing lungs using single cell RNA-seq analysis. We find that lung tumors dramatically alter myeloid cell subsets, such that novel cell subclusters appear specifically in tumor tissue. Furthermore, we report that CSF1Ri treatment controls tumor growth in a model of lung adenocarcinoma in a CD8⁺ T cell dependent manner, selectively redistributes tumor-associated myeloid cell clusters in the tumor, and simultaneously stimulates T cell infiltration into the tumor stroma. Whether the changes in myeloid substates are important for drug-induced tumor T cell infiltration and control of tumor growth remains to be clarified. Taken

together, these findings should help define the immune cell subsets that regulate tumor progression positively or negatively in KP tumors, with the goal to define new therapeutic targets for anticancer therapies. In addition, our work can be feasibly extended to ask whether and how these novel substates can serve as prognostic indicators for disease outcome in patients.

4.4 Discussion and Future Directions

Follow-up studies to this work are on-going with the goal to harness the unique properties of the scRNA-seq dataset to answer key questions regarding immune cell subsets (and their interactions) within the tumor stroma. This discussion will specifically focus on i) the relevance of distinct tumor-associated cell subsets to human cancer progression, ii) building a cellular and molecular interactome, iii) mechanisms of CSF1R inhibition-induced tumor control (relating to changes in myeloid cell subsets and T cell activity), and iv) therapeutic target discovery.

First, we aim to determine which myeloid cellular states or subsets are relevant to human disease. Recent interrogations of human microarray data has generated expansive databases that allow us to ask whether the expression of a particular gene or gene signature relates to disease progression. One study carefully linked the presence of distinct immune cell gene expression signatures to survival in a range of different cancer types[14]; the authors employed a method called CIBERSORT, which the group had previously developed with the goal to deconvolute leukocyte populations from complex transcriptome datasets[194]. To generate CIBERSORT, the authors used transcriptome data, from well-defined leukocyte populations isolated from healthy controls, together with machine learning approaches to create gene signatures that most accurately defined each immune cell subset. When applying CIBERSORT to patient tumor microarray datasets, they found many interesting relationships; for instance, increased neutrophils (as defined by the expression of specific gene signature) was associated with adverse outcome in a pan-cancer analysis, including NSCLC patients[14]. In contrast, gamma-delta T cell and plasma cell presence in solid tumors (excluding brain) associated with

favorable disease outcome. For other cell types, such as MM and DC populations, the relationships were less clear. Since the gene expression datasets used to computationally define leukocyte populations for CIBERSORT were mainly from blood or bone marrow samples from healthy controls, it is possible that the immune cell signatures do not adequately distinguish cell substates within the tumor microenvironment. Therefore, extending these analyses using tumor specific immune cell signatures may improve the cellular resolution and disease associations in patient tumors.

Using our dataset, we will test whether gene signatures specific to tumor-infiltrating immune cells can be associated with disease outcome in patients. To do this, we will generate immune cell signatures based on our single cell RNA-seq dataset from murine tumor tissue and ask whether high or low expression of such signatures relate to patient outcome (here we will harness publicly available datasets as those used by Gentles *et al.*[14] that include both gene expression data from tumors along with matched patient survival information). Preliminary explorations to this end suggest that we can feasibly distinguish cellular subtypes that associate with positive versus negative disease progression in human patients. Probing the molecular phenotypes of these subsets could help find key tumor promoting and inhibitory pathways in myeloid cells and lymphocytes, offering new prospects of prognostic markers and target discovery for human disease (see fourth discussion point).

Second, we are creating a cellular ‘interactome’ in which we exploit our ability to access the transcriptome of all tumor-infiltrating immune cells to map putative conversations between cells based on their respective ligand and receptor expression. This could be useful in creating a more comprehensive and dynamic view of the tumor microenvironment. We also plan to make the data on the complete tumor immune landscape available to the community as a user-friendly web-interface, which would allow other groups to explore the dataset for their unique purposes, such as to define the expression of a particular gene across clusters or ask which surface markers could be used to fractionate novel populations via flow cytometry for various purposes, including *ex vivo* assays or screens.

Third, in this study, we extended our analysis of tumor-infiltrating immune cells to a clinically relevant myeloid-based immunotherapy targeting the CSF1/CSF1R pathway. We found that CSF1R inhibition controlled KP tumor growth and resulted in distinct perturbations of both myeloid (e.g. MM4,6) and lymphoid cells (e.g. $CD8^+$ T cells) in the tumor. We are particularly interested in how the changes in myeloid subsets relates to the increased $CD8^+$ T cell infiltration and activity at the tumor site. Previous studies have shown that CSF1/R targeting can in some cases result in increased $CD8^+$ T cells at the tumor site (typically measured as $\%CD8^+$ T cells by flowcytometry without showing tissue distribution), but it is not clear whether CSF1Ri-induced effects on myeloid cells results in i) upregulation of chemotactic factors that recruit $CD8^+$ T cells, ii) promotion of $CD8^+$ T cell proliferation, or iii) relief of suppressive molecules. These questions are of high clinical relevance as tumor infiltration by $CD8^+$ T cells has emerged as one of the more reliable prognostic markers of increased survival in cancer patients and the ability to respond to checkpoint blockade therapy[11]. It is therefore of particular interest to clarify mechanisms of CSF1Ri-driven T cell infiltration.

We hypothesize that the decrease in MM4 and MM6 subtypes, that express Arg1 at high levels, could at least in part alleviate immunosuppression of tumor-infiltrating T cells[190–193]. Arg1 production by myeloid cells (macrophages and neutrophil/monocyte like cells in particular) can deplete arginine from the microenvironment, which is needed for $CD8^+$ T cell proliferation[190–193]. However, these changes in MM subsets may not be sufficient to explain the ability of the $CD8^+$ T cells to enter the tumor nodule. It is also possible that the observed changes in MM subsets in response to CSF1R could indirectly impact T cells via regulation of DC populations. DCs, and more specifically subsets thereof, are potent T cell activators. In particular, a tumor-infiltrating DC subset characterized by CD103 (and/or CD8) expression and dependence on the transcription factors *Zbtb46* and *Batf3* appear particularly poised for tumor antigen crosspresentation to and activation of antitumor $CD8^+$ T cell responses in several tumor models[16,195]. T cell infiltration was also restored in melanoma tumors by intratumoral adoptive transfer of *Batf3*- dependent DC populations into tumors[159]. There is precedent for macrophage-

mediated DC control. For example, in a model of chemotherapy-resistance, macrophage restrictedT cell activation by limiting DC expression of IL-12[158]. In our system, CSF1Ri treatment does not alter the frequency of DC subtypes; however, we are currently exploring whether the drug affects DC expression of T cell chemoattractants or co-stimulatory molecules. Alternatively, changes in MM subsets could alter the vasculature to facilitate T cell infiltration, as observed in a model of pancreatic cancer in which local irradiation resulted in macrophage polarization, vasculature normalization and T cell influx[143]. In addition to investigating myeloid cell responses to CSFRi, specifically interrogating putative changes in T cell gene expression in response to CSF1Ri, such as changes in the expression of genes encoding chemokine receptors, proliferation and cytotoxicity, will be important in defining which signaling pathway that drives tumor T cell recruitment. Further analyzing these populations, *in silico* and *in vivo*, should help to elucidate these interactions.

Fourth, we plan to harness our single cell dataset on myeloid cell substates with the goal to identify putative cellular and molecular therapeutic targets. Initially, we will focus our search to cell populations that appear relevant to human disease (either positively or negatively) as discussed above. This may include several myeloid cell subtypes. Then, we will curate a list of genes encoding surface receptors, transcription factors, or secreted proteins that are most selectively expressed by these populations. The single cell nature of the dataset should be at a significant advantage here since it captures heterogeneity within cell subsets that would be missed using bulk analysis, which could allow for more specific antitumoral vs protumoral drug targets. In contrast, depleting cells more broadly may have undesirable side effects or toxicities that could affect cells that are beneficial for the host (e.g. depleting all neutrophils as opposed to a particular tumor-infiltrating subset could result in immunosuppression and susceptibility to infections). After defining the most unique markers relevant for a given myeloid cell subset, we can then ask questions regarding the functions of these cells *in vivo*. In the most ideal scenario, these subsets will express distinct surface markers that are typically more amenable to therapeutic targeting. Additionally, we can use pharmacological inhibitors or genetic mouse

models to reduce or augment the function of defined cell subsets or genes. The technological advances in CRISPR/Cas9 technologies should also permit relatively feasible experimental setups (compared to historical methods of generating new mouse models) to address the function of several target genes. We are currently starting these experiments, which should help to clarify the tumor supporting or inhibiting capacities of distinct myeloid cell substates or associated molecular mediators in regulating tumor growth and to reveal clinically relevant targets.

To conclude, in this study we have begun to catalogue the immune cell landscape in the healthy and tumor-bearing lung using single cell RNAseq analysis. In particular, we have defined new cell myeloid cell subsets that appear exclusively in tumor tissue; whether these subsets are functionally relevant for tumor progression in mice and associate with disease outcome in patients is currently being tested. Targeting KP tumors with myeloid-based immunotherapy (CSF1Ri) controls tumor progression and results in distinct perturbations of tumor-associated myeloid substates that may be important for drug efficacy and T cell influx to tumors. Our results should help to delineate myeloid cell activation states in tumors and of drug actions on such states, as well as provide novel resources to expand both basic and clinical discovery.

4.5 Experimental procedures

Mice and Tumor Models

C57BL/6 wild type mice were obtained from Jackson Laboratory. All animal experiments were performed according to approved IACUC guidelines. The lung adenocarcinoma cell line KP1.9, derived from lung tumor nodules of a male C57BL/6 *Kras*$^{LSL\text{-}G12D/WT}$;*Trp53*$^{Flox/Flox}$ (referred to as KP) mouse was kindly provided by Dr. A. Zippelius, University Hospital Basel, Switzerland. The cell line was maintained in Iscove's DMEM media supplemented with 10% fetal bovine serum (FBS) and 1% penicillin/streptomycin. To generate lung tumors, KP1.9 cells ($2.5x10^5$ cells in 100µl PBS) were injected intravenously (i.v.) into C57BL/6 mice. Age matched mice were used as tumor-free controls. Female C57BL/6 mice were euthanized between 43-44 days and male mice between 30-31 days post i.v. tumor cell injection. Tumor burden was analyzed by measuring post-mortem lung weight and by histological analyses of lung tissue sections using hematoxylin and eosin (H&E) stainings. Experiments to generate biological replicates were performed on separate days (and included mice from two distinct cohorts of tumor-injected mice). Experimental and control samples were processed on the same day.

Drug Treatments

KP1.9 lung or flank tumor-bearing female C57BL/6 mice were treated with the CSF1R inhibitor drug BLZ945 intraperitoneally (i.p.; or in indicated experiments i.v.). The drug was applied daily at a dose of 100mg/kg of body weight. BLZ945 was synthesized at the Center for Systems Biology at MGH using a 2-hydroxypropyl-β-cyclodextrin formulation. The concentration of BLZ945 was determined using liquid chromotography-mass spectrometry by comparing to a standard curve generated using DMF or DMSO solutions of BLZ945.

Lung tumor-bearing mice were treated with BLZ945 for two weeks and flank tumor-bearing mice for eight days. In parallel, tumor-bearing control mice were injected with the vehicle (2-hydroxypropyl-β-cyclodextrin) that was used for BLZ945 drug formulation.

In indicated experiments for depletion of $CD8^+$ T cells, lung tumor-bearing C57BL/6 female mice were injected i.p. with anti-CD8 monoclonal antibodies (mAb, clone 53-6.72, 200µg/mouse, BioXcell). The mAb injection started 25 days after i.v. KP1.9 tumor cell injection and four days before the first BLZ945 drug treatment. Anti-CD8 mAb injection was continued every 2-3 day until the end of the experiment.

Isolation of $CD45^+$ Cells through Flow Cytometry-based Cell Sorting

KP1.9 lung tumor-bearing and tumor-free control mice were euthanized and perfused with 1xPBS to remove the majority of circulating immune cells. Lungs were harvested and weighed to determine tumor burden. One lung lobe was removed and processed for histological stainings. Tumor tissue and adjacent tumor-free tissue of tumor-bearing mice as well as lung tissue of tumor-free control mice was dissected with surgical fine scissors and digested in RPMI medium containing 0.2mg/ml collagenase type I (Worthington Biochemical Corporation) for 15min at 37°C while shaking at 700rpm.

To generate a single cell suspension, the digested tissue was passed through a 70µM cell strainer and cells were washed using FACS buffer (1xPBS with 0.5% BSA and 2mM EDTA). Single cell suspensions were stained with CD45-PB mAbs (clone 30-F11, Biolegend) for 20min at 4°C and 7-aminoactinomycin (7AAD, Sigma) was used to exclude dead cells. Purity of sorted cells was assessed and exceeded >95%. $CD45^+$ live cells were sorted into 100% FBS using a FACSAria cell sorter (BD) and immediately prepared for single cell RNAseq analysis and in parallel for further investigation by flow cytometry.

Single cell RNAseq

Single cell RNA sequencing was performed according to the inDrops protocol[177]. Briefly, sorted $CD45^+$ cells from mouse lung tissue were co-encapsulated into ~3 nl droplets together with hydrogel beads, containing photocleavable barcoding primers. To barcode the transcripts from each individual cell, the cells were then lysed to release their mRNA content, barcoding

primers were released by UV light, and reverse transcription was performed. cDNA libraries were then prepared for next-generation sequencing as described[177]. Sequencing was performed at a depth of ~50,000 read per cell (Illumina NextSeq). The number of cells sequenced per sample varied depending on the experiment, but ranged in the thousands.

Bioinformatics Analyses

Preprocessing: A cell-by-gene digital expression matrix was produced by a previously described custom pipeline[177], which was modified to accommodate recent changes to the library preparation protocol. The current implementation, which performs alignment with bowtie, UMI-based amplification and barcode selection, is available from the online depository Github (https://github.com/indrops/indrops). The reference used was GRCm38 (Dec. 2011), available from UCSC genome browser database.

Doublet and dead cell removal

Barcodes with low number of reads (<250) were assumed to derive from cells with compromised integrity and were discarded during preprocessing.
Potential doublets deriving from technical considerations in the InDrops system were removed with a doublet identification algorithm. The doublet rate in InDrops experiment has been previously assessed at 2.5%. To simulate its impact, we generated "artificial" doublets by randomly sampling and combining observed transcriptomes, and constructed a kNN graph of the simulated and experimentally observed cells. This allowed us to compute a doublet score for each observed cell by counting the number of its simulated doublet neighbors and using density propagation for smoothing. The cells within the top 2.5% doublet scores were removed. To account for doublets stemming from biological considerations (e.g. mechanical interaction or adhesion between specific cell types), we applied a further doublet removal step after clustering. Specifically, clusters were tested for robustness by comparing the similarity of individual cell

transcriptomes to their assigned clusters and to all other clusters. In robust clusters, 80% -100% of the cells were most similar to their own cluster centroid. Two clusters with low robustness (<60%) were identified as potential experimental artifacts. One of these clusters was identified as a possible doublet cluster due to a co-occurrence of granulocyte and monocyte markers. Another was found to be composed of heterogeneous cell types with consistently high mitochondrial reads and was labeled a dead cell cluster. Both of these clusters were removed from further consideration.

Dimensionality reduction, visualization and clustering

We performed dimensionality reduction on the data as follows. Genes with mean expression >0.03 and coefficient of variation (standard deviation/mean) >2 were z-score normalized and used to perform principal components analysis (PCA) of the cells down to 60 dimensions. A kNN graph (k=5) was constructed using Euclidean distance in the resulting PC space.

The kNN graph was visualized using a force-directed layout using a custom interactive software interface called SPRING 7. Only trivial manual steps (e.g. rotation and “shaking”) were taken to improve visualization after the initial data loading. It is important to emphasize that the manipulations affect visualization only. All subsequent analyses depend on the graph adjacency matrix, which is not affected by any of the changes to the graph layout. To improve visual presentation of gene expression on the resulting layout, the data was smoothed by diffusing the gene expression values with a random walk over the kNN graph, controlled by a parameter corresponding to the termination probability. To identify cell types and states in an unbiased way, we performed spectral decomposition of the kNN graph and applied density clustering using DBSCAN to the resulting space.

Batch effects

In the first set of experiments, we observed a batch effect on the granulocyte population derived from healthy lung, which displayed a slightly higher percent of mitochondrial reads and was likely due to a slight variation in extraction and processing conditions. To prevent this effects distorting subsequent data analysis, we selected variable genes from one of biological replicates and used that set to calculate principal component (PC) gene loadings. Cells from both replicates were then projected into the reduced space, and all subsequent analysis was performed on the reduced PC space.

IMMGEN Bayesian classifier

To classify each cell into a known immune cell type, we use gene expression profiles from the Immgen consortium. We assign each (cell, profile) pair a score corresponding to the probability of the cell deriving from that profile. The score is the product of the probabilities of the observed gene expression for each gene in the cell given the gene expression observed in the profile.

Cell type-specific gene selection

For each of the 6 major immune cell categories (Gn,MM,DC,NK,T,B), we identified differentially expressed genes between cells within the group vs. all other immune cells. To be considered for differential gene expression analysis, genes had to be expressed by at least 1% of cells in at least one of the two groups of cells compared. Genes with a FDR<0.05 were considered cell-type specific if expressed at least 1.5 higher in that cell type compared to any other cell type. The heatmap in Figure 4.1 displays the first 100 most specific genes for each cell type. For within-category cell state-specific gene selection (not shown), the same procedure was used, except that all comparisons were limited to cells within a given category. For example, the selection of genes specific to DC1-4 was limited to dendritic cells.

Differential gene expression analysis

For differential genes expression analysis (DGE) between two groups of cells, we used a parameter-free permutation-based test to calculate p-values, with the difference in means as the test statistic. We accounted for multiple hypothesis testing with a false discovery rate (FDR) of 5% using the Benjamini-Hochberg procedure[128].

$CD8^+$ T cell analysis pathway analysis

Gene set enrichment pathway analysis of $CD8^+$ T cell gene expression data from BLZ945-treated lung tumors and vehicle-treated tumor free was done as previously described (Chapter 2.6 Experimental Procedures).

Histology and Immunohistochemistry

Lung tissue samples were formaldehyde-fixed and paraffin-embedded following standard procedures. Tissue sections were prepared and stained with H&E using the Shandon Varistain Gemini ES Automated Slide Stainer (Thermo Scientific).

Immunohistochemistry stainings were performed as described earlier[46]. Briefly, lung sections were dried at 60°C for 1h, dewaxed and rehydrated before treated with heat-induced antigen-retrieval prior immunostaining. The sections were incubated in 10 mM sodium-citrate (pH6.0) buffered solution containing 0.05% Tween and heated at 120°C for 2min using a pressure cooker. To obtain consistent and reliable staining the LabVision Autostainer 360 (Thermo Scientific) was used. The sections were pretreated using BLOXALL endogenous enzyme blocking solution (Vector Laboratories) for 5min to destroy endogenous alkaline phosphatase and peroxidase activity. After blocking with serum, the sections were incubated with rabbit anti-CD3 (clone SP7, Abcam) or rat anti-mouse CD8a (clone 4SM15, Affymetrix/ eBioscience) mAbs for 1h followed by several washes and respective secondary ImmPRESS polymer detection systems (Vector Laboratories) according to manufacturer's

recommendations. The Vulcan Fast Red Chromogen Kit 2 (red staining; Biocare Medical) and the DAB Quanto System (brown staining; Thermo Scientific) were applied as substrates and hematoxylin used as counterstain. The NanoZoomer 2.0-RS slide scanner system (Hamamatsu) was used for image documentation. CD3 stained images were analyzed and pixel areas per tumor area calculated using Fiji software.

Statistical Analysis

For tumor measurements (lung weight, tumor area, tumor volume) and immunohistochemistry-based quantifications, results were presented as mean ± SEM. One-way ANOVA followed by Tukey's or Dunnett's multiple comparisons test or two-tailed Student's t test were performed when appropriate. *P* value <0.05 or less was used to denote statistical significance (*p<0.05, **p<0.01, ***p<0.01).

Chapter 5: Additional contributions

5.1 Overview

In this chapter, I briefly summarize several projects to which I have contributed to during my thesis. These broadly include findings involving systemic cancer-related host immune responses, the role of microbiota in cytotoxic-induced antitumor immune responses, and the use of imaging to study drug uptake in, and tissue distribution of tumor-infiltrating myeloid cells. Together, these studies provide related and complementary findings to our contributions presented in Chapter 2-4 .

5.2 Systemic cancer-host interactions

5.2.1 SCS macrophages suppress melanoma by restricting tumor-derived vesicle-B cell interactions.

Pucci F, Garris C, Lai CP, Newton A, Pfirschke C, **Engblom C**, Alvarez D, Sprachman M, Evavold C, Magnuson A, von Andrian UH, Glatz K, Breakefield XO, Mempel TR, Weissleder R, Pittet MJ.
Science. 2016 Apr 8;352(6282):242-6.

Tumor-derived vesicles (tEVs) have been proposed as a key mechanism of cancer cell-exerted effects on the local and systemic microenvironment. However, tEV distribution in the host has mainly been studied using bolus injections of vesicles isolated ex vivo from cancer cell lines or tumor microenvironments. To address this, Pucci et al. designed experimental tools in which tEVs were produced endogenously by tumors and their body-wide distribution and uptake by host cells could be measured in the tumor microenvironment or in distant organs (lymph nodes, bone marrow, spleen, etc). In this study, we found that tumor-derived extracellular vesicles were captured by lymph node macrophages and that these macrophages suppressed

protumoral B cell- associated responses. Sub-capsular sinus (SCS) macrophages thus functioned as a barrier to tEVs drained from the tumor via the lymph and disruption of this barrier (which occurred after chemotherapy or could be experimentally induced via lymph node macrophage depletion) resulted in accelerated tumor growth. Taken together, this study defined a previously unappreciated interaction between tEVs and lymp node resident SCS macrophages that was important in restricting B cell-driven tumor promoting mechanisms; these findings add to a literature showing diverse functions of macrophages in the context of cancer and important tEV functions influencing disease progression.

Attributions: For this project, I performed protein array analysis of tumor cell lines with reduced capacity to produce microvesicles and assisted with *in vivo* experiments, experimental design, data analysis, and co-edited the manuscript.

5.2.2 PF4 Promotes Platelet Production and Lung Cancer Growth.

Pucci F, Rickelt S, Newton AP, Garris C, Nunes E, Evavold C, Pfirschke C, **Engblom C**, Mino-Kenudson M, Hynes RO, Weissleder R, Pittet MJ.
Cell Rep. 2016 Nov 8;17(7):1764-1772.

Tumor cells may act on host cells in the local tumor microenvironment, but they can also affect distant tissues through the release of soluble mediators. This mode of interaction remains incompletely understood. In this work, *in silico* screening of tumor-associated elevated plasma proteins was done to identify new candidate molecules of interest, through an analysis pipeline relating patient tumor gene expression with disease outcome, i.e. survival. Here, we identified that elevated levels of on such candidate, PF4 (CXCL4), was associated with poorer survival in lung adenocarcinoma patients. Further investigations revealed that *Pf4* was also upregulated in lung adenocarcinoma models in mice, and had distinct effects on bone marrow hematopoiesis that impacted primary tumor growth. Specifically, PF4 overproduction by lentiviral delivery in

Kras-mutated lung adenocarcinomas amplified megakarypoiesis in the bone marrow, triggered platelet accumulation at the tumor site, and increased cancer outgrowth. Platelets had tumor-promoted properties since therapeutically targeting platelets reduced lung adenocarcinoma outgrowth. These findings place PF4 as a novel endocrine regulator of host protumoral immune responses involving platelets.

Attributions: For this study, I performed mouse experiments, analyzed data, and helped to edit the manuscript.

5.3 Anticancer immune effects requires an intact microbiota

5.3.1 The intestinal microbiota modulates the anticancer immune effects of cyclophosphamide.

Viaud S1, Saccheri F, Mignot G, Yamazaki T, Daillère R, Hannani D, Enot DP, Pfirschke C, **Engblom C**, Pittet MJ, Schlitzer A, Ginhoux F, Apetoh L, Chachaty E, Woerther PL, Eberl G, Bérard M, Ecobichon C, Clermont D, Bizet C, Gaboriau-Routhiau V, Cerf-Bensussan N, Opolon P, Yessaad N, Vivier E, Ryffel B, Elson CO, Doré J, Kroemer G, Lepage P, Boneca IG, Ghiringhelli F, Zitvogel L.
Science. 2013 Nov 22;342(6161):971-6.

Certain cytotoxic chemotherapeutics control tumor growth at least in part via antitumor immune responses. It has become clear that the gut microbiota can critically control immune processes at steady and diseased states, but whether the gut microbiota influence antitumor immune responses to anticancer therapies had not been reported previously. This study showed that cyclophosphamide treatment disrupted the gut mucosal integrity in mice and that cyclophosphamide-induced antitumor responses were reduced in germ-free mice or mice treated with antibiotics. A concomitant published study also showed that antibiotics or germ-free

conditions abrogated chemotherapy-triggered antitumoral immune responses (involving TLR4-dependent ROS-expressing myeloid cells) using other models. Taken together, these studies presented seminal work showing the relevance of the microbiome in generating chemtherapy-induced antitumor responses.

Attributions: For this article, I performed experiments and analyzed data testing whether antibiotic vancomycin administration limited the cyclophosphamide-based therapeutic response in a genetic mouse model of lung cancer.

5.4 Imaging tumor-infiltrating macrophages

5.4.1 Predicting therapeutic nanomedicine efficacy using a companion magnetic resonance imaging nanoparticle.

Miller MA, Gadde S, Pfirschke C, **Engblom C**, Sprachman MM, Kohler RH, Yang KS, Laughney AM, Wojtkiewicz G, Kamaly N, Bhonagiri S, Pittet MJ, Farokhzad OC, Weissleder R.
Sci Transl Med. 2015 Nov 18;7(314):314ra183.

Therapeutic nanoparticles have emerged as a promising tool to optimize drug delivery in various diseases, including cancer. This study tested whether magnetic resonance imaging of a companion nanoparticle could help predict the *in vivo* distribution of therapeutic nanoparticles (carrying cytotoxic drugs) in order to more accurately predict therapeutic efficacy. Using xenograft tumor models, we found that the magnetic nanoparticles accumulated in tumor-associated immune cells to comparable degrees. Among the hematopoietic cells, the majority of the nanoparticles were taken up by macrophages and granulocytes. Taken together, this study demonstrated that companion nanoparticle imaging could help predict treatment efficacy with therapeutic nanoparticles in mice.

Attributions: For this article, I performed FACS analysis of mouse tumors to compare therapeutic versus magnetic nanoparticle uptake in tumor cells and immune cells.

5.4.2 Tumour-associated macrophages act as a slow-release reservoir of nano-therapeutic Pt(IV) pro-drug.

Miller MA, Zheng YR, Gadde S, Pfirschke C, Zope H, **Engblom C**, Kohler RH, Iwamoto Y, Yang KS, Askevold B, Kolishetti N, Pittet M, Lippard SJ, Farokhzad OC, Weissleder R.
Nat Commun. 2015 Oct 27;6:8692.

This study investigated nanoparticle and drug uptake and distribution in the tumor microenvironment. Here, fluorescently labeled platinum pro-drug was encapsulated in nanoparticles (labeled with a distinct fluorophore) and imaged *in vivo* over time. Microscopy and ex vivo flow cytometry analysis revealed that nanoparticles preferentially accumulated in tumor associated macrophages (TAMs). This uptake was important because TAMs slowly released platinum drug to the surrounding tissue over time and their depletion reduced therapeutic efficacy of the platinum loaded nanoparticles.

Attributions: For this project, I performed FACS analysis of nanoparticle versus drug distribution in immune infiltrates and tumor cells.

5.4.3 Heterogeneity of macrophage infiltration and therapeutic response in lung carcinoma revealed by 3D organ imaging.

Cuccarese MF, Dubach JM, Pfirschke C, **Engblom C,** Garris C, Miller MA, Pittet MJ, Weissleder R. Nat Commun. 2017 Feb 8;8:14293.

Macrophage populations display diverse phenotypes in tumors and there is an urgent need to clarify their functions and tissue distribution in vivo. To address this issue, this study used whole tissue clearing techniques and nanoparticle-based macrophage labeling to image and quantify TAM density and tumor tissue penetrance, along with tumor burden. The results demonstrated high heterogeneity in TAM distribution throughout the KP lung tumor tissue, even within same animal. Targeting macrophages using a tyrosine kinase inhibitor (PLX3397), aimed at both CSF1R and cKIT, resulted in a spatial re-organization of TAMs (without apparent cell depletion), with amplified TAM infiltration of tumor nodules in controlled tumors. This study is complementary to our analysis of TAMs in KP tumor tissue using single cell RNAseq (Chapter 4) and provides novel insight to the diversity of TAM distribution throughout lung tumor tissue.

Attributions: For this study, I assisted with mouse tumor experiments, experimental design, and performed flow cytometry analysis.

5.5 Conclusion

The research summarized in the preceding sections represent additional and complementary information to what constitutes the main theme of the thesis (Chapter 2-4). In particular, Section 5.2 presents two studies that further unravel modes of systemic interactions between tumors and distant organs (e.g. tEVs and draining lymph nodes versus PF4 and the bone marrow). Combined, these studies reinforce the idea that tumors and remote immune responses, including hematopoiesis, are linked and should be further explored. Furthermore, the findings introduced in Section 5.3 broadens our understanding of chemotherapy-induced antitumor immune responses (Chapter 3) to also include the importance of the microbiota. These findings are clinically relevant since many patients undergoing chemotherapy require treatment with antibiotics. Finally, the last collection of studies introduced here (Section 5.4)

feature the fact that tumor-host interactions can be investigated using multiple vantage points, including exploiting macrophages' phagocytic properties for in vivo imaging, for diagnostic purposes, and to improve drug pharmacokinetics. The article referenced in Subsection 5.4.3 is particularly relevant to the research in Chapter 4, as it defines spatial reorganization of TAMs in response to a CSF1R targeting agent; relating the distribution of TAMs within the tumor along with their gene expression profiles should further advance the definition of their relevant tumor-associated functions. In summary, the studies in Chapter extend the main goals of this thesis with supplemental basic mechanisms and therapeutic explorations of tumor-immune interactions in the local and systemic tissue microenvironment.

Chapter 6: Summary and Future directions

The findings presented in this thesis are part of a larger effort within the cancer immunology field dedicated to understanding the underlying mechanisms and diversity of tumor-immune interactions both within and outside the local tumor microenvironment. By considering that components in the host are locally and globally interdependent, whether it be on a molecular, cellular or organismal level, one can better appreciate the complex dynamics of immune responses influencing disease progression and therapy. Measuring and interpreting this type of complexity is a serious challenge; nevertheless, it is critical to understand the full spectrum of cancer-exerted effects on the host (including those related to anticancer therapies) and how these responses can be best harnessed for treatments across cancer types and individuals.

A growing body of evidence from preclinical studies, including our own, suggest that there is substantial diversity within tumor-infiltrating neutrophil, macrophage, and DC phenotypes and functional properties, which could be relevant to human cancer pathology. Future studies should therefore aim to understand the heterogeneous repertoire of tumor-associated myeloid cells specifically in cancer patients. Furthermore, systemic cancer-host interactions remain less explored both in patients and animal models, but our findings that tumors interact with the bone marrow stroma to propel its own growth via myeloid cells (Chapter 2), along with previous work from our lab[24,25,27,51] and others[19,22,23,196,197], emphasize the importance of studying tumor-associated myeloid responses that occur outside the local stroma. It will also be important to further investigate the effects of anticancer therapy-related effects on myeloid responses in patients. Regardless of the question, critically interrogating myeloid cell functions in human patients, whether they refute or confirm preclinical phenotypes, should help fuel discoveries regarding myeloid-related phenotypes and functions in patient tumors.

Thus, a more complete understanding of the human immune cell repertoire should help define which tumor-associated cell populations are the most amenable to therapeutic targeting,

with the goal to best potentiate current anticancer therapies as well as define new therapeutic targets. Currently, one of the burning questions in tumor immunology is how to most efficiently expand the number of patients that respond to ICB, since for the patients who do respond, ICB may offer unprecedented durable control of tumor progression[4,11]. ICB treatment resistance can play out as a lack of initial response, partial response, or initial response followed by relapse of the disease[4]. Tumor infiltration by T cells (specifically cytotoxic T cells) has emerged as one of the more robust predictors of treatment efficacy and disease outcome, yet many tumors lack a robust T cell presence. Targeting other components of the tumor stroma (either directly or indirectly) to activate T cells and facilitate their influx into tumors, presents an intriguing possibility to dramatically increase ICB responders[198].

In this work, we show that T cell infiltration can be achieved either by inducing immunogenic cell death (Chapter 3) by careful selection of appropriate chemotherapeutics towards a particular tumor. It is plausible that patients whose tumors lack T cells, may benefit from optimizing their chemotherapeutic regime to facilitate T cell infiltration. Approximately ~60% of late stage NSCLC patients already receive some type of chemotherapy; therefore, although chemotherapy may not be the end-goal treatment, screening drugs for immunogenicity towards a patient's own tumors, may serve as a feasible and relatively inexpensive (these drugs are already FDA-approved) way to sensitize patients to ICB.

More generally, various manipulations of the tumor stroma could be beneficial in this context by supplying T cells with tumor antigens, stimulating T cell proliferation, changing the stromal landscape to facilitate T cell-tumor interactions, and stimulating a T cell phenotype amenable to ICB targeting[198,199]. Targeting myeloid components could be useful in combination with other anticancer therapies, such as cytotoxic or targeted therapies, or promoting antitumor myeloid phenotypes for treatment success. For example, as we showed in Chapter 4, CSF1R inhibition resulted in a robust tumor control and T cell expansion at the tumor site; this type of treatment might be particularly appropriate to boost T cell activity in macrophage-rich tumor microenvironments. Tumor cell intrinsic signaling also impacts T cell tumor infiltration[199], and

therefore, better understanding the effect of cancer cell-intrinsic mutations and signaling on the tumor microenvironment could also provide new powerful ways to enhance T cell influx into tumors.

New technologies should offer opportunities to both ask fundamental questions related to tumor progression and to improve therapeutic targeting. Exciting new developments in techniques such as single cell analysis of the transcriptome (e.g. DropSeq)[127,200] or protein level(CyTOF)[180,201], protein mass-spectrometry[202], high throughput protein analysis[203], application of machine learning techniques to biology[14], or novel CRISPR screens[204] are already helping to propel such investigations. These techniques are centered around the goal to learn more from less, e.g. they are particularly amenable to studying human cancers were sample size is often a restriction. Additionally, clinical imaging technologies (e.g. magnetic resonance imaging and positron emission tomography) could be used to dynamically and non-invasively monitor myeloid cell activity and repertoires, in combination with tumor growth[86]. More directed delivery of anticancer therapies, whether the target is the immune system or not, also has the potential to dramatically improve cancer therapy, with the aim to maximize treatment efficacy and minimize toxic side effects. Examples of these include injectable biomaterials that could serve as localized vaccine approaches[205], or nanoparticle-encapsulation of drugs that could result in more directed drug delivery or improved pharmacokinetics[206]. However, as discussed, systemic drug effects may be desirable and in some cases required for treatment efficacy, and therefore, careful mechanistic investigations of drug-host-cancer interactions are needed.

The field of cancer immunology is making remarkable strides; the last decade has seen a considerable transformation in the types of treatments offered to patients, an advancement of the available technologies used to interrogate and manipulate tumor-host interactions, and an increased interest in tumor immunology within the research community. Within this area of research, our findings provide new insights into both local and systemic tumor-host interactions that warrant further investigation.

References

1. Torre, L. A., Siegel, R. L., Ward, E. M. & Jemal, A. Global Cancer Incidence and Mortality Rates and Trends--An Update. *Cancer Epidemiol Biomarkers Prev* **25**, 16-27 (2016).

2. Miller, K. D. et al. Cancer treatment and survivorship statistics, 2016. *CA Cancer J Clin* **66**, 271-289 (2016).

3. Gotwals, P. et al. Prospects for combining targeted and conventional cancer therapy with immunotherapy. *Nat Rev Cancer* (2017).

4. Sharma, P., Hu-Lieskovan, S., Wargo, J. A. & Ribas, A. Primary, Adaptive, and Acquired Resistance to Cancer Immunotherapy. *Cell* **168**, 707-723 (2017).

5. Broz, M. L. & Krummel, M. F. The emerging understanding of myeloid cells as partners and targets in tumor rejection. *Cancer Immunol Res* **3**, 313-319 (2015).

6. Gajewski, T. F., Schreiber, H. & Fu, Y. X. Innate and adaptive immune cells in the tumor microenvironment. *Nat Immunol* **14**, 1014-1022 (2013).

7. Ruffell, B. & Coussens, L. M. Macrophages and therapeutic resistance in cancer. *Cancer Cell* **27**, 462-472 (2015).

8. Engblom, C., Pfirschke, C. & Pittet, M. J. The role of myeloid cells in cancer therapies. *Nat Rev Cancer* **16**, 447-462 (2016).

9. Coussens, L. M., Zitvogel, L. & Palucka, A. K. Neutralizing tumor-promoting chronic inflammation: a magic bullet. *Science* **339**, 286-291 (2013).

10. Vallentin, B. et al. Innate Lymphoid Cells in Cancer. *Cancer Immunol Res* **3**, 1109-1114 (2015).

11. Sharma, P. & Allison, J. P. The future of immune checkpoint therapy. *Science* **348**, 56-61 (2015).

12. Davis, B. P. & Rothenberg, M. E. Eosinophils and cancer. *Cancer Immunol Res* **2**, 1-8 (2014).

13. Gabrilovich, D. I. Myeloid-Derived Suppressor Cells. *Cancer Immunol Res* **5**, 3-8 (2017).

14. Gentles, A. J. et al. The prognostic landscape of genes and infiltrating immune cells across

human cancers. *Nat Med* **21**, 938-945 (2015).

15. Zhang, Q. W. et al. Prognostic significance of tumor-associated macrophages in solid tumor: a meta-analysis of the literature. *PLoS One* **7**, e50946 (2012).

16. Broz, M. L. et al. Dissecting the tumor myeloid compartment reveals rare activating antigen-presenting cells critical for T cell immunity. *Cancer Cell* **26**, 638-652 (2014).

17. Coffelt, S. B., Wellenstein, M. D. & de Visser, K. E. Neutrophils in cancer: neutral no more. *Nat Rev Cancer* **16**, 431-446 (2016).

18. McAllister, S. S. & Weinberg, R. A. The tumour-induced systemic environment as a critical regulator of cancer progression and metastasis. *Nat Cell Biol* **16**, 717-727 (2014).

19. Wu, W. C. et al. Circulating hematopoietic stem and progenitor cells are myeloid-biased in cancer patients. *Proc Natl Acad Sci U S A* **111**, 4221-4226 (2014).

20. Jiang, L. et al. Prognostic value of monocyte and neutrophils to lymphocytes ratio in patients with metastatic soft tissue sarcoma. *Oncotarget* **6**, 9542-9550 (2015).

21. Huang, S. H. et al. Prognostic value of pretreatment circulating neutrophils, monocytes, and lymphocytes in oropharyngeal cancer stratified by human papillomavirus status. *Cancer* **121**, 545-555 (2015).

22. Casbon, A. J. et al. Invasive breast cancer reprograms early myeloid differentiation in the bone marrow to generate immunosuppressive neutrophils. *Proc Natl Acad Sci U S A* **112**, E566-75 (2015).

23. Bayne, L. J. et al. Tumor-derived granulocyte-macrophage colony-stimulating factor regulates myeloid inflammation and T cell immunity in pancreatic cancer. *Cancer Cell* **21**, 822-835 (2012).

24. Cortez-Retamozo, V. et al. Angiotensin II drives the production of tumor-promoting macrophages. *Immunity* **38**, 296-308 (2013).

25. Pucci, F. et al. PF4 Promotes Platelet Production and Lung Cancer Growth. *Cell Rep* **17**, 1764-1772 (2016).

26. McAllister, S. S. et al. Systemic endocrine instigation of indolent tumor growth requires osteopontin. *Cell* **133**, 994-1005 (2008).

27. Pucci, F. et al. SCS macrophages suppress melanoma by restricting tumor-derived vesicle-B cell interactions. *Science* **352**, 242-246 (2016).

28. Zomer, A. et al. In Vivo imaging reveals extracellular vesicle-mediated phenocopying of metastatic behavior. *Cell* **161**, 1046-1057 (2015).

29. Wen, S. W. et al. The Biodistribution and Immune Suppressive Effects of Breast Cancer-Derived Exosomes. *Cancer Res* **76**, 6816-6827 (2016).

30. Gül, N. et al. Macrophages eliminate circulating tumor cells after monoclonal antibody therapy. *J Clin Invest* **124**, 812-823 (2014).

31. Qian, B. Z. et al. CCL2 recruits inflammatory monocytes to facilitate breast-tumour metastasis. *Nature* **475**, 222-225 (2011).

32. Condeelis, J. & Pollard, J. W. Macrophages: obligate partners for tumor cell migration, invasion, and metastasis. *Cell* **124**, 263-266 (2006).

33. Spiegel, A. et al. Neutrophils Suppress Intraluminal NK Cell-Mediated Tumor Cell Clearance and Enhance Extravasation of Disseminated Carcinoma Cells. *Cancer Discov* **6**, 630-649 (2016).

34. Hanna, R. N. et al. Patrolling monocytes control tumor metastasis to the lung. *Science* **350**, 985-990 (2015).

35. Sharma, S. K. et al. Pulmonary alveolar macrophages contribute to the premetastatic niche by suppressing antitumor T cell responses in the lungs. *J Immunol* **194**, 5529-5538 (2015).

36. Coffelt, S. B. et al. IL-17-producing γδ T cells and neutrophils conspire to promote breast cancer metastasis. *Nature* **522**, 345-348 (2015).

37. Alizadeh, D. et al. Doxorubicin eliminates myeloid-derived suppressor cells and enhances the efficacy of adoptive T-cell transfer in breast cancer. *Cancer Res* **74**, 104-118 (2014).

38. Germano, G. et al. Role of macrophage targeting in the antitumor activity of trabectedin. *Cancer Cell* **23**, 249-262 (2013).

39. Vincent, J. et al. 5-Fluorouracil selectively kills tumor-associated myeloid-derived suppressor cells resulting in enhanced T cell-dependent antitumor immunity. *Cancer Res* **70**, 3052-3061 (2010).

40. Kroemer, G., Galluzzi, L., Kepp, O. & Zitvogel, L. Immunogenic cell death in cancer therapy. *Annu Rev Immunol* **31**, 51-72 (2013).

41. Simpson, T. R. et al. Fc-dependent depletion of tumor-infiltrating regulatory T cells co-defines the efficacy of anti-CTLA-4 therapy against melanoma. *J Exp Med* **210**, 1695-1710 (2013).

42. Romano, E. et al. Ipilimumab-dependent cell-mediated cytotoxicity of regulatory T cells ex vivo by nonclassical monocytes in melanoma patients. *Proc Natl Acad Sci U S A* **112**, 6140-6145 (2015).

43. Bulliard, Y. et al. Activating Fc γ receptors contribute to the antitumor activities of immunoregulatory receptor-targeting antibodies. *J Exp Med* **210**, 1685-1693 (2013).

44. Pincetic, A. et al. Type I and type II Fc receptors regulate innate and adaptive immunity. *Nat Immunol* **15**, 707-716 (2014).

45. DuPage, M., Dooley, A. L. & Jacks, T. Conditional mouse lung cancer models using adenoviral or lentiviral delivery of Cre recombinase. *Nat Protoc* **4**, 1064-1072 (2009).

46. Pfirschke, C. et al. Immunogenic Chemotherapy Sensitizes Tumors to Checkpoint Blockade Therapy. *Immunity* **44**, 343-354 (2016).

47. Davies, L. C., Jenkins, S. J., Allen, J. E. & Taylor, P. R. Tissue-resident macrophages. *Nat Immunol* **14**, 986-995 (2013).

48. Ginhoux, F. & Jung, S. Monocytes and macrophages: developmental pathways and tissue homeostasis. *Nat Rev Immunol* **14**, 392-404 (2014).

49. Hanahan, D. & Coussens, L. M. Accessories to the crime: functions of cells recruited to the tumor microenvironment. *Cancer Cell* **21**, 309-322 (2012).

50. Gabrilovich, D. I., Ostrand-Rosenberg, S. & Bronte, V. Coordinated regulation of myeloid cells by tumours. *Nat Rev Immunol* **12**, 253-268 (2012).

51. Cortez-Retamozo, V. et al. Origins of tumor-associated macrophages and neutrophils. *Proc Natl Acad Sci U S A* **109**, 2491-2496 (2012).

52. Hoggatt, J., Kfoury, Y. & Scadden, D. T. Hematopoietic Stem Cell Niche in Health and Disease. *Annu Rev Pathol* **11**, 555-581 (2016).

53. Mercier, F. E., Ragu, C. & Scadden, D. T. The bone marrow at the crossroads of blood and immunity. *Nat Rev Immunol* **12**, 49-60 (2011).

54. Morrison, S. J. & Scadden, D. T. The bone marrow niche for haematopoietic stem cells. *Nature* **505**, 327-334 (2014).

55. Mendelson, A. & Frenette, P. S. Hematopoietic stem cell niche maintenance during homeostasis and regeneration. *Nat Med* **20**, 833-846 (2014).

56. Reagan, M. R. & Rosen, C. J. Navigating the bone marrow niche: translational insights and cancer-driven dysfunction. *Nat Rev Rheumatol* **12**, 154-168 (2016).

57. Karsenty, G., Kronenberg, H. M. & Settembre, C. Genetic control of bone formation. *Annu Rev Cell Dev Biol* **25**, 629-648 (2009).

58. Otto, F. et al. Cbfa1, a candidate gene for cleidocranial dysplasia syndrome, is essential for osteoblast differentiation and bone development. *Cell* **89**, 765-771 (1997).

59. Komori, T. et al. Targeted disruption of Cbfa1results in a complete lack of bone formation owing to maturational arrest of osteoblasts. *Cell* **89**, 755-764 (1997).

60. Ducy, P., Zhang, R., Geoffroy, V., Ridall, A. L. & Karsenty, G. Osf2/Cbfa1: a transcriptional activator of osteoblast differentiation. *Cell* **89**, 747-754 (1997).

61. Nakashima, K. et al. The novel zinc finger-containing transcription factor osterix is required for osteoblast differentiation and bone formation. *Cell* **108**, 17-29 (2002).

62. Weinreb, M., Shinar, D. & Rodan, G. A. Different pattern of alkaline phosphatase, osteopontin, and osteocalcin expression in developing rat bone visualized by in situ hybridization. *J Bone Miner Res* **5**, 831-842 (1990).

63. Mizuno, M. & Kuboki, Y. Osteoblast-related gene expression of bone marrow cells during the osteoblastic differentiation induced by type I collagen. *J Biochem* **129**, 133-138 (2001).

64. Feng, J. Q. et al. Loss of DMP1 causes rickets and osteomalacia and identifies a role for osteocytes in mineral metabolism. *Nat Genet* **38**, 1310-1315 (2006).

65. Schaffler, M. B., Cheung, W. Y., Majeska, R. & Kennedy, O. Osteocytes: master orchestrators of bone. *Calcif Tissue Int* **94**, 5-24 (2014).

66. Calvi, L. M. et al. Osteoblastic cells regulate the haematopoietic stem cell niche. *Nature*

425, 841-846 (2003).

67. Zhang, J. et al. Identification of the haematopoietic stem cell niche and control of the niche size. *Nature* **425**, 836-841 (2003).

68. Visnjic, D. et al. Conditional ablation of the osteoblast lineage in Col2.3deltatk transgenic mice. *J Bone Miner Res* **16**, 2222-2231 (2001).

69. Visnjic, D. et al. Hematopoiesis is severely altered in mice with an induced osteoblast deficiency. *Blood* **103**, 3258-3264 (2004).

70. Wu, J. Y. et al. Osteoblastic regulation of B lymphopoiesis is mediated by Gs{alpha}-dependent signaling pathways. *Proc Natl Acad Sci U S A* **105**, 16976-16981 (2008).

71. Zhu, J. et al. Osteoblasts support B-lymphocyte commitment and differentiation from hematopoietic stem cells. *Blood* **109**, 3706-3712 (2007).

72. Yu, V. W. et al. Specific bone cells produce DLL4 to generate thymus-seeding progenitors from bone marrow. *J Exp Med* **212**, 759-774 (2015).

73. Ding, L. & Morrison, S. J. Haematopoietic stem cells and early lymphoid progenitors occupy distinct bone marrow niches. *Nature* **495**, 231-235 (2013).

74. Greenbaum, A. et al. CXCL12 in early mesenchymal progenitors is required for haematopoietic stem-cell maintenance. *Nature* **495**, 227-230 (2013).

75. Fulzele, K. et al. Myelopoiesis is regulated by osteocytes through Gsα-dependent signaling. *Blood* **121**, 930-939 (2013).

76. Arai, F. et al. Tie2/angiopoietin-1 signaling regulates hematopoietic stem cell quiescence in the bone marrow niche. *Cell* **118**, 149-161 (2004).

77. Nilsson, S. K. et al. Osteopontin, a key component of the hematopoietic stem cell niche and regulator of primitive hematopoietic progenitor cells. *Blood* **106**, 1232-1239 (2005).

78. Hoggatt, J. et al. Differential stem- and progenitor-cell trafficking by prostaglandin E2. *Nature* **495**, 365-369 (2013).

79. Ding, L., Saunders, T. L., Enikolopov, G. & Morrison, S. J. Endothelial and perivascular cells maintain haematopoietic stem cells. *Nature* **481**, 457-462 (2012).

80. Raaijmakers, M. H. et al. Bone progenitor dysfunction induces myelodysplasia and secondary leukaemia. *Nature* **464**, 852-857 (2010).

81. Kode, A. et al. Leukaemogenesis induced by an activating β-catenin mutation in osteoblasts. *Nature* **506**, 240-244 (2014).

82. Logothetis, C. J. & Lin, S. H. Osteoblasts in prostate cancer metastasis to bone. *Nat Rev Cancer* **5**, 21-28 (2005).

83. Ferraro, F. et al. Diabetes impairs hematopoietic stem cell mobilization by altering niche function. *Sci Transl Med* **3**, 104ra101 (2011).

84. Terashima, A. et al. Sepsis-Induced Osteoblast Ablation Causes Immunodeficiency. *Immunity* **44**, 1434-1443 (2016).

85. Zaheer, A. et al. In vivo near-infrared fluorescence imaging of osteoblastic activity. *Nat Biotechnol* **19**, 1148-1154 (2001).

86. Weissleder, R. & Pittet, M. J. Imaging in the era of molecular oncology. *Nature* **452**, 580-589 (2008).

87. Wu, J. Y., Scadden, D. T. & Kronenberg, H. M. Role of the osteoblast lineage in the bone marrow hematopoietic niches. *J Bone Miner Res* **24**, 759-764 (2009).

88. Cubillos-Ruiz, J. R. et al. ER Stress Sensor XBP1 Controls Antitumor Immunity by Disrupting Dendritic Cell Homeostasis. *Cell* **161**, 1527-1538 (2015).

89. Ang, Z., Er, J. Z. & Ding, J. L. The short-chain fatty acid receptor GPR43 is transcriptionally regulated by XBP1 in human monocytes. *Sci Rep* **5**, 8134 (2015).

90. Nguyen, D. X. et al. WNT/TCF signaling through LEF1 and HOXB9 mediates lung adenocarcinoma metastasis. *Cell* **138**, 51-62 (2009).

91. Directors, C. C. F. T. M. C. O. L. A. et al. Gene expression-based survival prediction in lung adenocarcinoma: a multi-site, blinded validation study. *Nat Med* **14**, 822-827 (2008).

92. Zhang, M. et al. Osteoblast-specific knockout of the insulin-like growth factor (IGF) receptor gene reveals an essential role of IGF signaling in bone matrix mineralization. *J Biol Chem* **277**, 44005-44012 (2002).

93. Nozawa, H., Chiu, C. & Hanahan, D. Infiltrating neutrophils mediate the initial angiogenic

switch in a mouse model of multistage carcinogenesis. *Proc Natl Acad Sci U S A* **103**, 12493-12498 (2006).

94. Shojaei, F. et al. Bv8 regulates myeloid-cell-dependent tumour angiogenesis. *Nature* **450**, 825-831 (2007).

95. Kowanetz, M. et al. Granulocyte-colony stimulating factor promotes lung metastasis through mobilization of $Ly6G^{+}Ly6C^{+}$ granulocytes. *Proc Natl Acad Sci U S A* **107**, 21248-21255 (2010).

96. Fridlender, Z. G. et al. Polarization of tumor-associated neutrophil phenotype by TGF-beta: “N1” versus “N2” TAN. *Cancer Cell* **16**, 183-194 (2009).

97. Wculek, S. K. & Malanchi, I. Neutrophils support lung $^{\text{colonization}}$ of metastasis-initiating breast cancer cells. *Nature* **528**, 413-417 (2015).

98. Templeton, A. J. et al. Prognostic role of neutrophil-to-lymphocyte ratio in solid tumors: a systematic review and meta-analysis. *J Natl Cancer Inst* **106**, dju124 (2014).

99. Peinado, H. et al. Melanoma exosomes educate bone marrow progenitor cells toward a pro-metastatic phenotype through MET. *Nat Med* **18**, 883-891 (2012).

100. Kanaji, N. et al. Paraneoplastic syndromes associated with lung cancer. *World J Clin Oncol* **5**, 197-223 (2014).

101. Christopher, M. J. & Link, D. C. Granulocyte colony-stimulating factor induces osteoblast apoptosis and inhibits osteoblast differentiation. *J Bone Miner Res* **23**, 1765-1774 (2008).

102. Bowers, M. et al. Osteoblast ablation reduces normal long-term hematopoietic stem cell self-renewal but accelerates leukemia development. *Blood* **125**, 2678-2688 (2015).

103. Onan, D. et al. The chemokine Cxcl1 is a novel target gene of parathyroid hormone (PTH)/ PTH-related protein in committed osteoblasts. *Endocrinology* **150**, 2244-2253 (2009).

104. Taichman, R. S. & Emerson, S. G. Human osteoblasts support hematopoiesis through the production of granulocyte colony-stimulating factor. *J Exp Med* **179**, 1677-1682 (1994).

105. Bettigole, S. E. & Glimcher, L. H. Endoplasmic reticulum stress in immunity. *Annu Rev Immunol* **33**, 107-138 (2015).

106. Bettigole, S. E. et al. The transcription factor XBP1 is selectively required for eosinophil

differentiation. *Nat Immunol* **16**, 829-837 (2015).

107. Percopo, C. M. et al. SiglecF^{+}Gr1hi eosinophils are a distinct subpopulation within the lungs of allergen-challenged mice. *J Leukoc Biol* **101**, 321-328 (2017).

108. Houghton, A. M. et al. Neutrophil elastase-mediated degradation of IRS-1 accelerates lung tumor growth. *Nat Med* **16**, 219-223 (2010).

109. Di Mitri, D. et al. Tumour-infiltrating Gr-1^{+} myeloid cells antagonize senescence in cancer. *Nature* **515**, 134-137 (2014).

110. Eruslanov, E. B. et al. Tumor-associated neutrophils stimulate T cell responses in early-stage human lung cancer. *J Clin Invest* **124**, 5466-5480 (2014).

111. Granot, Z. et al. Tumor entrained neutrophils inhibit seeding in the premetastatic lung. *Cancer Cell* **20**, 300-314 (2011).

112. Finisguerra, V. et al. MET is required for the recruitment of anti-tumoural neutrophils. *Nature* **522**, 349-353 (2015).

113. Schmielau, J. & Finn, O. J. Activated granulocytes and granulocyte-derived hydrogen peroxide are the underlying mechanism of suppression of t-cell function in advanced cancer patients. *Cancer Res* **61**, 4756-4760 (2001).

114. Kusmartsev, S., Nefedova, Y., Yoder, D. & Gabrilovich, D. I. Antigen-specific inhibition of CD8^{+} T cell response by immature myeloid cells in cancer is mediated by reactive oxygen species. *J Immunol* **172**, 989-999 (2004).

115. Mohamed, M. M. & Sloane, B. F. Cysteine cathepsins: multifunctional enzymes in cancer. *Nat Rev Cancer* **6**, 764-775 (2006).

116. Shree, T. et al. Macrophages and cathepsin proteases blunt chemotherapeutic response in breast cancer. *Genes Dev* **25**, 2465-2479 (2011).

117. Läubli, H. et al. Engagement of myelomonocytic Siglecs by tumor-associated ligands modulates the innate immune response to cancer. *Proc Natl Acad Sci U S A* **111**, 14211-14216 (2014).

118. Macauley, M. S., Crocker, P. R. & Paulson, J. C. Siglec-mediated regulation of immune cell function in disease. *Nat Rev Immunol* **14**, 653-666 (2014).

119. Beatson, R. et al. The mucin MUC1 modulates the tumor immunological microenvironment through engagement of the lectin Siglec-9. *Nat Immunol* **17**, 1273-1281 (2016).

120. Buch, T. et al. A Cre-inducible diphtheria toxin receptor mediates cell lineage ablation after toxin administration. *Nat Methods* **2**, 419-426 (2005).

121. Srinivas, S. et al. Cre reporter strains produced by targeted insertion of EYFP and ECFP into the ROSA26 locus. *BMC Dev Biol* **1**, 4 (2001).

122. Bouxsein, M. L. et al. Guidelines for assessment of bone microstructure in rodents using micro-computed tomography. *J Bone Miner Res* **25**, 1468-1486 (2010).

123. Wein, M. N. et al. SIKs control osteocyte responses to parathyroid hormone. *Nat Commun* **7**, 13176 (2016).

124. Liu, E. S. et al. 1,25-Dihydroxyvitamin D Alone Improves Skeletal Growth, Microarchitecture, and Strength in a Murine Model of XLH, Despite Enhanced FGF23 Expression. *J Bone Miner Res* **31**, 929-939 (2016).

125. Dempster, D. W. et al. Standardized nomenclature, symbols, and units for bone histomorphometry: a 2012 update of the report of the ASBMR Histomorphometry Nomenclature Committee. *J Bone Miner Res* **28**, 2-17 (2013).

126. Courties, G. et al. Ischemic stroke activates hematopoietic bone marrow stem cells. *Circ Res* **116**, 407-417 (2015).

127. Klein, A. M. et al. Droplet barcoding for single-cell transcriptomics applied to embryonic stem cells. *Cell* **161**, 1187-1201 (2015).

128. Benjamini, Y. & Hochberg, Y. Controlling the False Discovery Rate: A Practical and Powerful Approach to Multiple Testing. *Journal of the Royal Statistical Society* **57**, 289-300 (1995).

129. Subramanian, A. et al. Gene set enrichment analysis: a knowledge-based approach for interpreting genome-wide expression profiles. *Proc Natl Acad Sci U S A* **102**, 15545-15550 (2005).

130. Mootha, V. K. et al. PGC-1alpha-responsive genes involved in oxidative phosphorylation are coordinately downregulated in human diabetes. *Nat Genet* **34**, 267-273 (2003).

131. Davidson-Pilon, C. Lifelines. *Github repository* (2016).

132. Topalian, S. L., Drake, C. G. & Pardoll, D. M. Immune Checkpoint Blockade: A Common Denominator Approach to Cancer Therapy. *Cancer Cell* **27**, 450-461 (2015).

133. Schreiber, R. D., Old, L. J. & Smyth, M. J. Cancer immunoediting: integrating immunity's roles in cancer suppression and promotion. *Science* **331**, 1565-1570 (2011).

134. Schumacher, T. N. & Schreiber, R. D. Neoantigens in cancer immunotherapy. *Science* **348**, 69-74 (2015).

135. Rooney, M. S., Shukla, S. A., Wu, C. J., Getz, G. & Hacohen, N. Molecular and genetic properties of tumors associated with local immune cytolytic activity. *Cell* **160**, 48-61 (2015).

136. Fridman, W. H., Pages, F., Sautes-Fridman, C. & Galon, J. The immune contexture in human tumours: impact on clinical outcome. *Nat Rev Cancer* **12**, 298-306 (2012).

137. Torre, L. A. et al. Global cancer statistics, 2012. *CA Cancer J Clin* **65**, 87-108 (2015).

138. Tumeh, P. C. et al. PD-1 blockade induces responses by inhibiting adaptive immune resistance. *Nature* **515**, 568-571 (2014).

139. Rizvi, N. A. et al. Cancer immunology. Mutational landscape determines sensitivity to PD-1 blockade in non-small cell lung cancer. *Science* **348**, 124-128 (2015).

140. Herbst, R. S. et al. Predictive correlates of response to the anti-PD-L1 antibody MPDL3280A in cancer patients. *Nature* **515**, 563-567 (2014).

141. Topalian, S. L. et al. Safety, activity, and immune correlates of anti-PD-1 antibody in cancer. *N Engl J Med* **366**, 2443-2454 (2012).

142. Zitvogel, L., Galluzzi, L., Smyth, M. J. & Kroemer, G. Mechanism of action of conventional and targeted anticancer therapies: reinstating immunosurveillance. *Immunity* **39**, 74-88 (2013).

143. Klug, F. et al. Low-dose irradiation programs macrophage differentiation to an $iNOS^{+}$/M1 phenotype that orchestrates effective T cell immunotherapy. *Cancer Cell* **24**, 589-602 (2013).

144. Shalapour, S. et al. Immunosuppressive plasma cells impede T-cell-dependent immunogenic chemotherapy. *Nature* **521**, 94-98 (2015).

145. Gubin, M. M. et al. Checkpoint blockade cancer immunotherapy targets tumour-specific mutant antigens. *Nature* **515**, 577-581 (2014).

146. Olive, K. P. et al. Inhibition of Hedgehog signaling enhances delivery of chemotherapy in a mouse model of pancreatic cancer. *Science* **324**, 1457-1461 (2009).

147. DuPage, M. et al. Endogenous T cell responses to antigens expressed in lung adenocarcinomas delay malignant tumor progression. *Cancer Cell* **19**, 72-85 (2011).

148. Postow, M. A. et al. Nivolumab and Ipilimumab versus Ipilimumab in Untreated Melanoma. *N Engl J Med* (2015).

149. Wolchok, J. D. et al. Nivolumab plus ipilimumab in advanced melanoma. *N Engl J Med* **369**, 122-133 (2013).

150. Oliver, T. G. et al. Chronic cisplatin treatment promotes enhanced damage repair and tumor progression in a mouse model of lung cancer. *Genes Dev* **24**, 837-852 (2010).

151. Schiavoni, G. et al. Cyclophosphamide synergizes with type I interferons through systemic dendritic cell reactivation and induction of immunogenic tumor apoptosis. *Cancer Res* **71**, 768-778 (2011).

152. Sato, E. et al. Intraepithelial $CD8^+$ tumor-infiltrating lymphocytes and a high $CD8^+$/regulatory T cell ratio are associated with favorable prognosis in ovarian cancer. *Proc Natl Acad Sci U S A* **102**, 18538-18543 (2005).

153. Gao, Q. et al. Intratumoral balance of regulatory and cytotoxic T cells is associated with prognosis of hepatocellular carcinoma after resection. *J Clin Oncol* **25**, 2586-2593 (2007).

154. Ghiringhelli, F. et al. $CD4^+CD25^+$ regulatory T cells suppress tumor immunity but are sensitive to cyclophosphamide which allows immunotherapy of established tumors to be curative. *Eur J Immunol* **34**, 336-344 (2004).

155. Lutsiak, M. E. et al. Inhibition of CD4(+)25+ T regulatory cell function implicated in enhanced immune response by low-dose cyclophosphamide. *Blood* **105**, 2862-2868 (2005).

156. De Palma, M. & Lewis, C. E. Macrophage regulation of tumor responses to anticancer therapies. *Cancer Cell* **23**, 277-286 (2013).

157. Apetoh, L. et al. Toll-like receptor 4-dependent contribution of the immune system to anticancer chemotherapy and radiotherapy. *Nat Med* **13**, 1050-1059 (2007).

158. Ruffell, B. et al. Macrophage IL-10 blocks $CD8^+$ T cell-dependent responses to chemotherapy by suppressing IL-12 expression in intratumoral dendritic cells. *Cancer Cell* **26**, 623-637 (2014).

159. Spranger, S., Bao, R. & Gajewski, T. F. Melanoma-intrinsic β-catenin signalling prevents anti-tumour immunity. *Nature* **523**, 231-235 (2015).

160. Tesniere, A. et al. Immunogenic death of colon cancer cells treated with oxaliplatin. *Oncogene* **29**, 482-491 (2010).

161. Gou, H. F., Huang, J., Shi, H. S., Chen, X. C. & Wang, Y. S. Chemo-immunotherapy with oxaliplatin and interleukin-7 inhibits colon cancer metastasis in mice. *PLoS One* **9**, e85789 (2014).

162. Peer, D. et al. Nanocarriers as an emerging platform for cancer therapy. *Nat Nanotechnol* **2**, 751-760 (2007).

163. Chauhan, V. P. et al. Normalization of tumour blood vessels improves the delivery of nanomedicines in a size-dependent manner. *Nat Nanotechnol* **7**, 383-388 (2012).

164. Ciampricotti, M. et al. Chemotherapy response of spontaneous mammary tumors is independent of the adaptive immune system. *Nat Med* **18**, 344-6; author reply 346 (2012).

165. Lu, L. et al. Combined PD-1 blockade and GITR triggering induce a potent antitumor immunity in murine cancer models and synergizes with chemotherapeutic drugs. *J Transl Med* **12**, 36 (2014).

166. Murray, P. J. et al. Macrophage activation and polarization: nomenclature and experimental guidelines. *Immunity* **41**, 14-20 (2014).

167. Ginhoux, F., Schultze, J. L., Murray, P. J., Ochando, J. & Biswas, S. K. New insights into the multidimensional concept of macrophage ontogeny, activation and function. *Nat Immunol* **17**, 34-40 (2016).

168. Noy, R. & Pollard, J. W. Tumor-associated macrophages: from mechanisms to therapy. *Immunity* **41**, 49-61 (2014).

169. Kessenbrock, K., Plaks, V. & Werb, Z. Matrix metalloproteinases: regulators of the tumor microenvironment. *Cell* **141**, 52-67 (2010).

170. Harney, A. S. et al. Real-Time Imaging Reveals Local, Transient Vascular Permeability, and Tumor Cell Intravasation Stimulated by TIE2hi Macrophage-Derived VEGFA. *Cancer*

Discov **5**, 932-943 (2015).

171. Lewis, J. S., Landers, R. J., Underwood, J. C., Harris, A. L. & Lewis, C. E. Expression of vascular endothelial growth factor by macrophages is up-regulated in poorly vascularized areas of breast carcinomas. *J Pathol* **192**, 150-158 (2000).

172. Sierra, J. R. et al. Tumor angiogenesis and progression are enhanced by Sema4D produced by tumor-associated macrophages. *J Exp Med* **205**, 1673-1685 (2008).

173. Kuang, D. M. et al. Activated monocytes in peritumoral stroma of hepatocellular carcinoma foster immune privilege and disease progression through PD-L1. *J Exp Med* **206**, 1327-1337 (2009).

174. Biswas, S. K. & Mantovani, A. Macrophage plasticity and interaction with lymphocyte subsets: cancer as a paradigm. *Nat Immunol* **11**, 889-896 (2010).

175. Carretero, R. et al. Eosinophils orchestrate cancer rejection by normalizing tumor vessels and enhancing infiltration of CD8(+) T cells. *Nat Immunol* **16**, 609-617 (2015).

176. Wang, Z., Gerstein, M. & Snyder, M. RNA-Seq: a revolutionary tool for transcriptomics. *Nat Rev Genet* **10**, 57-63 (2009).

177. Zilionis, R. et al. Single-cell barcoding and sequencing using droplet microfluidics. *Nat Protoc* **12**, 44-73 (2017).

178. Weinreb, C., Wolock, S. & Klein, A. SPRING: a kinetic interface for visualizing high dimensional single-cell expression data. *bioRxiv* (2016).

179. Heng, T. S., Painter, M. W. & Immunological, G. P. C. The Immunological Genome Project: networks of gene expression in immune cells. *Nat Immunol* **9**, 1091-1094 (2008).

180. Spitzer, M. H. et al. IMMUNOLOGY. An interactive reference framework for modeling a dynamic immune system. *Science* **349**, 1259425 (2015).

181. Gautier, E. L. et al. Gene-expression profiles and transcriptional regulatory pathways that underlie the identity and diversity of mouse tissue macrophages. *Nat Immunol* **13**, 1118-1128 (2012).

182. Boller, S. & Grosschedl, R. The regulatory network of B-cell differentiation: a focused view of early B-cell factor 1 function. *Immunol Rev* **261**, 102-115 (2014).

183. Pyonteck, S. M. et al. CSF-1R inhibition alters macrophage polarization and blocks glioma progression. *Nat Med* **19**, 1264-1272 (2013).

184. Strachan, D. C. et al. CSF1R inhibition delays cervical and mammary tumor growth in murine models by attenuating the turnover of tumor-associated macrophages and enhancing infiltration by CD8(+) T cells. *Oncoimmunology* **2**, e26968 (2013).

185. Xu, J. et al. CSF1R signaling blockade stanches tumor-infiltrating myeloid cells and improves the efficacy of radiotherapy in prostate cancer. *Cancer Res* **73**, 2782-2794 (2013).

186. Mok, S. et al. Inhibition of colony stimulating factor-1 receptor improves antitumor efficacy of BRAF inhibition. *BMC Cancer* **15**, 356 (2015).

187. Escamilla, J. et al. CSF1 receptor targeting in prostate cancer reverses macrophage-mediated resistance to androgen blockade therapy. *Cancer Res* **75**, 950-962 (2015).

188. Zhu, Y. et al. CSF1/CSF1R blockade reprograms tumor-infiltrating macrophages and improves response to T-cell checkpoint immunotherapy in pancreatic cancer models. *Cancer Res* **74**, 5057-5069 (2014).

189. Quail, D. F. et al. The tumor microenvironment underlies acquired resistance to CSF-1R inhibition in gliomas. *Science* **352**, aad3018 (2016).

190. Chang, C. I., Liao, J. C. & Kuo, L. Macrophage arginase promotes tumor cell growth and suppresses nitric oxide-mediated tumor cytotoxicity. *Cancer Res* **61**, 1100-1106 (2001).

191. Rodriguez, P. C. et al. Arginase I in myeloid suppressor cells is induced by COX-2 in lung carcinoma. *J Exp Med* **202**, 931-939 (2005).

192. Geiger, R. et al. L-Arginine Modulates T Cell Metabolism and Enhances Survival and Antitumor Activity. *Cell* **167**, 829-842.e13 (2016).

193. Bronte, V., Serafini, P., Mazzoni, A., Segal, D. M. & Zanovello, P. L-arginine metabolism in myeloid cells controls T-lymphocyte functions. *Trends Immunol* **24**, 302-306 (2003).

194. Newman, A. M. et al. Robust enumeration of cell subsets from tissue expression profiles. *Nat Methods* **12**, 453-457 (2015).

195. Hildner, K. et al. Batf3 deficiency reveals a critical role for CD8alpha^{+} dendritic cells in cytotoxic T cell immunity. *Science* **322**, 1097-1100 (2008).

196. Ugel, S. et al. Immune tolerance to tumor antigens occurs in a specialized environment of the spleen. *Cell Rep* **2**, 628-639 (2012).

197. Beatty, G. L. et al. Exclusion of T Cells From Pancreatic Carcinomas in Mice Is Regulated by Ly6C(low) F4/80(+) Extratumoral Macrophages. *Gastroenterology* **149**, 201-210 (2015).

198. Joyce, J. A. & Fearon, D. T. T cell exclusion, immune privilege, and the tumor microenvironment. *Science* **348**, 74-80 (2015).

199. Spranger, S. Mechanisms of tumor escape in the context of the T-cell-inflamed and the non-T-cell-inflamed tumor microenvironment. *Int Immunol* **28**, 383-391 (2016).

200. Macosko, E. Z. et al. Highly Parallel Genome-wide Expression Profiling of Individual Cells Using Nanoliter Droplets. *Cell* **161**, 1202-1214 (2015).

201. Spitzer, M. H. & Nolan, G. P. Mass Cytometry: Single Cells, Many Features. *Cell* **165**, 780-791 (2016).

202. Calligaris, D. et al. Application of desorption electrospray ionization mass spectrometry imaging in breast cancer margin analysis. *Proc Natl Acad Sci U S A* **111**, 15184-15189 (2014).

203. Ullal, A. V. et al. Cancer cell profiling by barcoding allows multiplexed protein analysis in fine-needle aspirates. *Sci Transl Med* **6**, 219ra9 (2014).

204. Wagner, D. E. & Klein, A. M. Genetic screening enters the single-cell era. *Nat Methods* **14**, 237-238 (2017).

205. Gu, L. & Mooney, D. J. Biomaterials and emerging anticancer therapeutics: engineering the microenvironment. *Nat Rev Cancer* **16**, 56-66 (2016).

206. Shi, J., Kantoff, P. W., Wooster, R. & Farokhzad, O. C. Cancer nanomedicine: progress, challenges and opportunities. *Nat Rev Cancer* **17**, 20-37 (2017).

207. Casanova, J.L., Abel, L. & Quintana-Murci, L. Human TLRs and IL-1Rs in host defense: natural insights from evolutionary, epidemiological, and clinical genetics. *Annu. Rev. Immunol.* **29**, 447–491 (2011).

Appendix 1
The role of myeloid cells in cancer therapies (Engblom et al. NRC 2016)
Reprinted from Nature Reviews Cancer with permission.

The role of myeloid cells in cancer therapies

Camilla Engblom[1,2], Christina Pfirschke[1]* and Mikael J. Pittet[1]*

Abstract | Recent clinical trials have demonstrated the ability to durably control cancer in some patients by manipulating T lymphocytes. These immunotherapies are revolutionizing cancer treatment but benefit only a minority of patients. It is thus a crucial time for clinicians, cancer scientists and immunologists to determine the next steps in shifting cancer treatment towards better cancer control. This Review describes recent advances in our understanding of tumour-associated myeloid cells. These cells remain less studied than T lymphocytes but have attracted particular attention because their presence in tumours is often linked to altered patient survival. Also, experimental studies indicate that myeloid cells modulate key cancer-associated activities, including immune evasion, and affect virtually all types of cancer therapy. Consequently, targeting myeloid cells could overcome limitations of current treatment options.

Innate immune system
A system comprising various cell types that together provide defence to the host against infection and injury and orchestrate inflammatory responses. Unlike adaptive immune cells, innate immune cells express only germline-encoded pattern recognition receptors and generally they do not provide long-lasting immunity; however, they can activate the adaptive immune system through a process known as antigen presentation.

[1]Center for Systems Biology, Massachusetts General Hospital Research Institute and Harvard Medical School, Boston, Massachusetts 02114, USA.
[2]Graduate Program in Immunology, Harvard Medical School, Boston, Massachusetts 02115, USA.
**These authors contributed equally to this work.*
Correspondence to M.J.P.
mpittet@mgh.harvard.edu

doi:10.1038/nrc.2016.54
Published online 24 June 2016

Until the beginning of the twenty-first century, cancer was largely considered to be a cell-autonomous disease, with malignant growth driven by genetic mutations within tumour cells. More recently, it has become clear that heterotypic interactions between neoplastic and seemingly normal host cells also profoundly regulate cancer progression. Most notably, tumour-infiltrating T lymphocytes are now regarded as a key component of the tumour microenvironment because therapeutically activating these cells can durably control various cancer types[1]. These advances are not only revolutionizing cancer therapy but have also validated immune cell targeting as a relevant approach to fight human cancer. Considering that tumour microenvironments are home to diverse cell types[2] and that current immunotherapies benefit only a minority of patients[1], it is important to identify whether other components of the tumour microenvironment can be additional relevant therapeutic targets.

This Review focuses on myeloid cells, which belong to the innate immune system. Myeloid cells and their phagocytic activities were first discovered by Élie Metchnikoff[3] more than a century ago when his landmark starfish larvae microscopy studies showed that infection sites accumulate leukocytes that ingest and eliminate foreign material. In mammals, myeloid cells are among the most important defenders against infection. They are also essential in tissue homeostasis[4,5] and crucial in initiating, sustaining or inhibiting T cell immunity[6,7]. Emerging evidence indicates that myeloid cells affect cancer progression by interacting directly with tumour cells and indirectly by enabling a tumour stroma that promotes cancer growth[8–10]. The importance of myeloid cells in cancer is not entirely surprising: tumours do not use *de novo* mechanisms to interact with host components but instead employ pre-existing physiological programmes, particularly those involved with wound healing, that engage myeloid cells[11]. The interplay between myeloid cells and adaptive immunity is also emerging as an important regulator of cancer progression, with tumour-associated myeloid cells probably having an important role in cancer immune evasion.

Myeloid cells comprise various cellular subtypes and are operationally divided into mononuclear and polymorphonuclear cells (FIG. 1). Mononuclear phagocytes include macrophages, which reside in virtually all tissues, where they perform location-specific functions including the regulation of tissue homeostasis, immune surveillance and inflammation[12,13]. Mononuclear phagocytes also include dendritic cells (DCs), which consist of distinct subsets. Classic DCs (cDCs) form the predominant DC subset and are specialized to sample antigens in tissues and to migrate to local draining lymph nodes to induce antigen-specific T cell immunity or tolerance[6,7]; cDCs also control T cell responses within nonlymphoid tissues, including solid tumours[8,14]. Plasmacytoid DCs (pDCs) are another DC subset that is uniquely able to produce interferon-α (IFNα) and may also regulate cancer progression[15]. Macrophages and DCs can have various origins[5,16] but those that accumulate in tumours derive mostly from circulating precursors, called monocytes[17] and pre-DCs[18], respectively, which are themselves produced by bone marrow-derived haematopoietic stem cells (HSCs). Polymorphonuclear phagocytes,

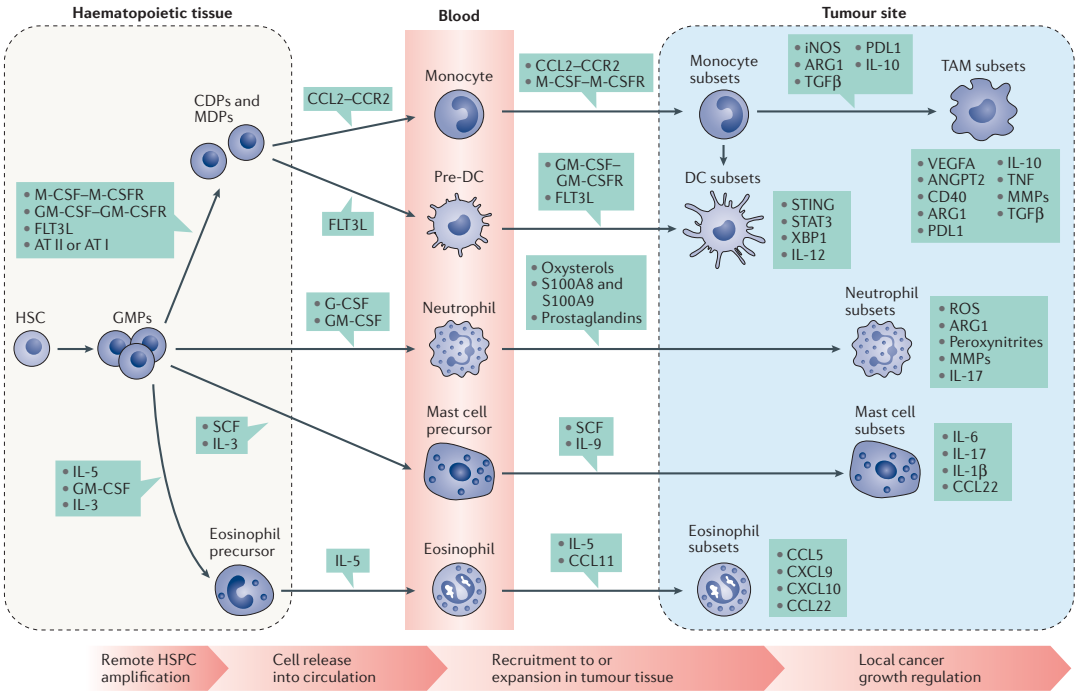

Figure 1 | **Developmental pathways of myeloid cells.** Discrete developmental activities control step-wise progression from haematopoietic stem cells (HSCs) to tumour-infiltrating myeloid cells. These activities occur in different body locations and include haematopoietic stem and progenitor cell (HSPC) amplification in haematopoietic tissues such as the bone marrow; release of the newly produced cells into peripheral blood; recruitment of the circulating precursors into the tumour stroma; and functional activities of the infiltrating cells within the tumour microenvironment. All these processes can be amplified or regulated by (distant) tumours. Molecular regulators of these processes are candidate drug targets to control myeloid cells as they progress along their developmental pathways. Myeloid-derived suppressor cells (MDSCs) can release factors shown here for neutrophils and/or monocytic cells. ANGPT2, angiopoietin 2; ARG1, arginase 1; AT, angiotensin; CCL, chemokine (C-C motif) ligand; CCR, C-C chemokine receptor; CDP, common dendritic cell progenitor; CXCL, chemokine (C-X-C motif) ligand; DC, dendritic cell; FLT3L, Fms-like tyrosine kinase 3 ligand; G-CSF, granulocyte colony-stimulating factor; GM-CSF, granulocyte–macrophage colony-stimulating factor; GM-CSFR, GM-CSF receptor; GMP, granulocyte–macrophage progenitor; IL, interleukin; iNOS, nitric oxide synthase 2, inducible; M-CSF, macrophage colony-stimulating factor; M-CSFR, M-CSF receptor; MDP, monocyte and dendritic cell progenitor; MMPs, matrix metalloproteinases; PDL1, programmed cell death 1 ligand 1; ROS, reactive oxygen species; SCF, stem cell factor; STAT3, signal transducer and activator of transcription 3; STING, stimulator of interferon genes; TAM, tumour-associated macrophage; TGFβ, transforming growth factor-β; TNF, tumour necrosis factor; VEGFA, vascular endothelial growth factor A; XBP1, X-box binding protein 1.

often referred to as granulocytes, also derive from HSCs and include neutrophils, eosinophils, mast cells and basophils. These cells can accumulate in diseased sites where they release toxic and inflammatory agents that protect the host against various insults, including bacterial and parasitic infections[19–21]. So-called myeloid-derived suppressor cells (MDSCs) broadly include immature myeloid progenitors and monocyte- and granulocyte-like cells and are functionally defined based on their ability to suppress T cell activation *in vitro*[22]. MDSCs are viewed as distinct from terminally differentiated myeloid cells such as macrophages and DCs; however, it is important to recognize that macrophages can also exhibit T cell-suppressive activity[23,24]. The phenotypes of tumour-associated MDSCs can be distinct from those of resting monocytes and neutrophils; however, whether monocytes and neutrophils compared with MDSCs are different cell types or cellular states remains disputed and in appreciation of this complexity we discuss them together.

In this Review, we first summarize current knowledge on the various, and sometimes seemingly opposing, contributions of myeloid cells to cancer progression. We also highlight how these cells and their precursors are regulated locally and systemically by tumours. We then explore the ways in which myeloid cells are affected by anticancer drugs and influence treatment outcome. Finally, we discuss how myeloid cells can be targeted therapeutically and outline next-generation therapeutic

Macrophages
Differentiated cells of the mononuclear phagocyte lineage that can clear dead cells and foreign particles through a process called phagocytosis. Macrophages assume tissue- and microenvironment-specific phenotypes to regulate tissue homeostasis, immunity and inflammation; they are essential protectors against injury and infections but also contribute to many diseases, including cancer.

Dendritic cells
(DCs). Crucial antigen-presenting cells for immune control. DCs typically have a probing morphology and localize in T cell areas of lymphoid organs to activate specific $CD4^+$ and $CD8^+$ T cells, but they can also be found in nonlymphoid tissues, such as the tumour stroma.

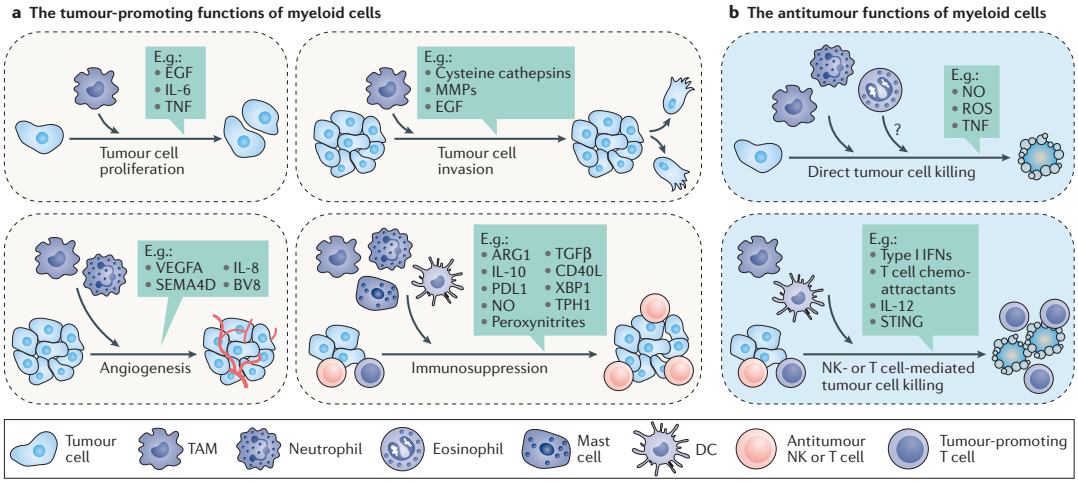

Figure 2 | **The tumour-promoting and antitumour functions of myeloid cells. a** | The tumour-promoting functions of myeloid cells include direct stimulation of tumour cell proliferation by cytokines and growth factors, enhanced tumour vascularization by angiogenic stimulators, increased tumour cell invasion by secreting enzymes and other factors and suppression of antitumour natural killer (NK) cells or T cells by various intracellular, cell surface and secreted factors. **b** | The antitumour functions of myeloid cells include: direct tumour cell killing by cellular signalling molecules and induction of tumour cell elimination by other cells, including NK and $CD8^+$ T cells. ARG1, arginase 1; DC, dendritic cell; EGF, epidermal growth factor; IL, interleukin; IFNs, interferons; MMPs, matrix metalloproteinases; NO, nitric oxide; PDL1, programmed cell death 1 ligand 1; ROS, reactive oxygen species; SEMA4D, semaphorin 4D; STING, stimulator of interferon genes; TAM, tumour-associated macrophage; TGFβ, transforming growth factor-β; TNF, tumour necrosis factor; TPH1, tryptophan 5-hydroxylase 1; VEGFA, vascular endothelial growth factor A; XBP1, X-box binding protein 1.

Monocytes
Bone marrow-derived mononuclear phagocytes, crucial in protection against infections and in immune homeostasis, which when deployed to tissues can differentiate into a macrophage, and under certain conditions, a dendritic cell. Monocytes are typically divided into two subtypes: patrolling monocytes and inflammatory monocytes.

Neutrophils
Polymorphonuclear cells that develop and mature in the bone marrow, exist at high numbers in circulation and can be rapidly recruited to a site of injury or inflammation. Neutrophils can release potent biologically active antimicrobial enzymes, which are directly involved in clearance of infection.

Eosinophils
Granulocytic cells that are known mostly for their involvement in asthmatic disease and parasitic infections. Eosinophils are found primarily in the circulation, gut and thymic tissue but can be rapidly deployed into various tissues during inflammation to expel their granular content.

approaches that could better exploit myeloid cells to more effectively tailor treatment options for individual patients. Our overall goal is to guide readers, with nuance and cautious optimism, through the current understanding of myeloid cells in both human and mouse cancers.

Tumour-infiltrating myeloid cells

The definition of whether myeloid cells are relevant to cancer is currently largely based on two types of investigation. First, pathologists have begun to address whether the presence of tumour-infiltrating myeloid cells can predict patient outcomes. Typically, these studies are based on immunohistochemical analysis of tumour biopsies and are performed at the time of diagnosis (that is, in the absence of treatment). The results provide correlative, but not causative, links between myeloid cell content in the tumour stroma and disease progression. Furthermore, these data depend on a limited set of cellular markers that are seldom cell-type specific and may vary considerably across tissues and cancer types[25]. Nonetheless, these studies provide a window into myeloid cell involvement in human cancer, and the information obtained has diagnostic, prognostic and therapeutic potential. Second, animal and *in vitro* studies have started to investigate how myeloid cells regulate tumour progression. These investigations generally position myeloid cells as tumour-promoting components, with notable exceptions.

Macrophages. Tumour-associated macrophages (TAMs) frequently emerge as abundant immune cells in the tumour stroma in a broad range of cancers. However, the heterogeneity of macrophages[12,26,27] makes it challenging to define specific markers for these cells and additional methods are needed to accurately identify them. Currently, the intracellular glycoprotein CD68 is widely used in clinical studies as a TAM marker but it also detects other cell types[28,29] and does not identify the functional states of cells. The scavenger receptor CD163 (also known as M130 in humans) is also used to define TAMs, sometimes with concomitant CD68 staining. Studies using these markers revealed a significant association between high densities of TAM-like cells and poor prognosis in numerous cancer types including breast, thyroid, head and neck, liver, bladder, kidney, pancreatic, ovarian, oral, endometrial and lung cancer, as well as Hodgkin lymphoma[25,30,31].

These pathology findings are in accord with animal studies that show that TAMs can enhance cancer growth by producing mediators that shape the tumour microenvironment (FIG. 2a). Such mediators include growth factors and cytokines that support tumour cell survival and proliferation (for example, epidermal growth factor (EGF), interleukin 6 (IL-6) and tumour necrosis factor (TNF))[10,23]; extracellular matrix degrading enzymes (for example, matrix metalloproteinases (MMPs) and cysteine cathepsins) and other factors that modulate tissue architecture and favour tumour cell migration,

Mast cells
Crucial innate effector cells that are rich in granules that contain various immunoregulatory molecules. Upon stimulation by pathogens, allergens or endogenous factors, mast cells can rapidly degranulate and profoundly affect local and systemic tissue homeostasis, as exemplified by anaphylaxis.

Basophils
Circulating granulocytic cells known to mediate allergic responses and host defence against parasitic infections. Basophilic granules are a rich source of inflammatory mediators, including the vasodilator histamine and the anticoagulant heparin.

Tertiary lymphoid structures
Ectopic lymph node-like arrangements that form in tissues under pathophysiological conditions and that seem to facilitate local lymphocyte activation.

invasion and metastasis[32–34]; and pro-angiogenic agents that enable nutrient and oxygen delivery to tumours (for example, vascular endothelial growth factor A (VEGFA), IL-8 and semaphorin 4D (SEMA4D))[23,35,36]. TAMs can also promote cancer immune evasion by expressing cell surface proteins and releasing soluble factors that display immunosuppressive functions and blunt antitumour immunity (for example, arginase 1 (ARG1), IL-10, programmed cell death 1 ligand 1 (PDL1) and transforming growth factor-β (TGFβ))[23,24,37].

However, clinical studies also suggest that TAMs may have divergent functions[25]. For instance, high densities of CD68$^+$ cells have been associated with improved survival in colon[38], gastric[39] and endometrial[40] cancer. The functional state of TAMs may help to define whether these cells promote or suppress tumours. Indeed, macrophages can display a spectrum of activation states that fulfil specific functions and are often catalogued as classically (M1) or alternatively (M2) activated cells. Both M1-like and M2-like cells can have protective functions, for example, by eliminating intracellular bacteria and controlling parasite infections, respectively. These two macrophage populations are often distinguished based on their inducing stimuli (for example, Toll-like receptor (TLR) ligands and IFNs for M1 cells and IL-4, IL-10, TGFβ and glucocorticoids for M2 cells) or their secretion profiles and transcriptional activity (for example, expression of *Il12*, nitric oxide synthase 2, inducible (*Nos2*; which encodes iNOS), macrophage receptor with collagenous structure (*Marco*), suppressor of cytokine signalling 3 (*Socs3*) for M1 cells; *Rela*, *Socs2*, Krüppel-like factor 4 (*Klf4*) and *Arg1* for M2 cells)[13,41,42]. Categorizing macrophages based on these signatures has limitations[27] — for instance, because M1 and M2 profiles are artificial *in vitro* extremes and TAM phenotypes typically go beyond simple M1 and M2 denominations — yet it has enabled an insight into the role of macrophages during physiological and disease processes. In growing tumours, TAMs often show M2-like phenotypes[24], which foster tumour cell growth and invasion, enhance tumour angiogenesis and blunt antitumour T cell functions. In mice, perivascular CD163$^+$ TAMs have been identified as cells expressing alternative activation markers, whereas some CD163^{lo} TAMs in necrotic tumour regions activate inflammatory pathways[43]. It is possible that some M1-like macrophages are involved in cancer control by directly killing tumour cells, producing angiostatic factors and/or stimulating antitumour T cell functions[44–46] (FIG. 2b). In support of these ideas, M2-like TAMs, compared with M1-like TAMs, were associated with less favourable prognosis in a pan-cancer analysis[47]. More sensitive characterization of TAM phenotypes and functions is needed to clarify whether the M1 and M2 classification is sufficient to predict pro-tumoural versus anti-tumoural TAM functions in various cancer types.

Dendritic cells. Unlike TAMs, DCs are not abundant at the tumour site but must be considered because they can efficiently present extracellular antigens on major histocompatibility complex (MHC) class I molecules to enable antitumour CD8$^+$ T cell activation[8] (FIG. 2b). Accordingly, high densities of tumour-infiltrating DCs, particularly cDCs, may be beneficial[48,49]. In lung cancer, high cDC densities are associated with increased T cell activation[48,50]. Additionally, activated cDCs and T cells can cluster within tertiary lymphoid structures in tumours from patients with lung cancer[49], a pattern that provides further evidence for DC–T cell interactions at tumour sites.

The relative abundance of anti-tumoural versus pro-tumoural DCs and the degree to which tumours co-opt DCs may vary between individuals and cancer types. In support of this idea, a rare tumour-infiltrating CD103$^+$ (CD103 is also known as integrin αE) cDC population seems poised to cross-present antigens and activate CD8$^+$ T cells in several mouse models[51]. Additionally, an elevated ratio of CD103^{hi}/CD103^{lo} expression in the tumour stroma is associated with increased overall survival for patients with breast, head and neck or lung cancer[51]. CD103$^+$ DCs, although sparsely distributed in the tumour stroma, may thus display distinct antitumour immune functions.

Simultaneously, tumours can suppress the antitumour activity of DCs[52]. For example, ovarian tumour cells in mice can activate the transcription factor X-box binding protein 1 (XBP1) in DCs, thereby rendering them dysfunctional[53]. XBP1 induces an endoplasmic reticulum stress response that enables oxidized lipids to accumulate in DCs and blunts T cell priming by these DCs[53] (FIG. 2a). DC functions can also be suppressed upon activation of the β-catenin signalling pathway in cancer cells[54], by tumour-derived cyclooxygenases[55] and by IL-10-producing TAMs[56].

Besides cDCs, pDCs can also accumulate in the tumour stroma; however, tumour-infiltrating cDCs and pDCs may have divergent functions. Interestingly, high CD123$^+$ (CD123 is also known as IL3Rα) pDC content in breast tumour biopsies correlated with decreased 5-year overall and relapse-free survival[57]. Similar results were reported for patients with melanoma[58].

There is an urgent need to be able to identify antitumour DCs in a broad range of cancer patients. Most likely, these DCs are rare and share attributes with other DC subsets; therefore, their characterization will require a careful assessment of DC functional states that goes beyond generic DC surface markers. Also, because mouse and human DCs express different markers[59,60] it will be important to define whether findings hold true across species.

Neutrophils, monocytes and MDSCs. The abundance of tumour-infiltrating neutrophils, monocytes and MDSCs is associated with advanced cancer stage and decreased disease-free and overall survival in patients with various tumour types, including lung adenocarcinoma, breast cancer and colorectal carcinoma[47,61]. Similarly, elevated levels of circulating monocytes[62,63], neutrophils[62,63] and MDSCs[64] often correlate with poorer clinical outcome. Mouse monocytes can be operationally divided into lymphocyte antigen 6 complex, locus C (Ly6C)^{lo} cells, which patrol the vasculature at steady state and clear damaged endothelial cells, and Ly6C^{hi} cells, which can differentiate into macrophages or DCs upon extravasation into

diseased tissues[17]. Many tumours in mice selectively expand Ly6C^{hi} monocytes, which seed tumour-promoting TAMs[37,65–67]. By contrast, Ly6C^{lo} monocytes are typically not expanded by tumours but may suppress metastasis, as discussed below.

In mice, both Ly6C^{hi} monocytic and granulocytic cells are positive for CD11b (also known as integrin αM) and Gr1 (a cell surface antigen that comprises both Ly6C and Ly6G epitopes). These markers are also used to define MDSCs, which can suppress antitumour T cells to varying degrees[22,68]. Key myeloid-mediated T cell suppressive mechanisms include secretion or expression of immunoregulatory factors, including ARG1 (REF. 69), nitric oxide (NO)[70], PDL1 (REF. 37), TGFβ[71] and cyclooxygenase 2 (COX2; also known as PTGS2)[72] among others[10]. These myeloid cells also produce reactive oxygen species (ROS) and peroxynitrite, which can interfere with MHC–T cell interactions[73], suppress T cell migration[74] and activate regulatory T cells (T_{reg} cells) via CD40–CD40L interactions to induce tolerance to tumour cell-expressed antigen[75] (FIG. 2a). Monocytic cells may preferentially use NO and cytokines to suppress immune responses, whereas granulocytic cells seem to preferentially use ROS[10].

In addition to suppressing antitumour immunity, neutrophils may promote tumour growth by limiting cancer cell senescence[76], promoting angiogenesis[77], triggering thrombosis via neutrophil extracellular traps[78], inducing genotoxic damage[79] and recruiting other tumour-promoting cells[80]. Because it is challenging to distinguish MDSCs from neutrophils and monocytes in both humans and mice[68], many functions attributed to MDSCs may apply to neutrophils and/or monocytes, and vice versa.

Neutrophils and monocytes may also limit tumour progression in certain settings[81] (FIG. 2b). For example, neutrophils can display anti-tumoural cytotoxic activities in some mouse models of cancer[82,83] and promote T cell activation when retrieved from patients with early-stage lung cancer[84]. Taken together, these studies demonstrate that neutrophils and monocytes are likely to be important modulators of tumour growth, but their tumour-associated functions may diverge. Our understanding of the mechanisms that determine whether neutrophils and monocytes will accelerate or restrict tumour growth in human cancer patients remains limited, but might depend on several factors, such as tumour stage and the local tissue microenvironment.

Other tumour-infiltrating myeloid cells. Although their tumour-associated functions remain much less studied, eosinophils and mast cells are other granulocytes that may regulate cancer progression. Intriguingly, the presence of tumour-infiltrating eosinophils, or their local degranulation, has been associated with favourable prognosis in oral squamous cell carcinoma and prostate and colon cancer[85,86], and tumour infiltration by eosinophils can suppress metastatic melanoma progression in mice[87]. Eosinophils may secrete cytotoxic proteins with direct anti-tumoural activities[85] and promote anti-tumour CD8$^+$ T cell immunity at least in some contexts[88] (FIG. 2b). In contrast to eosinophils, mast cells are often viewed as tumour-promoting cells[89]. For example, mast cells produce tryptophan 5-hydroxylase 1 (TPH1), which exhausts tryptophan. Such nutrient deprivation liberates immunoregulatory metabolites and thereby promotes immune suppression[90]. Mast cells may foster tumour outgrowth by activating cancer-promoting T_{reg} cells (which suppress antitumour immunity)[91–93], monocytes and neutrophils[93,94] and B cells[89] in mice (FIG. 2a). In support of these results, tumour infiltration by mast cells was linked to poorer disease outcome in patients with colorectal cancer[95]. However, other reports show conflicting results[96,97], which may reflect the divergent functions of mast cells during tumour progression or in different tumour microenvironments, as discussed above for other types of myeloid cell. Additionally, most mouse studies have used *Kit*-mutant genetic mouse models which, in addition to lacking mast cells, have KIT-dependent anomalies such as anaemia and sterility (*Kit*$^{W/Wv}$ mutant mice) or the less severe splenic myeloid and megakaryocytic hyperplasia (*Kit*$^{W-sh/W-sh}$ mutant mice)[98]. New Cre recombinase-based models of mast cell deficiency circumvent this issue[99,100]. Using one of these models, mast cells were reportedly dispensable for tumour growth in genetically induced oncogenic *Kras*^{G12D}-driven pancreatic cancer[101]. Whether this is true for other tumour types, or patients, requires investigation.

Myeloid cells have emerged as crucial regulators of tumour progression, but our ability to distinguish tumour-promoting versus inhibitory cells in patients remains a major challenge for all myeloid cell subsets. Future analyses of clinical samples should aim to go beyond 'cell types' and instead focus on cellular functions; this may be achieved by harnessing recent technological advances, as discussed further in the Perspectives section below.

Systemic tumour–myeloid cell interplay

As cancer is a systemic disease, we extend our discussion of tumour–myeloid cell interactions to the entire body. We first examine how some tumours affect myeloid cell components well beyond the local tissue microenvironment and then consider how myeloid cell subsets in various body compartments can regulate tumour cell dissemination and metastasis.

The systemic impact of cancer on myeloid cells. Besides unravelling crucial anti- and pro-tumoural interactions between myeloid cells and cancer cells within the local tumour microenvironment, research during the past decade has revealed that tumours can regulate myeloid cells before they enter the tumour stroma (FIG. 3). Indeed, whereas many tissue macrophages are produced during embryogenesis and are maintained in adults[102], circulating monocytes contribute the vast majority of TAMs in mouse mammary[65] and lung[67] tumours and TAMs can be continually and rapidly replaced during cancer progression[65–67]. TAMs may proliferate in some tumours[103], although TAM amplification is contributed mostly by circulating precursor recruitment[65–67,103]. Animal studies further indicate that the macrophage colony-stimulating

Regulatory T cells
(T_{reg} cells). Specialized T cells that are functionally defined by their ability to confer peripheral tolerance to self, commensal and environmental antigens. T_{reg} cell accumulation in tumours can suppress antitumour immunity and is associated with poor prognosis in many cancers.

Degranulation
Release of cytotoxic and other molecules from secretory vesicles, also called granules, that are initially stored in some innate immune cells, for example, neutrophils, eosinophils and mast cells.

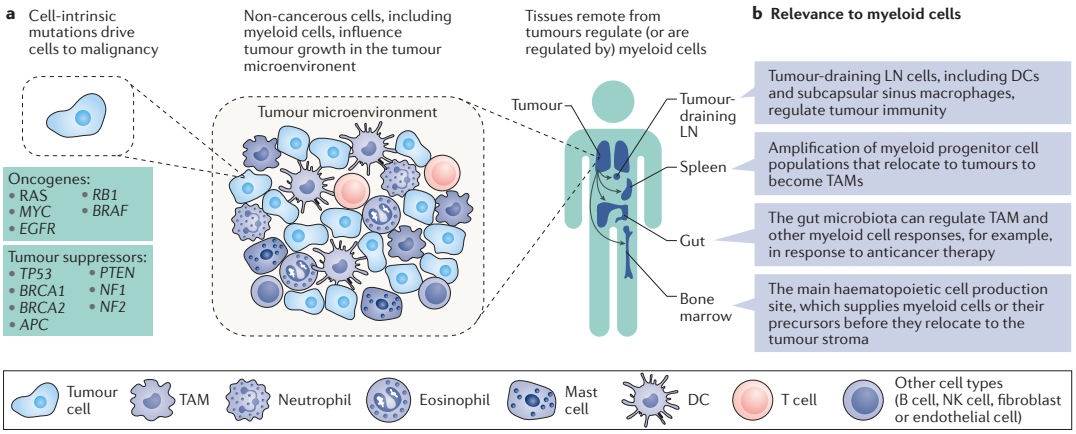

Figure 3 | **Cell-intrinsic, local and systemic regulation of cancer. a** | Cancer can be analysed at different levels and scales. Whereas tumour cell-intrinsic mutations are important drivers of tumour progression (left panel), tumour microenvironment host cells, including T cells and myeloid cells, also alter tumour growth (middle panel). Additionally, whole-body dynamics of anti- and pro-tumoural responses become important when considering that most tumour-infiltrating myeloid cells are continuously replaced by recruited circulating precursors and that immune responses are controlled in tissues distant from the tumour (right panel). Note that lung cancer is used here as a representative tumour stroma. **b** | Listed here are tissues that regulate myeloid cell production or participation in tumour-associated processes. APC, adenomatous polyposis coli; DC, dendritic cell; EGFR, epidermal growth factor receptor; LN, lymph node; NF, neurofibromin; NK, natural killer; RB1, retinoblastoma 1; TAM, tumour-associated macrophage.

factor (M-CSF)–M-CSF receptor (M-CSF–M-CSFR; also known as CSF1–CSF1R) and C-C motif chemokine ligand 2–C-C motif chemokine receptor 2 (CCL2–CCR2) pathways are crucial regulators of TAM recruitment and maintenance. The CCL2–CCR2 pathway is a central axis of TAM recruitment because it not only attracts circulating monocytes to tumours[104,105] but also mobilizes bone marrow-derived monocyte precursors to the periphery[66,106]. Similarly, M-CSF overexpression accelerates TAM recruitment and tumour growth, whereas genetic ablation of M-CSF reduces TAM density and delays tumour progression to malignancy[107,108]. Correspondingly, human studies revealed positive associations between CCL2 and/or M-CSF overexpression and poor prognosis in many cancer types, including breast[109,110], pancreatic[111], colorectal[112], hepatocellular[113] and endometrial[114] tumours. Also, myeloid chemoattractants are elevated in human tumours[110,113,115] and increased numbers of monocytes in peripheral blood correlate with poorer survival of cancer patients[63]. In contrast to TAMs, subcapsular sinus macrophages do not derive from circulating monocytes and can suppress melanoma progression in mice by physically limiting the systemic spread of tumour-derived vesicles in tumour-draining lymph nodes[116].

In comparison with macrophages, less is known about the origins and recruitment of other tumour-infiltrating myeloid cells, although many of them probably derive from circulating cells[7]. In the absence of disease, most DCs originate from circulating pre-DCs. In tumour-bearing mice, adoptively transferred pre-DCs can also produce tumour-infiltrating DCs[18]. Furthermore, mammary tumour DCs can be maintained independently of M-CSF[51], suggesting that these cells have a monocyte-independent origin. Different tumour-associated DC populations may be maintained by distinct developmental and amplification mechanisms. In mammary tumours, overexpressed Fms-related tyrosine kinase 3 ligand (FLT3L), a cytokine that is structurally similar to M-CSF, selectively expands CD103$^+$ DCs[51], whereas granulocyte–macrophage colony-stimulating factor (GM-CSF) amplifies tumour-infiltrating CD103$^-$ DCs. CD103$^+$ and CD103$^-$ DCs also depend on the expression of distinct transcription factors: zinc finger and BTB domain-containing protein 46 (*Zbtb46*), interferon regulatory factor 8 (*Irf8*) and basic leucine zipper transcriptional factor ATF-like 3 (*Batf3*) control CD103$^+$ DCs whereas *Irf4* expression controls their CD103$^-$ counterparts[117–120]. Accordingly, *Batf3* is required to produce DCs that promote antitumour immunity and control tumour progression in mice[119]. Monocytes also produce bona fide DCs in some inflammatory conditions[121]. Tumour-infiltrating neutrophils turn over within days in mouse models[122]; tumoural and/or systemic accumulation of these cells and other granulocytes is regulated by growth factors (for example, G-CSF, GM-CSF and VEGFA)[10,123,124] and various other components (for example, S100A8, S100A9, high mobility group protein B1 (HMGB1), oxysterols, IL-17 and prostaglandins)[10,122,125]. Some tumours also amplify myeloid cells or their precursors in remote body locations through various mechanisms, including the release of tumour-derived signals that extend far beyond the tumour stroma (BOX 1).

M-CSF–M-CSFR
(macrophage-colony stimulating factor and its receptor, also known as CSF1–CSF1R). A haematopoietic growth factor–receptor pair that is required for proper development, survival and maintenance of the monocyte and macrophage cell lineage.

CCL2–CCR2
(chemokine (C-C motif) ligand/receptor 2). A chemokine–receptor pair that mediates monocyte release from the bone marrow and, in the context of cancer, entry into the tumour microenvironment.

Premetastatic sites
Sites in which metastasis will occur. These sites are thought to be primed for tumour cell engraftment by factors that are secreted by the primary tumour and by bone marrow-derived haematopoietic cells that are recruited locally.

Natural killer (NK) cells
Cytotoxic lymphocytes that are crucial to the innate immune system and that provide rapid responses to eliminate abnormal cells, such as virus-infected cells and tumour cells.

The impact of myeloid cells on metastasis. Some tumour cells acquire the ability to invade their surrounding tissue, enter and survive in the circulation, extravasate into distant tissue and grow[126]. Myeloid cells may be involved at each step of the metastatic cascade. For example, mouse macrophages at primary tumour sites can promote tumour cell migration and entry into blood (FIG. 4a) via a paracrine EGF–M-CSF macrophage–tumour cell loop[127]. The presence of macrophages next to endothelial cells and tumour cells also predicts cancer metastatic behaviour in at least some subtypes of human breast cancer[128]. Additionally, TAMs can enhance tumour cell intravasation by producing VEGFA, which increases vascular permeability[32]. Once in the circulation, tumour cells can be scavenged by liver-resident macrophages through phagocytosis, which could help to reduce metastases[9,129] (FIG. 4b). However, macrophage-mediated phagocytosis of circulating cancer cells is limited by tumour cell upregulation of CD47, which binds to signal regulatory protein-α (SIRPα) on macrophages and functions as a 'do not eat me' signal[130,131]. Some myeloid cells at premetastatic sites also foster tumour cell seeding by promoting aberrant vascular formation[132] (FIG. 4c). Ly6C^{lo} 'patrolling' monocytes, which largely remain in the circulation, may prevent lung metastasis by scavenging tumour-derived material in the tumour microvasculature and attracting anti-tumoural natural killer (NK) cells locally[133]. However, Ly6C^{hi} 'inflammatory' monocytes, which differentiate into tumour-promoting TAMs, enhance lung metastasis in a CCL2- and VEGFA-dependent manner[104]. These findings highlight the distinct functions and tropisms of subsets of monocytes, and their opposing roles in metastasis. Neutrophils can also support tumour cell intravasation and seeding. For example, neutrophil secretion of leukotrienes, controlled by arachidonate 5-lipoxygenase (ALOX5), promotes mouse lung colonization by metastasis-initiating breast cancer cells[134]. Neutrophils also augment tumour cell intraluminal survival by suppressing NK cell antitumour activity and further facilitate tumour cell extravasation by secreting IL-1β and MMPs[135]. Neutrophils[125] and macrophages[136] further regulate metastasis outgrowth; for example, by suppressing antitumour immunity, although the function of these cells may vary[81,82] (FIG. 4d). The underlying mechanisms that govern anti- versus pro-tumour myeloid cell functions in the development of human metastases require investigation, but potentially have crucial implications for therapy.

Box 1 | **Myeloid cell production away from the tumour stroma**

Some tumours produce soluble factors that act over extended distances in the body to actively induce myeloid cell production from haematopoietic stem and progenitor cells (HSPCs)[123,124,187]. Studies in mice have identified that granulocyte colony-stimulating factor (G-CSF) expands haematopoietic stem cells and myeloid progenitors in the bone marrow and leads to the amplification of tumour-associated macrophages (TAMs) and other myeloid cells[123]. In cancer patients, haematopoiesis is also typically enriched and skewed towards myelopoiesis[226]. Elevated levels of circulating granulocyte–macrophage progenitors (GMPs) are found across different tumour types and high blood levels of GMPs correlate with poor survival[226]. The cellular fate and tissue destination of expanded progenitors cannot be easily addressed in patients; however, adoptive cell transfer studies in mice have shown that bone marrow-derived GMPs produce TAMs[51,67] and tumour-infiltrating dendritic cells (DCs)[51] in mouse models of lung and breast cancer. The bone marrow is the main site of haematopoiesis in the adult[227], but extramedullary tissues such as the spleen also contribute TAMs in a genetic mouse model of lung adenocarcinoma driven by *Kras*^{G12D} and loss of *Trp53* (KP mice)[67]. The spleen is a monocyte reservoir in mice[228] and humans[67,229], and mouse splenic monocytes can be mobilized to distant injured tissues[228,230] and tumours[67,187], where they differentiate into macrophages. Some cancer patients and tumour-bearing mice also amplify splenic HSPCs that can produce monocytes[231]. These findings support the existence of monocyte production both inside and outside the bone marrow in humans, although whether extramedullary tissues contribute a substantial number of TAMs (and/or other myeloid cells) in human cancer is unknown. Also, the bone marrow contains dynamic microenvironments that produce monocytes in both the steady state and inflammation, and spleen-derived macrophages are predominantly products of inflammation; yet, whether these niches generate functionally different cells requires study. Interestingly, the peptide hormone angiotensin II, which is overexpressed in KP tumour-bearing mice, specifically augments extramedullary TAM progenitors[187], suggesting that different molecular pathways regulate TAM production from medullary and extramedullary tissue. Medullary and extramedullary tissues can also contribute tumour-promoting neutrophils in mouse models of metastatic breast cancer[135]. Combined, these studies support the notion of cancer as a systemic disease: tumours control and are controlled by processes that occur both within and outside the local tumour microenvironment. Investigations that further probe long-range mechanisms of myeloid cell-mediated tumour control should reveal additional tumour–host communication pathways that could serve as new clinical targets.

Myeloid cells in cancer therapies

The relevance of myeloid cells to current cancer treatments remains largely unexplored, particularly in the clinical setting, although virtually all therapeutic modalities, including surgery, chemotherapy, radiotherapy, immunotherapy and targeted therapy, probably involve these cells. Notably, myeloid cells are required to clear killed tumour cells and orchestrate the healing response that follows treatment-induced cancer regression. Furthermore, emerging evidence indicates that myeloid cells and cancer treatments are linked at other, sometimes unexpected, levels and that these connections can strikingly influence treatment outcome, either positively or negatively (TABLE 1). Below, we discuss recent discoveries, obtained mostly from experimental studies, related to the interplay between myeloid cells and various cancer treatments.

Myeloid cells and cytotoxic therapies. Decades ago, radiotherapies and chemotherapies were developed to kill dividing tumour cells. These treatments remain the primary therapies for many cancer types even though their efficacy is often limited. Tumour microenvironment analysis in experimental mouse models suggests that TAMs and other phagocytes can negatively influence the outcome of cytotoxic treatment. For example, TAMs can promote drug resistance by producing cysteine cathepsins that protect tumour cells from being killed by the chemotherapeutic agent taxol[137] and by secreting the immunoregulatory cytokine IL-10, which impairs drug-induced CD103$^+$ DC accumulation in tumours and antitumour CD8$^+$ T cell activity[56]. Consequently, suppressing TAMs can improve therapy: M-CSFR targeting enhances radiotherapies against mouse prostate[138] and mammary[139] tumours and

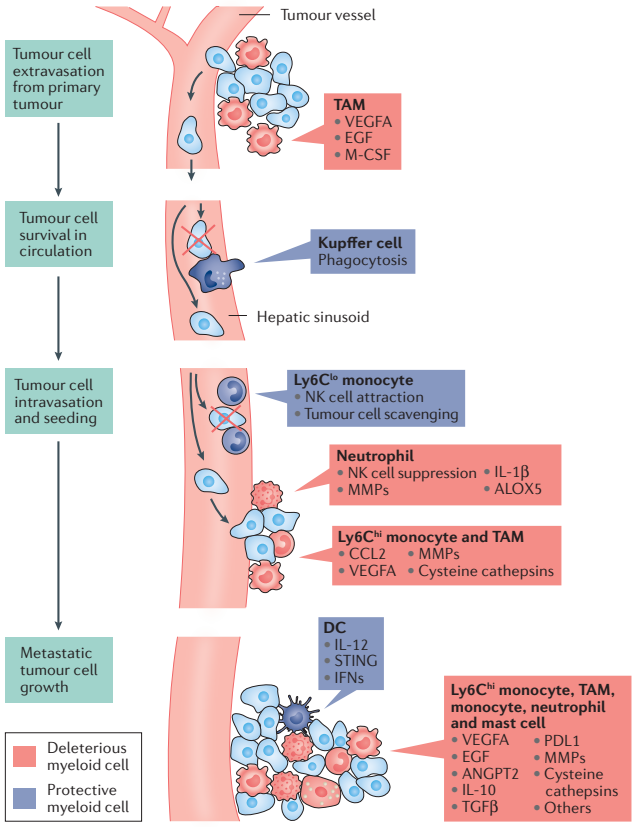

Figure 4 | **Myeloid cell regulation of metastasis.** To metastasize, tumour cells need to enter the bloodstream, survive in the circulation, extravasate and proliferate in distant tissues. Myeloid cells can both promote and limit these different steps. Some tumour-associated macrophages (TAMs) in primary tumours can increase vascular permeability and promote tumour cell migration and intravasation. Liver-resident macrophages (Kupffer cells) or other cells that filter blood, such as some macrophages in the spleen, may sample and reduce the number of circulating tumour cells. However, CD47 expression on tumour cells could at least in part explain the persistence of some tumour cells in circulation by acting as a 'do not eat me' signal to macrophages. Tumour cells exiting the bloodstream may interact with various myeloid cells. Lymphocyte antigen 6 complex, locus C ($Ly6C^{lo}$) monocytes may prevent metastasis by scavenging tumour-derived material and reducing tumour cell extravasation; $Ly6C^{lo}$ monocytes may not kill tumour cells directly but instead attract natural killer (NK) cells to accomplish this task. $Ly6C^{hi}$ monocytes and TAMs may instead favour metastasis by inducing the production of chemokines and growth factors. Neutrophils can also support metastasis initiation by suppressing antitumour NK cell activity and enhancing tumour cell extravasation and migration. Myeloid cells at metastatic sites can both promote and inhibit growth and persistence of metastatic cancer cells; similarly to their functions at primary tumour sites (FIG. 2). Cells in red and blue depict deleterious and protective myeloid cells, respectively. Specific factors or activities associated with defined myeloid cells are also listed. ALOX5, arachidonate 5-lipoxygenase; ANGPT2, angiopoietin 2; CCL2, chemokine (C-C motif) ligand 2; DC, dendritic cell; EGF, epidermal growth factor; IL, interleukin; IFNs, interferons; M-CSF, macrophage colony-stimulating factor; MMPs, matrix metalloproteinases; PDL1, programmed cell death 1 ligand 1; STING, stimulator of interferon genes; TGFβ, transforming growth factor-β; VEGFA, vascular endothelial growth factor A.

M-CSF blockade ameliorates paclitaxel treatment efficacy against mammary tumours in mice[140], indicating that these TAMs promote cancer. Neutrophils and/or MDSCs also seem to limit the efficacy of radiotherapy as depletion of $Ly6G^+$ cells can improve the outcome of irradiated mice bearing colon carcinoma[141].

The interplay between cytotoxic therapies and myeloid cells goes both ways: myeloid cells can regulate treatment efficacy but cytotoxic therapies can also control myeloid cells. For example, some chemotherapeutic agents may reduce the numbers of myeloid cells by eliminating them directly or by limiting bone marrow-derived myeloid progenitors. Accordingly, trabectedin[142], doxorubicin[143] and 5-fluorouracil[144] can control tumour growth not only by killing cancer cells but also by reducing the number of TAMs and other tumour-promoting phagocytes. For example, trabectedin selectively induces caspase-8-dependent apoptosis in monocytes and TAMs, which is probably due to a unique expression pattern of TNF-related apoptosis-inducing ligand (TRAIL) receptors in these cells[142]. Instead, some chemotherapeutic agents may amplify myeloid cells. For example, paclitaxel increases TAM accumulation in mammary tumours in mice by stimulating M-CSF production by mammary epithelial cells[140]. This process is relevant to treatment because M-CSF blockade in combination with paclitaxel improves survival. Also, we have limited knowledge of the impact of drug treatment on the dynamics between TAMs and their progenitors but it is possible that reactivated haematopoiesis after drug clearance[145] transiently accelerates TAM production in myeloablated hosts.

Although these findings suggest that suppressing TAMs can improve cytotoxic chemotherapies, complete TAM elimination may be undesirable in some contexts. For example, local irradiation of tumours with low-dose ionizing radiation in a transgenic mouse model of pancreatic cancer stimulates $iNOS^+$ TAM accumulation; these cells may help to normalize the tumour vasculature and promote T cell influx into otherwise non-T cell-infiltrated tumours, thereby improving tumour control and mouse survival[146]. Furthermore, platinum-based oxaliplatin treatment against various mouse cancer models triggers TAMs and neutrophils to produce ROS[147], which mediate DNA damage and apoptosis. Oxaliplatin therapy response in a transplantable model of colon carcinoma requires both Toll-like receptor 4 (TLR4), which is expressed by myeloid cells, and an intact microbiota, suggesting the importance of myeloid cell–microbiota interactions in regulating drug effects[147]. Additionally, TAMs may be useful drug depots because they can accumulate large quantities of nanoparticles containing cytotoxic compounds and then release their payload to neighbouring tumour cells[148]. These TAMs are beneficial to the host because TAM depletion reduces treatment efficacy[148].

Tumour-infiltrating DCs are typically thought to improve cytotoxic therapies. For example, oxaliplatin and several anthracyclines can kill tumour cells through a process called immunogenic cell death, which involves ATP and HMGB1 release as well as calreticulin surface expression by dying tumour cells[149]. These effector

Table 1 | **Protective and deleterious contributions of TAMs and DCs to anticancer therapies**

	Protective myeloid cell contributions	Deleterious (but therapeutically targetable) myeloid cell contributions
Chemotherapy	• Chemotherapy promotes antitumour DC recruitment to tumours[150] • Chemotherapy-induced differentiation or infiltration of antigen-presenting cells stimulates antitumour T cell immunity[153,154] • Macrophages can be drug depots for nanotherapeutics[148]	• TAM suppression by IL-10R blockade improves chemotherapy[56] • TAM suppression by CCR2 or M-CSFR blockade improves chemotherapy[140,184] • Inhibition of TAM-derived cysteine cathepsins improves chemotherapy[137]
Radiotherapy	• Ionizing radiation induces antitumour adaptive immunity via STING and type I IFN-dependent signalling in DCs[156] • Local low-dose ionizing radiation instigates macrophage differentiation into iNOS$^+$ M1-like cells that support antitumour T cell immunity[146]	• TAM suppression by M-CSFR blockade improves radiotherapy[138,139] • Irradiation-induced intratumoural SDF1α recruits cancer-promoting TAMs[232]
mAb-based immunotherapy	• CD20 mAb-mediated removal of tumour cells depends on Fc receptors expressed by phagocytes[160,161,233] • CD40 mAb-mediated control of pancreatic tumours involves activation of tumoricidal macrophages[195] • Successful CTLA4 mAb therapy involves phagocyte-mediated T_{reg} cell depletion[164,165,234]	• TAM reprogramming by M-CSFR inhibition improves immune checkpoint blockade therapy[169] • PDL1 blockade on monocytes augments antitumour immunity[37] • Depletion of extratumoural macrophages enhances CD40 mAb therapy[235]
Adoptive cell immunotherapy	• Successful adoptive T cell therapy requires CD103$^+$ DCs[51] • DC adoptive transfer instigates tumour infiltration by T cells and sensitizes tumours to anti-PDL1 and anti-CTLA4 therapies[54]	TAM suppression by M-CSFR blockade improves adoptive cell therapy[236,242]
Small-molecule based therapy	• JAK2–STAT3 targeting causes DC activation and differentiation[178] • Histidine-rich glycoprotein-polarized TAMs promote antitumour immunity and vessel normalization[237] • KIT inhibition stimulates antitumour NK cell activation via DCs[238] • MEK and BRAF inhibitors revert BRAF-mutated melanoma-induced DC suppression[176,177] • Bortezomib stimulates DCs to induce antitumour T cell immunity[239]	• Inhibition of TNF production by macrophages improves therapies that target the MAPK pathway[171] • Inhibition of VEGFA production by macrophages improves BRAF inhibitor treatment[172] • TAM suppression by M-CSFR blockade improves BRAF inhibitor therapy by increasing antitumour immunity[173] • M-CSFR blockade controls TAM recruitment and improves antiangiogenic therapy[240] • TAM depletion improves tyrosine protein kinase inhibitor therapy[241]

CCR2, chemokine (C-C motif) receptor 2; CTLA4, cytotoxic T lymphocyte-associated antigen 4; DC, dendritic cell; IFN, interferon; IL, interleukin; iNOS, nitric oxide synthase 2, inducible; JAK2, Janus kinase 2; mAb, monoclonal antibody; M-CSFR, macrophage colony-stimulating factor receptor; NK cell, natural killer cell; PDL1, programmed cell death 1 ligand 1; SDF1α, stromal-derived factor 1α; STAT3, signal transducer and activator of transcription 3; STING, stimulator of interferon genes; TAM, tumour-associated macrophage; TNF, tumour necrosis factor; T_{reg} cell, regulatory T cell; VEGFA, vascular endothelial growth factor A.

molecules modulate DCs: ATP release results in DC recruitment into the tumour bed[150], calreticulin stimulates tumour antigen engulfment by DCs[151] and HMGB1 enhances the capacity for antigen presentation by DCs to T cells[152]. In mouse models, anthracyclines stimulate tumour infiltration by CD11b$^+$ CD11c$^+$ Ly6C^{hi} DC-like cells that are necessary for treatment efficacy[153]. Because these antitumour cells do not require *Batf3* (REF. 153), they instead may derive from inflammatory monocytes[121]. Similarly, chemotherapies can increase HMGB1 levels in mouse lung tumours and induce tumour infiltration of DC-like myeloid subsets[154]. Radiotherapies can also trigger tumour infiltration by DC-like cells that foster antitumour T cell immunity[155–157].

Myeloid cells and monoclonal antibody-based immunotherapies. Harnessing the immune system can durably control cancer in some patients while limiting side effects[1]. In the years to come, immunotherapy will probably become the backbone of cancer treatment, as either monotherapy or as part of combination therapies. Many immunotherapy approaches involve immunoglobulin G (IgG) monoclonal antibodies (mAbs) that can either target cancer cells (for example, rituximab targets CD20$^+$ non-Hodgkin lymphoma cells), stimulate antitumour T cell immunity (for example, nivolumab and pembrolizumab antagonize the T cell immune-checkpoint receptor programmed cell death protein 1 (PD1; also known as PDCD1)) or inhibit angiogenesis (for example, bevacizumab targets VEGFA)[158]. Some of these therapeutic mAbs may directly control tumours by inducing apoptosis or inhibiting cell proliferation, but others depend on additional host components, such as complement cascade proteins and Fcγ-receptor (FcγR)-positive cells[158]. Indeed, IgG mAbs contain a variable Fab domain that confers binding specificity but also a constant Fc domain that bridges antibody-coated targets with FcγR$^+$ cells, which include macrophages and DCs[158,159].

FcγRs can be either activating or inhibitory. Cross-linking activating receptors (namely, FcγRI, FcγRIIA, FcγRIIC and FcγRIIIA in humans and FcγRI, FcγRIII and FcγRIV in mice) on the phagocyte surface can trigger cytotoxic or phagocytic elimination of mAb-coated target cells. This process probably contributes to the *in vivo* activities of many therapeutic mAbs[158,159]. For example, rituximab depletes non-Hodgkin lymphoma cells via FcγR-mediated monocyte and macrophage cytotoxicity[158,160]. Similar mechanisms occur with the mAbs trastuzumab (anti-ERBB2) and daratumumab (anti-CD38), which are used against ERBB2$^+$ breast

Fcγ-receptor
(FcγR). A surface-bound protein receptor expressed by phagocytes and other cell types, which binds to the constant heavy chain (Fc) region of an antibody and mediates cell clearance mechanisms. FcγRs, for which four different classes are known (FcγRI, FcγRII, FcγRIII and FcγRIV), bind to the Fc region of immunoglobulin G antibodies.

cancer[161] and multiple myeloma[162], respectively. In mice treated with antitumour mAbs, FcγR-mediated killing by Kupffer cells also eliminates circulating tumour cells that transit through the liver[129].

Similarly, engaging activated FcγRs expressed by myeloid cells influences the activities of T cell immune checkpoint blockers. Ipilimumab (anti-cytotoxic T-lymphocyte-associated antigen 4 (CTLA4)), which amplifies antitumour T cell activity while restricting immunosuppressive T_{reg} cells[163], reduces T_{reg} cell counts via FcγR-mediated phagocytosis[164]. Treatment-induced tumour control and T_{reg} cell depletion in mice both depend on FcγRIV, which is expressed by TAMs[164]. Also, patients with melanoma who respond to ipilimumab treatment have more FcγRIIIA$^+$ CD16$^+$ blood monocytes than non-responders[165]. The inhibitory receptor FcγRIIB, which is conserved in both humans and mice, also regulates mAb-based immunotherapies. Mice treated with agonistic CD40 mAbs require FcγRIIB crosslinking to stimulate myeloid cell maturation and activate CD8$^+$ T cells. This process controls cancer growth even in the absence of all activating FcγRs[166].

Taken together, these studies identify myeloid cells and FcγRs as important executors of responses to various immunotherapies, but FcγR-mediated activation may also have deleterious effects. As an example, endogenous IgGs can foster mouse squamous cell carcinoma progression by stimulating FcγRs on macrophages and mast cells[89]. Further investigation is needed to clarify how FcγR-mediated myeloid cell responses affect treatment outcomes and, by extension, how they can be harnessed for therapy. The results of FcγR engagement in a given microenvironment will probably be controlled by several variables, including the IgG Fc composition, the diversity of inhibitory and activating FcγRs engaged by IgGs, and the cell types expressing these FcγRs. Engineered mAbs that lack Fc domains, such as single-chain variable domain fragments[167], are considered for therapy in part because their reduced binding to FcγR$^+$ cells improves penetration into tumours; yet, how the absence of FcγR-mediated myeloid cell activation affects treatment outcome in humans requires study.

Myeloid cells may also influence mAb-based immunotherapies independently of FcγRs. First, Fab domains of some therapeutic mAbs can bind to tumour-infiltrating DCs and TAMs. PDL1 mAbs, for example, may control cancer growth at least in part by acting on PDL1$^+$ phagocytes[37,168]. Additionally, tumour-infiltrating DCs may be required for successful immunotherapies. In melanoma, active β-catenin signalling results in CD103$^+$ DC and T cell exclusion from the tumour stroma, but bone marrow-derived DCs injected into these tumours instigate T cell recruitment and sensitize tumours to anti-PDL1 and anti-CTLA4 therapy[54]. Also, immunogenic chemotherapeutics can upregulate TLR4 on tumour-infiltrating CD103$^+$ DC-like cells; TLR4$^+$ cells promote tumour infiltration by CD8$^+$ T cells, a process that sensitizes tumours to anti-CTLA4 or anti-PD1 therapy[154]. In contrast to tumour-infiltrating DCs, TAMs may antagonize immune checkpoint therapies. Indeed, inhibited M-CSFR signalling improves anti-CTLA4 and anti-PD1 therapy in mouse models of pancreatic cancer[169]. This indicates that agents that target myeloid cells and immune checkpoint blockers influence non-redundant mechanisms and can be more successful in combination. Manipulating TAM functions while boosting tumour-infiltrating DCs may further expand the proportion of patients who respond to current immunotherapies.

Myeloid cells and small-molecule based therapies. The development of small-molecule compounds that target cancers harbouring specific genetic alterations and/or molecular compositions has transformed cancer therapy. Genetic testing of somatic mutations is now a routine clinical procedure and an increasing number of molecularly targeted drugs are becoming available. These drugs can dramatically shrink tumours, but these effects are typically short-lasting. There is thus an urgent need to dissect the underlying tumour resistance mechanisms and find new avenues to improve the efficacy of small-molecule therapeutics. Myeloid cells may be relevant in both cases. Notably, in both human and mouse gastrointestinal cancers the tyrosine-kinase inhibitor imatinib induces M2 macrophage-associated genes and suppresses inflammatory cytokine production in TAMs[170], and genetically removing TNF in myeloid cells delays resistance to MAPK inhibitors in a mouse model of BRAF-driven melanoma[171]. Consequently, blocking M-CSFR signalling improves the efficacy of BRAF inhibitors[172] and extends survival in melanoma-bearing mice[173]. Blocking M-CSFR signalling similarly ameliorates antiangiogenic drug efficacy against mouse lung carcinomas[174]. Inhibition of the hepatocyte growth factor receptor MET, which is a molecular drug target for several cancers, including that of the lung[175], may also negatively influence neutrophil cytotoxicity and antitumour activities[82]. Interestingly, however, some targeted drugs may have positive effects on myeloid cells: MEK and BRAF inhibitors can revert BRAF-mutated melanoma-induced DC suppression *in vitro*[176,177], and molecular targeting of the Janus kinase 2–signal transducer and activator of transcription 3 (JAK2–STAT3) pathway can promote DC activation[178]. Additionally, long-term treatment with imatinib dramatically reduces the numbers of mast cells in patients with chronic myeloid leukaemia and in mice, although it is not clear if this is relevant to treatment outcome[179]. Future studies should reveal whether manipulating myeloid cells or molecular pathways involving these cells enables targeted therapies to produce more durable responses in patients.

Targeting myeloid cells to limit cancer

The relevance of tumour-infiltrating myeloid cells in cancer progression and therapy has spurred interest in therapeutically targeting these cells. One strategy is to reduce numbers of myeloid cells such as TAMs, which may be achieved by targeting TAMs themselves or their precursors (FIG. 3). Because myeloid cells can contribute

both anti- and pro-tumoural activities, modulating their functions, rather than depleting the cells, is another attractive option.

Manipulating myeloid cell numbers. Different myeloid cell depletion strategies, including pharmacological and genetic approaches, have been used to successfully control tumour progression in various mouse models[180]. In mice, broad depleting strategies that target CD11b-, Gr1- or Ly6G-expressing myeloid cells, delay tumour progression in several, but not all, experimental settings[125,140,181]. Rather than exclusively affecting myeloid cells at the tumour site, these strategies typically affect myeloid cell populations systemically; by extension, the observed antitumour effects could be driven at least partially by altered extratumoural myeloid cells. Because monocyte recruitment to tumours and TAM maintenance depend strongly on CCL2–CCR2 and M-CSF–M-CSFR signalling, these pathways are promising targets for depleting TAMs more selectively[23,25]. Different approaches using mAbs[104,169,182], small-molecule inhibitors[169,183,184] or nanoparticle-based gene expression silencing[67,185] can limit TAM accumulation and control disease progression in various mouse models of cancer. Drug regimen schedules, however, may profoundly affect clinical outcomes. Indeed, interrupting CCL2 blockade treatment in mice can result in sudden monocyte release from the bone marrow, which increases metastasis formation and accelerates death[145]. Furthermore, targeting the M-CSF–M-CSFR pathway can have different outcomes: it controls tumours in some cancer models[182,183,186], whereas others require combination with an additional treatment[56,138–140]. Accordingly, drugs that target the CCL2–CCR2 or M-CSF–M-CSFR pathway are being evaluated in patients both as monotherapies[182] and in combination with anticancer agents[25]. In mice, tumour phagocyte replenishment can also be controlled by limiting tumour-induced myelopoiesis. For instance, targeting production of GM-CSF[124] or angiotensin II[187] reduces monocyte and neutrophil-like cells or TAMs, respectively, and suppresses tumour progression. G-CSF inhibition may also reduce bone marrow production[123] and release[188] of tumour-promoting myeloid precursors.

Current myeloid cell depletion strategies have limitations: they can delay tumour progression but may be insufficient to eliminate or durably control cancer in mice on their own[125,140,169,187]. Also, myeloid cell ablation may have undesirable clinical side effects, such as increased risk of infections, that must be considered in translating these treatments for patient use.

Manipulating myeloid cell phenotypes. Strategies that modulate, rather than ablate, tumour-infiltrating phagocytes may not only harness their antitumour properties but also circumvent the drawbacks of phagocyte depletion strategies. Interestingly, in some cases, M-CSFR targeting induces tumour regression without depleting TAMs[186]. The drug-induced antitumour mechanisms probably involve changing TAM phenotypes, including downregulation of M2 macrophage-associated genes. A model of pancreatic cancer showed similar results[169], although M-CSFR blockade simultaneously reduced the TAM infiltrate. Besides M-CSF–M-CSFR targeting, other strategies may skew myeloid cell functions and exploit their antitumour potential. For instance, inhibiting the receptor tyrosine kinase MERTK triggers a pro-inflammatory TAM phenotype, increases $CD8^+$ T cell infiltration and improves tumour control in mice[189,190]. Several US Food and Drug Administration (FDA)-approved small-molecule compounds inhibit the MERTK pathway although they were not originally developed for this purpose[190]. Myeloid cell functions are also regulated at the epigenetic level; as an example, drugs that interfere with chromatin remodelling, such as bromodomain and extra-terminal motif proteins[191,192], or histone deacetylase (HDAC) inhibitors[193,194], can affect inflammatory macrophage phenotypes. Other approaches to the modulation of macrophage functions include local low-dose ionizing radiation[146] and CD40 targeting, which can trigger macrophages to kill tumour cells[195]. Whether these treatments repolarize individual TAMs or modulate the tumour microenvironment by reducing and expanding distinct TAM subtypes remains unclear, yet it seems that TAM 'reprogramming' without massive TAM depletion can effectively control cancer progression in at least some settings.

Strategies to amplify the ability of DCs to stimulate effective antitumour T cell responses have long been considered[14]. GM-CSF is typically used to amplify DCs *in vitro* and can promote antitumour immunity *in vivo*[196]. For example, an FDA-approved vaccine, sipuleucel-T, uses *in vitro* GM-CSF-expanded patient DCs primed with prostate antigens to stimulate antitumour T cells[197]. However, GM-CSF may have pleiotropic effects on myeloid cells: it can expand T cell-activating DCs but also bone marrow-derived TAM progenitors and other immunosuppressive myeloid cells[124]. Defining when GM-CSF benefits or harms the host requires study, although evidence indicates that the microenvironment in which GM-CSF is produced can dictate the function of this cytokine[198].

Other approaches consist of modifying DCs to boost protective antitumour immunity and prevent tumour-induced exhaustion. Recent evidence indicates that cytosolic DNA sensing by stimulator of interferon genes (STING) induces type I IFN production and enables DCs to activate antitumour $CD8^+$ T cell responses[199]. STING agonists can potently activate this pathway in mice[200,201]. Encapsulating STING agonists into nanoparticles further amplifies DC-mediated antitumour immunity[202] and STINGVAX, a vaccine that uses GM-CSF-producing cells in combination with STING agonists, can regress mouse tumours that are otherwise poorly immunogenic[203]. The small-molecule compound DMXAA (also known as vadimezan), which was originally developed as a tumour-vascular disrupting agent, targets STING in mice[204]. Clinical trial results were disappointing but may be explained by the finding that human STING has an amino acid substitution that makes it insensitive to DMXAA[204]. New investigations involving human-specific STING agonists are under way.

Intriguingly, the absence of STING also improves tumour control and $CD8^+$ T cell activity in a mouse model of lung cancer[205].

Other strategies to activate DCs in tumours include upregulating the co-stimulatory molecules CD80, CD86 and CD40 (REF. 206), the T cell-stimulating cytokine IL-12 (REFS 56,207) or the immunostimulatory microRNA miR-155 (REF. 208); or suppressing the transcription factor STAT3 (REF. 209), the stress response factor XBP1 (REF. 53) or the β-catenin pathway[54]. Implanting physical scaffolds that incorporate a combination of immunoregulatory components into tumour-bearing subjects could be useful to optimize tumour-infiltrating DC activation *in situ*[210–212].

Perspectives

Although knowledge of phagocyte biology in cancer has exploded in recent years, we still have a limited understanding of how the various myeloid cell subtypes function *in vivo* during tumour progression and how drugs alter the activity of these cells. Functional imaging of intact microenvironments in mice[213] should help to address these questions and could be achieved by combining new mouse models and reporters, single-cell *in vivo* imaging technology and new computational analysis[32,214–216]. *In vivo* imaging is important because of its ability to define both temporally and spatially how different cells interact with their environment, respond to drugs and mediate immunosuppressive or tumoricidal actions[213]. Understanding these processes is crucial to defining how therapies fail or work within complex tissue environments.

Additionally, in the future we must uncover which myeloid cells are crucial to human disease, how cancer therapeutic agents modulate human myeloid cells and how these perturbations regulate treatment efficacy. We propose two major areas of emphasis to address these questions and obtain knowledge that can be harnessed to improve current treatment options (FIG. 5).

First, we need to decipher the complex repertoires of tumour-infiltrating myeloid cells in patients. Our increasing ability to analyse phagocyte content in tumours should help to uncover whether specific signatures can be used to reveal diagnostic and prognostic information, tailor treatments, monitor responses to therapy and/or predict drug resistance in individual patients. Human phagocyte studies remain limited by the scarcity of biopsy material, without which it is difficult to identify and manipulate tumour-infiltrating cell populations. However, techniques such as novel single-cell RNAseq approaches (for example, DropSeq)[217,218], single-cell mass cytometry (CyTOF)[219], protein mass spectrometry[220] and high-throughput protein analysis from fine-needle aspirates[221] permit the extraction of substantially more information from limited tissue samples, which should help to discriminate between tumour-promoting and tumour-suppressing cells and, in turn, improve patient stratification and survival prediction. Additionally, myeloid cells could be mapped noninvasively in patients. Given their naturally high endocytosis activity, macrophages efficiently accumulate nanomaterials, which can then be detected by commonly used clinical imaging technologies, such as magnetic resonance imaging (MRI) and positron emission tomography (PET)[222]. Imaging of peripheral TAMs could also be used to delineate tumour margins noninvasively and serve as an aid for planning surgery[223].

Second, we should learn whether clinical interventions that manipulate myeloid cells have therapeutic benefit. Clinicians have already launched clinical trials with promising therapeutics that target TAMs or tumour-infiltrating DCs[25,224]. These investigations are relevant not only because we urgently need new treatment options against many cancers, but also because they consider crucial cellular components in the tumour microenvironment that often remain overlooked. Given that most cancer therapies affect myeloid cells, it is important to evaluate whether myeloid cell-targeting agents mitigate the limitations of other treatments. These studies should test different regimens, such as simultaneous versus sequential drug administration, because these variables can affect the outcome of combinatorial treatments[225]. Manipulating myeloid cell responses could have varied positive

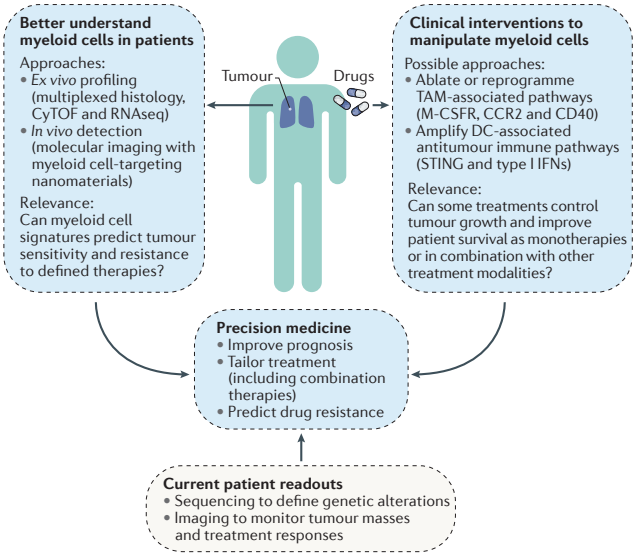

Figure 5 | **Towards a more comprehensive understanding of human tumours and relevant therapeutic targets.** Major areas of emphasis for research on myeloid cells in cancer include expanding our knowledge of the complex repertoires of these cells in cancer patients (top left panel) and uncovering whether interventions that affect these cells have therapeutic benefit (top right panel). Each box indicates possible approaches to address these issues, and their relevance. This knowledge, combined with information available from current patient readouts, should help clinicians to optimize precision medicine approaches (bottom blue panel). CCR2, chemokine (C-C motif) receptor 2; CyTOF, single-cell mass cytometry; DC, dendritic cell; IFNs, interferons; M-CSFR, macrophage colony-stimulating factor receptor; RNAseq, RNA sequencing; STING, stimulator of interferon genes; TAM, tumour-associated macrophage.

consequences: they may suppress some cancers that resist current treatments and/or sensitize tumours to other drugs or augment their therapeutic efficacy. For instance, current therapies with T cell immune checkpoint blockers can be highly successful but benefit only a small subset of patients. Myeloid cell-targeting agents could be used to increase the number of patients who respond to treatment and consequently trigger more pronounced antitumour effects in these patients.

The types of investigation mentioned above, whether their hypotheses are demonstrated or refuted, will help to define next-generation cancer treatments. The results may guide precision medicine approaches by revealing tumour microenvironmental components that vary drastically between tumours, direct tumour growth and influence drug responses. For example, tumours rich in TAMs or subsets thereof may be better controlled with therapies that incorporate phagocyte-targeting agents, whereas tumours that are poorly infiltrated by DCs may be suppressed more efficiently using drugs that foster DC recruitment to tumours and promote long-lasting antitumour T cell immunity. Overall, uncovering the intricate mechanisms that govern myeloid cells in human cancer is an ongoing challenge; nonetheless, the wealth of mouse data and the growing knowledge from human cancer studies suggest a central role for myeloid cells that warrants their consideration in future diagnostic and therapeutic approaches.

1. Sharma, P. & Allison, J. P. The future of immune checkpoint therapy. *Science* **348**, 56–61 (2015).
2. Hanahan, D. & Coussens, L. M. Accessories to the crime: functions of cells recruited to the tumor microenvironment. *Cancer Cell* **21**, 309–322 (2012).
3. Metchnikoff, E. Der Kampf der Phagocyten gegen Krankeitserreger. *Virchows Arch.* **96**, 177–195 (1884).
4. Arandjelovic, S. & Ravichandran, K. S. Phagocytosis of apoptotic cells in homeostasis. *Nat. Immunol.* **16**, 907–917 (2015).
5. Lavin, Y. *et al.* Regulation of macrophage development and function in peripheral tissues. *Nat. Rev. Immunol.* **15**, 731–744 (2015).
6. Steinman, R. M. Decisions about dendritic cells: past, present, and future. *Annu. Rev. Immunol.* **30**, 1–22 (2012).
7. Merad, M. *et al.* The dendritic cell lineage: ontogeny and function of dendritic cells and their subsets in the steady state and the inflamed setting. *Annu. Rev. Immunol.* **31**, 563–604 (2013).
8. Broz, M. L. & Krummel, M. F. The emerging understanding of myeloid cells as partners and targets in tumor rejection. *Cancer Immunol. Res.* **3**, 313–319 (2015).
9. Qian, B. Z. & Pollard, J. W. Macrophage diversity enhances tumor progression and metastasis. *Cell* **141**, 39–51 (2010).
10. Gabrilovich, D. I. *et al.* Coordinated regulation of myeloid cells by tumours. *Nat. Rev. Immunol.* **12**, 253–268 (2012).
11. Dvorak, H. F. Tumors: wounds that do not heal. Similarities between tumor stroma generation and wound healing. *N. Engl. J. Med.* **315**, 1650–1659 (1986).
12. Davies, L. C. *et al.* Tissue-resident macrophages. *Nat. Immunol.* **14**, 986–995 (2013).
13. Murray, P. J. & Wynn, T. A. Protective and pathogenic functions of macrophage subsets. *Nat. Rev. Immunol.* **11**, 723–737 (2011).
14. Palucka, K. & Banchereau, J. Cancer immunotherapy via dendritic cells. *Nat. Rev. Cancer* **12**, 265–277 (2012).
15. Swiecki, M. & Colonna, M. The multifaceted biology of plasmacytoid dendritic cells. *Nat. Rev. Immunol.* **15**, 471–485 (2015).
16. Guilliams, M. *et al.* Dendritic cells, monocytes and macrophages: a unified nomenclature based on ontogeny. *Nat. Rev. Immunol.* **14**, 571–578 (2014).
17. Pittet, M. J. *et al.* The journey from stem cell to macrophage. *Ann. NY Acad. Sci.* **1319**, 1–18 (2014).
18. Diao, J. *et al.* Recruitment and differentiation of conventional dendritic cell precursors in tumors. *J. Immunol.* **184**, 1261–1267 (2010).
19. Galli, S. J. *et al.* Phenotypic and functional plasticity of cells of innate immunity: macrophages, mast cells and neutrophils. *Nat. Immunol.* **12**, 1035–1044 (2011).
20. Nathan, C. Neutrophils and immunity: challenges and opportunities. *Nat. Rev. Immunol.* **6**, 173–182 (2006).
21. Rosenberg, H. F. *et al.* Eosinophils: changing perspectives in health and disease. *Nat. Rev. Immunol.* **13**, 9–22 (2013).
22. Lu, T. *et al.* Tumor-infiltrating myeloid cells induce tumor cell resistance to cytotoxic T cells in mice. *J. Clin. Invest.* **121**, 4015–4029 (2011).
23. Noy, R. & Pollard, J. W. Tumor-associated macrophages: from mechanisms to therapy. *Immunity* **41**, 49–61 (2014).
24. Biswas, S. K. & Mantovani, A. Macrophage plasticity and interaction with lymphocyte subsets: cancer as a paradigm. *Nat. Immunol.* **11**, 889–896 (2010).
25. Ruffell, B. & Coussens, L. M. Macrophages and therapeutic resistance in cancer. *Cancer Cell* **27**, 462–472 (2015).
26. Lavin, Y. *et al.* Tissue-resident macrophage enhancer landscapes are shaped by the local microenvironment. *Cell* **159**, 1312–1326 (2014).
27. Ginhoux, F. *et al.* New insights into the multidimensional concept of macrophage ontogeny, activation and function. *Nat. Immunol.* **17**, 34–40 (2016).
28. Pulford, K. A. *et al.* Distribution of the CD68 macrophage/myeloid associated antigen. *Int. Immunol.* **2**, 973–980 (1990).
29. Kaiserling, E. *et al.* Aberrant expression of macrophage-associated antigens (CD68 and Ki-M1P) by Schwann cells in reactive and neoplastic neural tissue. Light- and electron-microscopic findings. *Mod. Pathol.* **6**, 463–468 (1993).
30. Zhang, Q. W. *et al.* Prognostic significance of tumor-associated macrophages in solid tumor: a meta-analysis of the literature. *PLoS ONE* **7**, e50946 (2012).
31. Steidl, C. *et al.* Tumor-associated macrophages and survival in classic Hodgkin's lymphoma. *N. Engl. J. Med.* **362**, 875–885 (2010).
Detailed study showing decreased overall survival of patients whose tumours are infiltrated by macrophages.
32. Harney, A. S. *et al.* Real-time imaging reveals local, transient vascular permeability, and tumor cell intravasation stimulated by TIE2hi macrophage-derived VEGFA. *Cancer Discov.* **5**, 932–943 (2015).
33. Mohamed, M. M. & Sloane, B. F. Cysteine cathepsins: multifunctional enzymes in cancer. *Nat. Rev. Cancer* **6**, 764–775 (2006).
34. Kessenbrock, K. *et al.* Matrix metalloproteinases: regulators of the tumor microenvironment. *Cell* **141**, 52–67 (2010).
35. Lewis, J. S. *et al.* Expression of vascular endothelial growth factor by macrophages is up-regulated in poorly vascularized areas of breast carcinomas. *J. Pathol.* **192**, 150–158 (2000).
36. Sierra, J. R. *et al.* Tumor angiogenesis and progression are enhanced by Sema4D produced by tumor-associated macrophages. *J. Exp. Med.* **205**, 1673–1685 (2008).
37. Kuang, D. M. *et al.* Activated monocytes in peritumoral stroma of hepatocellular carcinoma foster immune privilege and disease progression through PD-L1. *J. Exp. Med.* **206**, 1327–1337 (2009).
38. Forssell, J. *et al.* High macrophage infiltration along the tumor front correlates with improved survival in colon cancer. *Clin. Cancer Res.* **13**, 1472–1479 (2007).
39. Ohno, S. *et al.* The degree of macrophage infiltration into the cancer cell nest is a significant predictor of survival in gastric cancer patients. *Anticancer Res.* **23**, 5015–5022 (2003).
40. Ohno, S. *et al.* Correlation of histological localization of tumor-associated macrophages with clinicopathological features in endometrial cancer. *Anticancer Res.* **24**, 3335–3342 (2004).
41. Sica, A. & Mantovani, A. Macrophage plasticity and polarization: *in vivo* veritas. *J. Clin. Invest.* **122**, 787–795 (2012).
42. Lawrence, T. & Natoli, G. Transcriptional regulation of macrophage polarization: enabling diversity with identity. *Nat. Rev. Immunol.* **11**, 750–761 (2011).
43. Squadrito, M. L. *et al.* MicroRNA-mediated control of macrophages and its implications for cancer. *Trends Immunol.* **34**, 350–359 (2013).
44. Hibbs, J. B. *et al.* Macrophage cytotoxicity: role for L-arginine deiminase and imino nitrogen oxidation to nitrite. *Science* **235**, 473–476 (1987).
45. Nathan, C. F. *et al.* Extracellular cytolysis by activated macrophages and granulocytes. II. Hydrogen peroxide as a mediator of cytotoxicity. *J. Exp. Med.* **149**, 100–113 (1979).
46. Urban, J. L. *et al.* Tumor necrosis factor: a potent effector molecule for tumor cell killing by activated macrophages. *Proc. Natl Acad. Sci. USA* **83**, 5233–5237 (1986).
47. Gentles, A. J. *et al.* The prognostic landscape of genes and infiltrating immune cells across human cancers. *Nat. Med.* **21**, 938–945 (2015).
Meta-analysis of distinct leukocyte subsets posits neutrophils as significant predictors of poor patient survival for diverse solid tumour types.
48. Goc, J. *et al.* Dendritic cells in tumor-associated tertiary lymphoid structures signal a Th1 cytotoxic immune contexture and license the positive prognostic value of infiltrating CD8$^+$ T cells. *Cancer Res.* **74**, 705–715 (2014).
49. Dieu-Nosjean, M. C. *et al.* Long-term survival for patients with non-small-cell lung cancer with intratumoral lymphoid structures. *J. Clin. Oncol.* **26**, 4410–4417 (2008).
50. Ladányi, A. *et al.* Density of DC-LAMP$^+$ mature dendritic cells in combination with activated T lymphocytes infiltrating primary cutaneous melanoma is a strong independent prognostic factor. *Cancer Immunol. Immunother.* **56**, 1459–1469 (2007).
51. Broz, M. L. *et al.* Dissecting the tumor myeloid compartment reveals rare activating antigen-presenting cells critical for T cell immunity. *Cancer Cell* **26**, 638–652 (2014).
Identification of a discrete DC type in the tumour microenvironment that promotes antitumour immunity.
52. Gabrilovich, D. Mechanisms and functional significance of tumour-induced dendritic-cell defects. *Nat. Rev. Immunol.* **4**, 941–952 (2004).
53. Cubillos-Ruiz, J. R. *et al.* ER stress sensor XBP1 controls anti-tumor immunity by disrupting dendritic cell homeostasis. *Cell* **161**, 1527–1538 (2015).
54. Spranger, S. *et al.* Melanoma-intrinsic β-catenin signalling prevents anti-tumour immunity. *Nature* **523**, 231–235 (2015).
Oncogenic β-catenin signalling prevents CD103$^+$ DC recruitment to tumours, which limits tumour infiltration by T cells and sensitivity to immune checkpoint blockade.

55. Zelenay, S. *et al.* Cyclooxygenase-dependent tumor growth through evasion of immunity. *Cell* **162**, 1257–1270 (2015).
56. Ruffell, B. *et al.* Macrophage IL-10 blocks $CD8^+$ T cell-dependent responses to chemotherapy by suppressing IL-12 expression in intratumoral dendritic cells. *Cancer Cell* **26**, 623–637 (2014).
The efficacy of M-CSF blockade can rely on suppressing IL-10 production by TAMs, which otherwise prevent antitumour DC and $CD8^+$ T cell activation.
57. Treilleux, I. *et al.* Dendritic cell infiltration and prognosis of early stage breast cancer. *Clin. Cancer Res.* **10**, 7466–7474 (2004).
58. Jensen, T. O. *et al.* Intratumoral neutrophils and plasmacytoid dendritic cells indicate poor prognosis and are associated with pSTAT3 expression in AJCC stage I/II melanoma. *Cancer* **118**, 2476–2485 (2012).
59. Dzionek, A. *et al.* BDCA-2, BDCA-3, and BDCA-4: three markers for distinct subsets of dendritic cells in human peripheral blood. *J. Immunol.* **165**, 6037–6046 (2000).
60. Haniffa, M. *et al.* Human tissues contain CD141hi cross-presenting dendritic cells with functional homology to mouse $CD103^+$ nonlymphoid dendritic cells. *Immunity* **37**, 60–73 (2012).
61. Parker, K. H. *et al.* Myeloid-derived suppressor cells: critical cells driving immune suppression in the tumor microenvironment. *Adv. Cancer Res.* **128**, 95–139 (2015).
62. Jiang, L. *et al.* Prognostic value of monocyte and neutrophils to lymphocytes ratio in patients with metastatic soft tissue sarcoma. *Oncotarget* **6**, 9542–9550 (2015).
63. Huang, S. H. *et al.* Prognostic value of pretreatment circulating neutrophils, monocytes, and lymphocytes in oropharyngeal cancer stratified by human papillomavirus status. *Cancer* **121**, 545–555 (2015).
64. Gabitass, R. F. *et al.* Elevated myeloid-derived suppressor cells in pancreatic, esophageal and gastric cancer are an independent prognostic factor and are associated with significant elevation of the Th2 cytokine interleukin-13. *Cancer Immunol. Immunother.* **60**, 1419–1430 (2011).
65. Movahedi, K. *et al.* Different tumor microenvironments contain functionally distinct subsets of macrophages derived from $Ly6C^{high}$ monocytes. *Cancer Res.* **70**, 5728–5739 (2010).
66. Sawanobori, Y. *et al.* Chemokine-mediated rapid turnover of myeloid-derived suppressor cells in tumor-bearing mice. *Blood* **111**, 5457–5466 (2008).
67. Cortez-Retamozo, V. *et al.* Origins of tumor-associated macrophages and neutrophils. *Proc. Natl Acad. Sci. USA* **109**, 2491–2496 (2012).
68. Marvel, D. & Gabrilovich, D. I. Myeloid-derived suppressor cells in the tumor microenvironment: expect the unexpected. *J. Clin. Invest.* **125**, 3356–3364 (2015).
69. Vasquez-Dunddel, D. *et al.* STAT3 regulates arginase-I in myeloid-derived suppressor cells from cancer patients. *J. Clin. Invest.* **123**, 1580–1589 (2013).
70. Mazzoni, A. *et al.* Myeloid suppressor lines inhibit T cell responses by an NO-dependent mechanism. *J. Immunol.* **168**, 689–695 (2002).
71. Young, M. R. *et al.* Suppression of T cell proliferation by tumor-induced granulocyte-macrophage progenitor cells producing transforming growth factor-β and nitric oxide. *J. Immunol.* **156**, 1916–1922 (1996).
72. Mao, Y. *et al.* Melanoma-educated $CD14^+$ cells acquire a myeloid-derived suppressor cell phenotype through COX-2-dependent mechanisms. *Cancer Res.* **73**, 3877–3887 (2013).
73. Nagaraj, S. *et al.* Altered recognition of antigen is a mechanism of $CD8^+$ T cell tolerance in cancer. *Nat. Med.* **13**, 828–835 (2007).
74. Molon, B. *et al.* Chemokine nitration prevents intratumoral infiltration of antigen-specific T cells. *J. Exp. Med.* **208**, 1949–1962 (2011).
75. Pan, P. Y. *et al.* Immune stimulatory receptor CD40 is required for T-cell suppression and T regulatory cell activation mediated by myeloid-derived suppressor cells in cancer. *Cancer Res.* **70**, 99–108 (2010).
76. Di Mitri, D. *et al.* Tumour-infiltrating $Gr\text{-}1^+$ myeloid cells antagonize senescence in cancer. *Nature* **515**, 134–137 (2014).
77. Shojaei, F. *et al.* Bv8 regulates myeloid-cell-dependent tumour angiogenesis. *Nature* **450**, 825–831 (2007).
78. Demers, M. *et al.* Cancers predispose neutrophils to release extracellular DNA traps that contribute to cancer-associated thrombosis. *Proc. Natl Acad. Sci. USA* **109**, 13076–13081 (2012).
79. Wilson, C. L. *et al.* NFκB1 is a suppressor of neutrophil-driven hepatocellular carcinoma. *Nat. Commun.* **6**, 6818 (2015).
80. Ortiz, M. L. *et al.* Immature myeloid cells directly contribute to skin tumor development by recruiting IL-17-producing $CD4^+$ T cells. *J. Exp. Med.* **212**, 351–367 (2015).
81. Granot, Z. *et al.* Tumor entrained neutrophils inhibit seeding in the premetastatic lung. *Cancer Cell* **20**, 300–314 (2011).
82. Finisguerra, V. *et al.* MET is required for the recruitment of anti-tumoural neutrophils. *Nature* **522**, 349–353 (2015).
83. Fridlender, Z. G. *et al.* Polarization of tumor-associated neutrophil phenotype by TGF-β: "N1" versus "N2" TAN. *Cancer Cell* **16**, 183–194 (2009).
84. Eruslanov, E. B. *et al.* Tumor-associated neutrophils stimulate T cell responses in early-stage human lung cancer. *J. Clin. Invest.* **124**, 5466–5480 (2014).
85. Davis, B. P. & Rothenberg, M. E. Eosinophils and cancer. *Cancer Immunol. Res.* **2**, 1–8 (2014).
86. Nielsen, H. J. *et al.* Independent prognostic value of eosinophil and mast cell infiltration in colorectal cancer tissue. *J. Pathol.* **189**, 487–495 (1999).
87. Tepper, R. I. *et al.* An eosinophil-dependent mechanism for the antitumor effect of interleukin-4. *Science* **257**, 548–551 (1992).
88. Carretero, R. *et al.* Eosinophils orchestrate cancer rejection by normalizing tumor vessels and enhancing infiltration of $CD8^+$ T cells. *Nat. Immunol.* **16**, 609–617 (2015).
Eosinophils can contribute to tumour immunity by promoting tumour infiltration by T cells and polarizing TAMs.
89. Andreu, P. *et al.* FcRγ activation regulates inflammation-associated squamous carcinogenesis. *Cancer Cell* **17**, 121–134 (2010).
Activating Fcγ receptors expressed by myeloid cells can foster a tumour-promoting microenvironment.
90. Nowak, E. C. *et al.* Tryptophan hydroxylase-1 regulates immune tolerance and inflammation. *J. Exp. Med.* **209**, 2127–2135 (2012).
91. Blatner, N. R. *et al.* In colorectal cancer mast cells contribute to systemic regulatory T-cell dysfunction. *Proc. Natl Acad. Sci. USA* **107**, 6430–6435 (2010).
92. Gounaris, E. *et al.* Mast cells are an essential hematopoietic component for polyp development. *Proc. Natl Acad. Sci. USA* **104**, 19977–19982 (2007).
93. Yang, Z. *et al.* Mast cells mobilize myeloid-derived suppressor cells and T_{reg} cells in tumor microenvironment via IL-17 pathway in murine hepatocarcinoma model. *PLoS ONE* **5**, e8922 (2010).
94. Saleem, S. J. *et al.* Cutting edge: mast cells critically augment myeloid-derived suppressor cell activity. *J. Immunol.* **189**, 511–515 (2012).
95. Malfettone, A. *et al.* High density of tryptase-positive mast cells in human colorectal cancer: a poor prognostic factor related to protease-activated receptor 2 expression. *J. Cell. Mol. Med.* **17**, 1025–1037 (2013).
96. Bindea, G. *et al.* Spatiotemporal dynamics of intratumoral immune cells reveal the immune landscape in human cancer. *Immunity* **39**, 782–795 (2013).
97. Väyrynen, J. P. *et al.* Detailed analysis of inflammatory cell infiltration in colorectal cancer. *Br. J. Cancer* **109**, 1839–1847 (2013).
98. Katz, H. R. & Austen, K. F. Mast cell deficiency, a game of kit and mouse. *Immunity* **35**, 668–670 (2011).
99. Feyerabend, T. B. *et al.* Cre-mediated cell ablation contests mast cell contribution in models of antibody- and T cell-mediated autoimmunity. *Immunity* **35**, 832–844 (2011).
100. Dudeck, A. *et al.* Mast cells are key promoters of contact allergy that mediate the adjuvant effects of haptens. *Immunity* **34**, 973–984 (2011).
101. Schönhuber, N. *et al.* A next-generation dual-recombinase system for time- and host-specific targeting of pancreatic cancer. *Nat. Med.* **20**, 1340–1347 (2014).
102. Ginhoux, F. & Jung, S. Monocytes and macrophages: developmental pathways and tissue homeostasis. *Nat. Rev. Immunol.* **14**, 392–404 (2014).
103. Franklin, R. A. *et al.* The cellular and molecular origin of tumor-associated macrophages. *Science* **344**, 921–925 (2014).
104. Qian, B. Z. *et al.* CCL2 recruits inflammatory monocytes to facilitate breast-tumour metastasis. *Nature* **475**, 222–225 (2011).
105. Kitamura, T. *et al.* CCL2-induced chemokine cascade promotes breast cancer metastasis by enhancing retention of metastasis-associated macrophages. *J. Exp. Med.* **212**, 1043–1059 (2015).
106. Serbina, N. V. & Pamer, E. G. Monocyte emigration from bone marrow during bacterial infection requires signals mediated by chemokine receptor CCR2. *Nat. Immunol.* **7**, 311–317 (2006).
107. Lin, E. Y. *et al.* Colony-stimulating factor 1 promotes progression of mammary tumors to malignancy. *J. Exp. Med.* **193**, 727–740 (2001).
Evidence from mice that M-CSF promotes mammary cancer metastasis.
108. Kubota, Y. *et al.* M-CSF inhibition selectively targets pathological angiogenesis and lymphangiogenesis. *J. Exp. Med.* **206**, 1089–1102 (2009).
109. Richardsen, E. *et al.* Macrophage-colony stimulating factor (CSF1) predicts breast cancer progression and mortality. *Anticancer Res.* **35**, 865–874 (2015).
110. Ueno, T. *et al.* Significance of macrophage chemoattractant protein-1 in macrophage recruitment, angiogenesis, and survival in human breast cancer. *Clin. Cancer Res.* **6**, 3282–3289 (2000).
111. Groblewska, M. *et al.* Serum levels of granulocyte colony-stimulating factor (G-CSF) and macrophage colony-stimulating factor (M-CSF) in pancreatic cancer patients. *Clin. Chem. Lab Med.* **45**, 30–34 (2007).
112. Mroczko, B. *et al.* Serum macrophage-colony stimulating factor levels in colorectal cancer patients correlate with lymph node metastasis and poor prognosis. *Clin. Chim. Acta* **380**, 208–212 (2007).
113. Zhu, X. D. *et al.* High expression of macrophage colony-stimulating factor in peritumoral liver tissue is associated with poor survival after curative resection of hepatocellular carcinoma. *J. Clin. Oncol.* **26**, 2707–2716 (2008).
114. Smith, H. O. *et al.* The role of colony-stimulating factor 1 and its receptor in the etiopathogenesis of endometrial adenocarcinoma. *Clin. Cancer Res.* **1**, 313–325 (1995).
115. Kirma, N. *et al.* Elevated expression of the oncogene c-fms and its ligand, the macrophage colony-stimulating factor-1, in cervical cancer and the role of transforming growth factor-β1 in inducing c-fms expression. *Cancer Res.* **67**, 1918–1926 (2007).
116. Pucci, F. *et al.* SCS macrophages suppress melanoma by restricting tumor-derived vesicle–B cell interactions. *Science* **352**, 242–246 (2016).
Macrophages in the subcapsular sinus of tumour-draining lymph nodes can suppress cancer outgrowth by blocking the spread of tumour-derived extracellular vesicles.
117. Satpathy, A. T. *et al.* Zbtb46 expression distinguishes classical dendritic cells and their committed progenitors from other immune lineages. *J. Exp. Med.* **209**, 1135–1152 (2012).
118. Schiavoni, G. *et al.* ICSBP is essential for the development of mouse type I interferon-producing cells and for the generation and activation of $CD8\alpha^+$ dendritic cells. *J. Exp. Med.* **196**, 1415–1425 (2002).
119. Hildner, K. *et al.* Batf3 deficiency reveals a critical role for $CD8\alpha^+$ dendritic cells in cytotoxic T cell immunity. *Science* **322**, 1097–1100 (2008).
120. Suzuki, S. *et al.* Critical roles of interferon regulatory factor 4 in $CD11b^{high}CD8\alpha^-$ dendritic cell development. *Proc. Natl Acad. Sci. USA* **101**, 8981–8986 (2004).
121. Cheong, C. *et al.* Microbial stimulation fully differentiates monocytes to DC-SIGN/$CD209^+$ dendritic cells for immune T cell areas. *Cell* **143**, 416–429 (2010).
122. Raccosta, L. *et al.* The oxysterol–CXCR2 axis plays a key role in the recruitment of tumor-promoting neutrophils. *J. Exp. Med.* **210**, 1711–1728 (2013).
123. Casbon, A. J. *et al.* Invasive breast cancer reprograms early myeloid differentiation in the bone marrow to generate immunosuppressive neutrophils. *Proc. Natl Acad. Sci. USA* **112**, E566–E575 (2015).
124. Bayne, L. J. *et al.* Tumor-derived granulocyte–macrophage colony-stimulating factor regulates myeloid inflammation and T cell immunity in pancreatic cancer. *Cancer Cell* **21**, 822–835 (2012).
125. Coffelt, S. B. *et al.* IL-17-producing γδ T cells and neutrophils conspire to promote breast cancer metastasis. *Nature* **522**, 345–348 (2015).
Neutrophils can suppress pulmonary and lymph node metastasis by suppressing antitumour T cell activity locally.
126. Talmadge, J. E. & Fidler, I. J. AACR centennial series: the biology of cancer metastasis: historical perspective. *Cancer Res.* **70**, 5649–5669 (2010).

127. Condeelis, J. & Pollard, J. W. Macrophages: obligate partners for tumor cell migration, invasion, and metastasis. *Cell* **124**, 263–266 (2006).
128. Rohan, T. E. *et al.* Tumor microenvironment of metastasis and risk of distant metastasis of breast cancer. *J. Natl Cancer Inst.* **106**, dju136 (2014).
129. Gül, N. *et al.* Macrophages eliminate circulating tumor cells after monoclonal antibody therapy. *J. Clin. Invest.* **124**, 812–823 (2014).
Kupffer cells (liver macrophages) can phagocytose circulating tumour cells; antitumour antibodies that bind Fcγ receptors on Kupffer cells can trigger tumour cell elimination.
130. Willingham, S. B. *et al.* The CD47-signal regulatory protein α (SIRPa) interaction is a therapeutic target for human solid tumors. *Proc. Natl Acad. Sci. USA* **109**, 6662–6667 (2012).
131. Steinert, G. *et al.* Immune escape and survival mechanisms in circulating tumor cells of colorectal cancer. *Cancer Res.* **74**, 1694–1704 (2014).
132. Yan, H. H. *et al.* Gr-1$^+$CD11b$^+$ myeloid cells tip the balance of immune protection to tumor promotion in the premetastatic lung. *Cancer Res.* **70**, 6139–6149 (2010).
133. Hanna, R. N. *et al.* Patrolling monocytes control tumor metastasis to the lung. *Science* **350**, 985–990 (2015).
So-called patrolling monocytes are enriched in the lung tumour vasculature and prevent tumour cell invasion into the lungs by scavenging tumour material and recruiting NK cells.
134. Wculek, S. K. & Malanchi, I. Neutrophils support lung colonization of metastasis-initiating breast cancer cells. *Nature* **528**, 413–417 (2015).
Neutrophils can promote tumour cell colonization of lung premetastatic niches by producing leukotrienes.
135. Spiegel, A. *et al.* Neutrophils suppress intraluminal NK-mediated tumor cell clearance and enhance extravasation of disseminated carcinoma cells. *Cancer Discov.* **6**, 630–649 (2016).
Neutrophils can promote lung tumour metastasis by inhibiting NK cells and producing factors that facilitate tumour cell extravasation.
136. Sharma, S. K. *et al.* Pulmonary alveolar macrophages contribute to the premetastatic niche by suppressing antitumor T cell responses in the lungs. *J. Immunol.* **194**, 5529–5538 (2015).
137. Shree, T. *et al.* Macrophages and cathepsin proteases blunt chemotherapeutic response in breast cancer. *Genes Dev.* **25**, 2465–2479 (2011).
138. Xu, J. *et al.* CSF1R signaling blockade stanches tumor-infiltrating myeloid cells and improves the efficacy of radiotherapy in prostate cancer. *Cancer Res.* **73**, 2782–2794 (2013).
139. Shiao, S. L. *et al.* TH2-polarized CD4$^+$ T cells and macrophages limit efficacy of radiotherapy. *Cancer Immunol. Res.* **3**, 518–525 (2015).
140. DeNardo, D. G. *et al.* Leukocyte complexity predicts breast cancer survival and functionally regulates response to chemotherapy. *Cancer Discov.* **1**, 54–67 (2011).
Targeting TAMs with an M-CSFR inhibitor substantially ameliorates chemotherapy against breast cancer in mice.
141. Deng, L. *et al.* Irradiation and anti-PD-L1 treatment synergistically promote antitumor immunity in mice. *J. Clin. Invest.* **124**, 687–695 (2014).
142. Germano, G. *et al.* Role of macrophage targeting in the antitumor activity of trabectedin. *Cancer Cell* **23**, 249–262 (2013).
143. Alizadeh, D. *et al.* Doxorubicin eliminates myeloid-derived suppressor cells and enhances the efficacy of adoptive T-cell transfer in breast cancer. *Cancer Res.* **74**, 104–118 (2014).
144. Vincent, J. *et al.* 5-Fluorouracil selectively kills tumor-associated myeloid-derived suppressor cells resulting in enhanced T cell-dependent antitumor immunity. *Cancer Res.* **70**, 3052–3061 (2010).
145. Bonapace, L. *et al.* Cessation of CCL2 inhibition accelerates breast cancer metastasis by promoting angiogenesis. *Nature* **515**, 130–133 (2014).
146. Klug, F. *et al.* Low-dose irradiation programs macrophage differentiation to an iNOS$^+$/M1 phenotype that orchestrates effective T cell immunotherapy. *Cancer Cell* **24**, 589–602 (2013).
Tumour irradiation with local low-dose ionizing radiation can stimulate TAM differentiation, which results in CD8$^+$ T cell recruitment to the tumour site.
147. Iida, N. *et al.* Commensal bacteria control cancer response to therapy by modulating the tumor microenvironment. *Science* **342**, 967–970 (2013).
The microbiota can activate antitumour myeloid cell functions in response to chemotherapy.
148. Miller, M. A. *et al.* Tumour-associated macrophages act as a slow-release reservoir of nano-therapeutic Pt(IV) pro-drug. *Nat. Commun.* **6**, 8692 (2015).
149. Kroemer, G. *et al.* Immunogenic cell death in cancer therapy. *Annu. Rev. Immunol.* **31**, 51–72 (2013).
150. Michaud, M. *et al.* Autophagy-dependent anticancer immune responses induced by chemotherapeutic agents in mice. *Science* **334**, 1573–1577 (2011).
151. Obeid, M. *et al.* Calreticulin exposure dictates the immunogenicity of cancer cell death. *Nat. Med.* **13**, 54–61 (2007).
152. Apetoh, L. *et al.* Toll-like receptor 4-dependent contribution of the immune system to anticancer chemotherapy and radiotherapy. *Nat. Med.* **13**, 1050–1059 (2007).
153. Ma, Y. *et al.* Anticancer chemotherapy-induced intratumoral recruitment and differentiation of antigen-presenting cells. *Immunity* **38**, 729–741 (2013).
154. Pfirschke, C. *et al.* Immunogenic chemotherapy sensitizes tumors to checkpoint blockade therapy. *Immunity* **44**, 343–354 (2016).
Immunogenic chemotherapies can make tumours responsive to immune checkpoint blockade by activating antitumour myeloid cell functions.
155. Burnette, B. C. *et al.* The efficacy of radiotherapy relies upon induction of type I interferon-dependent innate and adaptive immunity. *Cancer Res.* **71**, 2488–2496 (2011).
156. Deng, L. *et al.* STING-dependent cytosolic DNA sensing promotes radiation-induced type I interferon-dependent antitumor immunity in immunogenic tumors. *Immunity* **41**, 843–852 (2014).
157. Gupta, A. *et al.* Radiotherapy promotes tumor-specific effector CD8$^+$ T cells via dendritic cell activation. *J. Immunol.* **189**, 558–566 (2012).
158. Pincetic, A. *et al.* Type I and type II Fc receptors regulate innate and adaptive immunity. *Nat. Immunol.* **15**, 707–716 (2014).
159. Bournazos, S. *et al.* The role of Fc–FcγR interactions in IgG-mediated microbial neutralization. *J. Exp. Med.* **212**, 1361–1369 (2015).
160. Uchida, J. *et al.* The innate mononuclear phagocyte network depletes B lymphocytes through Fc receptor-dependent mechanisms during anti-CD20 antibody immunotherapy. *J. Exp. Med.* **199**, 1659–1669 (2004).
161. Clynes, R. A. *et al.* Inhibitory Fc receptors modulate *in vivo* cytotoxicity against tumor targets. *Nat. Med.* **6**, 443–446 (2000).
162. Overdijk, M. B. *et al.* Antibody-mediated phagocytosis contributes to the anti-tumor activity of the therapeutic antibody daratumumab in lymphoma and multiple myeloma. *MAbs* **7**, 311–321 (2015).
163. Pardoll, D. M. The blockade of immune checkpoints in cancer immunotherapy. *Nat. Rev. Cancer* **12**, 252–264 (2012).
164. Simpson, T. R. *et al.* Fc-dependent depletion of tumor-infiltrating regulatory T cells co-defines the efficacy of anti-CTLA-4 therapy against melanoma. *J. Exp. Med.* **210**, 1695–1710 (2013).
165. Romano, E. *et al.* Ipilimumab-dependent cell-mediated cytotoxicity of regulatory T cells *ex vivo* by nonclassical monocytes in melanoma patients. *Proc. Natl Acad. Sci. USA* **112**, 6140–6145 (2015).
CTLA4 antibodies can eliminate T_{reg} cells by engaging CD16$^+$ monocytes; patients with melanoma who have more of these myeloid cells respond better to anti-CTLA4 therapy.
166. Li, F. & Ravetch, J. V. Inhibitory Fcγ receptor engagement drives adjuvant and anti-tumor activities of agonistic CD40 antibodies. *Science* **333**, 1030–1034 (2011).
167. Ahmad, Z. A. *et al.* scFv antibody: principles and clinical application. *Clin. Dev. Immunol.* **2012**, 980250 (2012).
168. Curiel, T. J. *et al.* Blockade of B7-H1 improves myeloid dendritic cell-mediated antitumor immunity. *Nat. Med.* **9**, 562–567 (2003).
169. Zhu, Y. *et al.* CSF1/CSF1R blockade reprograms tumor-infiltrating macrophages and improves response to T-cell checkpoint immunotherapy in pancreatic cancer models. *Cancer Res.* **74**, 5057–5069 (2014).
M-CSFR blockade can enhance antigen presentation, which augments antitumour T cell immunity and response to immune checkpoint blockade therapy.
170. Cavnar, M. J. *et al.* KIT oncogene inhibition drives intratumoral macrophage M2 polarization. *J. Exp. Med.* **210**, 2873–2886 (2013).
171. Smith, M. P. *et al.* The immune microenvironment confers resistance to MAPK pathway inhibitors through macrophage-derived TNFα. *Cancer Discov.* **4**, 1214–1229 (2014).
172. Wang, T. *et al.* BRAF inhibition stimulates melanoma-associated macrophages to drive tumor growth. *Clin. Cancer Res.* **21**, 1652–1664 (2015).
173. Mok, S. *et al.* Inhibition of colony stimulating factor-1 receptor improves antitumor efficacy of BRAF inhibition. *BMC Cancer* **15**, 356 (2015).
174. Zeisberger, S. M. *et al.* Clodronate-liposome-mediated depletion of tumour-associated macrophages: a new and highly effective antiangiogenic therapy approach. *Br. J. Cancer* **95**, 272–281 (2006).
175. Gherardi, E. *et al.* Targeting MET in cancer: rationale and progress. *Nat. Rev. Cancer* **12**, 89–103 (2012).
176. Ott, P. A. *et al.* Inhibition of both BRAF and MEK in *BRAF*^{V600E} mutant melanoma restores compromised dendritic cell (DC) function while having differential direct effects on DC properties. *Cancer Immunol. Immunother.* **62**, 811–822 (2013).
177. Ott, P. A. & Bhardwaj, N. Impact of MAPK pathway activation in *BRAF*^{V600} melanoma on T cell and dendritic cell function. *Front. Immunol.* **4**, 346 (2013).
178. Nefedova, Y. *et al.* Activation of dendritic cells via inhibition of Jak2/STAT3 signaling. *J. Immunol.* **175**, 4338–4346 (2005).
179. Cerny-Reiterer, S. *et al.* Long-term treatment with imatinib results in profound mast cell deficiency in Ph$^+$ chronic myeloid leukemia. *Oncotarget* **6**, 3071–3084 (2015).
180. Chow, A. *et al.* Studying the mononuclear phagocyte system in the molecular age. *Nat. Rev. Immunol.* **11**, 788–798 (2011).
181. Srivastava, M. K. *et al.* Myeloid suppressor cell depletion augments antitumor activity in lung cancer. *PLoS ONE* **7**, e40677 (2012).
182. Ries, C. H. *et al.* Targeting tumor-associated macrophages with anti-CSF-1R antibody reveals a strategy for cancer therapy. *Cancer Cell* **25**, 846–859 (2014).
Administration of an M-CSFR mAb substantially reduces TAM numbers and results in objective responses in patients with diffuse-type giant cell tumours.
183. Strachan, D. C. *et al.* CSF1R inhibition delays cervical and mammary tumor growth in murine models by attenuating the turnover of tumor-associated macrophages and enhancing infiltration by CD8$^+$ T cells. *Oncoimmunology* **2**, e26968 (2013).
184. Mitchem, J. B. *et al.* Targeting tumor-infiltrating macrophages decreases tumor-initiating cells, relieves immunosuppression, and improves chemotherapeutic responses. *Cancer Res.* **73**, 1128–1141 (2013).
185. Leuschner, F. *et al.* Therapeutic siRNA silencing in inflammatory monocytes in mice. *Nat. Biotechnol.* **29**, 1005–1010 (2011).
186. Pyonteck, S. M. *et al.* CSF-1R inhibition alters macrophage polarization and blocks glioma progression. *Nat. Med.* **19**, 1264–1272 (2013).
M-CSFR blockade functionally modulates, but does not deplete, TAMs and regresses established glioblastoma in mice.
187. Cortez-Retamozo, V. *et al.* Angiotensin II drives the production of tumor-promoting macrophages. *Immunity* **38**, 296–308 (2013).
188. Petit, I. *et al.* G-CSF induces stem cell mobilization by decreasing bone marrow SDF-1 and up-regulating CXCR4. *Nat. Immunol.* **3**, 687–694 (2002).
189. Cook, R. S. *et al.* MerTK inhibition in tumor leukocytes decreases tumor growth and metastasis. *J. Clin. Invest.* **123**, 3231–3242 (2013).
190. Graham, D. K. *et al.* The TAM family: phosphatidylserine sensing receptor tyrosine kinases gone awry in cancer. *Nat. Rev. Cancer* **14**, 769–785 (2014).
191. Nicodeme, E. *et al.* Suppression of inflammation by a synthetic histone mimic. *Nature* **468**, 1119–1123 (2010).
192. Ivashkiv, L. B. Epigenetic regulation of macrophage polarization and function. *Trends Immunol.* **34**, 216–223 (2013).
193. Wang, H. *et al.* Histone deacetylase inhibitor LAQ824 augments inflammatory responses in macrophages through transcriptional regulation of IL-10. *J. Immunol.* **186**, 3986–3996 (2011).

194. Chen, X. *et al.* Requirement for the histone deacetylase Hdac3 for the inflammatory gene expression program in macrophages. *Proc. Natl Acad. Sci. USA* **109**, E2865–E2874 (2012).
195. Beatty, G. L. *et al.* CD40 agonists alter tumor stroma and show efficacy against pancreatic carcinoma in mice and humans. *Science* **331**, 1612–1616 (2011). **Treatment with an agonist CD40 antibody can control cancer in mice by recruiting antitumour macrophages, independently of T cells.**
196. Dranoff, G. *et al.* Vaccination with irradiated tumor cells engineered to secrete murine granulocyte-macrophage colony-stimulating factor stimulates potent, specific, and long-lasting anti-tumor immunity. *Proc. Natl Acad. Sci. USA* **90**, 3539–3543 (1993).
197. Hammerstrom, A. E. *et al.* Cancer immunotherapy: sipuleucel-T and beyond. *Pharmacotherapy* **31**, 813–828 (2011).
198. Rauch, P. J. *et al.* Innate response activator B cells protect against microbial sepsis. *Science* **335**, 597–601 (2012).
199. Woo, S. R. *et al.* STING-dependent cytosolic DNA sensing mediates innate immune recognition of immunogenic tumors. *Immunity* **41**, 830–842 (2014).
200. Corrales, L. *et al.* Direct activation of STING in the tumor microenvironment leads to potent and systemic tumor regression and immunity. *Cell Rep.* **11**, 1018–1030 (2015).
201. Barber, G. N. STING: infection, inflammation and cancer. *Nat. Rev. Immunol.* **15**, 760–770 (2015).
202. Hanson, M. C. *et al.* Nanoparticulate STING agonists are potent lymph node-targeted vaccine adjuvants. *J. Clin. Invest.* **125**, 2532–2546 (2015).
203. Fu, J. *et al.* STING agonist formulated cancer vaccines can cure established tumors resistant to PD-1 blockade. *Sci. Transl Med.* **7**, 283ra52 (2015). **STING agonists can stimulate DCs to promote antitumour immunity and sensitivity to immune checkpoint blockade therapy.**
204. Conlon, J. *et al.* Mouse, but not human STING, binds and signals in response to the vascular disrupting agent 5,6-dimethylxanthenone-4-acetic acid. *J. Immunol.* **190**, 5216–5225 (2013).
205. Lemos, H. *et al.* STING promotes the growth of tumors characterized by low antigenicity via IDO activation. *Cancer Res.* **76**, 2076–2081 (2016).
206. Hubo, M. *et al.* Costimulatory molecules on immunogenic versus tolerogenic human dendritic cells. *Front. Immunol.* **4**, 82 (2013).
207. Shurin, G. V. *et al.* Chemotherapeutic agents in noncytotoxic concentrations increase antigen presentation by dendritic cells via an IL-12-dependent mechanism. *J. Immunol.* **183**, 137–144 (2009).
208. Cubillos-Ruiz, J. R. *et al.* Reprogramming tumor-associated dendritic cells *in vivo* using miRNA mimetics triggers protective immunity against ovarian cancer. *Cancer Res.* **72**, 1683–1693 (2012).
209. Yu, H. *et al.* STATs in cancer inflammation and immunity: a leading role for STAT3. *Nat. Rev. Cancer* **9**, 798–809 (2009).
210. Ali, O. A. *et al. In situ* regulation of DC subsets and T cells mediates tumor regression in mice. *Sci. Transl Med.* **1**, 8ra19 (2009).
211. Bencherif, S. A. *et al.* Injectable cryogel-based whole-cell cancer vaccines. *Nat. Commun.* **6**, 7556 (2015).
212. Kim, J. *et al.* Injectable, spontaneously assembling, inorganic scaffolds modulate immune cells *in vivo* and increase vaccine efficacy. *Nat. Biotechnol.* **33**, 64–72 (2015).
213. Pittet, M. J. & Weissleder, R. Intravital imaging. *Cell* **147**, 983–991 (2011).
214. Nakasone, E. S. *et al.* Imaging tumor–stroma interactions during chemotherapy reveals contributions of the microenvironment to resistance. *Cancer Cell* **21**, 488–503 (2012).
215. Leimgruber, A. *et al.* Behavior of endogenous tumor-associated macrophages assessed *in vivo* using a functionalized nanoparticle. *Neoplasia* **11**, 459–468 (2009).
216. Chittajallu, D. R. *et al. In vivo* cell-cycle profiling in xenograft tumors by quantitative intravital microscopy. *Nat. Methods* **12**, 577–585 (2015).
217. Klein, A. M. *et al.* Droplet barcoding for single-cell transcriptomics applied to embryonic stem cells. *Cell* **161**, 1187–1201 (2015).
218. Macosko, E. Z. *et al.* Highly parallel genome-wide expression profiling of individual cells using nanoliter droplets. *Cell* **161**, 1202–1214 (2015).
219. Spitzer, M. H. *et al.* An interactive reference framework for modeling a dynamic immune system. *Science* **349**, 1259425 (2015).
220. Calligaris, D. *et al.* Application of desorption electrospray ionization mass spectrometry imaging in breast cancer margin analysis. *Proc. Natl Acad. Sci. USA* **111**, 15184–15189 (2014).
221. Ullal, A. V. *et al.* Cancer cell profiling by barcoding allows multiplexed protein analysis in fine-needle aspirates. *Sci. Transl Med.* **6**, 219ra9 (2014).
222. Weissleder, R. *et al.* Imaging macrophages with nanoparticles. *Nat. Mater.* **13**, 125–138 (2014).
223. Nahrendorf, M. *et al.* Hybrid PET-optical imaging using targeted probes. *Proc. Natl Acad. Sci. USA* **107**, 7910–7915 (2010).
224. Bloy, N. *et al.* Trial watch: dendritic cell-based anticancer therapy. *Oncoimmunology* **3**, e963424 (2014).
225. Lynch, T. J. *et al.* Ipilimumab in combination with paclitaxel and carboplatin as first-line treatment in stage IIIB/IV non-small-cell lung cancer: results from a randomized, double-blind, multicenter phase II study. *J. Clin. Oncol.* **30**, 2046–2054 (2012).
226. Wu, W. C. *et al.* Circulating hematopoietic stem and progenitor cells are myeloid-biased in cancer patients. *Proc. Natl Acad. Sci. USA* **111**, 4221–4226 (2014).
227. Morrison, S. J. & Scadden, D. T. The bone marrow niche for haematopoietic stem cells. *Nature* **505**, 327–334 (2014).
228. Swirski, F. K. *et al.* Identification of splenic reservoir monocytes and their deployment to inflammatory sites. *Science* **325**, 612–616 (2009).
229. Van der Laan, A. M. *et al.* Monocyte subset accumulation in the human heart following acute myocardial infarction and the role of the spleen as monocyte reservoir. *Eur. Heart J.* **35**, 376–385 (2014).
230. Dutta, P. *et al.* Myocardial infarction accelerates atherosclerosis. *Nature* **487**, 325–329 (2012).
231. Bronte, V. & Pittet, M. J. The spleen in local and systemic regulation of immunity. *Immunity* **39**, 806–818 (2013).
232. Kozin, S. V. *et al.* Recruitment of myeloid but not endothelial precursor cells facilitates tumor regrowth after local irradiation. *Cancer Res.* **70**, 5679–5685 (2010).
233. Tedder, T. F. *et al.* Fcγ receptor-dependent effector mechanisms regulate CD19 and CD20 antibody immunotherapies for B lymphocyte malignancies and autoimmunity. *Springer Semin. Immunopathol.* **28**, 351–364 (2006).
234. Bulliard, Y. *et al.* Activating Fc γ receptors contribute to the antitumor activities of immunoregulatory receptor-targeting antibodies. *J. Exp. Med.* **210**, 1685–1693 (2013).
235. Beatty, G. L. *et al.* Exclusion of T cells from pancreatic carcinomas in mice is regulated by $Ly6C^{low}$ $F4/80^{+}$ extratumoral macrophages. *Gastroenterology* **149**, 201–210 (2015).
236. Sluijter, M. *et al.* Inhibition of CSF-1R supports T-cell mediated melanoma therapy. *PLoS ONE* **9**, e104230 (2014).
237. Rolny, C. *et al.* HRG inhibits tumor growth and metastasis by inducing macrophage polarization and vessel normalization through downregulation of PlGF. *Cancer Cell* **19**, 31–44 (2011).
238. Borg, C. *et al.* Novel mode of action of c-kit tyrosine kinase inhibitors leading to NK cell-dependent antitumor effects. *J. Clin. Invest.* **114**, 379–388 (2004).
239. Chang, C. L. *et al.* Immune mechanism of the antitumor effects generated by bortezomib. *J. Immunol.* **189**, 3209–3220 (2012).
240. Priceman, S. J. *et al.* Targeting distinct tumor-infiltrating myeloid cells by inhibiting CSF-1 receptor: combating tumor evasion of antiangiogenic therapy. *Blood* **115**, 1461–1471 (2010).
241. Zhang, W. *et al.* Depletion of tumor-associated macrophages enhances the effect of sorafenib in metastatic liver cancer models by antimetastatic and antiangiogenic effects. *Clin. Cancer Res.* **16**, 3420–3430 (2010).
242. Mok, S. *et al.* Inhibition of CSF-1 receptor improves the antitumor efficacy of adoptive cell transfer immunotherapy. *Cancer Res.* **74**, 153–161 (2014).

Acknowledgements
The authors thank members of the Pittet laboratory and of the Massachusetts General Hospital (MGH) Center for Systems Biology for critical discussions and acknowledge all contributors to the field whose work we could not cite owing to space limitations. This work was supported in part by the Samana Cay MGH Research Scholar Fund, National Institutes of Health (NIH) grants P50-CA86355, R21 CA190344 and R01-AI084880 (to M.J.P.), the Boehringer Ingelheim Fonds (to C.E.) and the Deutsche Forschungsgemeinschaft (DFG) PF809/1-1 (to C.P.).

Competing interests statement
The authors declare no competing interests.

Appendix 2 Supplementary Materials for Chapter 2

A2.1 Supplementary Figures (Chapter 2)

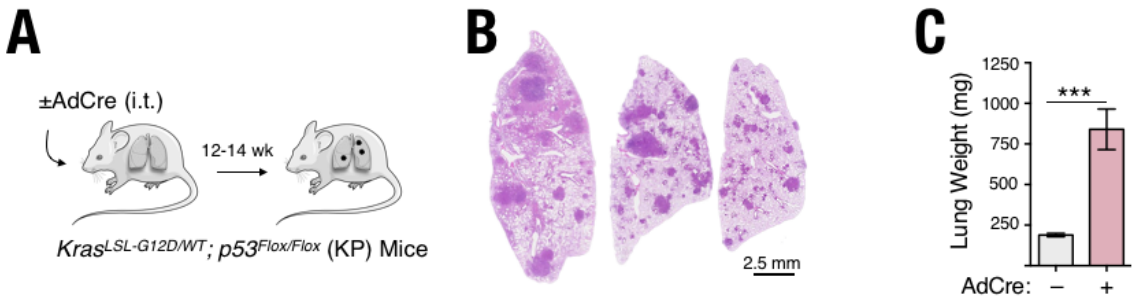

Figure S2.1. Lung adenocarcinoma development in KP mice.

(A) In KP mice lung tumors are initiated through i.t. delivery of AdCre virus.

(B) Representative H&E staining of lung lobe sections from KP tumor-bearing mice (+AdCre) post-tumor induction.

(C) Lung weight of KP lung tumor-bearing and tumor-free mice from OsteoSense experiment presented in Figure 2.1A-B (n = 5-6).
***p<0.001; AdCre: Adenovirus-Cre.

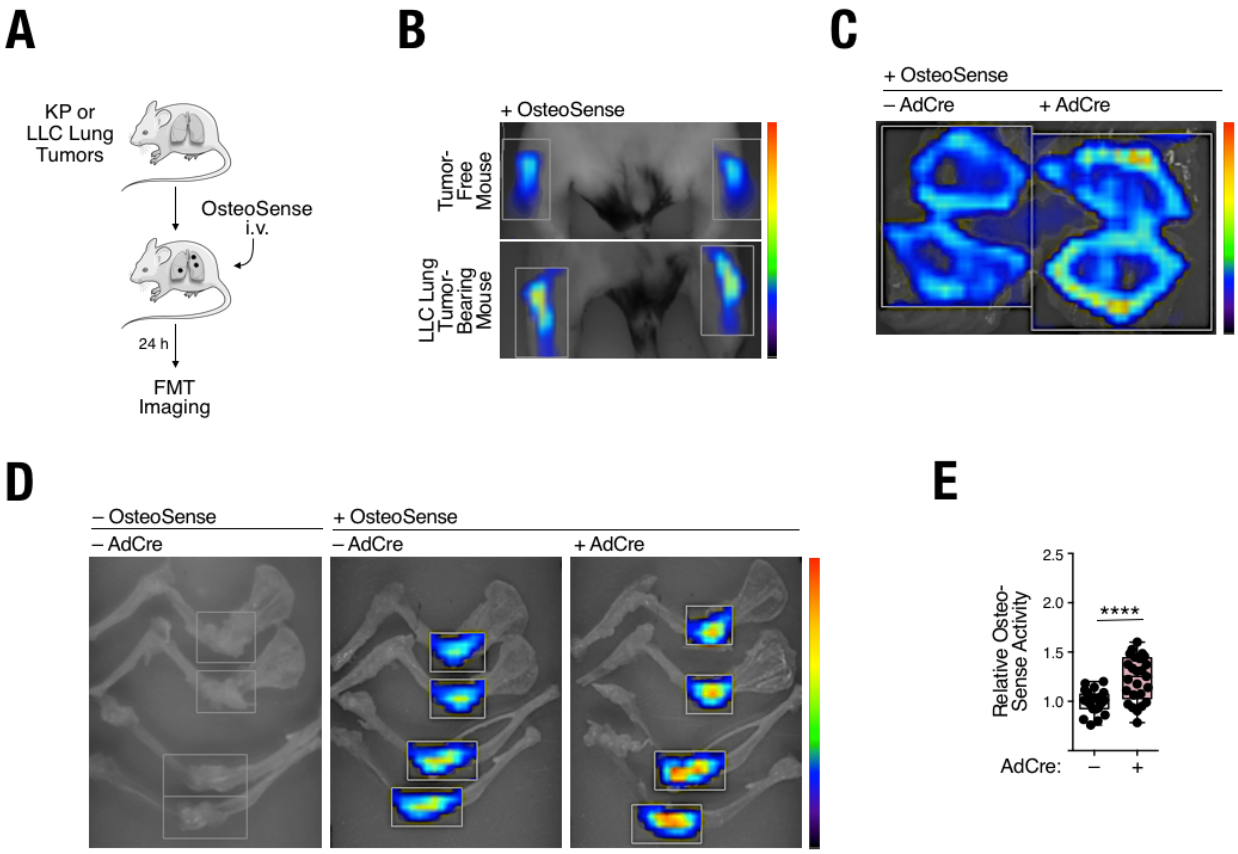

Figure S2.2 Extended OsteoSense FMT analysis.

(A) Experimental outline of OsteoSense injections into KP or LLC lung tumor-bearing or tumor-free mice and subsequent FMT readout.

(B) Representative FMT images of OsteoSense signal in the femoral-tibial joint of LLC tumor-bearing mice and tumor-free control mice.

(C) Representative *ex vivo* FMT OsteoSense signal in the rib cage of KP tumor-bearing (+AdCre) and tumor-free mice (–AdCre).

(D) Representative *ex vivo* FMT images of long bones in mice with or without tumors (±AdCre) and injected or not with OsteoSense (±OsteoSense).

(E) *Ex vivo* OsteoSense signal in bones (n = 24-25) in various compartments including femoral-tibial joint, elbow joint, ribs sternum, vertebrae and pelvic bone. OsteoSense-injected mice as in (A). ****p<0.0001; AdCre: Adenovirus-Cre; FMT: Fluorescence-mediated tomography.

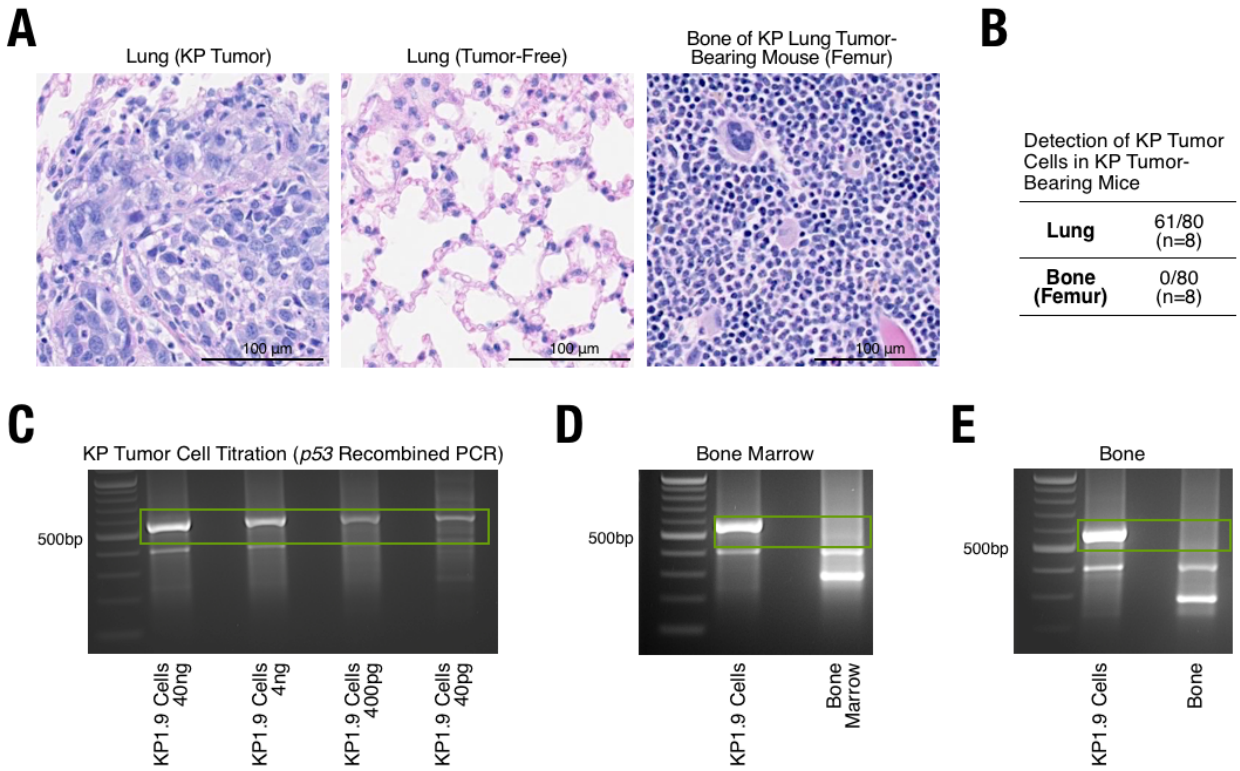

Figure S2.3 KP lung tumor cells do not detectably metastasize to the bone.

(A) Representative images of lung tumor tissue (left), tumor-free lung tissue (middle) and femur from a KP lung tumor-bearing mouse (right).

(B) Scoring of the presence of tumor cells in sections described in (A). 10 sections were scored per mouse (20x), n = 8 mice total per group.

(C) Detection of recombined p53 1lox (only present in tumor cells) by PCR. Recombined p53 1lox band: 612bp; WT band: 288bp; background band: 400 bp. KP.19 tumor cells were titrated to determine the PCR's detection sensitivity (1 cell approximately contains 6 pg of DNA).

(D-E) P53 PCR from DNA isolated from whole bone marrow (D) or calvarial bone (E) of KP lung tumor-bearing mice and compared to DNA isolated from KP1.9 tumor cells as in (C).

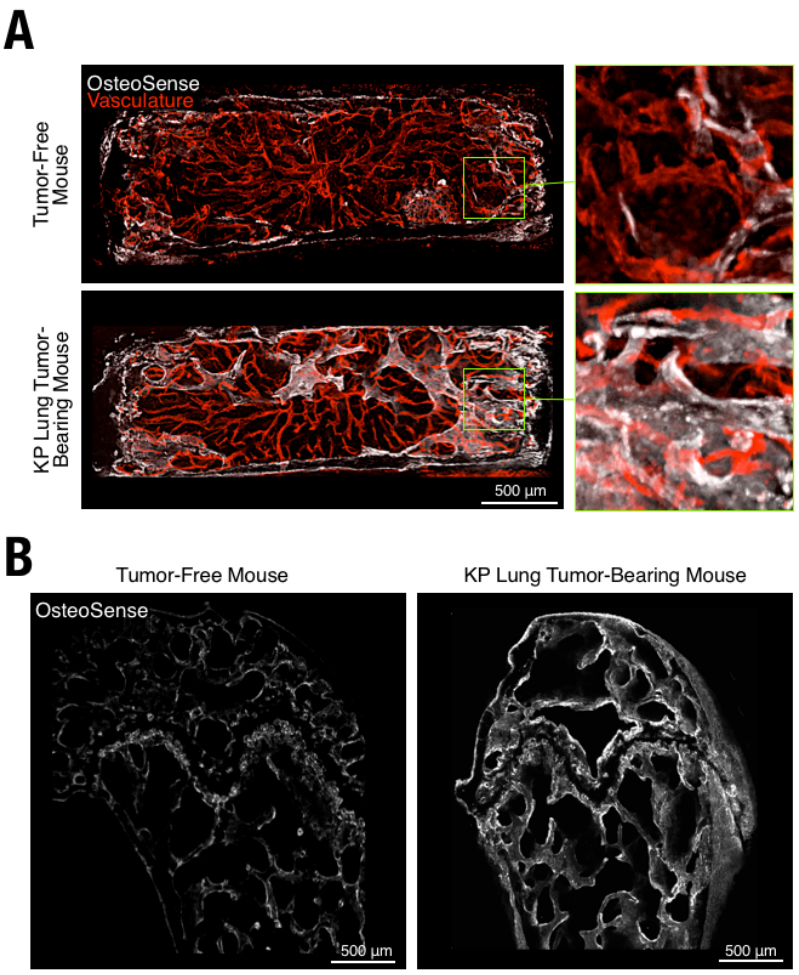

Figure S2.4 Extended OsteoSense microscopy analysis.

(A) Additional confocal microscopy images as presented in Figure 1C of OsteoSense (white) and vasculature signal (red, labeled with anti-Sca-1, anti-CD31 and anti-CD144 mAbs) in the sternum of KP1.9 lung tumor-bearing or tumor-free mice.

(B) *Ex vivo* confocal microscopy of the femur from KP tumor-bearing or tumor-free mice showing OsteoSense signal (white).

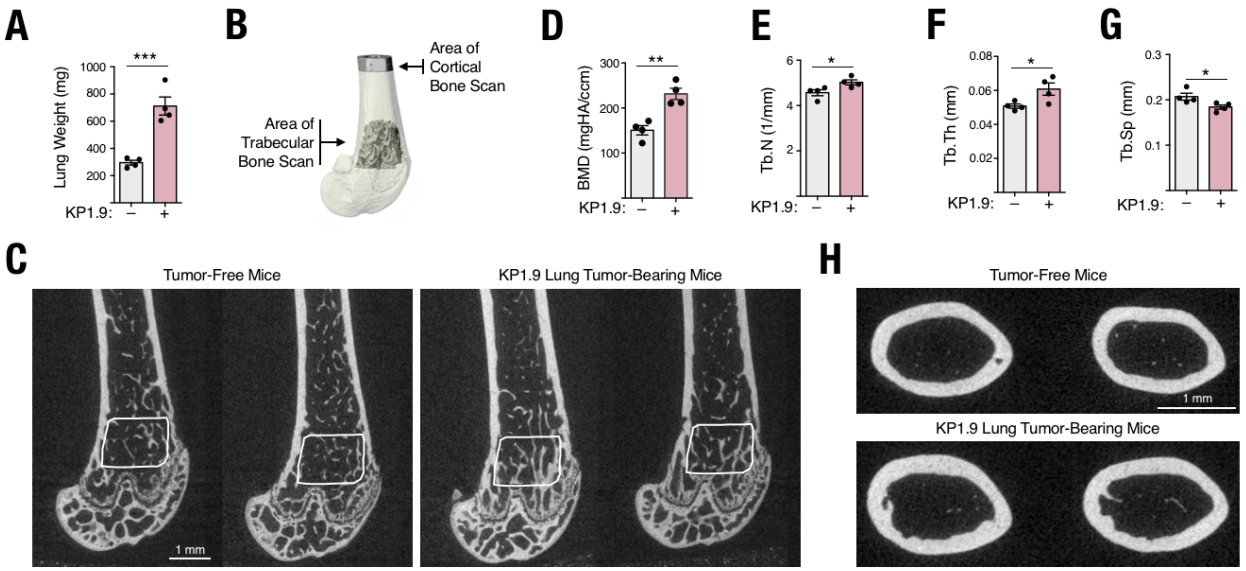

I

				Femoral Metaphysis (Trabecular Bone Architecture)						Femoral Midshaft (Cortical Bone Properties)								
		Body weight (g)	Bone length (mm)	BV/TV (%)	ConnD. (1/mm³)	BMD (mgHA/ccm)	Tb.N (1/mm)	Tb.Th (mm)	Tb.Sp (mm)	Ct. Th (mm)	Ct. TMD (mgHA/ccm)	Ct.Ar (mm²)	Ma.Ar (mm²)	Tt.Ar (mm²)	Ct.Ar/Tt.Ar (%)	Ct. Porosity (%)	pMOI (mm⁴)	Imax (mm⁴)	Imin (mm⁴)
KP1.9 Lung Tumor-Bearing Mice	*Mean*	27.7	15.8	25.0	164.5	231.0	5.02	0.061	0.184	0.190	1135.9	0.950	1.19	2.14	44.5	0.156	0.531	0.357	0.173
	SD	2.4	0.1	2.7	21.8	25.0	0.23	0.007	0.009	0.011	11.1	0.049	0.11	0.10	3.2	0.029	0.030	0.017	0.016
Tumor-Free Mice	*Mean*	27.4	15.3	14.5	129.3	150.0	4.56	0.051	0.207	0.177	1135.4	0.804	1.05	1.85	43.6	0.196	0.401	0.277	0.123
	SD	2.1	0.4	2.4	23.3	21.0	0.26	0.003	0.015	0.010	12.2	0.039	0.13	0.16	2.6	0.016	0.055	0.040	0.016
P value (T-test)		*0.834*	*0.063*	*0.001*	*0.069*	*0.003*	*0.038*	*0.037*	*0.038*	*0.129*	*0.953*	*0.004*	*0.154*	*0.021*	*0.679*	*0.050*	*0.006*	*0.010*	*0.005*

Figure S2.5 Extended µCT analysis.

Lung tumor burden and bone parameters (µCT analysis of femurs) were measured in mice bearing KP1.9 lung tumors.

(A) Lung weight of mice analyzed for µCT, Goldner Trichrome (Figure 2.2A), Von Kossa staining (Figure 2.2D).

(B) Diagram of the trabecular and cortical bone areas that were scanned using µCT in Figure 2.1D and Figure S2.5C-I.

(C) Representative images of µCT scans of trabecular bone. Scale bar 1mm.

(D) Bone mineral density (BMD).

(E) Trabecular number (Tb.N).

(F) Trabecular thickness (Tb.Th).

(G) Trabecular separation (Tb.Sp).

(H) Representative images of µCT scans of cortical bone from tumor-free and KP1.9 lung tumor-bearing mice.

(I) Combination of all parameters investigated in the femurs using µCT and presented in panels A to H. **p*<0.05, ***p*<0.01, ****p*<0.001.

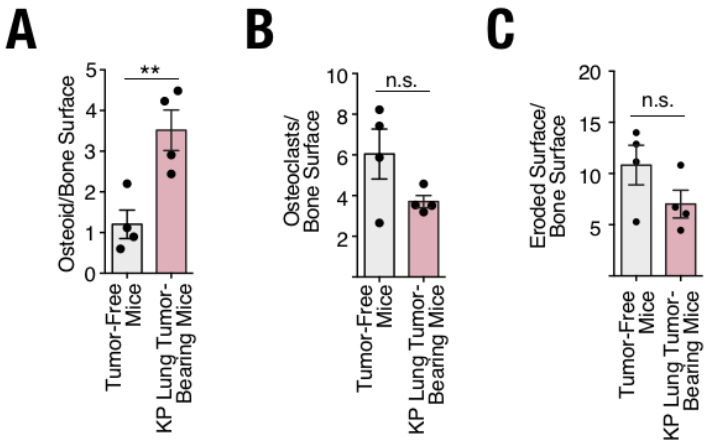

Figure S2.6 Extended bone histomorphometry analysis.

Cellular composition of trabecular bone was evaluated in KP1.9 lung tumor-bearing and tumor-free mice (see also Figure 2.2A).

(A) Osteoid surface/bone surface.

(B) Osteoclasts/bone surface.

(C) Eroded surface/bone surface.

$^{**}p<0.01$, n.s. not significant.

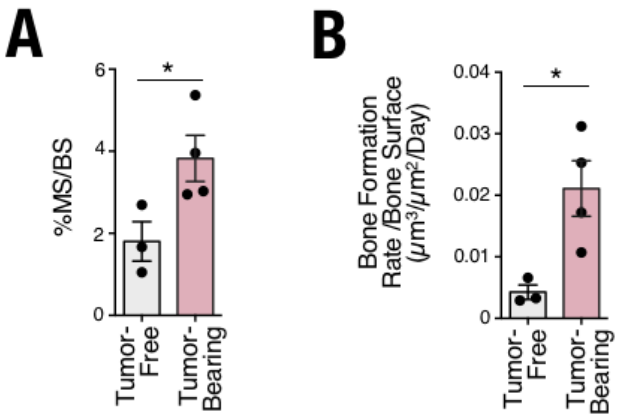

Figure S2.7 *In vivo* bone histomorphometry.

(A) Mineral apposition rate calculated on femur sections of mice (n = 3-4) based on calcein and demeclocycline labeling.

(B) Bone formation rate per bone surface for mice as in (A).
*p<0.05.

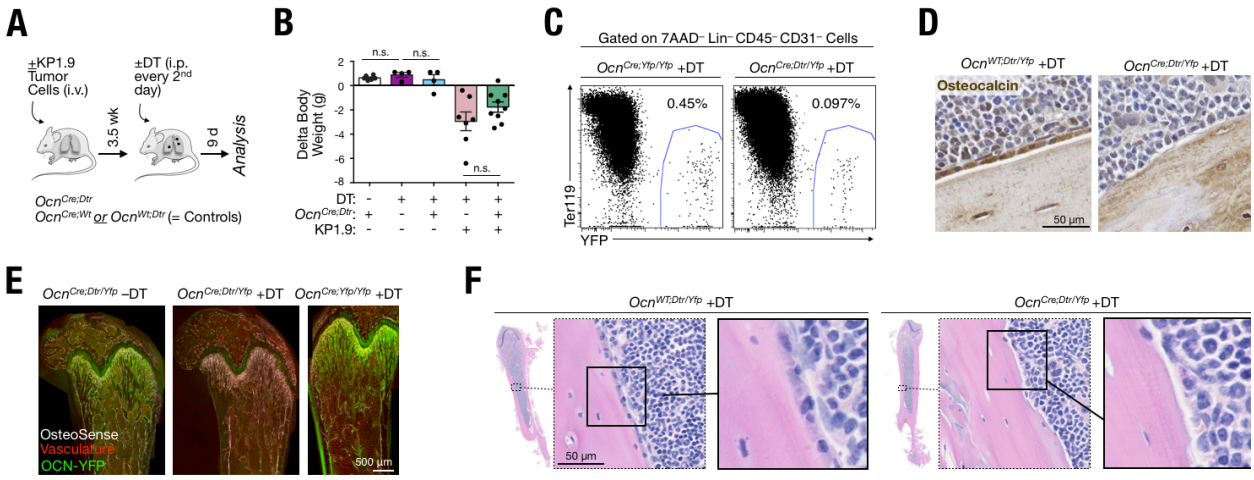

Figure S2.8 Reduction of Ocn⁺ cells in Ocn$^{Cre;Dtr/Yfp}$ mice following diphtheria toxin (DT) treatment.

(A) Experimental outline for DT-mediated Ocn⁺ cell depletion in mice with or without cancer.

(B) Delta body weight of mice treated as in (A) (n = 4-9).

(C) Bone marrow cells from DT-treated Ocn$^{Cre;Dtr}$ and Ocn$^{Cre;Yfp/Yfp}$ mice were stained by flow cytometry to identify YFP⁺ Ocn⁺ cells. Representative dot plots are shown (pre-gated on 7AAD⁻ CD45⁻ CD31⁻ cells).

(D) Representative Ocn IHC staining (brown) on bone sections of control and Ocn$^{Cre;Dtr/Yfp}$ mice.

(E) Representative *ex vivo* confocal microscopy images identify Ocn⁺ cells (green) in bone tissue (femur) of Ocn$^{Cre;Dtr/Yfp}$ mice treated or not with DT and in DT-treated control mice. Bone is visualized by OsteoSense (white) and vasculature (red; stained *in vivo* with anti-CD31, anti-Sca1 and anti-CD144 mAbs).

(F) H&E staining of decalcified paraffin-embedded femur sections of DT-treated control and Ocn$^{Cre;Dtr/Yfp}$ mice with magnification of Ocn⁺ cells.

n.s. not significant.

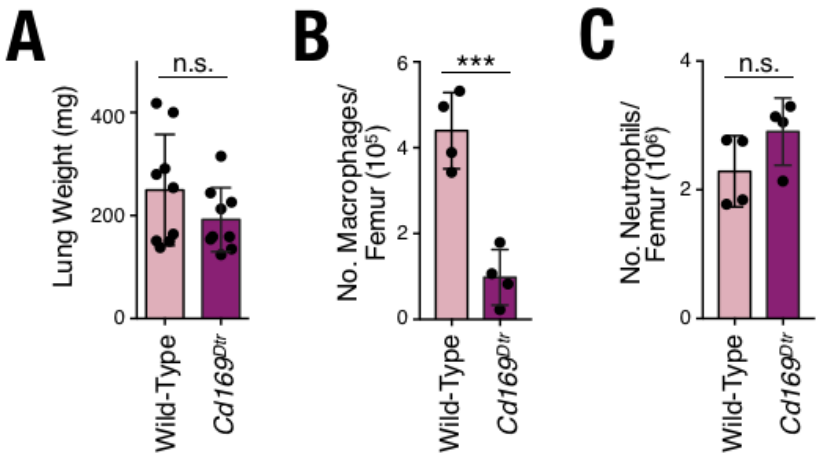

Figure S2.9 Diphtheria toxin (DT) control experiments in bone marrow of DT-treated *Cd169^{Dtr}* mice.

(A) Lung weight as proxy of tumor burden in *Cd169^{Dtr}* mice or control mice (n = 9).

(B) Flow cytometry-based evaluation of bone marrow macrophage cell numbers per femur after DT-treatment in the same mice as in (A) (n = 4).

(C) Flow cytometry-based evaluation of bone marrow neutrophil cell numbers per femur after DT-treatment in the same mice as in (A) (n = 4).

***p<0.001; n.s. not significant.

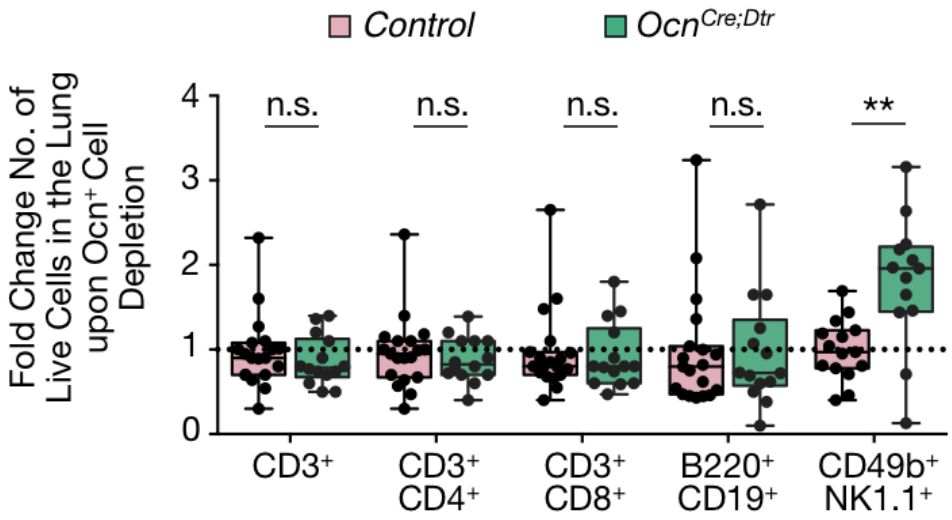

Figure S2.10 KP tumor-infiltrating lymphocyte counts in DT-treated control and *Ocn*$^{Cre;Dtr}$ mice.

Lymphocyte populations including T cells (CD3$^+$, CD3$^+$CD4$^+$, CD3$^+$CD8$^+$), B cells (B220$^+$CD19$^+$) and NK cells (CD49b$^+$NK1.1$^+$) were quantified *ex vivo* by flow cytometry. Results are shown relative to control mice (n = 13-19). *p<0.05; n.s. not significant.

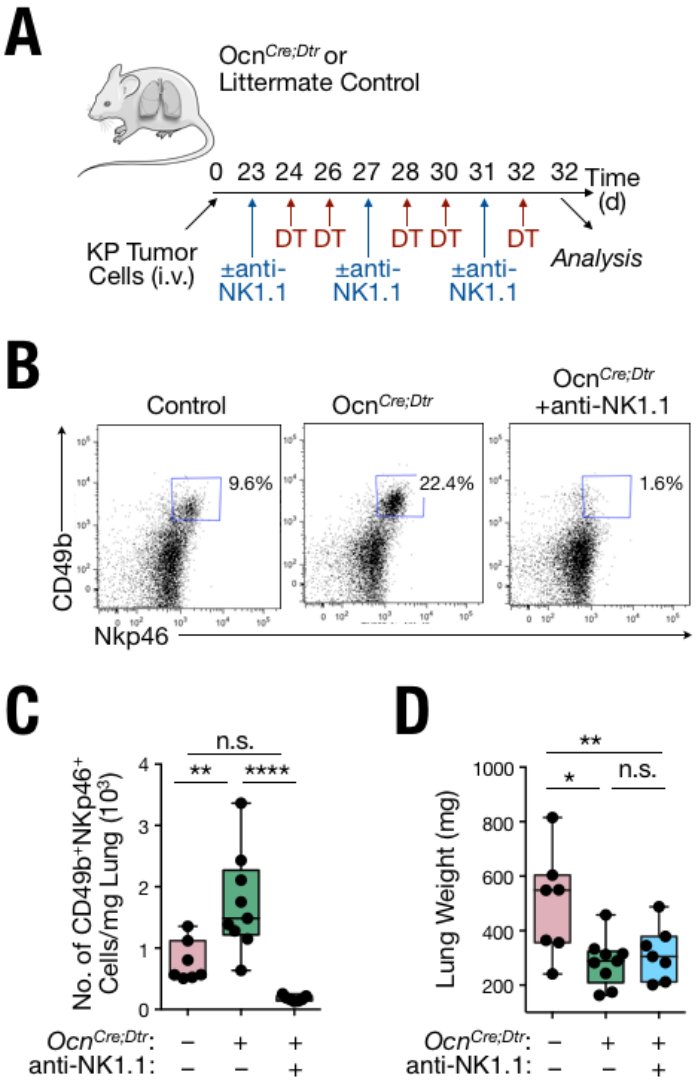

Figure S2.11 NK cell depletion does not restore tumor burden in osteoblast-reduced lung tumor-bearing mice.

(A) Experimental layout of Ab-based NK1.1 cell depletion in KP1.9 tumor-bearing mice with either normal or reduced osteoblasts.

(B) Flow cytometry-based verification of NK cell depletion in lung tumor tissue of *Ocn*$^{Cre;Dtr}$ mice treated as in (A). Representative dot plots are shown.

(C) Quantification of CD49b^{+}Nkp46^{+} cells per mg lung tissue of mice treated as in (A) (n = 7-9).

(D) Lung weight as a proxy for tumor burden in mice treated as in (A) (n = 7-9).

*p<0.05, **p<0.01, ****p<0.0001, n.s. not significant; DT: diphtheria toxin.

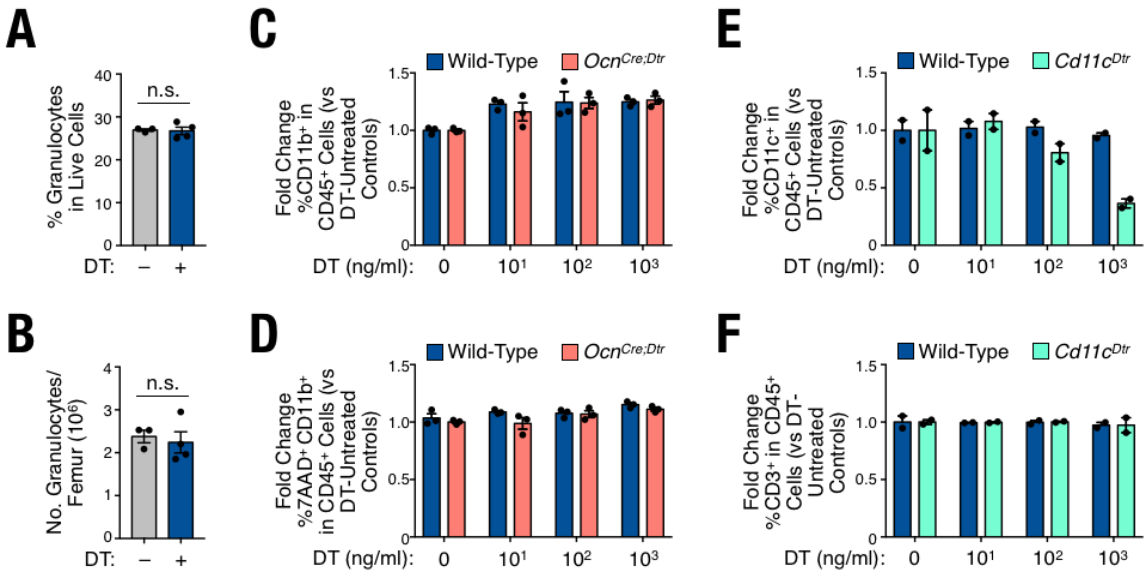

Figure S2.12 Controls for DT- and Cre-DTR-mediated effects on hematopoietic cells.

(A-B) Percentage (A) and cell number per femur (B) of granulocytes, quantified by flow cytometry in bone marrow of wild-type (WT) mice treated or not with DT, treated as in Figure S2.8A (n = 4).

(C) Splenocytes from WT or *Ocn*$^{Cre;Dtr}$ mice were incubated *in vitro* with increasing doses of DT. Percentage of CD11b$^+$ cells among CD45$^+$ cells was calculated by flow cytometry after 20 h of treatment. Results are normalized to untreated cells from each genotype.

(D) Percentage of dead 7AAD$^+$ CD11b$^+$ cells was calculated by flow cytometry as in (C).

(E-F) Positive control experiments to verify DT's ability to kill diphtheria toxin receptor (DTR)$^+$ cells *in vitro*. Splenocytes from WT or *Cd11c*^{Dtr} mice were treated with DT and the percentage of CD11c$^+$ (DTR$^+$) cells (E) and CD3$^+$ (DTR$^-$) cells (F) were calculated by flow cytometry as in (C).
n.s. not significant; DT: diphtheria toxin.

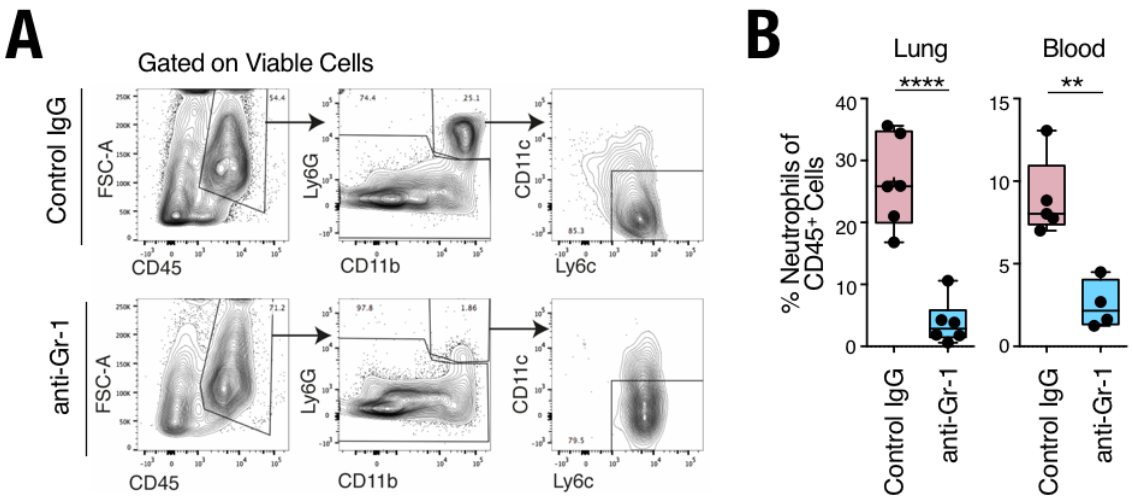

Figure S2.13 Controls for neutrophil depletion.

(A) Representative contour plots of flow cytomety-based evaluation of neutrophils in isolated lung tumor nodules from KP mice. Neutrophils were defined as live $CD45^+$ $CD11b^+$ $Ly\text{-}6G^+$ $CD11c^-$ $Ly\text{-}6C^+$ cells.

(B) The percent of neutrophils defined as in (A) was investigated in lung tumor nodules (left) and blood (right) of KP mice treated with anti-Gr-1 or isotype control mAbs, respectively (6 tumor nodules; n = 3-5 mice/group).
$^{**}p<0.01$, $^{****}p<0.0001$

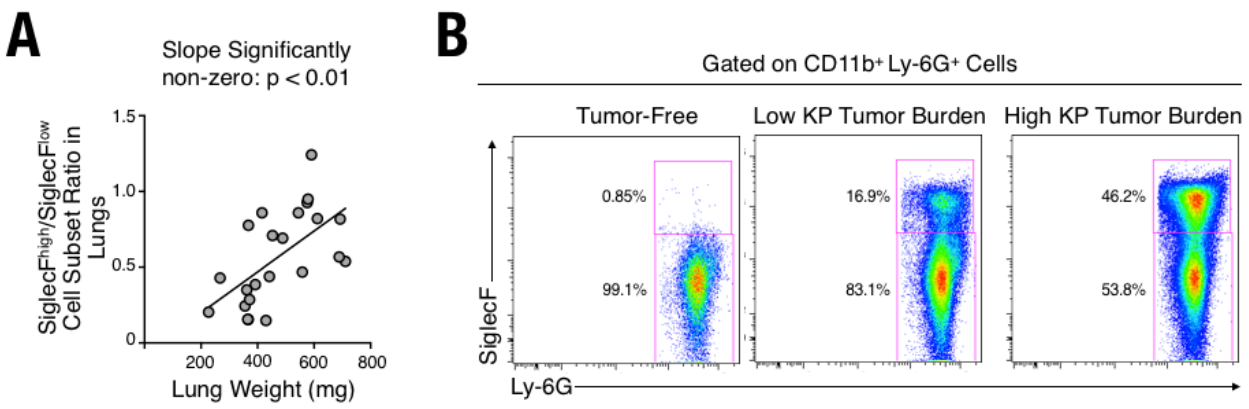

Figure S2.14 SiglecF^{high} granulocytes (CD11b^{+} Ly-6G^{+}) in lung tumors expand during tumor progression.

(A) Ratio between lung SiglecF^{high} and SiglecF^{low} granulocytes (measured by flow cytometry) plotted against lung weight (proxy of tumor burden) of KP1.9 lung tumor-bearing mice (n = 17).

(B) Representative dot plots showing SiglecF vs Ly-6G expression in tumor-free lungs (left), lungs with low KP tumor burden (middle) and lungs with high KP tumor burden (right).

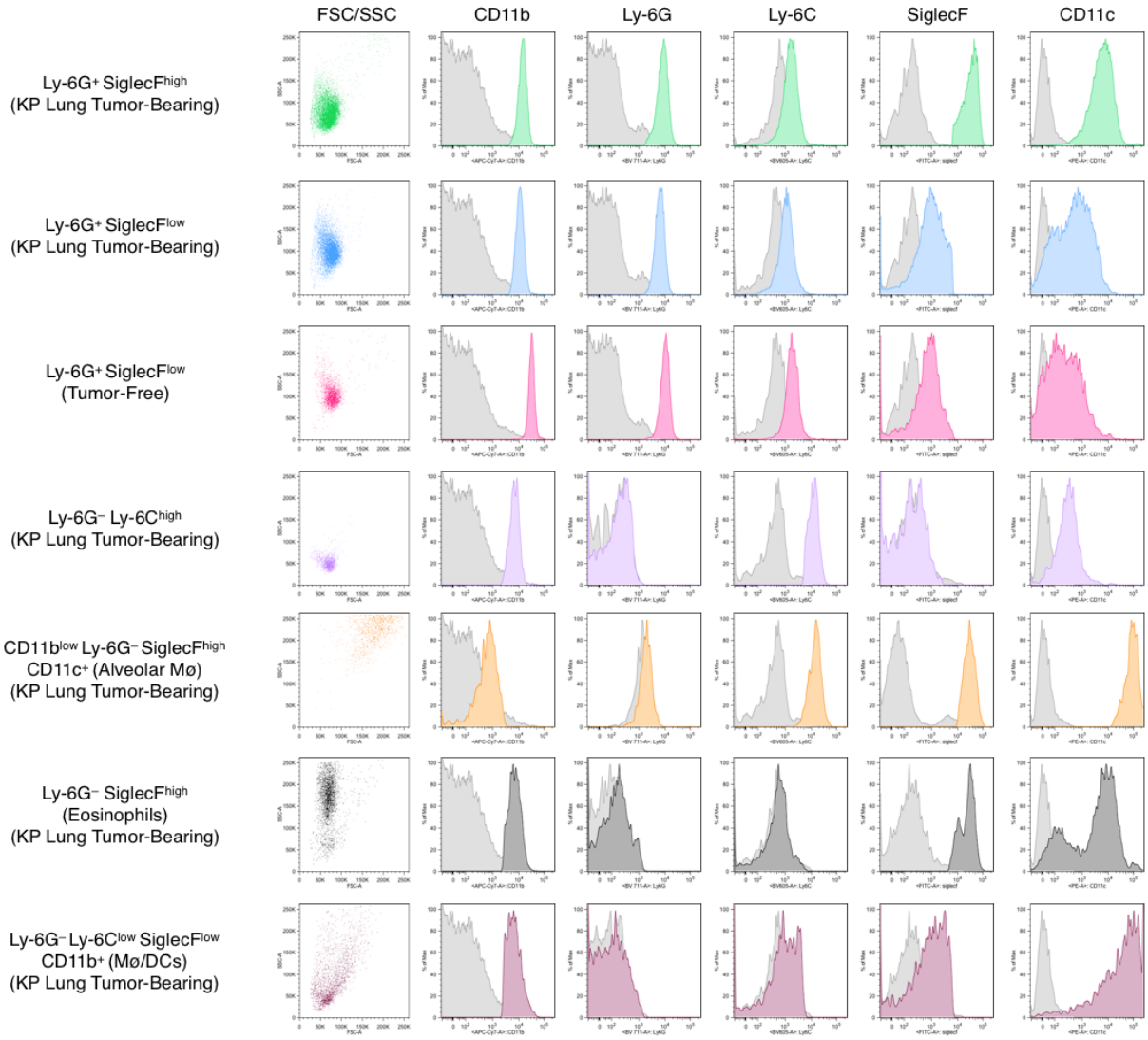

Figure S2.15 Phenotyping of SiglecF^{high} granulocytes in the tumor microenvironment by flow cytometry reveals a neutrophil-like phenotype.

Representative flow cytometry histograms showing forward and side scatter profiles, as well as expression of five cell surface myeloid-associated markers, for: Ly-6G$^+$ SiglecF^{high} cells in KP tumor-bearing mice, Ly-6G$^+$ SiglecF^{low} cells in KP tumor-bearing mice (neutrophil-like), Ly-6G$^+$ SiglecF^{low} cells in tumor-free mice (neutrophil-like), Ly-6G$^-$ Ly-6C$^+$ cells in KP tumor-bearing mice (monocyte-like), CD11b^{low} Ly-6G$^-$ SiglecF^{high} CD11c$^+$ cells in KP tumor-bearing mice (alveolar macrophages), Ly-6G$^-$ SiglecF^{high} cells in KP tumor-bearing mice (eosinophil-like), and remaining Ly-6G$^-$ Ly-6C^{low} SiglecF^{low} CD11b$^+$ cells (including macrophages/dendritic cells). Grey histograms indicate unstained or fluorescence-minus-one (FMO) control samples. According to this analysis, Ly-6G$^+$ SiglecF^{high} cells closely resemble the neutrophil populations found in both healthy and tumor tissue and are distinct from other SiglecF$^+$ cells in the tumor microenvironment, including alveolar macrophages and eosinophils.

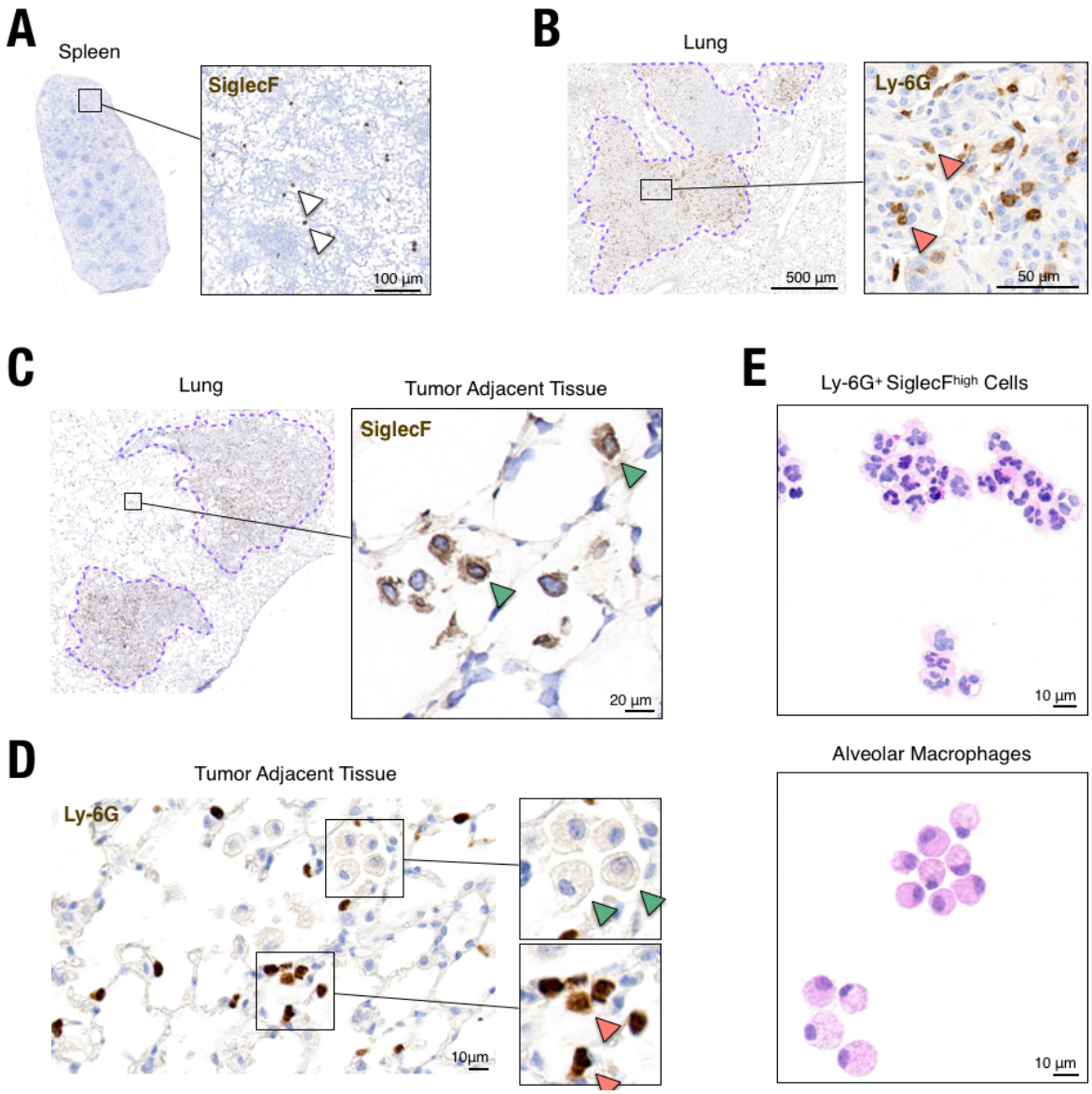

Figure S2.16 SiglecF$^+$ cells in tumor-free areas resemble alveolar macrophages.

(A) IHC based anti-SiglecF mAb validation on murine spleen sections (positive cells are highlighted with white arrowheads).

(B) Ly-6G$^+$ cells (red arrowheads) in KP lung tumor tissue. Tumor area is highlighted with a dotted purple line.

(C) SiglecF IHC staining in lung tumor-free tissue of KP1.9 tumor-bearing mice shows cells with macrophage like phenotype (green arrowheads). Tumor area is highlighted with a dotted purple line.

(D) Ly-6G$^+$ cells (red arrowheads) and Ly-6G$^-$ cells, the latter with macrophage-like morphology, (green arrowheads) in tumor-adjacent lung tissue.

(E) Representative H&E stained cytospins of Ly-6G$^+$ SiglecF^{high} cells (top) and alveolar macrophages (bottom). See also Figure 2.4A.

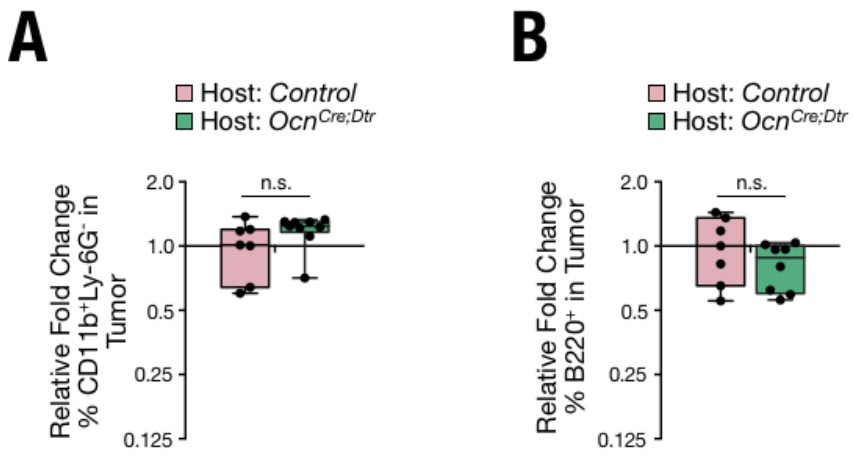

Figure S2.17 CD45.1 myeloid and lymphocyte progeny in osteoblast sufficient and reduced mice.

Fate mapping experiment to evaluate CD45.1$^+$ Lin$^-$ cKit$^+$ hematopoietic precursor's ability to produce myeloid and lymphocyte progeny in lung tumors of CD45.2$^+$ *Ocn*$^{Cre;Dtr}$ or CD45.2$^+$ control mice (see also Figure 2.4E).

(A) Percent of CD11b$^+$ Ly-6G$^-$ cells in lung tumor tissue of *Ocn*$^{Cre;Dtr}$ vs control mice. Data are relative to those observed in host control mice.

(B) Percent of B220$^+$ cells in lung tumor tissue of *Ocn*$^{Cre;Dtr}$ vs control mice, as shown in (A).
n.s. not significant.

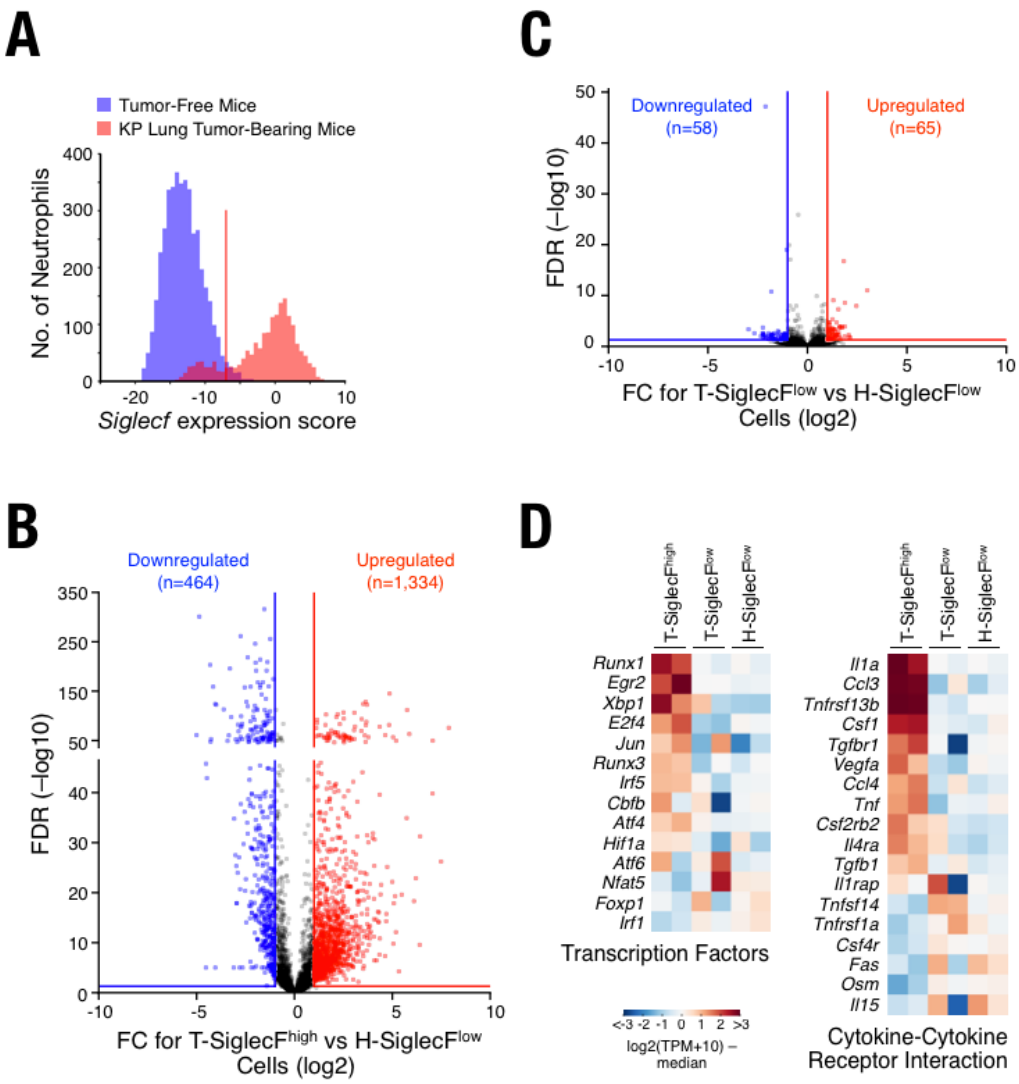

Figure S2.18 Phenotyping of SiglecF^{high} cells in the tumor microenvironment by single cell RNAseq analysis.

(A) SiglecF^{+} gene signature score based on single cell analysis of granulocytes from KP1.9 lung tumors or healthy controls. Hematopoietic cells were FACS sorted and 6,020 cells were defined as granulocytes.

(B) Volcano plot showing significantly differential gene expression between T-SiglecF^{high} and H-SiglecF^{low} cells.

(C) Volcano plot highlighting significantly differential gene expression between T-SiglecF^{low} and H-SiglecF^{low} cells.

(D) Heat-maps showing relative gene expression of levels of transcription factors (left) and cytokine or cytokine receptors (right) in T-SiglecF^{high}, T-SiglecF^{low} and H-SiglecF^{low} cells.

A

Positive Enrichment in T-SiglecF^{high} vs T-SiglecF^{low} Cells

Database	Gene set	NES	FDR q-val
HALLMARK	Myc targets_v1	2.102	0.000
HALLMARK	Myc targets_v2	1.759	0.004
HALLMARK	E2F targets	1.680	0.012
KEGG	N-Glycan biosynthesis	1.706	0.016
KEGG	Pyrimidine metabolism	1.709	0.018
KEGG	Proteasome	1.771	0.021
KEGG	RNA degradation	1.710	0.022
HALLMARK	Oxidative phosphorylation	1.623	0.022
KEGG	Oxidative phosphorylation	1.677	0.022
KEGG	Spliceosome	1.740	0.026
KEGG	Ribosome	1.718	0.026
HALLMARK	DNA repair	1.578	0.026
HALLMARK	Fatty acid metabolism	1.583	0.030
HALLMARK	Unfolded protein response	1.542	0.036
KEGG	Lysosome	1.623	0.040
KEGG	Purine metabolism	1.486	0.129
KEGG	RNA polymerase	1.491	0.133
KEGG	Neuroactive ligand- receptor interaction	1.447	0.172
KEGG	Arachidonic acid metabolism	1.424	0.199
HALLMARK	Mtorc1 siglaning	1.357	0.210
HALLMARK	Tgfb signaling	1.359	0.232
HALLMARK	Peroxisome	1.336	0.235
GO	RNA splicing	1.726	0.160
GO	Energy derivation by oxidation of organic compounds	1.618	0.230

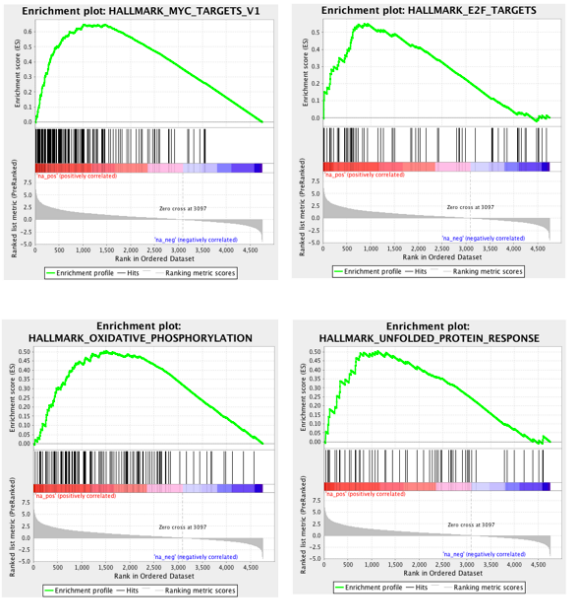

B

Negative Enrichment in T-SiglecF^{high} vs T-SiglecF^{low} Cells

Database	Gene set	NES	FDR q-val
HALLMARK	Interferon alpha response	-1.958	0.019
KEGG	Aldosterone regulated sodium reabsorption	-1.687	0.141
GO	Metal ion transport	-1.841	0.142
HALLMARK	Interferon gamma response	-1.358	0.230

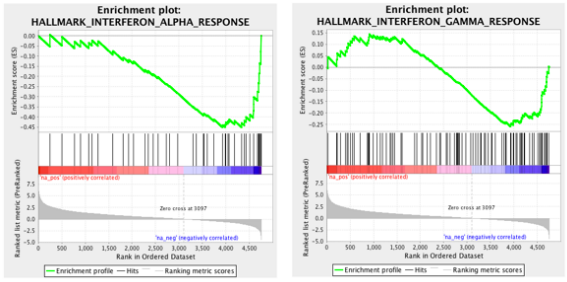

Figure S2.19 Gene set enrichment analysis of T-SiglecF^{high} cells.

(A-B) Positively (A) and negatively (B) enriched gene sets in T-SiglecF^{high} vs T-SiglecF^{low} cells (left). Enrichment plots of selected gene sets (right).

A2.2 Supplementary Tables (Chapter 2)

		KRAS$^+$ NSCLC patients (n=35)	*KRAS*$^+$ control patients (n=35)	*p value*	*KRAS*$^-$ NSCLC patients (n=35)	*KRAS*$^-$ control patients (n=35)	*p value*	All NSCLC patients (n=70)	All control patients (n=70)	*p value*
Age (years)	*Mean*	62.69	62.77	*0.9701*	67.03	66.66	*0.8698*	64.86	64.71	*0.9303*
	SD	9.514	9.564		10.16	8.67		10.01	9.271	
BMI (kg/m2)	*Mean*	27.09	27.34	*0.8572*	26.37	26.32	*0.9703*	26.73	26.83	*0.9137*
	SD	6.647	5.172		6.297	4.435		6.437	4.81	
Number of Men/Women		13/35	13/35		13/35	13/35		26/70	26/70	
Thoracic Bone Density (HU)	*Mean*	170	131.8	***0.0001***	165.4	135.2	***0.0056***	167.7	133.5	***<0.0001***
	SD	42.08	35.47		51.16	35.89		46.56	35.46	

Table S2.1 Information of *KRAS* positive NSCLC patients and control patients.

Control patients had undergone non-contrast chest CT using the same imaging protocols as the *KRAS*$^+$ NSCLC patient group. Both groups were identified and 1:1 matched for sex, age and BMI within ±2 years and ±2 kg/m^2, respectively. Control patients with either active malignancy, chronic illness or medication use that is known to affect bone metabolism were excluded. NSCLC: non-small cell lung cancer; BMI: Body Mass Index.

Table S2.2

SiglecF correlated and anticorrelated genes used for murine neutrophil gene signature.

SiglecF correlated genes (top 50)

Gene name	r (Spearman correlation coefficient)	*p value*
Siglecf	1.00	0.00E+00
Clec4n	0.51	0.00E+00
Hexb	0.48	0.00E+00
Ltc4s	0.46	1.56E-307
mt-Nd1	0.42	1.10E-254
Scimp	0.42	7.83E-253
mt-Nd2	0.41	2.83E-246
B4galt1	0.41	2.43E-237
mt-Nd3	0.40	2.95E-234
Ppia	0.40	3.19E-226
Cdkn1a	0.40	6.52E-225
Bhlhe40	0.39	2.13E-217
mt-Atp6	0.39	2.44E-217
Xbp1	0.37	1.09E-198
AA467197	0.37	2.58E-196
mt-Cytb	0.37	3.30E-195
Ptma	0.36	1.38E-186
Id2	0.36	3.47E-179
Rgs10	0.35	4.09E-177
mt-Nd4	0.35	2.38E-176
Gm11410	0.33	2.66E-156
Rps28	0.33	1.99E-154
Itgax	0.33	1.01E-148
Gpr171	0.32	4.10E-147
Entpd3	0.32	4.16E-147
mt-Co3	0.32	3.71E-146
Mrpl52	0.32	1.62E-139
Bcl2a1b	0.32	4.00E-139
Ms4a6d	0.31	3.08E-134
mt-Nd5	0.31	8.01E-134
mt-Co2	0.31	3.24E-133
Id1	0.31	8.96E-132
Ffar2	0.30	2.56E-125
Atp6v0c	0.30	8.52E-124
Cish	0.30	8.54E-122
Rps18	0.29	1.53E-119
Pald1	0.29	2.16E-118
Runx1	0.29	3.56E-118
RP23-27H19.7	0.29	3.04E-117
Rps29	0.29	3.66E-117
Adgre1	0.29	1.80E-114
Rps17	0.29	6.84E-114
Clec5a	0.29	4.45E-113
Ubash3b	0.29	5.10E-113
Ier3	0.28	9.36E-113
Ski	0.28	5.58E-109
Fam105a	0.28	3.92E-108
Car4	0.28	8.33E-108
Krtcap2	0.28	2.87E-107
Bcl2a1d	0.28	5.45E-106

SiglecF anticorrelated genes (top 50)

Gene name	r (Spearman correlation coefficient)	*p value*
S100a6	-0.40	1.68E-224
Tmsb4x	-0.37	5.83E-191
S100a11	-0.36	1.18E-188
Retnlg	-0.35	2.96E-173
Slpi	-0.35	7.96E-169
Dusp1	-0.34	3.21E-166
Ccl6	-0.33	2.26E-149
Sell	-0.32	2.51E-141
H2-D1	-0.30	8.87E-124
Actg1	-0.29	5.15E-115
Msrb1	-0.28	6.07E-111
Fos	-0.27	2.55E-104
Mmp8	-0.27	3.35E-104
S100a9	-0.27	1.12E-103
Taldo1	-0.26	1.76E-91
Hdc	-0.25	3.07E-87
Grina	-0.24	1.00E-81
Slc16a3	-0.24	6.82E-81
Pglyrp1	-0.24	1.04E-80
Adam8	-0.24	2.58E-80
Slc2a3	-0.23	7.52E-73
S100a8	-0.23	5.48E-72
Clec4d	-0.22	1.65E-68
Lyz2	-0.22	1.90E-66
Anxa2	-0.22	9.11E-66
Lyz1	-0.21	4.68E-63
Osm	-0.21	8.86E-63
Mxd1	-0.21	9.41E-62
Retnlb	-0.21	2.50E-60
Lsp1	-0.20	6.07E-57
Gda	-0.20	9.97E-55
Csf3r	-0.20	3.99E-53
Alox5ap	-0.20	9.97E-53
Lcn2	-0.19	2.30E-49
Txn1	-0.19	7.44E-48
Mmp9	-0.18	2.06E-47
Zfp36	-0.18	1.28E-44
Tpm4	-0.18	2.09E-44
Hp	-0.18	4.64E-44
Samhd1	-0.17	1.48E-41
C5ar1	-0.17	1.87E-41
Selplg	-0.17	1.73E-40
Txn-ps1	-0.17	3.01E-40
Mcemp1	-0.17	4.86E-40
Cd300lb	-0.16	2.60E-37
Rassf3	-0.16	1.02E-36
Emb	-0.16	1.41E-36
Tgfbi	-0.16	8.09E-36
Cxcr2	-0.16	1.21E-35
AB124611	-0.16	4.13E-35

Table S2.3

Differentially expressed genes between T-SiglecF^{high} and T-SiglecF^{low} cells (top/bottom 100 genes).

Differentially expressed genes in T-SiglecF^{high} vs T-SiglecF^{low} cells

Upregulated		*Upregulated (Continued)*	
Gene symbol	**log2 Fold Change**	**Gene symbol**	**log2 Fold Change**
Spp1	8.869	Rcc2	4.384
Ltc4s	7.253	Prss2	4.329
Gpr171	7.078	Psmd3	4.297
Ralgds	6.824	Ctsc	4.253
Rab15	6.553	Tcof1	4.248
Scimp	6.413	Erdr1	4.235
Samm50	6.143	Trio	4.208
Il1a	6.044	Dapk1	4.203
Adamdec1	6.011	Pebp1	4.202
Mreg	5.990	Odc1	4.202
Nme2	5.986	Tmem86a	4.168
Cox16	5.965	Slc23a2	4.146
Cxcl14	5.886	Pald1	4.144
Tmem147	5.862	Abi3	4.135
Lrp1	5.829	Rgs10	4.130
Adora2b	5.642	Siglecf	4.129
H1f0	5.622	Src	4.115
Gm20390	5.608	Snx8	4.105
Tnfrsf13b	5.582	Ccdc86	4.095
Nme1	5.481	Nucks1	4.074
Armc1	5.480	Plagl2	4.063
Tmem126a	5.295	Bola2	4.042
Pnn	5.271	Gm13092	3.999
Mif	5.229	Nt5e	3.983
Ranbp1	5.183	G3bp1	3.964
Hexb	5.183	Slco4a1	3.948
Naa40	5.146	Ddx21	3.944
Lgmn	5.116	Ptgs1	3.943
Ms4a6d	5.109	Sptssa	3.942
Dnajc19-ps	5.102	Ormdl1	3.935
Rpl36a-ps3	5.078	Tubb6	3.932
P2ry14	5.068	Cish	3.929
Pdia4	5.042	Aars	3.928
Acp5	4.965	B4galt1	3.919
Gm4076	4.918	Mcoln1	3.912
S1pr2	4.891	Igfbp6	3.903
Fundc2	4.863	Nop10	3.888
Hspa9	4.825	U2af1l4	3.851
Ffar2	4.796	Mrpl52	3.847
Hsd17b12	4.795	Mrpl42	3.829
Dbi	4.728	Zranb2	3.824
Car4	4.604	Nckap5l	3.815
Elk3	4.558	Ilf3	3.770
Rhoq	4.496	Nhp2	3.755
Mat2a	4.469	Ccl3	3.749
Slc45a4	4.450	Gns	3.739
Ddt	4.408	Rnf187	3.728
E2f4	4.404	mt-Nd2	3.705
Gm14542	4.401	2210016F16Rik	3.675
Polr2m	4.392	Polr2f	3.654

Differentially expressed genes in T-SiglecF^{high} vs T-SiglecF^{low} cells

Downregulated		*Downregulated (Continued)*	
Gene symbol	**log2 Fold Change**	**Gene symbol**	**log2 Fold Change**
S100a11	-2.067	Stx11	-2.474
Camk1d	-2.068	Wfdc17	-2.477
Zfp516	-2.076	Sergef	-2.479
Dck	-2.094	Tbc1d10c	-2.480
Itgal	-2.094	Asprv1	-2.481
Tacstd2	-2.100	Zfp426	-2.484
Lilra6	-2.103	Lcn2	-2.488
Gm5150	-2.110	Gpr141	-2.494
Abtb1	-2.120	S100a6	-2.516
Tnfsf14	-2.129	Fam129a	-2.524
Pira2	-2.140	Prr5l	-2.532
Klf3	-2.143	Trpm2	-2.573
Prkar2b	-2.147	Gm12854	-2.601
Gm11951	-2.152	Slc40a1	-2.632
Ifi27l2a	-2.155	Mrgpra2b	-2.634
Slc16a3	-2.159	Mrgpra2a	-2.666
Coq10b	-2.162	Dhrs9	-2.672
Rtp4	-2.189	Retnla	-2.678
Kif21b	-2.192	6430548M08Rik	-2.728
Chrm3	-2.203	Wfdc21	-2.747
Kcnj2	-2.209	Mgst1	-2.785
Trim30b	-2.216	Pglyrp1	-2.787
Sepp1	-2.239	Lrrk2	-2.805
Gm15448	-2.241	Slc2a6	-2.818
St8sia4	-2.243	Plk2	-2.827
Gm9733	-2.243	Stfa2	-2.835
Sgms2	-2.245	Slc2a3	-2.869
Fosb	-2.251	Ddx60	-2.962
Gm14608	-2.253	Mid1ip1	-3.064
Gm14548	-2.262	Stfa2l1	-3.079
Mcemp1	-2.265	9830107B12Rik	-3.104
Gpcpd1	-2.268	Xdh	-3.125
AB124611	-2.294	Gm7665	-3.176
Sfxn5	-2.294	A530064D06Rik	-3.260
Chil1	-2.296	Slpi	-3.306
Ifitm3	-2.304	Retnlb	-3.332
Gpr65	-2.310	Rnf144a	-3.383
Ndrg1	-2.320	Carns1	-3.428
Snai1	-2.326	AC109138.1	-3.428
Slc44a1	-2.331	Rdh12	-3.433
Arhgap15	-2.333	Sell	-3.695
Gm7676	-2.349	Padi4	-3.703
Tmem71	-2.349	Ifitm6	-3.910
Fam65b	-2.352	Scnn1a	-3.959
Ifitm1	-2.375	Mmp8	-3.985
Steap4	-2.387	Bmx	-4.028
Fyb	-2.413	Retnlg	-4.082
Vnn3	-2.432	Rgs18	-4.154
Adam8	-2.443	Ly6g	-4.277
Klf2	-2.458	Scrg1	-4.379

Table S2.3 (Continued)

Differentially expressed genes between T-SiglecF^{high} and H-SiglecF^{low} cells (top/bottom 100 genes).

Differentially expressed genes in T-SiglecF^{high} vs H-SiglecF^{low} cells

Upregulated		*Upregulated (Continued)*	
Gene symbol	**log2 Fold Change**	**Gene symbol**	**log2 Fold Change**
Scimp	7.881	Erdr1	3.841
Car4	7.496	Hemk1	3.831
Ltc4s	7.070	Havcr2	3.810
Ffar2	7.059	Src	3.806
Pald1	6.423	Pdcd1lg2	3.791
Adamdec1	6.395	Bcl2a1d	3.779
Ms4a6d	6.210	Banf1	3.773
Il1a	6.102	Nt5e	3.772
Cish	5.871	S100a1	3.724
Hexb	5.748	Ccdc86	3.722
Gpr171	5.733	B3gnt7	3.717
H1f0	5.478	Lgmn	3.712
Hbegf	5.330	Tuba1b	3.707
Rgs10	5.190	Xbp1	3.698
Acp5	5.179	Elk3	3.685
Trio	5.148	Gm20390	3.681
P2ry14	5.083	2510009E07Rik	3.681
Spp1	5.049	Gm13092	3.676
Mrpl52	5.034	AA467197	3.674
1810011H11Rik	4.999	Bcl2a1b	3.649
Clec4n	4.863	Cdkn1a	3.641
Siglecf	4.830	Ccl3	3.631
Krtcap2	4.740	mt-Nd3	3.597
Rab15	4.692	Nme2	3.576
Prss2	4.681	Chil3	3.559
Bhlhe40	4.639	Upp1	3.556
Cxcl14	4.626	Icam1	3.554
Tnfrsf13b	4.432	Nme1	3.543
Hsd17b12	4.395	Ggta1	3.541
Adora2b	4.366	Gpr55	3.522
Mif	4.358	Ier3	3.519
B4galt1	4.354	Polr2m	3.517
Mreg	4.338	Igsf8	3.500
Hic1	4.312	Fundc2	3.484
Lsm7	4.311	Bcl2a1c	3.470
Gm10146	4.291	Tubb6	3.458
Ctsc	4.263	Gsto1	3.442
Il1rl2	4.186	mt-Nd2	3.436
Stx3	4.169	mt-Nd1	3.413
Camkk1	4.095	Dtx3	3.393
Ddt	4.090	Eps8	3.380
Igfbp6	4.081	Scd2	3.363
Ralgds	4.065	Aprt	3.357
Fam20c	4.061	Med12l	3.333
Nckap5l	4.054	Uck2	3.306
Entpd3	4.016	Mt1	3.298
Bcl2a1a	3.989	Mfsd12	3.297
Rhoq	3.898	Pebp1	3.279
Ranbp1	3.864	Prdm1	3.273
Mtss1	3.855	Tnfrsf26	3.268

Differentially expressed genes in T-SiglecF^{high} vs H-SiglecF^{low} cells

Downregulated		*Downregulated (Continued)*	
Gene symbol	**log2 Fold Change**	**Gene symbol**	**log2 Fold Change**
Lsp1	-2.004	Abtb1	-2.417
Ceacam2	-2.009	Sepp1	-2.418
Glipr1	-2.014	Lcn2	-2.453
E2f2	-2.025	Slc39a4	-2.466
Rnf125	-2.025	Lrrk2	-2.488
Rab11fip4	-2.028	Glis2	-2.514
Fosb	-2.029	Mcemp1	-2.546
Prkar2b	-2.031	Ifi27l2a	-2.551
AB124611	-2.037	9830107B12Rik	-2.599
Slc40a1	-2.039	Slc16a3	-2.647
H2-Q1	-2.047	Fpr1	-2.657
Taldo1	-2.073	Mgst1	-2.674
Dhrs7	-2.078	Gm12854	-2.711
Hacd4	-2.080	Trpm2	-2.721
Slc44a1	-2.100	Fam129a	-2.723
Tmcc1	-2.104	Rtp4	-2.737
F5	-2.114	Pglyrp1	-2.753
Wfdc21	-2.117	A530064D06Rik	-2.760
Atp1a3	-2.143	Ifi204	-2.777
Chil1	-2.152	S100a6	-2.796
Zfp516	-2.168	Plk2	-2.831
Acta2	-2.177	Thbd	-2.839
Ndrg1	-2.183	Xdh	-2.855
Ddx60	-2.186	Arhgap15	-2.887
Ceacam1	-2.187	Rgs18	-2.908
Zcchc8	-2.190	Slc2a6	-2.925
Pi16	-2.190	Carns1	-2.950
S100a11	-2.204	AC109138.1	-2.950
Vnn3	-2.220	Csad	-2.974
Phf1	-2.225	Gm7665	-2.997
Gm5068	-2.234	Mid1ip1	-3.013
Emb	-2.236	Tmem38a	-3.078
Pira2	-2.239	Slpi	-3.103
Dck	-2.247	Sergef	-3.228
Fyb	-2.249	Slc2a3	-3.293
Gpr141	-2.251	Retnla	-3.353
Gm15448	-2.258	Ifitm6	-3.419
Rccd1	-2.270	Scnn1a	-3.619
Fbxo31	-2.273	Rdh12	-3.996
Lilra6	-2.277	Sell	-4.048
Tmem71	-2.295	Rnf144a	-4.050
Stat4	-2.315	Padi4	-4.152
Stx11	-2.339	Ly6c1	-4.265
Asprv1	-2.345	Bmx	-4.281
6430548M08Rik	-2.345	Retnlb	-4.310
Aqp9	-2.352	Ly6g	-4.478
Dhrs9	-2.356	Scrg1	-4.521
Tpm4	-2.385	Retnlg	-4.526
Apobec1	-2.386	Mmp8	-4.860
Adam8	-2.386	Ly6c2	-5.001

Table S2.3 (Continued)

Differentially expressed genes between T-SiglecF^{low} and H-SiglecF^{low} cells (top/bottom 100 genes).

Differentially expressed genes in T-SiglecF^{low} vs H-SiglecF^{low} cells

Upregulated		*Upregulated (Continued)*	
Gene symbol	**log2 Fold Change**	**Gene symbol**	**log2 Fold Change**
Wfdc17	3.008	Rara	1.109
Ier3	2.462	Csf2rb2	1.099
Anxa7	2.146	Bcl2a1b	1.093
Tuba1b	2.075	Jak2	1.093
Cd244	2.070	Sla	1.092
Socs3	1.883	Fhod1	1.088
Il1rap	1.874	Stfa2	1.084
Entpd3	1.866	Itgax	1.068
Ifitm1	1.831	Csrnp1	1.066
Tagln2	1.748	AI467606	1.055
Xbp1	1.741	Rhob	1.054
Dhrs3	1.664	March1	1.021
B9d2	1.643	Isg20	1.019
Vrk1	1.635	Ddx54	1.011
Aplf	1.623		
Mefv	1.595		
Wfdc13	1.575		
Anxa6	1.559		
Gm7676	1.558		
Il13ra1	1.505		
Bcl2a1d	1.473		
Vim	1.467		
Gpr146	1.455		
Arhgef3	1.445		
Klhl18	1.428		
Phf8	1.405		
Clec4n	1.397		
Rsu1	1.371		
Id1	1.361		
Cd33	1.358		
Oaz2	1.311		
Prr5l	1.309		
Klf2	1.299		
Camk2g	1.288		
Tnfsf14	1.280		
Dennd4a	1.264		
Lrg1	1.262		
Tmc6	1.256		
Glipr2	1.256		
Rnf181	1.246		
Adam19	1.232		
Zfp36l1	1.230		
Lpin2	1.217		
Arid5a	1.185		
1600014C10Rik	1.171		
Nemf	1.158		
Rnasel	1.149		
Il4ra	1.146		
Hlx	1.135		
Stfa2l1	1.112		

Differentially expressed genes in T-SiglecF^{low} vs H-SiglecF^{low} cells

Downregulated		*Downregulated (Continued)*	
Gene symbol	**log2 Fold Change**	**Gene symbol**	**log2 Fold Change**
Gm13349	-1.030	Gm5068	-2.212
Fbxl3	-1.034	Gm9230	-2.220
Ctsd	-1.036	Cfap61	-2.239
Tmem189	-1.050	Ly6c2	-2.241
C3	-1.070	Plcl2	-2.258
Nmrk1	-1.073	H2-Q1	-2.338
Ptms	-1.081	Rccd1	-2.674
Adam28	-1.108	Sema3a	-2.966
Trim50	-1.110		
Mdh2	-1.118		
Casc4	-1.123		
Fpr1	-1.124		
Retn	-1.127		
Lgals9	-1.131		
Cybb	-1.170		
Gfod1	-1.190		
Lamtor4	-1.195		
Bag6	-1.257		
Camsap1	-1.264		
Pgam1	-1.301		
RP23-301L9.8	-1.322		
Elk1	-1.338		
Gm15542	-1.348		
Aqr	-1.378		
Slc27a4	-1.440		
Gm4918	-1.465		
F5	-1.488		
Rap1gap2	-1.521		
Trim56	-1.559		
Smyd4	-1.627		
Thbd	-1.630		
Rab3d	-1.669		
Nans	-1.716		
Tsg101	-1.719		
Ccdc6	-1.732		
Haus8	-1.744		
Smim4	-1.782		
Stard7	-1.793		
Fbxw2	-1.804		
Acta2	-1.819		
Gm10134	-1.836		
Gga3	-1.863		
Ly6c1	-1.945		
Pnoc	-1.961		
Rnaseh2c	-1.967		
Mvk	-2.058		
Thbs1	-2.112		
Xpo1	-2.122		
Gusb	-2.188		
Gm4477	-2.202		

Table S2.4

Human orthologs used for SiglecF^{high} neutrophil gene signature (patient survival analysis, Figure 2.6). Detailed in 2.6 Experimental Procedures.

Murine gene	Human ortholog	TPM SiglecF high	TPM SiglecF low	log 2fc
Spp1	SPP1	467.70	1.00	8.87
Ltc4s	LTC4S	316.28	2.07	7.25
Ralgds	RALGDS	113.33	1.00	6.82
Il1a	IL1A	171.81	2.60	6.04
Adamdec1	ADAMDEC1	286.55	4.44	6.01
H1f0	H1F0	116.58	2.37	5.62
Nme1	NME1	105.70	2.37	5.48
Hexb	HEXB	511.80	14.09	5.18
Car4	CA4	471.90	19.40	4.60
Mat2a	MAT2A	125.93	5.69	4.47
Ctsc	CTSC	191.99	10.07	4.25
Trio	TRIO	206.45	11.17	4.21
Slc23a2	SLC23A2	119.01	6.72	4.15
Rgs10	RGS10	174.08	9.95	4.13
Nt5e	NT5E	205.37	12.99	3.98
G3bp1	G3BP1	124.12	7.96	3.96
Ptgs1	PTGS1	118.72	7.72	3.94
Cish	CISH	378.56	24.85	3.93
B4galt1	B4GALT1	651.04	43.05	3.92
Igfbp6	IGFBP6	114.04	7.62	3.90
Mrpl52	MRPL52	166.50	11.57	3.85
Ccl3	CCL3 /// CCL3L1 /// CCL3L3	1595.07	118.64	3.75
Gns	GNS	320.38	23.99	3.74
Npm1	NPM1	193.55	16.49	3.55
Banf1	BANF1	230.67	21.89	3.40
Gstm1	GSTM5	205.92	20.33	3.34
Itm2c	ITM2C	150.86	15.07	3.32
Bhlhe40	BHLHE40	1081.80	108.43	3.32
Stx3	STX3	111.47	11.69	3.25
Cstb	CSTB	888.49	93.24	3.25
Colgalt1	COLGALT1	117.03	13.91	3.07
Basp1	BASP1	973.89	119.22	3.03
Hmga1	HMGA1	146.23	17.93	3.03
Fam105a	FAM105A	291.04	35.90	3.02
Ski	SKI	408.03	52.61	2.96
Uqcrb	UQCRB	102.89	13.30	2.95
Maff	MAFF	155.47	20.42	2.93
Id2	ID2 /// ID2B	574.31	76.75	2.90
Ppia	PPIA	1498.36	203.81	2.88
Rps19	RPS19	314.85	42.98	2.87
Arl8b	ARL8B	109.43	15.23	2.85
Gsto1	GSTO1	119.06	16.93	2.81
Runx1	LOC100506403 /// RUNX1	353.34	50.32	2.81
Cdkn1a	CDKN1A	2174.77	315.91	2.78
Cct2	CCT2	125.90	18.38	2.78
Vegfa	VEGFA	251.19	37.15	2.76
Itgb1	ITGB1	188.12	27.88	2.75
Ctsb	CTSB	880.50	132.22	2.74
Tnf	TNF	133.12	20.24	2.72
Csf1	CSF1	697.73	106.75	2.71
Atp6v1c1	ATP6V1C1	131.76	20.59	2.68
Eif4e	EIF4E	101.35	16.05	2.66
Rps18	RPS18	562.54	89.67	2.65
Pdia6	PDIA6	120.80	19.48	2.63
Adgre1	ADGRE1	385.17	62.36	2.63
Cd63	CD63	1109.89	180.25	2.62
Cct8	CCT8	150.27	24.69	2.61
Cox7b	COX7B	120.48	19.93	2.60
Dad1	DAD1	113.62	19.42	2.55
Aprt	APRT	136.59	23.64	2.53
Tsg101	TSG101	104.15	18.19	2.52
Anxa5	ANXA5	136.21	24.70	2.46
Eif4g1	EIF4G1	159.72	29.16	2.45
Srsf7	SRSF7	105.49	19.39	2.44
Rps27l	RPS27L	209.49	39.69	2.40
Bag1	BAG1	138.33	27.02	2.36
Rpn2	RPN2	148.57	29.77	2.32
Hic1	HIC1	110.19	22.13	2.32
Prdx1	PRDX1	112.82	22.67	2.32
Scamp3	SCAMP3	117.73	23.92	2.30
Dhx15	DHX15	218.80	44.52	2.30
Egr2	EGR2	430.48	87.95	2.29
Wsb2	WSB2	135.43	28.09	2.27
Sod2	LOC100129518 /// SOD2	118.07	24.67	2.26
Ppm1g	PPM1G	113.07	23.64	2.26
Prpf8	PRPF8	216.63	45.80	2.24
Mtdh	MTDH	296.49	63.06	2.23
Erh	ERH	120.97	25.85	2.23
Eif3a	EIF3A	207.15	44.94	2.20
Rnh1	FLJ23519 /// RNH1	276.42	60.37	2.19
Tgfbr1	TGFBR1	209.94	45.86	2.19
Nabp1	NABP1	120.52	26.41	2.19
Atp6v0c	ATP6V0C	3113.05	687.12	2.18
Aco2	ACO2	144.06	31.92	2.17
Set	SET	230.11	51.09	2.17
Rgcc	RGCC	160.74	36.08	2.16
Mdh2	MDH2	314.92	70.78	2.15
Pcna	PCNA	246.19	55.34	2.15
Sep15	Sep15	226.40	51.49	2.14
Tmed9	TMED9	170.01	39.09	2.12
2010107E04Rik	C14orf2	194.21	45.12	2.11
B4galnt1	B4GALNT1	245.18	57.30	2.10
Bcl2l1	BCL2L1	180.38	42.57	2.08
Chd8	CHD8	103.49	24.46	2.08
Nr4a2	NR4A2	165.41	39.61	2.06
Snw1	SNW1	102.66	24.59	2.06
Itpkb	ITPKB	120.70	29.54	2.03
Rpl15	RPL15	378.81	93.18	2.02
Emc6	EMC6	136.82	33.74	2.02
Casp8	CASP8	113.64	28.07	2.02

Table S2.5

Human orthologs used for SiglecF^{low} neutrophil gene signature (patient survival analysis, Figure 2.6). Detailed in 2.6 Experimental Procedures.

Murine gene	Human ortholog	TPM SiglecFhigh	TPM SiglecFlow	log2fc
Mmp8	MMP8	59.04	934.82	-3.98
Padi4	PADI4	11.61	151.21	-3.70
Sell	SELL	103.95	1346.65	-3.70
Slpi	SLPI	275.16	2721.63	-3.31
Mid1ip1	MID1IP1	18.35	153.54	-3.06
Slc2a3	SLC2A14 /// SLC2A3	67.14	490.34	-2.87
Plk2	PLK2	19.79	140.39	-2.83
Pglyrp1	PGLYRP1	113.30	781.78	-2.79
S100a6	S100A6	1679.50	9609.78	-2.52
Lcn2	LCN2	343.24	1924.96	-2.49
Klf2	KLF2	314.32	1727.35	-2.46
Adam8	ADAM8	148.22	806.14	-2.44
Fam65b	FAM65B	132.98	678.87	-2.35
Slc44a1	SLC44A1	23.60	118.77	-2.33
Ndrg1	NDRG1	35.38	176.69	-2.32
Gpr65	GPR65	84.99	421.29	-2.31
Ifitm3	IFITM3	123.20	608.61	-2.30
Chil1	CHI3L1	67.01	329.10	-2.30
Fosb	FOSB	76.36	363.46	-2.25
St8sia4	ST8SIA4	47.97	227.11	-2.24
Kcnj2	KCNJ2	59.32	274.27	-2.21
Klf3	KLF3	178.63	789.01	-2.14
Tacstd2	TACSTD2	50.89	218.11	-2.10
Itgal	ITGAL	257.89	1100.73	-2.09
Dck	DCK	143.53	612.62	-2.09
Anxa1	ANXA1	187.33	781.91	-2.06
Dfna5	DFNA5	31.57	131.32	-2.06
Dhrs7	DHRS7	92.81	385.50	-2.05
Isg20	ISG20	57.23	237.13	-2.05
Satb1	SATB1	47.25	195.00	-2.05
Pla2g7	PLA2G7	287.40	1180.08	-2.04
Taldo1	TALDO1	353.51	1449.04	-2.04
Aqp9	AQP9	35.92	146.16	-2.02
Mettl9	METTL9	46.08	187.31	-2.02
Tgfbi	TGFBI	190.53	754.55	-1.99
Vim	VIM	111.32	439.94	-1.98
Zyx	ZYX	317.10	1246.57	-1.97
Gadd45a	GADD45A	169.22	657.73	-1.96
Glrx	GLRX	66.76	253.81	-1.93
Tspan13	TSPAN13	92.79	350.00	-1.92
Lsp1	LSP1	343.49	1250.03	-1.86
Cd244	CD244	51.24	184.45	-1.85
Cnn2	CNN2	196.35	705.36	-1.84
Selplg	SELPLG	737.15	2625.29	-1.83
Nedd9	NEDD9	46.10	162.56	-1.82
Apobec1	APOBEC1	45.74	157.07	-1.78
Tmc6	TMC6	30.40	103.08	-1.76
Oaz2	OAZ2	38.38	129.04	-1.75
Mapk14	MAPK14	60.13	201.43	-1.74
Tmem43	TMEM43	49.61	165.60	-1.74
Xpo6	XPO6	65.40	217.46	-1.73
Vrk1	VRK1	102.12	338.02	-1.73
Sap30	SAP30	32.05	104.18	-1.70
Kif23	KIF23	35.94	116.33	-1.69
Hp	HP /// HPR	321.60	1039.71	-1.69
Ulk1	ULK1	57.11	183.33	-1.68
Fas	FAS	37.12	116.70	-1.65
Preb	PREB	81.73	256.42	-1.65
Clip1	CLIP1	91.36	284.74	-1.64
Dusp1	DUSP1	2514.86	7795.10	-1.63
Anxa2	ANXA2	405.71	1249.59	-1.62
Fbxl5	FBXL5	139.03	425.91	-1.62
Tsc22d3	TSC22D3	277.39	849.32	-1.61
Hmgb2	HMGB2	229.59	701.34	-1.61
Ifitm2	IFITM1 /// IFITM2	479.66	1459.02	-1.60
Fgl2	FGL2	628.91	1893.15	-1.59
Il15	IL15	48.89	147.02	-1.59
Cfp	CFP	48.39	144.64	-1.58
Sun2	SUN2	113.60	338.97	-1.58
Nfe2	NFE2	36.57	109.05	-1.58
Mrpl33	MRPL33	172.78	513.54	-1.57
Nadk	NADK	134.34	399.16	-1.57
Pacs1	PACS1	56.07	166.21	-1.57
Adrb2	ADRB2	106.65	315.75	-1.57
Snrk	SNRK	158.93	469.87	-1.56
Gpi1	GPI	86.76	253.14	-1.54
Bcl10	BCL10	118.07	343.10	-1.54
Notch2	NOTCH2	76.53	218.35	-1.51
Ap1s2	AP1S2	58.06	164.11	-1.50
St3gal6	ST3GAL6	61.81	174.40	-1.50
Grina	GRINA	618.93	1741.77	-1.49
Flna	FLNA	214.24	601.22	-1.49
Msrb1	MSRB1	935.04	2610.36	-1.48
Ube2h	UBE2H	97.44	270.18	-1.47
Hdc	HDC	634.15	1754.83	-1.47
Cpd	CPD	168.61	465.23	-1.46
Atxn7l1	ATXN7L1	94.75	259.65	-1.45
Evi2a	EVI2A	49.39	131.69	-1.41
Cdkn1b	CDKN1B	212.41	563.44	-1.41
Gmfg	GMFG	204.60	541.95	-1.41
Tnfrsf1a	TNFRSF1A	374.62	990.72	-1.40
Sorl1	SORL1	520.11	1369.36	-1.40
Fos	FOS	2721.55	7116.00	-1.39
Mxd1	MXD1	1143.78	2982.86	-1.38
Hck	HCK	82.85	214.87	-1.37
Rgs14	RGS14	71.70	185.79	-1.37
Nbeal2	NBEAL2	70.63	182.80	-1.37
Kctd12	KCTD12	376.84	966.40	-1.36
Rasa3	RASA3	118.54	303.14	-1.35
Ugcg	UGCG	41.06	104.87	-1.35

Appendix 3 Supplementary Materials for Chapter 3

A3.1 Supplementary figures (Chapter 3)

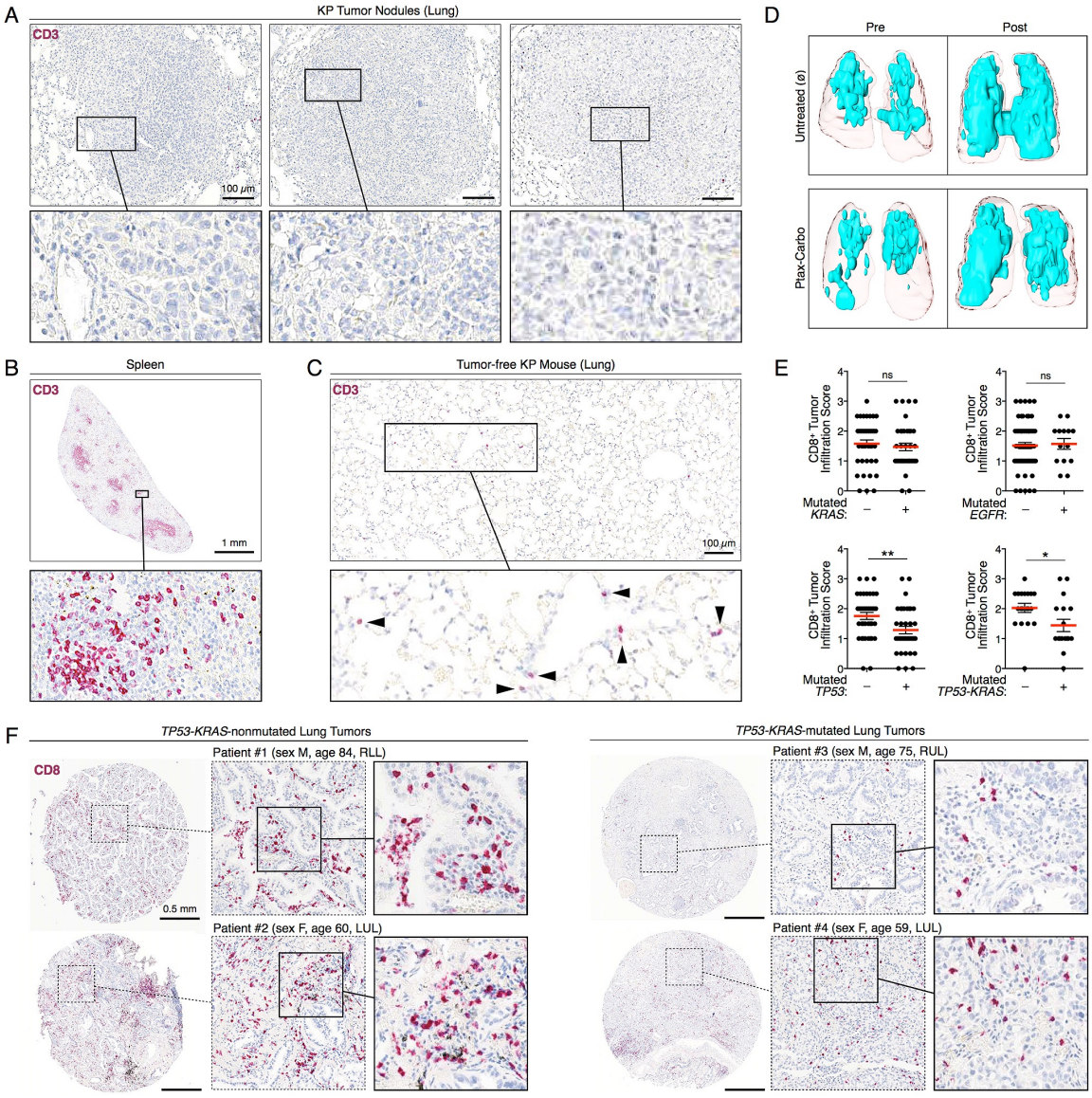

Figure S3.1 KP lung tumors lack infiltrating T cells, resist standard chemotherapy and reflect the human disease.

Related to Figure 3.1.
(**A-C**) Immunohistochemistry (IHC) of $CD3^+$ cells (red) in KP lung tumor nodules and tumor-free lung tissue as well as spleen tissue sections as reference positive control. Arrowheads in (C) show individual stained $CD3^+$ cells. (**D**) Magnetic resonance imaging (MRI)-based detection of lung tumors in KP mice. Surface renderings of MRI images show lungs from mice that were untreated (ø, top) or exposed to paclitaxel and carboplatin (Ptax-Carbo, bottom). Color-coded images show tumors (blue) and lungs (light pink) both pre- (left) and post-treatment (right). (**E**) $CD8^+$ cell tumor tissue infiltration score, based on IHC

Figure S3.1 (Continued)

staining (see F), in lung biopsies (nS=76) from non-small cell lung cancer patients with or without *KRAS* (top, left), *EGFR* (top, right) or *TP53* (bottom, left) mutations. The bottom, right panel shows patient biopsies with *TP53-KRAS* double mutations or without *TP53* and *KRAS* mutations. (**F**) Representative IHC for $CD8^+$ cells (red) in lung tumor patient biopsies from *TP53-KRAS*-nonmutated (left) and *TP53-KRAS*-mutated (right) lung tumors. Patient identifiers are noted above each biopsy (patient #, sex, age, location of biopsy in lung (LUL, left upper lobe; RLL, right lower lobe; RUL, right upper lobe)). Scale bars as indicated. Results are expressed as mean±SEM. *p<0.05; **p<0.01; ns, not significant.

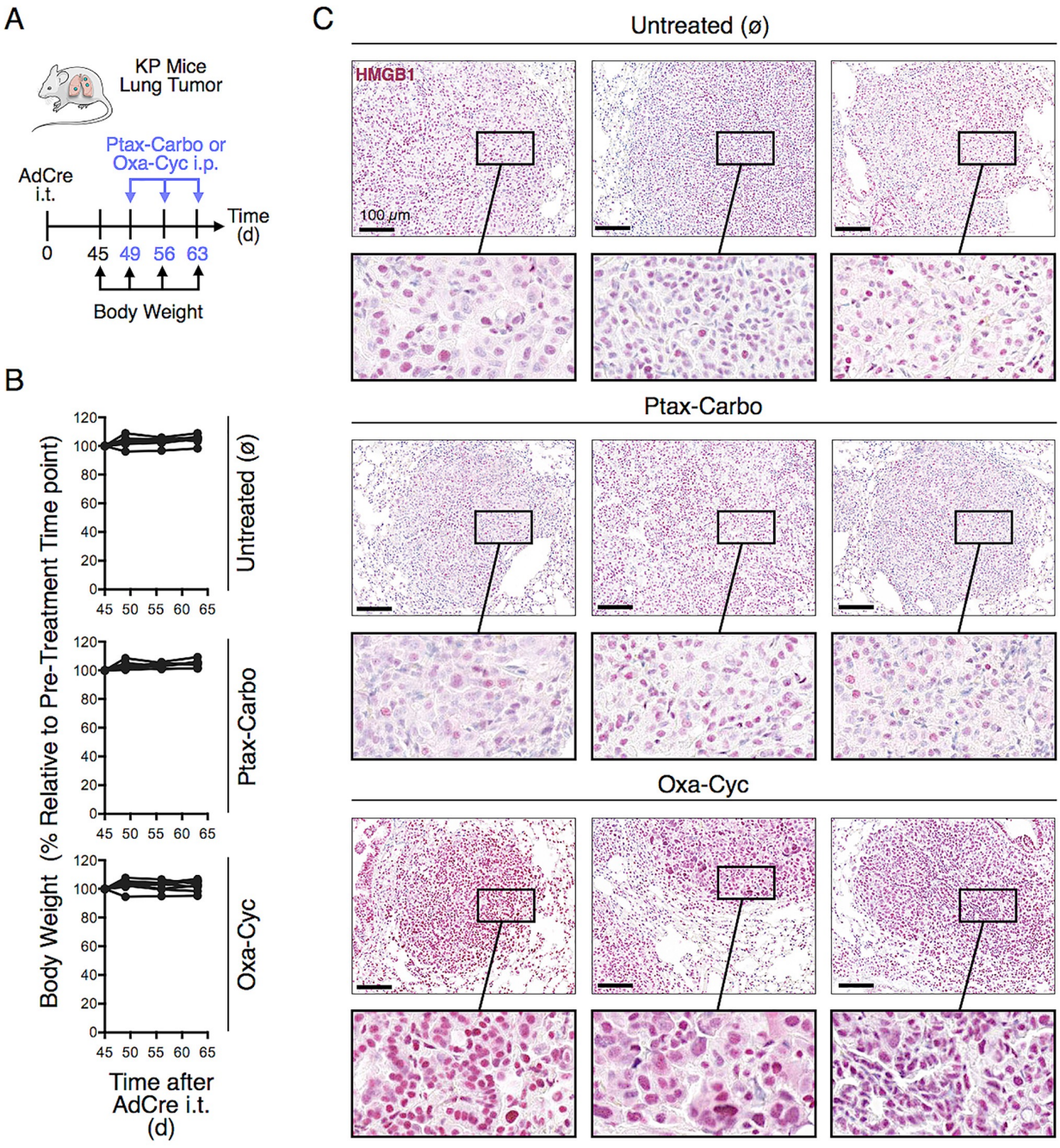

Figure S3.2 Oxa-Cyc chemotherapeutic drugs are well tolerated *in vivo* and increase HMGB1 nuclear staining in lung tumor cells of KP mice.

Related to Figure 3.2.
(**A, B**) Experimental scheme and body weight change of drug-treated KP mice relative to a pre-treatment time point. Each line represents an individual mouse (n=7-8 mice per group) that was either left untreated (ø) or exposed to Ptax-Carbo or Oxa-Cyc. (**C**) Representative HMGB1 (red) IHC staining of KP lung tumor tissue from control mice (ø) or mice exposed to Ptax-Carbo or Oxa-Cyc (see also Figure 2D). Scale bars: 100 μm. Ptax, Paclitaxel; Carbo, Carboplatin; Oxa, Oxaliplatin; Cyc, Cyclophosphamide.

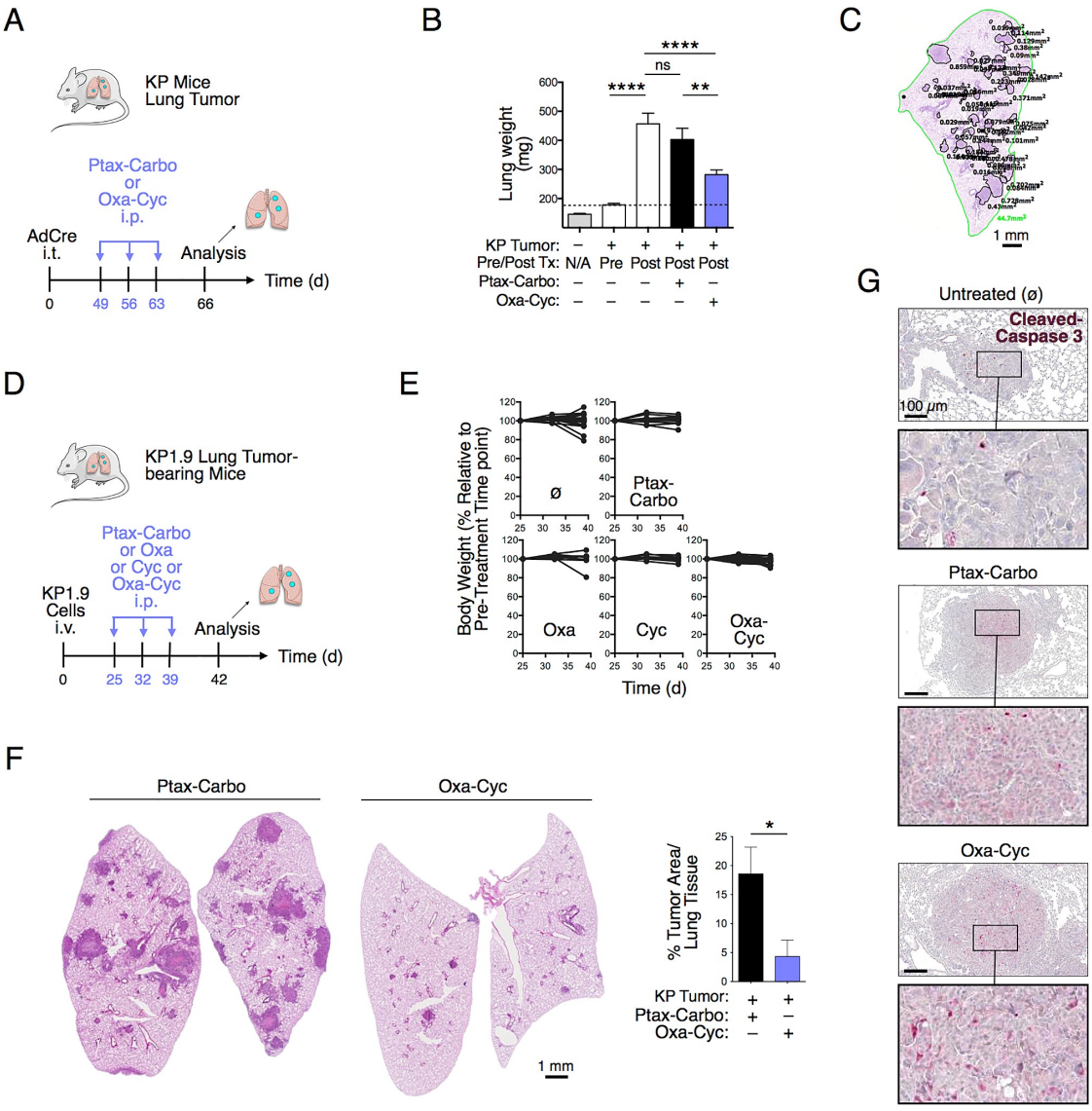

Figure S3.3 Oxa-Cyc suppresses lung tumor progression in KP mice and orthotopic KP1.9 tumor cell-bearing mice.

Related to Figure 3.3.
(**A**) Treatment scheme of tumor-bearing KP mice exposed to either Ptax-Carbo or Oxa-Cyc. (**B**) Lung weight as proxy for tumor burden (Cortez-Retamozo et al., 2012) of mice treated as in (A). 'Pre Tx' and 'Post Tx' define pre (d45) and post (d66) treatment time points, respectively (n=10-34 mice per group). (**C**) Example of lung tumor area quantification on a hematoxylin and eosin (H&E) stained section of a KP lung tumor lobe. Encircled tumor nodules (black) and total analyzed lobe (green) areas were used to calculate % tumor area/lung tissue area. (**D**) Experimental treatment scheme of orthotopic KP1.9 tumor cell-bearing mice treated or not with Ptax-Carbo, Oxa, Cyc or Oxa-Cyc. (**E**) Body weight change of mice treated (as in D) relative to a pre-treatment time point. Each line represents a single mouse (n=8-21 mice per group). (**F**) KP1.9 lung tumor burden identification and quantification in H&E stained lung sections of mice treated (as in D) (n=3-4 mice per group). (**G**) Cleaved-caspase 3 (red) IHC in lung tumor tissue from KP mice left untreated (ø) or treated with Ptax-Carbo or Oxa-Cyc. Scale bars: 100 μm. Results are expressed as mean±SEM. Oxa, Oxaliplatin; Cyc, Cyclophosphamide; Ptax, Paclitaxel; Carbo, Carboplatin; *p<0.05; **p<0.01; ****p<0.0001; ns, not significant; N/A, not applicable.

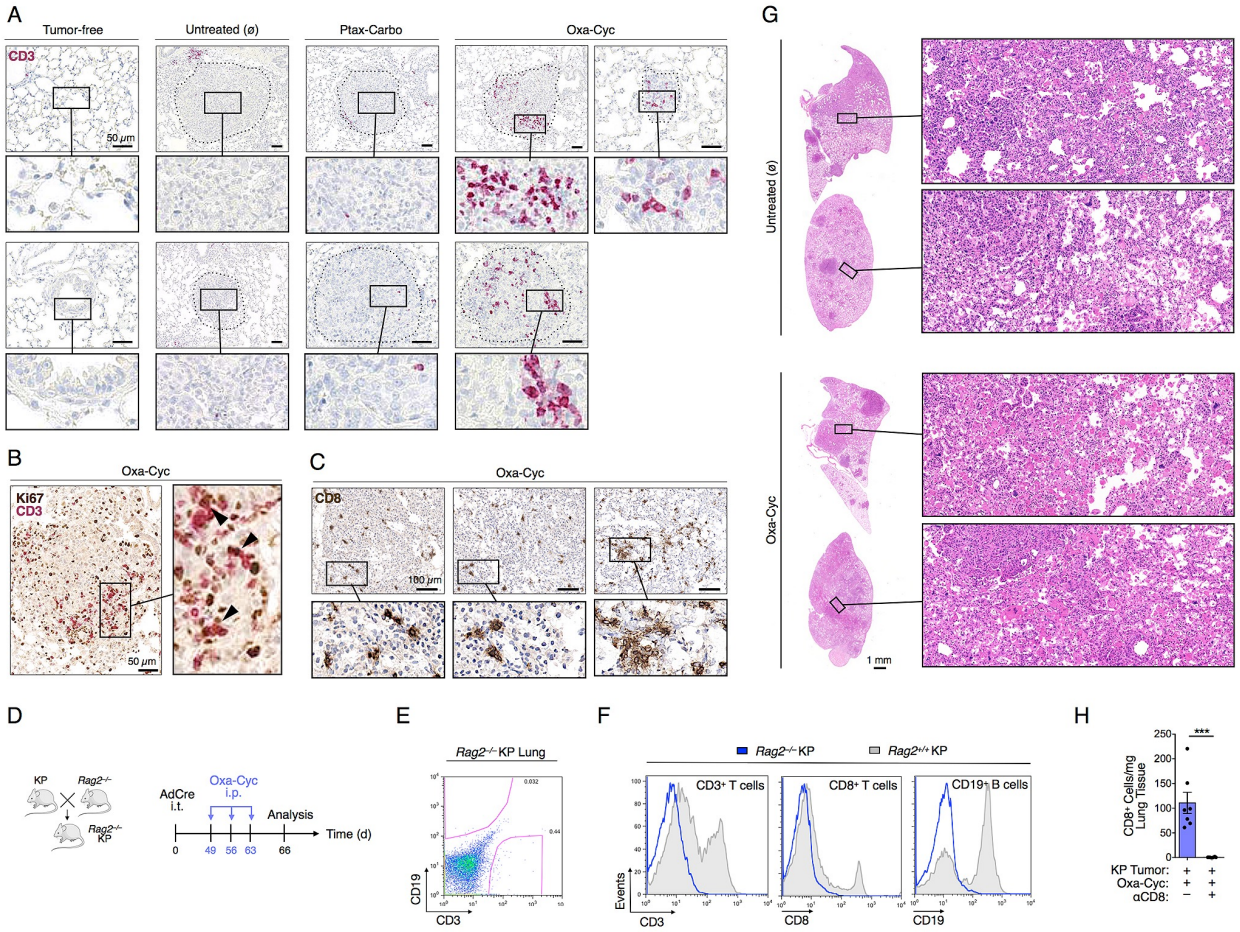

Figure S3.4 Oxa-Cyc instigates CD3⁺ T cell infiltration in lung tumor nodules of KP mice and fails to suppress tumor growth in *Rag2*$^{-/-}$ KP mice.

Related to Figure 3.4.
(**A**) IHC of CD3⁺ cells (red) in tumor-free lungs, tumor tissue of untreated KP mice (ø) and tumor tissue of KP mice exposed to Ptax-Carbo or Oxa-Cyc (see also Figure 4D). Scale bars: 50 μm. (**B**) Multiple IHC showing CD3⁺ (red) and Ki67⁺ (brown) cells in lung tumor tissue from Oxa-Cyc-treated KP mice. Arrowheads show CD3 and Ki67 co-localization. (**C**) IHC of CD8⁺ cells (brown) in lung tumor tissue of Oxa-Cyc-treated KP mice (see also Figure 4E). Scale bars: 100 μm. (**D-F**) Experimental approach (D) and immune profile of *Rag2*$^{-/-}$ KP mice. CD3 and CD19 flow cytometry profile (pre-gated on CD45⁺ cells) of single cell suspensions from lungs of *Rag2*$^{-/-}$ KP mice (E). CD3, CD8 and CD19 flow cytometry profile of single cell suspensions from lungs of *Rag2*$^{-/-}$ KP mice (blue) and spleens of *Rag2*$^{+/+}$ KP mice (grey) (F). (**G**) Lung tumor identification in H&E stained tissue sections of *Rag2*$^{-/-}$ KP mice either left untreated (ø, top) or exposed to Oxa-Cyc (bottom). (**H**) Flow cytometry-based quantification of CD8⁺ cell concentrations in lung tissue of Oxa-Cyc-treated tumor-bearing KP mice that did or did not receive anti-CD8 (αCD8) depleting mAb (n=6-7 mice per group). Results are expressed as mean±SEM. Oxa, Oxaliplatin; Cyc, Cyclophosphamide; Ptax, Paclitaxel; Carbo, Carboplatin; ***p<0.001; ns, not significant.

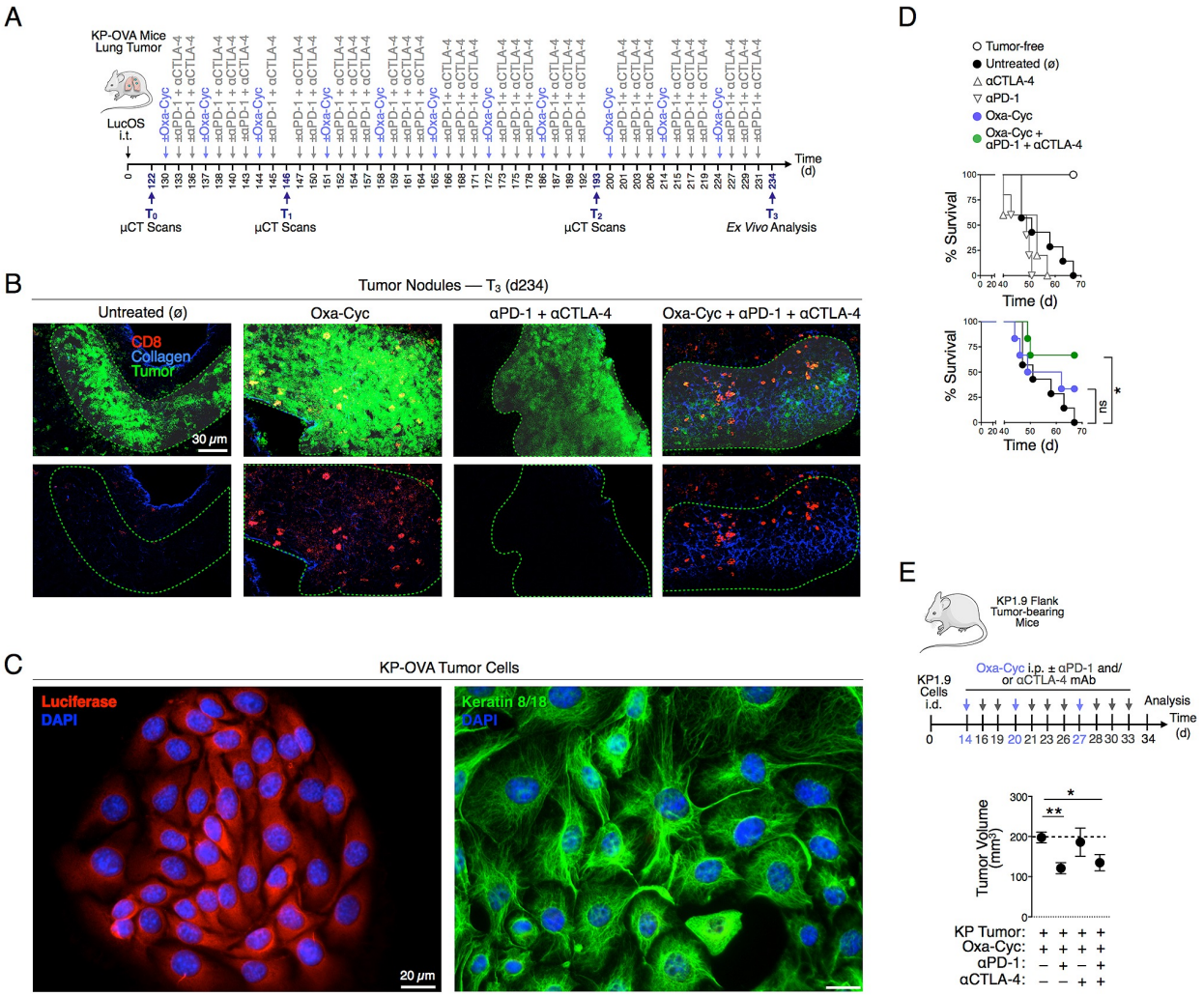

Figure S3.5 Oxa-Cyc fosters tumor nodule infiltration by CD8⁺ T cells and improves tumor growth control and survival of immune checkpoint blockade-treated lung tumor-bearing mice.

Related to Figure 3.6.
(**A**) Treatment scheme of a pre-clinical study in KP-OVA mice. The experimental scheme outlines when Oxa-Cyc (blue) and anti-PD-1 + anti-CTLA-4 (αPD-1 + αCTLA-4) mAbs (grey) were given to tumor-bearing KP-OVA mice. T_0, T_1, T_2 define micro-computed tomography (μCT) imaging time points whereas T_3 designates the *ex vivo* analysis time point (n=5 mice per group). (**B**) Multiphoton microscopy of CD8⁺ cell infiltration (red) into luciferase⁺ tumor areas (green, for visualization highlighted also by dashed green line) of lung tissue isolated from KP-OVA mice at time point T_3 left untreated (ø) or exposed to Oxa-Cyc and anti-PD-1 + anti-CTLA-4 mAbs either alone or in combination. The collagen network is shown in blue (see also Figure 6H). Scale bar: 30 μm. (**C**) *In vitro* validation of anti-luciferase Ab (red, left) used in (B) to detect luciferase-expressing tumor cells derived from KP-OVA mice. In addition, these KP-OVA tumor cells (KP-OVA-CG1 cell line) were stained with keratin 8/18 (green, right) to verify their epithelial origin. Cell nuclei (DAPI staining) are shown in blue. Scale bars: 20 μm. (**D**) Survival of tumor-free C57BL/6 mice (n=3) and of mice bearing orthotopic KP1.9 tumors, left untreated (ø) or exposed to anti-PD-1 mAbs, anti-CTLA-4 mAbs, Oxa-Cyc or combinations thereof (n=5-7 mice per group). (**E**) Oxa-Cyc improves anti-PD-1 mAb treatment in KP1.9 tumor-bearing mice. Experimental outline and tumor volume of Oxa-Cyc-treated mice also treated with anti-PD-1, anti-CTLA-4 or anti-PD-1 + anti-CTLA-4 mAbs (n=4-5 mice per group). Results are expressed as mean±SEM. Oxa, Oxaliplatin; Cyc, Cyclophosphamide; *p<0.05; **p<0.01; ns, not significant.

A3.2 Supplementary Experimental Procedures (Chapter 3)

Mice

Kras$^{LSL\text{-}G12D/+}$*;Trp53*$^{flox/flox}$ (referred to as KP) mice were used as a conditional mouse model of non-small cell lung cancer[1] and bred in our laboratory in the 129 background. Several experiments were replicated using KP mice in the C57BL/6 background. *Rag2*$^{-/-}$ mice (C57BL/6 background), *Tlr4*$^{-/-}$ mice (C57BL/6 background) and C57BL/6 wild type mice were obtained from the Jackson Laboratory. BALB/c wild type mice were purchased from Janvier Labs and C57BL/6 wild type mice (used for the MCA205 fibrosarcoma model) were obtained from Harlan Laboratories. All animal experiments were approved by the Massachusetts General Hospital Subcommittee on Research Animal Care, except experiments in BALB/c and MCA205-bearing C57BL/6 mice that were approved by the Ethical Committee of the Gustave Roussy Cancer Campus (Villejuif, France).

Tumor Models

To induce lung adenocarcinoma, KP mice were infected with an adenovirus expressing Cre recombinase (AdCre) by intratracheal intubation and inhalation (i.t.) or intranasal instillation (i.n.) as described previously[1]. AdCre was purchased from the University of Iowa Gene Transfer Vector Core. Treatment of i.t. infected 129 KP mice started on week 7 and of C57BL/6 KP mice on week 9 after AdCre infection, when lung adenocarcinomas are established and detectable by micro-computed tomography (μCT). Treatment of 129 KP mice infected i.n. started 12 weeks after AdCre infection. To study tumor-antigen specific T cell responses, lentiviral vectors (LucOS) containing two peptides of the ovalbumin (OVA) antigen ($OVA_{257\text{-}264}$ (CD8 epitope), $OVA_{323\text{-}339}$ (CD4 epitope)) and the SIY (SIYRYYGL) antigen fused to luciferase were used for KP mouse infection (these mice are referred to as KP-OVA mice). Lung tumors that develop in LucOS infected KP-OVA mice express the OVA and SIY antigens and luciferase as a tumor cell marker[2]. Treatment of i.t. infected 129 KP-OVA mice started 19 weeks after LucOS infection

when lung tumors are established and detectable by μCT. When indicated, murine KP1.9 lung tumor cells were injected into C57BL/6 mice intravenously (i.v., $2.5x10^5$ cells in 100 μl PBS) to develop orthotopic tumors. These mice reproducibly show macroscopic lung tumor nodules at 3 weeks post tumor cell injection. Evaluation of lung tumor burden in all three models included noninvasive high-resolution μCT or magnet resonance imaging (MRI) as detailed below (see section: Micro-Computed Tomography (μCT) and Magnet Resonance Imaging (MRI)), as well as lung weight measurements and histological analyses based on hematoxylin and eosin (H&E) staining of explanted lung tissue. In selected experiments, KP1.9 tumor cells were injected intradermally (i.d., $1x10^6$ cells in 50 μl PBS) into the flank of C57BL/6 mice; tumor dimensions were measured with a digital caliper and tumor volumes defined as ∏/6 x length x $width^2$. CT26 colon carcinoma cells given subcutaneously (s.c., $8x10^5$ cells in 100 μl PBS) into BALB/c mice and MCA205 fibrosarcoma cells injected (s.c., $8x10^5$ cells in 100 μl PBS) into C57BL/6 mice were followed over time using caliper-based measurements; tumor sizes were calculated as length x width.

Cell Lines

The lung adenocarcinoma cell line KP1.9 was derived from lung tumors of C57BL/6 KP mice and was kindly provided by Dr. A. Zippelius, University Hospital Basel, Switzerland. The lung adenocarcinoma cell lines KP L1-3, KP L1-5 and KP L2-9 were derived from 129 KP mouse lung tumors whereas the lung adenocarcinoma cell line KP-OVA-CG1 was generated from lung tumor tissue of C57BL/6 KP-OVA mice; these cell lines were all established in our laboratory. All lung adenocarcinoma cell lines were cultured in Iscove's DMEM media supplemented with 10% fetal bovine serum (FBS) and 1% penicillin/streptomycin. The colorectal carcinoma cell line CT26, obtained from ATCC, was maintained in RPMI 1640 medium supplemented with 10% FBS, 2 mM L-glutamine, 100 IU/ml penicillin G sodium salt, 100 μg/ml streptomycin sulfate, 1 mM sodium pyruvate and 1 mM non-essential amino acids. Murine fibrosarcoma MCA205 cells were cultured in RPMI 1640 medium supplemented with 10% FBS,

2 mM L-glutamine, 100 IU/ml streptomycin sulfate, 1 mM sodium pyruvate, 1 mM non-essential amino acids and 1 mM HEPES buffer.

Human Tumor Samples

Sections from paraffin-embedded biopsies of lung resections (n=76) from non-small cell lung cancer patients with known *KRAS* and *EGFR* gene mutation status were obtained from the Department of Pathology at Massachusetts General Hospital. TP53 immunohistochemistry (IHC) was conducted as described in detail below with anti-p53 monoclonal antibody (mAb; clone DO-7, Leica). *TP53* wild type or mutational status was assessed based on TP53 pattern expression as described[3] using the following scoring system: score 0 (complete absence of staining indicates *TP53* null mutation); score 1 (focal nuclear expression in up to 50% of tumor cells presents *TP53* wild type); score 2 (nuclear overexpression in more than 50% of tumor cells represents *TP53* missense mutation). Biopsies with score 0 or score 2 were categorized as *TP53* mutants and biopsies with score 1 as *TP53* wild type. All p53-stained biopsies were reviewed in a blinded manner. CD8 IHC was performed with anti-CD8 mAb clone C8/144B (DAKO) on subsequent sections and CD8 positive cell infiltration in tumor areas scored in the following categories: score 0 (less that 5% CD8 staining); score 1 (5-15% CD8 staining); score 2 (15-25% CD8 staining); score 3 (more than 25% CD8 positive stained cells). Two independent blinded evaluations were performed and presented as mean $CD8^+$ cell tumor infiltration score.

Micro-Computed Tomography (μCT) and Magnet Resonance Imaging (MRI)

Mice infected with AdCre or LucOS plasmids were anonymized and tumor burden noninvasively evaluated through *in vivo* lung imaging at different time points (pre- and post-treatment). During the measurements, the mice were anesthetized with isoflurane gas inhalation. μCT was acquired on a Siemens' Inveon system with a 80 kVp 500 mA cone beam μCT over 360 projections and reconstructed by modified Feldkamp cone beam reconstruction algorithm into isotropic 78 micron voxels (512 x 512 x 768 matrix). μCT tumor quantification was

performed by manual segmentation in OsiriX software (The OsiriX foundation). For the μCT 3D renderings, in AMIRA software (Visage Imaging Inc), the lungs were segmented using threshold bounded region growing with a seed placed in the lung. Respiratory-gated RARE T1 weighted MRI images were acquired on a Bruker pharmascan 4.7 tesla magnet with a echo time of 14.1 ms and a repetition time of 900 ms on a 256 x 256 x 18 image matrix (voxel size of 0.215 mm x 0.156 mm x 1.0 mm). Tumor quantification of MRI images was performed by region-based thresholding of the lungs, which were manually segmented utilizing OsiriX software. The threshold was determined as the average normal lung value (n=3). Surface renderings of MRI images were done using AMIRA software. μCT and MRI tumor quantification was performed blinded to treatment groups.

Mouse Histology, Immunohistochemistry (IHC) and Immunofluorescence Microscopy

For histological analysis of tumor burden in mice, lung tissues of tumor-bearing and control animals were harvested, formaldehyde-fixed and paraffin-embedded following standard procedures. Consecutive sections were prepared and stained with H&E using the Thermo Scientific™ Shandon Varistain™ Gemini ES Automated Slide Stainer (Thermo Scientific).

For IHC, lung tissue sections were prepared and dried at 60°C for 1 h, dewaxed and rehydrated before treated with heat-induced epitope-retrieval (HIER) during which the sections were incubated in 10 mM sodium-citrate (pH6.0) or 10 mM Tris (pH9.0) buffered solutions containing 0.05% Tween heated at 120°C for 2 min. To obtain consistent and reliable staining, automated staining systems (LabVision Autostainer 360, Thermo Scientific or Leica Bond, respectively) were used. The sections were cooled down to room temperature (RT) and placed in the Autostainer. To efficiently destroy all endogenous peroxidase and alkaline phosphatase activity in the tissue, the sections were pretreated using BLOXALL endogenous enzyme blocking solution (Vector Laboratories) for 10 min. After a blocking step with normal horse or goat serum, the sections were incubated with the individual primary Abs for 1 h followed by secondary ImmPRESS polymer detection systems (Vector Laboratories) according to the

manufacturers protocol. The Vulcan Fast Red Chromogen Kit 2 (red staining, Biocare Medical) and the DAB Plus Substrate System (brown staining, Thermo Scientific) were applied as substrates. Hematoxylin was used for counterstaining. Primary Abs used for IHC were: rabbit anti-CD3 (clone SP7, Abcam), rabbit anti-Ki67 (clone SP6, Abcam), rabbit anti-HMGB1 (polyclonal, Abcam), rabbit anti-cleaved-caspase 3 (polyclonal, Cell Signaling), rat anti-mouse CD4 (clone 4SM95, eBioscience). For multiple IHC, following HIER and blocking steps, the individual Abs were incubated consecutively using the chromogens indicated above. Based on the nuclear staining intensity of HMGB1 in lung tissue of KP mice with or without drug treatment, blinded scoring of stained sections was performed with the following criteria: score 0 (no HMGB1 nuclear staining); score 1 (low HMGB1 nuclear staining); score 2 (intermediate HMGB1 nuclear staining); score 3 (high HMGB1 nuclear staining).

For anti-CD8 IHC on murine lung tissue, frozen tissue sections of ~6 µm thickness were prepared using a cryostat (Leica). These sections were air-dried for at least 1 h and then fixed in acetone for 10 min at -20°C. Before incubation with Abs, the sections were rehydrated and permeabilized with PBS containing 0.2% Triton-X100 for 5 min, followed by several washes in PBS. Two primary rat anti-mouse CD8 Abs were used in parallel (clone YTS169.4, Abcam and clone 53-6.7, BD Biosciences) that both showed similar staining patterns. The NanoZoomer 2.0-RS slide scanner system (Hamamatsu) was used for image documentation.

For immunofluorescence microscopy, KP-OVA-CG1 cells were grown on coverslips, fixed in pre-cooled (-20°C) methanol for 5 min, followed by an incubation in -20°C cold acetone for 30 sec. After the cells had air dried, they were rehydrated in PBS and permeabilized using 0.2% Triton-X100 in PBS (5 min), rinsed in PBS and then incubated with the primary Abs (rabbit anti-firefly luciferase (polyclonal, Abcam) or mouse anti-keratin 8 (clone Ks 17.2, Progen) and mouse anti-keratin 18 (clone Ks 18.174, Progen)) in a wet chamber for 1 h. After three washing steps with PBS at RT for 5 min, the samples were incubated with the secondary Ab for 45 min, followed by an incubation step with DAPI (Sigma) for another 5 min. The cells were then washed twice with PBS for 5 min and once with Aqua dest. for 1 min at RT, air dried and then

mounted with Fluoromount-G (Southern Biotech). Immunofluorescence microscopic images were recorded with an Axiophot microscope (Carl Zeiss). The KP-OVA-CG1 cell line was used to validate the anti-luciferase Ab as a tool to stain for luciferase expression as a marker for KP-OVA tumor cells *in situ*, used in the multiphoton microscopy approach (see section: Multiphoton Microscopy). Accordingly, KP-OVA-CG1 cells derived from lung tissue of KP-OVA mice are positive not only for luciferase as expected but also for keratin 8/18 (i.e. of epithelial origin).

Multiphoton Microscopy

Small lung pieces containing tumor-bearing and tumor-free tissue areas were carefully removed from KP lungs using scalpels. After fixation with methanol/DMSO (4:1) for 1 h at 4ºC, lung tissues were permeabilized/stained with 1% Triton-X100, 10% goat serum, FcBlock (TruStain fcX™ anti-mouse CD16/32, clone 93, BioLegend) and unconjugated anti-luciferase Ab (polyclonal, Abcam; for the specificity of this Ab to stain tumor cells in KP-OVA mice see section: Mouse Histology, Immunohistochemistry (IHC) and Immunofluorescence Microscopy) at 4ºC overnight in 500 µl of PBS, while rocking. Samples were washed twice (0.5% Triton-X100, 10% goat serum at 4ºC overnight/overday in 5 ml of PBS, rocking) and then incubated with 1% Triton-X100, 10% goat serum, FcBlock, goat anti-rabbit IgG-APC (Life Technologies) and directly conjugated Abs (CD8a-PE, clone 53-6.7, BioLegend) at 4ºC overnight in 500 µl of PBS while rocking. Before imaging, lung tissue pieces were washed twice (5 ml PBS containing 0.5% Triton-X100, 10% goat serum, at 4ºC overnight/overday, rocking). Stained lung pieces were whole mounted on a slide in a PBS filled chamber restricted by vacuum grease. A coverslip was gently pressed down on the lung tissue. Multiphoton excitation was obtained through DeepSee Ti:sapphire lasers (Newport/Spectra-Physics) tuned to 920 nm to excite PE and APC. Whole lung tissue sections were acquired by square optical sections with 15% overlap to provide image areas as large as the whole stained tissue. Emitted fluorescence was detected on an Ultima multiphoton microscope (Prairie Technologies) through 460/50 (second harmonic generation), 665/65 (APC), 595/50 (PE) band-pass filters and non-descanned detectors to

generate 3-color images. The processed data shows $CD8^+$ cells (red, PE), $luciferase^+$ tumor cells (green, APC) and the collagen matrix (blue, second harmonic generation). Images were pre-processed in R statistical computing environment using RStudio and stitched/analyzed with Fiji software.

HMGB1 and Calreticulin In Vitro Assays

The KP L1-3, KP L1-5 and KP L2-9 tumor lines were seeded in tissue culture plates (24 well) one day before treatment with Docetaxel (Dtax, Sigma, 30 μM), Carboplatin (Carbo, Hospira, 500 μM), Oxaliplatin (Oxa, Teva, 300 μM), Mafosfamide (Maf, Sigma, 16.5, 33, 50 μg/ml) and/or Mitoxantrone (Mtx, Sigma, 4 μM) for 24 h. The cell culture plates were then centrifuged and the supernatants collected and stored at -80°C until measuring HMGB1 levels (HMGB1 ELISA Kit, IBL International GmbH). For the calreticulin assay, the cells were harvested from cell culture plates, washed with PBS and fixed with 0.25% formaldehyde for 5 min. Thereafter, the cells were washed twice with cold PBS, incubated with rabbit anti-calreticulin Ab (polyclonal, Abcam), diluted in cold blocking buffer (PBS containing 2% FBS) and incubated for 30 min on ice. The samples were then washed and incubated with anti-rabbit AlexaFluor 488 conjugated Ab (Life Technologies) in blocking buffer for 30 min on ice, followed by a final washing step. The cells were resuspended in cold PBS and investigated by flow cytometry (CyAn ADP analyzer, Beckman Coulter). Dead cells were excluded using DAPI.

In Vivo Drug Treatments

KP mice, KP-OVA mice and C57BL/6 mice bearing KP1.9 lung or flank tumors were either left untreated or received chemotherapeutic drugs once a week for three weeks. The following chemotherapy was given intraperitoneally (i.p.) diluted in 100 μl PBS (or in 200 μl PBS for Paclitaxel (Ptax)): Oxa (2.5 mg/kg of body weight), Cyclophosphamide (Cyc, Sigma, 50 mg/kg of body weight), Ptax (Hospira, 10 mg/kg of body weight) and Carbo (10 mg/kg of body weight).

BALB/c mice bearing CT26 flank tumors received one intratumoral injection of 50 µl PBS or chemotherapeutic drugs (Oxa (1.25 mg/kg of body weight) or Cisplatin (Sigma, 0.25 mg/kg of body weight)). MCA205 flank tumor-bearing C57BL/6 mice were treated with one intratumoral injection of 50 µl PBS or chemotherapy (Doxorubicin (Sigma, 2.9 mg/kg of body weight) or Cisplatin (0.25 mg/kg of body weight)).

Converting drug doses between species is complex and depends on a number of parameters (including species-defined drug metabolism). Nonetheless, according to FDA-guidelines on how to calculate the 'Human Equivalent Dose' from drug doses used in mice (e.g., Guidance for Industry, Estimating the Maximum Safe Starting Dose in Initial Clinical Trials for Therapeutics in Adult Healthy Volunteers, U.S. Department of Health and Human Services, Food and Drug Administration, Center for Drug Evaluation and Research (CDER), Pharmacology and Toxicology, July 2005), the drug concentrations used to treat KP mice correspond to the following in humans: Ptax 0.8 mg/kg; Carbo 0.8 mg/kg; Cyc 4 mg/kg; Oxa 0.2 mg/kg). These are within the range of the concentrations used in the clinic (Cyclophosphamide; Oxaliplatin; Carboplatin; Paclitaxel. In: UpToDate, UpToDate, Waltham, MA. (Accessed on October 27, 2015)) and are therefore unlikely to be unachievable due to toxicity. Thus the chemotherapeutic doses and schedules used in this study were not directly matched for human exposure but are within the range of the concentrations used in the clinic, after converting drug doses between species.

In indicated experiments, immune checkpoint blockade mAbs specific for PD-1 (clone 29F. 1A12, 200 µg/mouse, provided by Dr. G. J. Freeman) and CTLA-4 (clone 9D9, 100 µg/mouse, BioXcell) or isotype control Ab (clone MPC-11, 100 µg/mouse, BioXcell) were applied i.p. in 100 µl PBS. MCA205-bearing C57BL/6 mice received anti-PD-1 mAbs of clone RMP1-14 (250 µg/ mouse, BioXcell).

In Vivo CD8$^+$ Cell Depletion

For depletion of CD8$^+$ T cells, KP mice received anti-CD8 mAb i.p. (clone 53-6.72, 200 µg/mouse, BioXcell). The Ab was diluted in PBS and injections started 3 days before the first chemotherapeutic drug injection and were continued every 2-3 days until the end of the experiment. The efficacy of CD8$^+$ T cell depletion was verified by flow cytometry.

In Vivo experiments with In Vitro Drug Pre-Treated Tumor Cells

Where indicated, KP1.9 tumors cells were exposed to drugs before injection into mice. Specifically, KP1.9 tumor cells were incubated at 37°C for 20 h with either Oxa (300 µM) and Maf (50 µg/ml) or Ptax (100 µM) and Carbo (1000 µM) in cell culture medium (Iscove's DMEM, 10% FBS, 1% penicillin/streptomycin). Viable and dead *in vitro* drug-treated tumor cells ($5x10^5$ cells in 100 µl medium, either treated with Oxa-Maf or Ptax-Carbo) were counted using the trypan blue exclusion method. These cells were administered s.c. to the right flank of C57BL/6 mice on day -8, -4 and -2 before untreated KP1.9 tumor cells ($7x10^5$ cells in 50 µl PBS) were injected i.d. on day 0 to the ipsi- and contralateral flanks. For all of the vaccination time points, the proportion of dead *in vitro* drug-treated tumor cells was higher than 95%. In indicated experiments, mice received therapeutic in addition to prophylactic vaccinations with *in vitro* drug-treated KP1.9 cells on day 5 and 12 post KP1.9 tumor cell injection. Tumor burden of i.d. injected KP1.9 tumor cells was measured by a digital caliper and the volume was calculated ∏/6 x length x width^2.

Recovery of Cells from Murine Tissues

Single cell suspensions were prepared from murine lung, spleen and bone marrow. Lungs were harvested, cut into small pieces using scissors, digested with collagenase type I (0.2 mg/ml, Worthington Biochemical Corporation) in RPMI 1640 medium for 1 h at 37°C while shaking. Where indicated, equally sized pieces of tumor stroma and corresponding tumor-free adjacent tissue were isolated separately from lungs of Oxa-Cyc-treated or untreated tumor-bearing KP

mice using surgical fine scissors. These lung tissue biopsies were transferred into 2 ml reaction tubes, cut into small pieces and digested (0.2 mg/ml, collagenase type I) in RPMI 1640 medium for 30 min at 37°C while shaking. Femurs were harvested, cleaned and the bone marrow was flushed out using a syringe containing cold flow cytometry staining buffer (PBS with 0.5% BSA and 2 mM EDTA). Digested lung tissue as well as harvested spleen and bone marrow tissues were gently meshed through a 40 µM (or 70 µM) cell strainer using a plunger. Red blood cells were removed by Ack lysis (Lonza) according to the manufacturer's instructions. The resulting single-cell suspensions were washed and resuspended in staining buffer until used for flow cytometry.

Flow Cytometry

Single cell suspensions were incubated with FcBlock (TruStain fcX™ anti-mouse CD16/32, clone 93, BioLegend) for 15 min before staining with fluorescent conjugated Abs for 45 min at 4ºC. The cells were washed with flow cytometry staining buffer (PBS, 0.5% BSA, 2 mM EDTA) and 7-aminoactinomycin D (7AAD, Sigma) was used to exclude dead cells. Doublet cells were excluded based on their forward/side scatter properties. The number of lymphocytes and myeloid cells in a given tissue was calculated based on the percentage of each cell type identified by flow cytometry (LSRII, BD Biosciences) multiplied by the total number of cells in each organ (obtained by determining viable cell numbers based on the trypan blue exclusion method). Based on cell marker expression, the following cell types were identified by flow cytometry: $CD8^+$ T cells ($CD45^+CD3^+CD8^+$), Tregs ($CD45^+CD3^+CD4^+Foxp3^+$), B cells ($CD45^+CD19^+$), lymphocyte-like cells ($CD45^+Lin^+CD11b^-$), monocytes ($CD45^+Lin^-CD11b^+Ly\text{-}6C^{hi}$), granulocytes ($CD45^+Lin^+CD11b^+Ly\text{-}6C^{int}$), $CD11b^-$ cells ($CD45^+Lin^-CD11b^-$), $CD11b^+$ cells ($CD45^+CD11b^+$), $CD11b^+CD11c^+$ cells ($CD45^+Lin^-CD11b^+Ly\text{-}6C^-CD11c^+$), $CD11b^+CD11c^-$ cells ($CD45^+Lin^-CD11b^+Ly\text{-}6C^-CD11c^-$), DC-like cells ($Lin^-CD11b^+Gr\text{-}1^-CD11c^+CD103^+$). In general, the lineage (Lin) Ab mix contained the following anti-mouse Abs, purchased from BD Biosciences: CD90.2 (clone 53-2.1), B220 (clone RA3-6B2), NK1.1 (clone PK136), CD49b

(clone DX5), Ter119 (cloneTER-119) and Ly-6G (clone 1A8). The following anti-mouse Abs were used from eBioscience: Foxp3 (clone FJK-16s); from BioLegend: CD45 (clone 30-F11), CD3 (clone 145-2C11), CD8a (clone 53-6.7), CD8b (clone YTS156.7.7), CD11c (clone N418), TLR4 (clone SA15-21), CD103 (clone 2E7) and from BD Biosciences: CD4 (clone RM4-5), CD19 (clone 1D3), Ly-6C (clone AL-21), CD11b (clone M1/70), PD-1 (clone J43) and Gr-1 (clone RB6-8C5). Intracellular staining for Foxp3 was performed using the Cytofix/Cytoperm Fixation/ Permeabilization Kit (BD) according to manufactures procedures. Antigen-specific T cells in lung tissue of KP-OVA mice were stained with H-2Kb/$Ova_{257-264}$ SIINFEKL tretramer (TCMetrix). Flow cytometry data were analyzed in FlowJo v.8.8.7 (Tree Star, Inc.).

Statistics

Results were expressed as mean±SEM. Statistical tests included one-way ANOVA followed by Tukey's or Dunnett's multiple comparison test. When applicable, unpaired one-tailed and two-tailed Student's t tests using Welch's correction for unequal variances were used. Comparison of survival curves was performed with the Log-rank Mantel-Cox test. P values of 0.05 or less were considered to denote significance (*$p<0.05$; **$p<0.01$; ***$p<0.001$; ****$p<0.0001$; ns, not significant).

A3.3 References

1. DuPage, M., Dooley, A. L. & Jacks, T. Conditional mouse lung cancer models using adenoviral or lentiviral delivery of Cre recombinase. *Nat Protoc* **4**, 1064-1072 (2009).

2. DuPage, M. et al. Endogenous T cell responses to antigens expressed in lung adenocarcinomas delay malignant tumor progression. *Cancer Cell* **19**, 72-85 (2011).

3. Köbel, M. et al. The biological and clinical value of p53 expression in pelvic high-grade serous carcinomas. *J Pathol* **222**, 191-198 (2010).